PHD

Aqueous Dye Sensitized Solar Cells

Risbridger, Thomas

Award date:
2013

Awarding institution:
University of Bath

Aqueous Dye Sensitized Solar Cells

Thomas Arthur George Risbridger

A thesis submitted for the degree of Doctor of Philosophy

University of Bath

Department of Chemistry

July 2013

COPYRIGHT

_____

Thomas Risbridger

Abstract

Dye sensitized solar cells (DSSCs) have typically been produced using organic liquids such as acetonitrile as the electrolyte solvent. In real world situations water can permeate into the cell through sealing materials and is also likely to be introduced during the fabrication process. This is a problem as the introduction of water into cells optimized to use an organic solvent tends to be detrimental to cell performance. In this work DSSCs which are optimized to use water as the main electrolyte solvent are produced and characterized. Optimization of aqueous DSSCs resulted in cells with efficiencies up to 3.5% being produced.

In terms of characterization, it is generally seen in this work that aqueous DSSCs produce a lower photocurrent but similar photovoltage compared to DSSCs made using acetonitrile and reasons for this are examined in detail. The decreased ability of the aqueous electrolyte to wet the nanoporous TiO_2 compared to an acetonitrile electrolyte is found to be a key difficulty and several possible solutions to this problem are examined. By measuring the photocurrent output of aqueous cells as a function of xy position it can be seen that there is some dye dissolution near to the electrolyte filling holes. This is thought to be linked to pH and the effect of 4-tert-butylpyridine and may also decrease the photocurrent. It is found that there is little difference between the two types of cells in terms of the conduction band position and the reaction of electrons in the semiconductor with I_3^- in the electrolyte, explaining the similarity in photovoltage.

By altering the pH of the electrolyte in an aqueous cell it is found to be possible to change the TiO_2 conduction band position in the DSSC. This has a significant effect on the open circuit voltage and short circuit current of the cell, though the pH range available is limited by the fact that dye desorbs at high pH values.

Declaration of work done in conjunction with others

Most of the experimental work presented in this thesis was performed by the author. The two exceptions are some of the work on coadsorbates shown in Fig 4.18, 4.19, 4.20, 4.21 and table 4.2 which was done in conjunction with Jonathan McCree-Grey and some of the cyclic voltammetry shown in Fig 8.1, 8.3 and 8.6 which was done in conjunction with Tony Trofimczuk. Jonathan and Tony were undergraduate project students who worked under my supervison in the Cameron lab.

The SECM experiments in section 8.3.5 were performed at The National Physical Laboratory (NPL), Teddington under the supervision of Andy Wain and William Kylberg. The experiments performed using the laser setup for photocurrent/transmission mapping of DSSCs in chapter 5 were also performed at NPL under the supervision of Fernando Castro.

The model used in section 7.2.3.4 was based on suggestions and work by Laurie Peter.

Acknowledgements

I would like to thank Petra first of all for supervising me throughout this project – in particular I am grateful to her for being understanding and supportive when personal issues outside of my studies meant I had to have a few months away, but I am also extremely thankful for her knowledge, guidance and encouragement in the work itself. I would also like to thank Laurie for his input into my work – though I couldn't always keep up with his ideas, I have learnt a lot from his demonstrations and explanations.

I am grateful to Fernando Castro for teaching me to use the laser mapping setup at NPL and also to Andy Wain and William Kylberg for supervising me in the use of the SECM at the same institution. I would like to thank Shaik Zakeeruddin for providing the dye Z105 used in this work and Gerrit Boschloo for providing the dye D35. I would also like to thank Jonathan McCree-Grey and Tony Trofimczuk for their contribution to the results presented in this thesis.

I am grateful to everyone who has been part of the Cameron group over the time I have been in it; Adam, Ana, Becky, Ellie, Huaining, Kat, Kenneth, Pete and Shane and have enjoyed getting to know such a diverse group of people over the course of my studies.

Outside of work I am grateful to my family for their ongoing support. I have been blessed with an incredibly loving family who have looked after me when life has been tough and encouraged me to keep going as well as sharing in many happy times. So thanks Dad, Mum, Laura, Eleanor and Granny and Grandpa, you are all wonderful!

Finally, I'm grateful for my friends outside of chemistry here in Bath who have also been there for me in hard times and with whom I have also shared many happy times with. In particular I want to thank Adam F and Dom who have been there the whole way through and Adam R who has shared the PhD process and all that it entails with me.

List of abbreviations

Abbreviation/Symbol	Description
A	Area
CB	Conduction band
CE	Counter electrode
CIGS	$CuIn(Ga)Se_2$
CTAB	Hexadecyltrimethylammonium bromide
CV	Cyclic voltammetry/voltammogram
C_μ	Chemical capacitance
d	Film thickness
D_0	Diffusion coefficient of free electrons
DCA	Deoxycholic acid
DINHOP	bis-(3, 3-dimethyl-butyl)-phosphinic acid
D_n	Effective diffusion coefficient
DSSC	Dye Sensitized Solar Cell
E_A	Activation energy
E_C	Energy of CB
E_e	Electron energy
E_F	Fermi energy
$E_{F,Redox}$	Redox Fermi energy
E_g	Energy gap between bands in semiconductor
EIS	Electrochemical impedance spectroscopy
F	Faraday constant
f_e	Fermi distribution
FF	Fill factor
FTO	Fluorine-doped tin oxide
g(E)	Trap state distribution
GSCN	Guanidine thiocyanate
HMPA	bis(hydroxymethyl)phosphinic acid
HOMO	Highest occupied molecular orbital
HUPA	11-hydroxyundecyl-1-phosphinic acid
I_0	Illumination intensity

IHP	Inner Helmholtz Plane
IM	Intermolecular
IMPS	Intensity modulated photocurrent spectroscopy
IMVS	Intensity modulated photovoltage spectroscopy
IPCE	Incident photon to charge carrier efficiency
I_{SC}	Short circuit current
ITO	Tin-doped indium oxide
IV	Current-voltage
J_{SC}	Short circuit current density
k_B	Boltzmann constant
k_i	Rate constant for reaction of species i/rate constant for process i
LJP	Liquid junction potential
L_n	Diffusion length
LUMO	Lowest unoccupied molecular orbital
m	Non-ideality factor
MeCN	Acetonitrile
MPN	3-methoxypropionitrile
N_c	Density of states in CB
n_c	Number of free electrons
nE_F	Electron quasi Fermi energy
NREL	National Renewable Energy Laboratory
n_t	Number of trapped electrons
$N_{t,0}$	Total trap state density
OCVD	Open circuit voltage decay
OHP	Outer Helmholtz Plane
OPV	Organic photovoltaics
p	Porosity
PEG	Polyethylene glycol
PES	Photoelectron spectroscopy
P_{max}	Maximum power point
PMII	3-propyl-1-methylimidazolium iodide
PV	Photovoltaic
Pzc	Point of zero charge
q	Charge on an electron

QFE	Quasi Fermi energy
R_{CT}	Charge transfer resistance
RE	Reference electrode
R_{trans}	Transport resistance
SDS	Sodium dodecyl sulphate
SECM	Scanning Electrochemical Microscopy
T	Absolute temperature
T_0	Characteristic temperature
tBP	4-tert-butylpyridine
TCO	Thin conductive oxide
U	Photovoltage
UME	Ultramicroelectrode
VB	Valence band
V_{OC}	Open circuit voltage
WE	Working electrode
W_p	Watt peak
Z	Impedance
η	Efficiency
η	Overpotential
η_{col}	Electron collection efficiency
σ_n	Conductivity
$\sigma_n(\lambda)$	Optical cross section of electrons
τ_0	Electron lifetime of free electrons
τ_n	Effective electron lifetime
Φ	Phase difference
φ_{col}	Electron collection efficiency
φ_{inj}	Quantum efficiency of electron injection
ω	Angular frequency

Contents

Chapter 1: Introduction **1**

1.1 Energy Context 2

1.2 Renewable Energy 3

1.3 Solar Energy 4

1.3.1 First generation 4

1.3.2 Second generation 5

1.3.3 Third generation 6

1.4 Dye Sensitized Solar cells (DSSCs) 6

1.4.1 Device architecture 7

1.4.2 Operating principles and basic performance analysis 8

1.4.3 Semiconductor 11

1.4.4 Dye 12

1.4.4.1 N719 13

1.4.4.2 Z907 14

1.4.4.3 Coadsorbates 15

1.4.5 Cathode 17

1.4.6 Electrolyte 17

1.4.6.1 Solvent and solid systems 17

1.4.6.2 Redox mediator 18

1.4.6.3 Additives 19

1.4.7 Substrates 20

1.4.8 Problems facing DSSCs 20

1.4.9 Water based DSSCs 21

1.5 References 25

Chapter 2: Theory **33**

2.1 Introduction 35

2.2 Semiconductors 35

2.2.1 Band structure 35

2.2.2 Density of electrons 36

2.2.3 Electron state density 37

2.2.4 Electron state occupancy (Electron distribution) 37
2.2.5 n-type Doping 38
2.2.6 Quasi Fermi energy 38
2.2.7 Trapping states 39
2.2.8 Electron transport 40
2.3 Electrochemistry 41
2.3.1 Metal/Electrolyte interface 41
2.3.2 Surface charge 43
2.3.3 Electrochemical reaction 43
2.3.4 Mass transport 44
2.3.5 Electron transfer 44
2.3.6 Overpotential in a semiconductor 46
2.3.7 Three electrode cell 47
2.3.8 Measuring redox potential 48
2.3.9 Cyclic Voltammetry 49
2.3.10 Junction potential 50
2.4 Dye Sensitized Solar Cell operation 53
2.4.1 In the dark 53
2.4.2 Under illumination 54
2.4.2.1 Short circuit 54
2.4.2.2 Open circuit 56
2.5 Dye Sensitized Solar Cell performance 57
2.5.1 IV curve 57
2.5.2 Incident photon to charge carrier efficiency (IPCE) 59
2.5.3 Diffusion length 60
2.5.4 Continuity equation 61
2.6 Techniques 62
2.6.1 Infrared electron trapping density measurements 62
2.6.2 Open Circuit Voltage Decay (OCVD) 64
2.6.3 Frequency modulated techniques 67
2.6.3.1 Electrochemical Impedance Spectroscopy (EIS) 67
2.6.3.1.1 EIS for DSSCs 78

2.6.3.2 Intensity Modulated Photovoltage Spectroscopy (IMVS) 79
2.6.4 Surface tension and contact angle 81
2.6.5 Nanocalc 82
2.7 References 82

Chapter 3: Experimental 87
3.1 Introduction 88
3.2 DSSC fabrication 88
3.3 Film thickness 90
3.4 Current-voltage (IV) curves 90
3.5 IPCE 91
3.6 OCVD 92
3.7 IMVS 92
3.8 EIS 93
3.9 Electrochemistry 94
3.10 IR 94
3.11 pH 96
3.12 Redox potential 96
3.1 Contact angle 96
3.14 UV/Vis 96

Chapter 4: Optimization of aqueous dye sensitized solar cells 99
4.1 Introduction 100
4.2 Results 101
4.2.1 Initial testing; general observations 102
4.2.2 Electrolyte variations; use of additives with ionic liquid 105
4.2.3 Cell filling and nanoporous TiO_2 wetting 109
4.2.3.1 Surfactants – Triton X-100 110
4.2.3.2 Filling technique 112
4.2.3.3 UV treatment 113
4.2.4 Coadsorbates 116
4.2.5 Dye 122
4.3 Conclusions 126

4.4 References 126

Chapter 5: Spatially resolved measurements of dye sensitized solar cells 131

5.1 Introduction 132

5.2 Experimental 133

5.3 Results 136

5.3.1 Photocurrent mapping repeatability 136

5.3.2 Low resolution photocurrent mapping comparing water and acetonitrile DSSCs 140

5.3.3 Higher resolution photocurrent mapping and transmission mapping 145

5.3.3.1 AC5 (Acetonitrile cell, filled by vacuum without heating) 149

5.3.3.2 W4 (water cell, filled under vacuum but with no heat) 150

5.3.3.3 W5 (water cell, vacuum filling with heating) 150

5.3.3.4 Dye desorption 151

5.4 Conclusions 153

5.5 References 154

Chapter 6: Comparing dye sensitized solar cells made with aqueous and acetonitrile-based electrolytes 157

6.1 Introduction 158

6.2 Results 159

6.2.1 Electrochemical Impedance Spectroscopy: Relative conduction band position estimation 161

6.2.1.1 Conductivity 161

6.2.1.2 Chemical capacitance 164

6.2.2 Electrochemical Impedance Spectroscopy: Counter electrode charge transfer 166

6.2.3 Electron lifetime 167

6.2.4 Cell non-ideality 170

6.2.5 Iodide concentration variation 171

6.2.6 Electron diffusion length 178
6.3 Conclusions 180
6.4 References 181

Chapter 7: Influence of pH on the behaviour of aqueous dye sensitized solar cells 183
7.1 Introduction 184
7.2 Results 185
7.2.1 Effect of pH on cell performance 185
7.2.2 Effect of 4-tert-butylpyridine on cell performance 190
7.2.3 Transient infrared measurement of electrons 195
7.2.3.1 Open circuit voltage transients 195
7.2.3.2 Short circuit current transients 198
7.2.3.3 Water cell IR response model 201
7.2.3.4 Continuity equation modelling of trapped electrons under short circuit/open circuit conditions 210
7.3 Conclusions 211
7.4 References 212

Chapter 8: Dye regeneration and mass transport in aqueous dye sensitized solar cells 215
8.1 Introduction 216
8.2 Experimental 216
8.2.1 SECM 217
8.3 Results 217
8.3.1 Dye regeneration 217
8.3.2 Spectroelectrochemistry 225
8.3.3 Diffusion in the electrolyte 228
8.3.3.1 Potential effect 231
8.3.4 Photocurrent limits at high light intensity 236
8.3.5 Scanning Electrochemical Microscopy 241
8.4 Conclusions 246
8.5 References 247

Chapter 9: Conclusions **249**

Chapter 10: Future work **255**
10.1 Outlook 256
10.2 Future experimental work 257
10.3 References 258

Appendices **261**
Appendix A: Dye adsorption/desorption 261
Appendix B: Redox species equilibrium concentrations 265
Appendix C: Calculated Nernst potentials based on equilibrium concentration of redox species 266
Appendix D: Linear sweep measurement of aqueous water cell, scan rate/time dependence 268
Appendix E: Examples of EIS data for DSSCs 270
References 271

Chapter 1: Introduction

1.1 Energy Context
1.2 Renewable Energy
1.3 Solar Energy
    1.3.1 First generation
    1.3.2 Second generation
    1.3.3 Third generation
1.4 Dye Sensitized Solar cells (DSSCs)
    1.4.1 Device architecture
    1.4.2 Operating principles and basic performance analysis
    1.4.3 Semiconductor
    1.4.4 Dye
        1.4.4.1 N719
        1.4.4.2 Z907
        1.4.4.3 Coadsorbates
    1.4.5 Cathode
    1.4.6 Electrolyte
        1.4.6.1 Solvent and solid systems
        1.4.6.2 Redox mediator
        1.4.6.3 Additives
    1.4.7 Substrates
    1.4.8 Problems facing DSSCs
    1.4.9 Water based DSSCs
1.5 References

1.1 Energy context

This section introduces the broad context of the work this thesis is based on, focussing on global power requirements and the importance of meeting them in a manner which has the smallest possible negative impact on the planet.

In recent decades the global demand for energy has increased significantly[1]. Recent reports suggest that global energy consumption has almost doubled since 1973 and this trend of fast growth seems unlikely to change in the foreseeable future. However, as was the case then the production of this energy is still dominated by the use of fossil fuels: coal, oil and gas. Values published by the international energy agency show that in 1973 fossil fuels accounted for 86% of total global energy production and in 2012 81%, with the major difference made up by nuclear power and less than 1% by renewables[2]. The situation is slightly different when considering electricity production; fossil fuel use for this has dropped from 75% to 67% with around a 3% increase by renewable sources, which corresponds to a current global renewable power output of over 300GW (not including hydroelectric power)[3]. Although cleaner power plants are constantly being developed[4], the burning of fossil fuels has a significant negative environmental impact due to the creation of CO_2. Unless this gas can be captured or otherwise removed it contributes to increased global warming which has been predicted to ultimately lead to many damaging global environmental changes[5]. Fossil fuels are also a finite resource and so will eventually run out.

The significant point of the above statistics is that although a very large growth has been observed in the absolute quantity of energy being produced by renewable methods in recent years, this accounts for very little in the overall power production landscape. In order to continue to meet energy demand without significantly damaging the environment, power solutions which have minimal CO_2 output while being cheap and efficient have to be developed and are being developed. Such solutions have to then be implemented and this not only requires production of such systems, but also the will to produce them: this is often affected most significantly by economic factors.

1.2 Renewable energy

Renewable energy refers to power sources which do not use any finite resources that cannot be quickly regenerated, and does not say anything about the environmental impact of a power source. However many renewable energy systems do have a low environmental impact when producing power, though the system lifetime energy, which considers all energy costs including production, is not always taken into account when considering this[6]. There are numerous renewable energy types, three of the main ones are hydro, wind and solar, of which solar is currently the fastest growing. The difficulties in switching to renewable energy are largely due to the effectiveness of fossil fuels. Fossil fuels are usually the most simple and cheap method of producing energy. Though sophisticated technologies are often used to improve the efficiency and effectiveness of the various processes, the overall idea is very straightforward. Once the fuel in question has been obtained, which is usually through drilling or mining, it is transported to where it is required and then burnt to release its energy. These fuels also tend to have a high energy density and some, particularly oil, are easy to store, making them ideal as fuels for transport. The fact that they have been in use for a long time also means that infrastructure is based around their use, and cost of production is low.

Renewable energy tends to cost more to produce and be more difficult to implement, usually requiring specialised equipment to harvest the relevant energy source. Generally, it utilises large but ‘low density’ power sources; for example wind, where a large number of turbines are required in order to generate significant levels of power; or solar, where a large surface area is required. As such, there is significant ongoing effort to develop renewable sources, to make them cheaper and more effective[7]. It has been suggested that the technology is available to move significantly towards using a much higher proportion of renewable energy sources, but that a good deal more political will is required to make this a reality. However, there are some very good examples of countries moving significantly towards renewable energy sources. Germany has targets of 80% renewable energy production by 2050[8], while Denmark already produces 22% of its power through such sources[9]. Through the

utilisation of geothermal energy, Iceland currently produce 100% of its electricity through renewable sources[10].

1.3 Solar energy

Directly utilising light incident on the earth from the sun appears to be a very attractive method of energy production as it is such a large, long term energy resource. It has been estimated that approximately 1.2×10^{17}W of energy are incident on the earth's surface from the sun[11] and this is thousands of times more than global energy demand. However, this is over a very large surface area, and the actual power density is around several hundred Watts/m^2. Practically then, it is not as simple a resource to use as might be thought initially.

Since the first modern solar cell was produced in the 1950s with an efficiency of around 6%[12], work in the field has gradually increased. Initially this was not seen as an important area of study (with the exception of a few niche applications) largely due to the dominance of fossil fuels. As awareness about environmental issues and resource limits have increased, research into solar energy for large scale global power production has become increasingly important[13]. Solar technology as it currently stands tends to be split into three 'generations' of devices; first, second and third.

1.3.1 First generation

Solar cells that fall into this category are made from either single crystal or poly-crystalline silicon, fabricated from silicon wafers. Through separate doping of the bulk and one side of the silicon, a single p-n junction is created leading to photoactivity. At present the record efficiency for this class of materials is 25.0% (single crystal) for a lab cell and 22.9% (single crystal) for a module[14]. One of the major disadvantages of these types of devices is a low absorption coefficient, meaning thick wafers are required to absorb sufficient light to make the device useful – in excess of 200 μm. Si wafers have a very high energy requirement to process and as such this means there is an inherent high cost step in producing this type of cell. It has been suggested that in order to be

competitive economically, solar energy needs to be produced at a cost of around \$0.33/W_p[15] (where W_p is Watt-peak, the output power of a device at its maximum power point (see section 1.4.2)); in 2008 these devices produced energy at around \$4/W[13b]. Work by Rao et al. to reduce the thickness of Si wafers produced has led to efficiencies of about 14% for 25µm films. The group anticipates that processing will improve this to around 20% with the potential to produce power at around \$0.30/W_p[16]. At present, first generation solar cells are the most common in commercial production, accounting for around 85% of solar cell production in 2009[13a].

1.3.2 Second generation

A clear strategy for reducing device cost is to reduce the amount of material required. Second generation cells tend to be thin film devices and are made using a variety of different materials. The absorber materials have high absorption coefficients and tend to be deposited onto a substrate, rather than being made from a Si wafer. Examples include CdTe/CdS, GaAs, $CuIn(Ga)Se_2$ (CIGS), amorphous-Si and polycrystalline-Si. Record efficiencies vary in the group; GaAs cells have been made with efficiencies up to 28.8%[14], CdTe up to 17.3%[14] and CIGS up to 20.3%[17]. However, these all have problems in terms of high toxicity precursors or low material abundance and often require high vacuum techniques to produce, which will increase prices and environmental concerns if they start to be produced on a very large scale. At present production levels, CdTe cells have a price of about \$0.85/W_p. Second generation devices based on Si do not have any of these toxicity or feedstock problems, but efficiencies for these devices tend to be lower - about 10%[14]. There is also work in progress that looks to use materials that are more abundant and less toxic. One example is $Cu_2ZnSn(S,Se)_4$ (CZTS) with a recently published efficiency of 11.1%[18]. Production of this currently utilises the very dangerous chemical hydrazine, so it is not yet a commercialised system. Also included within the second generation group are slightly different technologies which utilise different materials including liquids. Examples include Dye Sensitized Solar Cells (DSSC) and Organic Photovoltaics (OPV) which both use very thin films. OPV devices use organic materials to form p-n junctions which have potential to be low cost and currently have demonstrated

efficiency up to 11.1% (National Renewable Energy Laboratory (NREL)). Record published DSSC devices have produced efficiencies of 12.3%[19] and will be discussed in more detail below. Devices similar to DSSCs but sensitized with perovskite materials have very recently seen a great deal of interest and recent progress in this area has been considerable. Solid state perovskite sensitized solar cell devices have been developed with efficiencies up to 15%[20].

1.3.3 Third Generation

Generally, cells in this category aim to get round some of the efficiency limits which effect the previous generations of cells particularly the Shockley–Queisser limit, while maintaining a low production cost. One of the losses experienced by solar cells is due to the fact that not all the energy incident on the cell can be easily used. Wavelengths of a lower energy than the band gap will not be absorbed, whereas some energy will be lost when photons with wavelengths of a higher energy than the device band gap are absorbed due to thermal relaxation of the excited electrons in the conduction band. There are several different approaches taken to try to minimise these losses. One is to use multiple junction devices, where several different material layers with different band gaps are combined in the same cell; another is to stack several single junction devices with complementary band gaps and connect them externally. A second is to create devices which produce more than one electron from photons with energy greater than the band gap, and a third is to reduce the thermal relaxation rate and make use of the higher energy electrons[13a,21]. High efficiency devices based on multiple junctions have reached 37.5% (InGaP/GaAs/InGaAs)[14], but these tend to be very expensive.

1.4 Dye Sensitized Solar Cells

The first design for a high efficiency DSSC is usually accredited to Gratzel and O'Regan[22]. Their production in 1991 of a device with an efficiency of 7.1% opened up a potential new route for producing low cost solar cells; the semiconductor materials used to produce these devices are cheap compared to Si wafers, and in comparison the production processes are not energy intensive. A 2007 study suggested that for large scale production of DSSCs,

prices would be in the region of 2.7-1.6€/W_p (3.5-2.1$/$W_p$) based on current technology and would fall to 1.6-0.9€/W_p (2.1-1.2$/$W_p$) due to projected reduction in material costs[23]. One of the leading companies in DSSC research, 3GSolar, has recently published an initial production cost goal of $1.25/$W_p$ for a large DSSC plant[24], with a longer term goal of $0.35/$W_p$[25]. At the present time however, DSSCs are not yet in large scale production. There are a number of companies including Dyesol, 3G solar and G24i Power Ltd which are using different methods to produce DSSCs for niche applications – such as on flexible substrates, or for indoor applications where the particular properties of the devices demonstrate an advantage over other technologies. Partnerships with other industries (for example between Dyesol and Tata Steel) are also being developed to produce integrated building materials which comprise DSSCs built directly onto products such as metal roof panels. In real world terms, it has recently been pointed out that dye cells show their best performance at a temperature near to a realistic normal operating temperature which is not the case for most other photovoltaic (PV) technologies[26]. DSSCs also tend to have a better low light response than other PVs as well as a better low incident angle light response[26].

1.4.1 Device architecture

DSSCs are made based on a variation of the following structure (Fig. 1.1). A transparent substrate is first coated with a thin conductive oxide (TCO) layer. A further thin layer of a metal oxide (termed a blocking layer) is deposited onto the substrate followed by a thicker layer of nano-porous metal oxide semiconductor measuring ~10 μm. In some cases a further thin metal oxide layer is then deposited on top of this. All of these are heated to anneal and produce good electrical contact. A sensitizing dye is then applied, usually via solution dyeing, to the nanoporous semiconductor. The cathode is produced on a conducting substrate by depositing a thin layer of a catalytic material, typically platinum, and the two electrodes are sealed together using a spacer. An ionic conduction material is introduced between the two electrodes – this tends to be liquid based containing a dissolved redox mediator, though other variations are considered below.

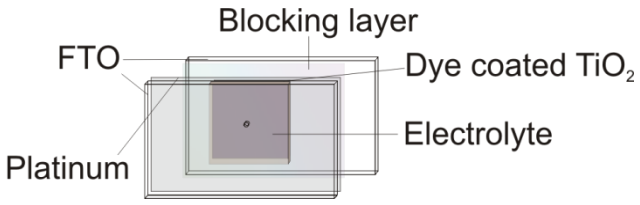

Fig 1.1 Standard DSSC architecture based on FTO coated glass substrate. Photoanode typically consists of nanoporous TiO_2 film (~10μm) dyed in sensitizing dye deposited onto compact TiO_2 'blocking layer' deposited onto substrate. Counter electrode typically consists of thin Pt layer deposited onto substrate. Electrolyte typically consists of I_2 and I^- in acetonitrile solvent and may contain additives such as tBP and GSCN.

1.4.2 Operating principles and basic performance analysis

A more detailed explanation of the dye cell operation and background physics/chemistry will be given in chapter 2. A basic explanation of the working principles is given here in order to better introduce the developments seen in recent decades regarding the various components.

Under incident illumination (Fig 1.2), a photon can be absorbed by a dye molecule resulting in excitation of an electron in that molecule to a higher energy state. Injection of this electron into the semiconductor can then occur, typically with high quantum efficiency (φ_{inj}). This electron diffuses through the semiconductor film until it reaches the TCO or combines with a hole in a loss mechanism. The now oxidised dye molecule is reduced by the reduced form of the redox mediator which then diffuses to the counter electrode and recombines with an electron which has travelled round the external circuit. Within this process there are a number of possible loss pathways (Fig 1.3). These include the relaxation of the dye excited state before injection, the recombination of an injected electron with an oxidised dye molecule and the reaction of an injected electron with the oxidised form of the redox mediator (see scheme 2.3).

The simplest performance measurements of a DSSC are based on the current –voltage (IV) curve (Fig 1.4), obtained by operating the cell under illumination

while varying the resistance between the electrodes. Three important parameters are obtained from such analysis; the open circuit voltage (V_{OC}), the short circuit current (I_{SC}) and the fill factor (FF). Fill factor is the ratio between actual maximum power or maximum power point (P_{max}) and the theoretical maximum power calculated from V_{OC} and I_{SC} (Equation 1.1). V_{OC} is the voltage at which the electron injection flux into the semiconductor is the same as the electron loss flux from the semiconductor but not to the substrate – i.e. where the output current is zero, and is equal to the potential difference between the electron quasi Fermi Energy (nE_F) in the semiconductor and the Nernst potential of the redox couple (Fig 1.2).

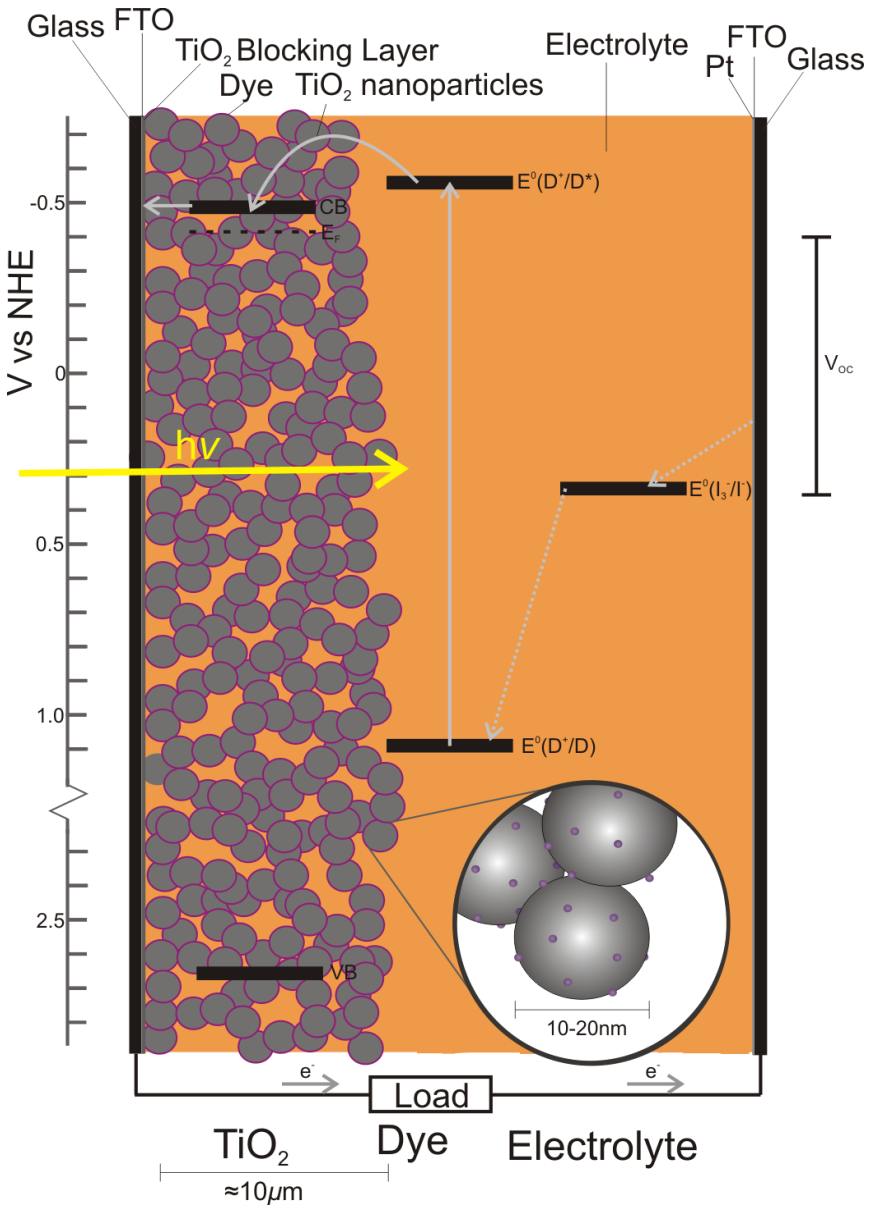

Fig 1.2 Energy level diagram for DSSC. Values based on refs[27,28]. Yellow line represents incident illumination, grey lines represent movement of electrons upon illumination.

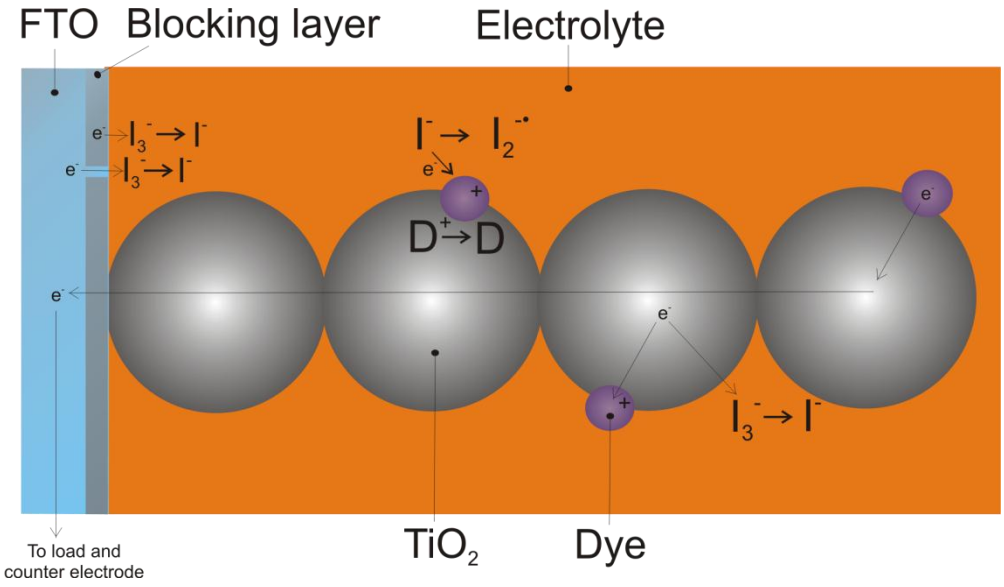

Fig 1.3 Possible mechanisms for electron loss after injection into semiconductor. Regeneration of oxidised dye by I^- is also shown.

I_{SC} is the current produced when there is no resistance between the electrodes, i.e. at a potential of zero. These three parameters are used to calculate cell efficiency (η) which is the ratio of cell output power to illumination input power (I_0) (Equation 1.2). Note that in most cases the short circuit current density (J_{SC}) (Equation 1.3) is used rather than I_{SC} to give a more useful value of photocurrent as it takes into account the cell area (A). In this case the illumination input power density is used to calculate efficiency.

$$FF = \frac{P_{\max}}{J_{SC} \times V_{OC}} \qquad \text{Equation 1.1}$$

$$\eta = \frac{J_{SC} \times V_{OC} \times FF}{I_0} \qquad \text{Equation 1.2}$$

$$J_{SC} = \frac{I_{SC}}{A} \qquad \text{Equation 1.3}$$

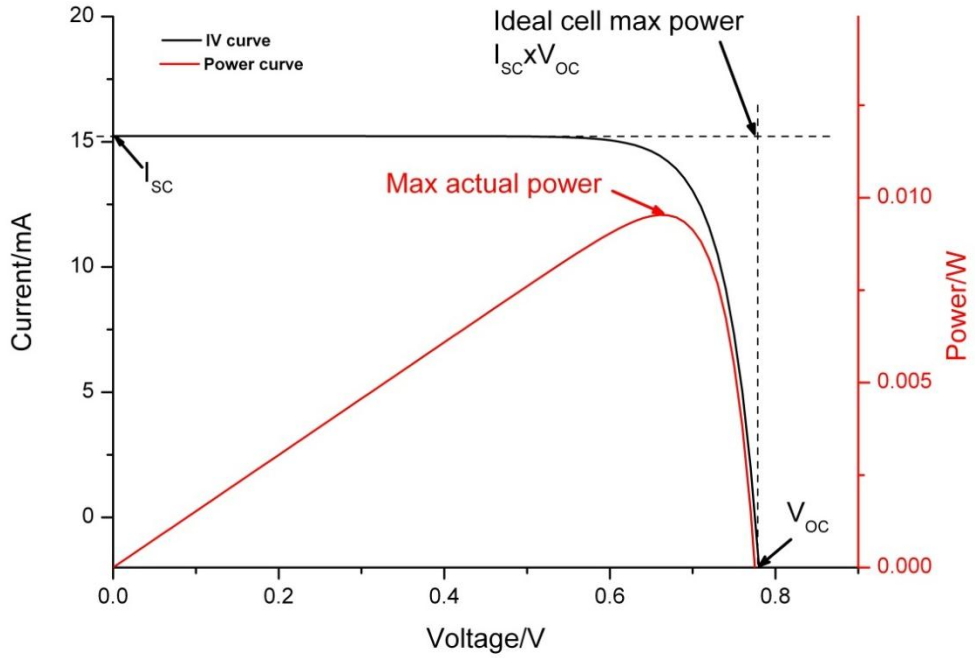

Fig 1.4 Simulated IV curve (black) and simulated power curve (red) showing performance characteristics including short circuit current (I_{SC}), open circuit voltage (V_{OC}) and max power point.

1.4.3 Semiconductor

In many other photovoltaic technologies the semiconductor is involved in several processes including light absorption, electron-hole pair generation, electron transport and hole transport. In a dye cell these events occur in different parts of the cell and in different materials, relaxing some of the material constraints that are otherwise present[29]. In the dye cell, the semiconductor plays a part in electron/hole separation (with the dye) and then in electron transport. As mentioned, it is also possible for free electrons in the semiconductor to combine with various oxidised species.

Typically, DSSCs use a 10 μm semiconductor layer made up of approximately 20 nm diameter nanoparticles of TiO_2. This use of a mesoporous semiconductor structure and the subsequent high surface area was one of the significant developments that made DSSCs possible, enabling a significant increase in the amount of adsorbed dye for a given cell area and greatly increasing light absorption[22]. Since this development, research based around the semiconductor has often focussed on morphology. Various attempts have been made to control semiconductor structure – for example by fabricating

nanotubes[30] so achieving longer diffusion lengths or developing other nanostructures with a high surface area[31]. However, the most successful developments related to the semiconductor have been the $TiCl_4$ treatment[28b] and using a scattering layer. The $TiCl_4$ treatment involves depositing a thin layer of very pure TiO_2 onto the mesoporous TiO_2, increasing dye adsorption and electron lifetime. A scattering layer is a thin layer of larger semiconductor particles of around 300 nm which are deposited onto the first layer. These scatter light back into the film, so increasing path length and light absorption therefore improving cell efficiency[32].

Over the period of their development, TiO_2 has been the semiconductor of choice for DSSCs. TiO_2 is a wide band gap semiconductor with a band gap of 3.2eV when in the anatase form[33], putting its light absorption in the UV region. Strong binding to dye molecules can be achieved, usually through carboxylate bonds, with several different bonding configurations being possible[34]. Two other metal oxides that have been examined for use in DSSCs are ZnO and SnO_2. ZnO has better electron transport properties[35] but reduced stability compared to TiO_2. Zn^{2+} is dissolved into the electrolyte due to the acidity of the dye binding group resulting ultimately in lower electron injection efficiency[36]. One reason for pursuing its use has been because large varieties of nanostructure can be produced with it[34a], and cells with performances up to around 7% have now been produced [35]. SnO_2 has a larger band gap but lower conduction band (CB) edge compared to TiO_2 and ZnO[33], reducing its effectiveness for systems optimized for these oxides. The best results for SnO_2 systems to date are 3.9%[37].

1.4.4 Dye

For a dye to give good performance in a DSSC there are several requirements. As the light harvesting part of the cell it must have strong absorption over the visible spectrum. It must have a readily accessible excited state that is higher in energy than the conduction band of the semiconductor that it is bound to, and it must exhibit strong binding to that semiconductor to facilitate high electron injection efficiency and produce stable cells over long periods. Its oxidised form must be stable enough so that it does not break down before the dye is

regenerated, and the dye must be stable enough to permit a very high number of turnovers before it degrades. How well a dye performs in terms of these parameters will vary depending on its environment, so dyes perform better or worse depending on the other materials used in the cell. Dye development has been a very large research focus within the DSSC field. Dyes developed include metal complexes based around ruthenium[28b,38] which are the most common, other metal complexes[39], organic dyes such as indolene[40] based compounds and so called donor-π-bridge-acceptor dyes[41]. The current record DSSC efficiency of 12.3% is held for a system which uses a Zinc based porphyrin dye[19]. Several dyes have been used in the work detailed in this thesis and the two main ones N719 and Z907 will now be considered in more detail.

1.4.4.1 N719

The N719[42] dye (Fig 1.5a) is an analogue of one of the first dyes used in DSSCs, N3[28b] which is made up of two bipyridyl ligands each having two carboxylic acid binding groups and two isothiocyanate ligands all coordinated to a central Ru(II) ion as shown in Fig 1.5b. However whilst the –COOH groups in N3 are fully protonated, in N719 one of the carboxylic groups on each bipyridyl ligand is deprotonated, with the subsequent carboxylate groups charge compensated by associated tetrabutylammonium cations. The carboxylic acid groups have strong binding with TiO_2, and subsequently fast electron injection rates are observed on a time scale of ≤57fs[43], with η_{inj} values very close to unity[28b]. This is aided by the relative energetic and spatial position of the dye LUMO relative to the TiO_2 conduction band position; the LUMO is approximately 0.15eV higher in energy[29]. In terms of excitation, the lowest energy electronic transition is a metal to ligand charge transfer, meaning the excited state electron density is based largely on the ligand to which the binding groups are attached, and this is an important factor leading to fast charge transfer[44]. A second useful characteristic of the dye relates to the recombination reaction. Once an electron has been injected into TiO_2, it might be expected to quickly react with the now oxidised dye. The rate of this reaction is in fact much slower than the rate of injection. This is largely due to the nature of the electron transfer between electrons in TiO_2 and the dye, which goes into a d orbital localised on the Ru metal, which is spatially removed from the TiO_2.

It is also slowed due to the orbital size reduction on going from Ru(II) to Ru(III)[44]. In addition, the potential of the $E(D^+/D)$ relative to $E(I_3^-/I^-)$ allows for fast dye regeneration (≤10 μs) after electron injection[45]. N719 is probably the most readily available DSSC dye, and as it has been shown to reproducibly give efficiencies of >10%[46] it is a sensible candidate for lab based DSSC work.

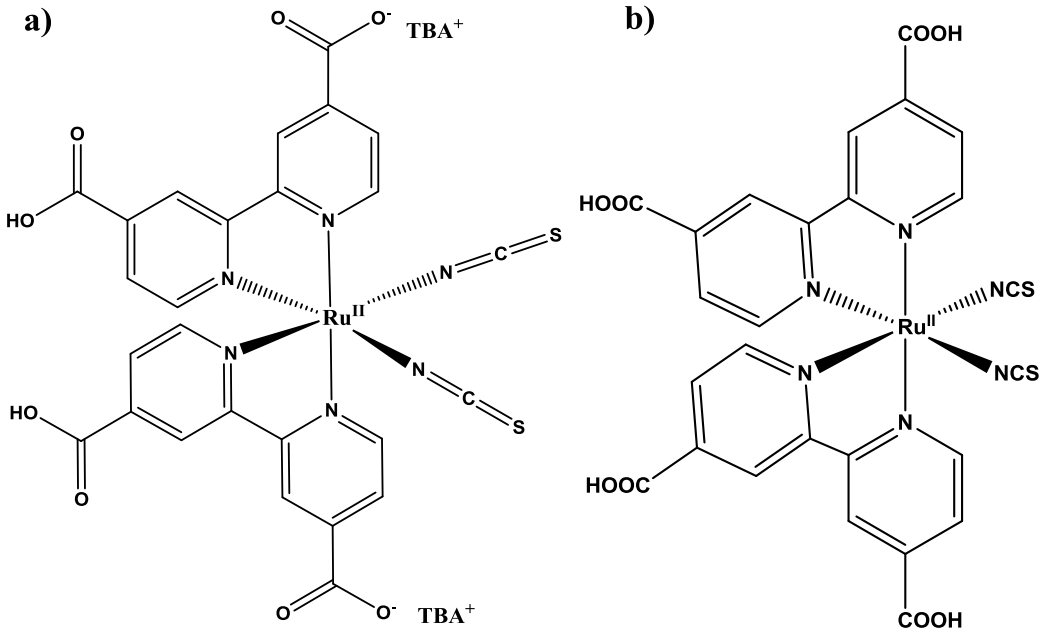

Fig 1.5 Ruthenium dyes a) N719, b) N3

1.4.4.2 Z907

The Z907[47] dye (Fig 1.6) is a further analogue of the N3 and N719 dyes with one long alkyl chain attached to each of both of the bipyridine groups. These groups increase the hydrophobicity of the dye, decreasing dye desorption relative to N719 and N3 when water is present. This infers extra stability when used in a dye cell which either has a small amount of water ingress over time, or that purposely uses water in the electrolyte. Recent state of the art devices made using this dye have achieved efficiencies of over 10.5%[48].

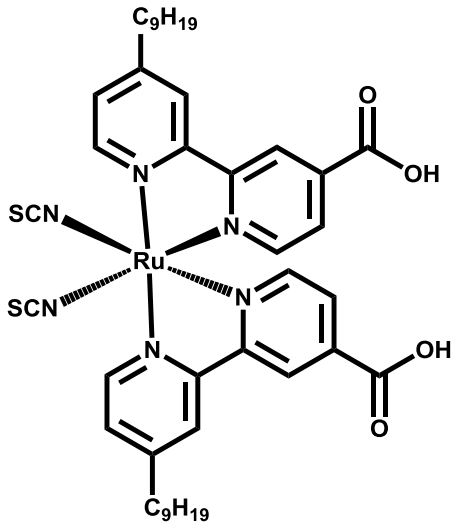

Fig 1.6 Ruthenium dye Z907

1.4.4.3 Coadsorbates

Along with the dye, several papers have been published where a second material such as chenodeoxycholic acid (Fig 1.7) or bis-(3, 3-dimethyl-butyl)-phosphinic acid (DINHOP) (Fig 1.8) is adsorbed onto the semiconductor as well as the dye. These coadsorbates have been found to have a number of effects on DSSCs. The first is related to aggregation between dye molecules. It has been seen with certain dyes that aggregates between molecules can form[49]. This has been observed to have several effects depending on the particular system. When an aggregate forms all the dye molecules absorb light, but the quantum efficiency of energy transfer to the semiconductor is lower than for monomers[49a]. This means less light is converted to electricity. In some cases aggregation can shift the absorption spectrum of the dye; a beneficial red shift was observed in the case of some indoline dyes[50] for example. Coadsorbate molecules tend to have binding groups similar to dyes such as carboxylic acid or phosphoric acid groups and also have long or bulky chains – similar bulky groups are often used in dye design[40]. When used, these are able to prevent aggregation by preventing the close approach of the dye molecules, so giving control over aggregate formation.

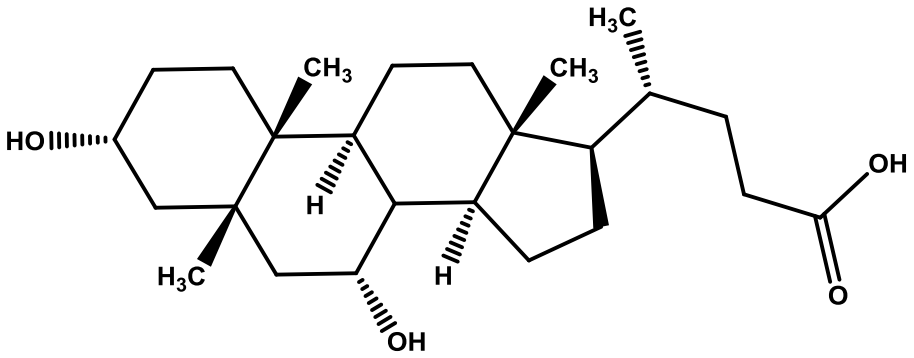

Fig 1.7 Chenodeoxycholic acid (coadsorbate).

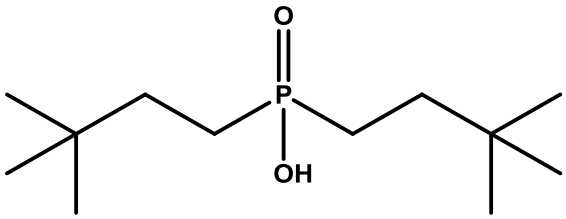

Fig 1.8 DINHOP (coadsorbate).

A second effect is related to the acidic nature of most coadsorbates. It has been suggested that this has an effect on the position of the TiO_2 conduction band (CB) edge, which is different for different coadsorbates. Deoxycholic acid was found to induce a small positive change in the potential of the CB due to the effect of the adsorbed coadsorbates and protons on the semiconductor surface charge, which had an effect on V_{OC}[51]. It seems likely that this effect is linked to the counter ion; when similar measurements were taken for tetrabutylammonium chenodeoxycholate, a negative change in the CB potential was observed[52]. A third effect is related to the back reaction between electrons in the semiconductor and the oxidised species in the redox mediator. It seems likely that coadsorbates can act to suppress this reaction by acting as a physical block preventing the approach of the oxidised species[53]. Different results have been seen for this effect however, and while significant reductions in back reaction rate have been observed[51], there are some cases where the use of coadsorbate seems to speed up this reaction[52]. A final effect worth noting is that coadsorbate molecules compete with dye molecules for surface adsorption sites, so lowering dye coverage[52]. However in most cases using coadsorbates leads to a small overall increase in DSSC performance[40,54].

1.4.5 Cathode

The main requirement of the counter electrode is to provide a stable electrode that enables facile electron transfer to occur reducing the oxidised form of the mediator. Materials are used which allow or enable fast electron transfer. Platinum is by far the most common[34a], but some other materials such as carbon have been considered[55].

1.4.6 Electrolyte

A great deal of work has been done in the previous two decades to improve the electrolyte composition to enhance DSSC performance. Despite this, the standard system used is still remarkably similar to that used in early publications. The most common systems use an organic solvent, a dissolved redox mediator – usually iodine and an iodide source, and have several other dissolved additives. The key task the electrolyte needs to perform is the fast transportation of positive charges from the dye where they are produced to the counter electrode. It is important that as far as possible these positive charges are prevented from recombining with electrons in the semiconductor. The open circuit potential of a DSSC is the difference between the Nernst potential of the redox couple in the electrolyte and the electron quasi Fermi energy (nE_F) in the semiconductor.

1.4.6.1 Solvent and solid systems

DSSCs have most often been based around liquid solvent systems such as acetonitrile, 3-methoxypropionitrile (MPN) and propylene carbonate[34a]. These have low viscosity allowing rapid diffusion of charge carriers so giving good performance. They also solubilise the standard redox mediators well without desorbing the sensitizer from the surface. The current highest efficiency DSSCs use variations of these liquid solvent systems[19]. It is important for the electrolyte to be stable over a long time and also to not leak out of the cell. One of the potential problems with organic liquids is their high volatility, which can lead to electrolyte evaporation[56]. One development that aims to get round this stability issue is the use of ionic liquids, which are significantly less volatile

while still showing reasonable diffusion rates, and devices made using these have shown efficiencies of 8.2%[57]. However, it seems likely that diffusion will ultimately be an issue with these compounds[34a,58]. Water is a solvent that has recently seen renewed interest, and will be considered in more detail in section 1.4.9. A slightly different approach which particularly aims to get round stability issues is to gel or polymerise the electrolyte system. The redox mediator still transports the charge in this case, but the system is much more solid. Using poly(vinylidenefluoride-*co*-hexafluoropropylene) to cause solidification of an MPN based electrolyte, a device performance of 6.1% was obtained by Wang and co-workers[47]. More recently, Huang et al achieved 7.6% using cyanoethylated hydroxypropyl cellulose and an ionic liquid system.[59] A final type of system that is under development uses solid hole conductors. This completely moves away from volatile liquids, and instead of transporting charge by molecular diffusion a charge hopping mechanism occurs[34a]. The most successful variants have used the polymeric materials 2,2′,7,7′-tetrakis(*N*,*N*-di-*p*-methoxyphenylamine)-9,9′-spirobifluorene (spiro-MeOTAD), with a highest efficiency of 5.1%[60].

1.4.6.2 Redox mediator

By far the most commonly used redox system is a mixture of iodine and iodide, setting up a redox potential based on I^-/I_3^-. It has been shown to be very effective at quickly regenerating many dyes from their oxidised state while at the same time the loss mechanism involving the reaction between electrons in the semiconductor and I_3^-has very slow kinetics so minimizes losses[61]. In most organic solvent systems diffusion of charge carrying species is also fast and does not limit the cell performance. However, it does have some disadvantages. A large overpotential is required for dye regeneration due to the complexity of the mechanism, reducing the maximum obtainable photovoltage[27]; iodine is also very corrosive to some metals which could potentially otherwise be used in DSSCs on electrodes to reduce resistance[62]. Although the I_2 source is simply iodine, various different materials have been used as the iodide source. The various different cations present in these materials have been shown to have a marked effect on cell performance, for example on the CB position and

recombination characteristics[63]. Li^+ is reported to be able to adsorb or intercalate into the TiO_2 lattice when electrons are injected as a charge compensation mechanism, leading to a change in the surface charge and subsequently lowering the CB position[63b,64].

For a long time it seemed that despite the limitations, no other redox couple would outperform the I^-/I_3^-system. Various different systems have been studied with varying degrees of success. Using a Br^-/Br_3^- redox system, Wang et al found they could generate an improved efficiency for an eosin-Y sensitized system compared to the I^-/I_3^- system[65]. Using the same redox couple with carbazole dyes, Teng et al generated voltages greater than 1V, and achieved efficiencies of 5.2%[66] - better than the I^-/I_3^- system using the same dyes. Interesting results have also been obtained using the pseudo-halogen system based on SeCN-/$(SeCN)_3^-$. Although earlier results using solvents were disappointing due to slow dye regeneration[67], Wang et al later showed that high efficiencies of over 8% could be achieved when the $SeCN^-$ source was an ionic liquid[68]. By carefully choosing sensitizer properties, Daeneke et al achieved efficiencies of 7.5% using the very common one electron ferrocene/ferrocenium redox couple which has advantages in terms of its tuneability and non-corrosive nature[69], demonstrating along with some of the systems mentioned above that the whole DSSC often needs to be adjusted to effectively incorporate different materials, particularly in terms of energy level matching. The most promising new type of redox mediators are based on complexes utilising the one electron Co(II)/Co(III) couple. Early work here saw efficiencies of 5.2%[70] and now by matching a Co(II)/Co(III) tris(bipyridyl) complex with a zinc porphyrin dye, Yella et al have achieved the current dye cell record of 12.3%[19].

1.4.6.3 Additives

By including additional materials in the electrolyte, performance improvements have often been achieved. One of the most common additives, first used in 1993 where it was shown to increase the V_{OC} in a cell by 280mV[28b], is 4-*tert*-butylpyridine (tBP). The reason for this V_{OC} change has been seen to be due firstly to a negative conduction band shift, indirectly caused by tBP acting as a

base so reducing proton adsorption at the TiO_2 surface and by adsorbing itself onto the surface so reducing cation adsorption (e.g. Li^+ when present or H^+). Secondly tBP is shown to be able to decrease the reaction between electrons in the semiconductor and I_3^- by blocking the surface[71]. One of the effects of shifting the CB potential has been shown to be a decrease in φ_{inj}[72].

Another commonly used additive is guanidine thiocyanate (GSCN). The compound has been shown to cause positive CB position changes[64,73], which have been suggested to cause a higher φ_{inj} by Zhang et al, based on current density measurements[73]. It has also been seen that recombination is reduced by this compound[64,73]. Finally, it has been suggested that GSCN in some way facilitates the self-assembly of dye molecules in the DSSC[74].

1.4.7 Substrates

The requirements of the conductive substrate are transparency, conductivity and stability for the photoanode, and conductivity and stability for the cathode (assuming illumination from the photoanode side). The material most often used for this is glass coated with a transparent layer of conducting oxide – the most common being tin-doped indium oxide (ITO) and fluorine-doped tin oxide (FTO)[75] which both exhibit low sheet resistance and high transparency. Various other materials have been considered, particularly flexible substrates including indium tin oxide-coated polyethylene naphthalate (ITO-PEN)[76], indium tin oxide-coated poly(ethylene terephthalate) (ITO-PET)[77] and Ti foil[78]. Stainless steel has also been used as a CE substrate, giving efficiencies of above 7.5%[79] and recently cells were produced on glass paper substrates, though with low efficiency[80].

1.4.8 Problems facing DSSCs

A number of problems need to be overcome before DSSCs can be a competitive PV technology. Module and cell efficiencies are still low compared to most other technologies, meaning DSSCs are not yet generally seen as a useful power system. Although they still have potential to be a low cost system as demonstrated by the cost figures shown in section 1.4, DSSC research has

seen only limited efficiency improvements in recent years, with the recent highest efficiency systems requiring many synthesis steps to produce[19]. At a fundamental level there is potential for significant efficiency improvements reaching 15%[34a] and which will likely require alteration of several components at once[61], but this has yet to be realised. Device stability is also an issue, and the loss of electrolyte and ingress of water have the potential to cause problems[56] in real systems, particularly on plastic substrates[81]. However, some results from long term stability tests are positive; Harikisun and Desilvestro have suggested that DSSCs could be stable for up to 40 years[82], while long term outdoor tests by Kato et al on low efficiency cells showed there was no loss of J_{SC}, but a slow deterioration of V_{OC} over more than two years[83].

1.4.9 Water based DSSCs

In early DSSC research, before high efficiency devices using high surface area semiconductors were produced, water was the electrolyte solvent of choice[84]. Early results using water as solvent tended to be reported only under monochromatic light and these gave power efficiencies up to 12%, with polychromatic power efficiencies of 1.2% by 1988[85]. However, in switching to organic solvents in the early 90s, a step change improvement in performance was observed[22] and water as a solvent has since been largely abandoned. A few studies have been performed, but it is generally seen that water is detrimental to DSSC performance.

As a result of the issues caused by the presence of water in DSSCs, caused due to both ingress over time and the practically unavoidable adsorption during production[62], and loss of volatile solvents, it has become more important to understand the effect of water on DSSCs and to negate these problems. Two main experimental approaches have been observed; to add a small amount of water and determine its effect on the cell[63b]; or to use water as a solvent and attempt to improve the efficiency of the system[86].

Several papers have focussed on understanding the effect water has on cell behaviour. Enright et al demonstrated a positive shift in the CB potential upon the addition of water to non-protic solvent systems based on flat-band potential

measurements[87] as highlighted by Liu et al, who noticed that the effect of water on photovoltage for DSSCs they had made was opposite to what they expected from this effect[63b]. They therefore suggested that adsorption of water onto the semiconductor surface could reduce the back reaction, leading to the increase in photovoltage they observed[63b]. Similar observations were recently published by Zhu et al, who estimated the CB shifts positively by about 40mV when 10 vol% water is added to an organic solvent due to increased local proton concentration at the semiconductor surface[88]. They also saw an increase in charge transfer resistance at the semiconductor|electrolyte interface, corresponding to reduced back reaction, and subsequently predicted an increase in charge-collection efficiency[88]. Mikoshiba et al similarly saw improvements in cell performance when using up to 10% water content in ionic liquid electrolytes, which they attributed to improvements in diffusion rates - though it is unclear if their cells were limited by diffusion – and a decrease in resistance at the counter electrode[89].

A second area of consideration has been the effect of water on dye and dye adsorption. Zakeeruddin reported on the stability of two different dyes in water in 2002, demonstrating a marked difference based on their water solubility. Cells made with the N3 dye were shown to degrade quickly in the presence of water, whereas cells made with a dye containing long alkyl chains were shown to be significantly more stable[90]. Liu et al interpret a drop in photocurrent in cells made with 10% water to be caused by either the dissolution of dye caused by the presence of water, or a weakening of dye bonding and subsequent reduction in φ_{inj} caused by water[63b]. This seems likely as when Zhu et al performed similar experiments using a more hydrophobic dye, they saw no drop in photocurrent when water concentration was increased[88]. This explanation was confirmed by Hahlin et al using photoelectron spectroscopy (PES), who determined that the amount of hydrophobic Z907 dye present on the semiconductor surface stayed essentially the same when small amounts of water (30%) were added to the ethanol (EtOH) solution in which measurements were done, whereas up to 20% of the dye was lost for a non-hydrophobic dye (N719)[91]. Though perhaps not relevant to the bulk of dyes used in DSSCs, Pan et al have shown that the use of water as a controlled pre-treatment can alter the surface of TiO_2 and induce a change in binding mode for cationic dyes. This

can have a beneficial effect on dye adsorption, and also was seen to blue shift the absorption spectrum[92].

The use of hydrophobic dyes has been one approach that leads to stronger binding of dyes in water systems. A second approach is to alter the binding group. As mentioned earlier, the most typically used binding group is the carboxylic acid group, however dye with some other groups have also been developed. One example is to use an hydroxamic acid linkage and this has been shown by McNamara et al to be effective in preventing dye desorption while at the same time achieving picosecond electron injection rates to TiO_2[93]. Another example is the use of phosphinic acid binding groups[94]. Hahlin et al have also noted that water can cause a change in the energy levels and HOMO-LUMO (Highest occupied molecular orbital-lowest unoccupied molecular orbital) gap size. As with desorption, they noticed essentially no change for a hydrophobic dye (Z907) and a more significant change for the non-hydrophobic dyes (N3, N719) measured[91]. Slight changes in absorption spectra have been observed in the presence of water for other dyes[95]. Regarding stability, other studies have found that water in a cell can lead to iodate formation, gradually causing cell degradation when cell pH is >7[56]. Lu et al found that some bis-benzimidazole based additives used as an alternative to tBP could improve the long term stability of DSSCs with 10% water added, based on their improved surface passivation[96]. When adding small fractions of water along with the surfactant Triton X-100, Jung et al saw increases in cell performance and stability[97].

A second group of studies are now beginning to see more interest, namely those which specifically use water as the main solvent rather than a minor additive. In 2010, Law et al published a 2.4% efficient, 1 cm^2 water based solar cell which used both water and ionic liquid as the 'solvent' system[95]. A significant positive shift in redox potential was observed compared to the cases with no water, though with no major change to V_{OC}. The main limit to photocurrent and subsequently cell performance was found to be diffusion of charge carrying species within the pore structure, which was suggested to be due to segregation of phases within the pores as well as the presence of dry pores. The presence of dry pores was also understood to prevent the

regeneration of dye molecules in those pores, subsequently preventing further electron injection from such molecules[95]. This paper has galvanised research in the area, and several works have since been published on similar topics. Before mentioning some of these, the work of Vargas-Florencia et al is noted, which demonstrated that different TiO_2 nanoparticle preparation procedures and their subsequently different film pore polydispersity resulted in variations in water permeation and diffusion rates[98].

Daeneke et al have looked at a variation that uses the simple ferri-ferrocyanide redox couple, stating advantages due to a low molar absorption coefficient in the visible range and the non-corrosive nature of the system[99]. These devices achieved efficiencies of up to 4.2% for an active area of 0.16 cm^2, but stability results were poor for white light illumination. By using a new organic redox couple based around thiolate/disulfide which has similar benefits to the ferri-ferrocyanide system, Tian et al have achieved 3.5% efficiencies with cell areas of 0.25 cm^2. By using a $[Co(bpy)_3]^{2+/3+}$ aqueous electrolyte system containing a small fraction of polyethylene glycol (PEG) along with the 'MK2' dye Xiang et al achieved a cell efficiency of 4.2%. This was improved further by decreasing charge transfer resistance at the counter electrode through the use of porous ITO coated with Pt, leading to an efficiency of 5.0%[100].

The $I_2^{-\bullet}$ species is usually thought to be important in the regeneration of oxidised dye. Boschloo et al determined the redox potential of the $I_2^{-\bullet}/I^-$ to be approximately 250 mV more positive in water than in acetonitrile, and they suggest this could therefore have a limiting effect on the regeneration and therefore injection kinetics of the dye[101]. Recently, Law et al produced cells with efficiencies above 4% for 0.16 cm^2 cells, and 3.9% for 1 cm^2 cells. Experimentally, the electrolyte wetting of the pores was seen to be very important, and was controlled largely by the use of coadsorbates. Relative iodine concentration was also found to be important, and it was suggested that free iodine plays a part in the back reaction in water. Free iodine levels were controlled to a degree by finding an optimum minimum concentration of I_2, and by the use of guanidine iodide, which was also believed to improve wetting[86].

Though it is clear that DSSCs made using water have a number of issues – not least the problems of lower performance and chemical stability, it is also interesting that so much progress has been made since the 2010 paper from Law et al[95]. It seems possible that some of the problems mentioned can be circumvented through the use of surface treatments to improve wetting, and future research into electrolyte materials may well be able to develop faster diffusing compounds which can be effectively matched to dyes to achieve higher efficiencies still. If this ever becomes the case, the obvious benefits of water will become important including its low toxicity, low cost, high abundance and low volatility. The bulk of this thesis will concentrate on the development and understanding of such water based DSSCs.

1.5 References

(1) IEA “Worldwide Trends in Energy Use and Efficiency,” International Energy Agency, 2008.

(2) IEA “Key World Energy Statistics,” International Energy Agancy, 2012.

(3) Sawin, J. L.; Bhattacharya, S. C.; Galàn, E. M.; McCrone, A.; Moomaw, W. R.; Sims, R.; Sonntag-O’Brien, V.; Sverrisson, F. “REN21.2012 Global Status Report,” Renewable Energy Policy Network for the 21st Century, 2012.

(4) Dovi, V. G.; Friedler, F.; Huisingh, D.; Klemes, J. J. *J Clean Prod* **2009**, *17*, 889.

(5) Metz, B. *Climate change 2007. Mitigation of climate change : contribution of Working Group III to the Fourth assessment report of the Intergovernmental Panel on Climate Change*; Cambridge University Press: Cambridge, 2007.

(6) (a) Turner, J. A. *Science* **1999**, *285*, 687(b) Varun; Bhat, I. K.; Prakash, R. *Renew Sust Energ Rev* **2009**, *13*, 1067.

(7) Johansson, T. B.; Burnham, L. *Renewable energy : sources for fuels and electricity*; Island Press: Washington, DC, 1993.

(8) Federal Ministry for the Environment, N. C. a. N. S. “Energy Concept for an Environmentally Sound, Reliable and Affordable Energy Supply,” Federal Ministry of Economics and Technology, 2010.

(9) Ministry of Climate, E. a. B. t. t. D. P. “Energy Policy Report 2012,” Ministry of Climate, Energy and Building to the Danish Parliament, 2012.
(10) Sveinsdóttir, P. S. “Energy Statistics in Iceland 2012,” Orkustofnun, 2013.
(11) Giribabu, L.; Kanaparthi, R. K.; Velkannan, V. *Chem Rec* **2012**, *12*, 306.
(12) Chapin, D. M.; Fuller, C. S.; Pearson, G. L. *J Appl Phys* **1954**, *25*, 676.
(13) (a) Avrutin, V.; Izyumskaya, N.; Morkoc, H. *Superlattice Microst* **2011**, *49*, 337(b) Bagnall, D. M.; Boreland, M. *Energ Policy* **2008**, *36*, 4390.
(14) Green, M. A.; Emery, K.; Hishikawa, Y.; Warta, W.; Dunlop, E. D. *Prog Photovoltaics* **2012**, *20*, 606.
(15) Kimbis, T. P. “Multi Year Program Plan 2008-2012,” U.S. Department of Energy, 2008.
(16) Rao, R. A.; Mathew, L.; Sarkar, D.; Smith, S.; Saha, S.; Garcia, R.; Stout, R.; Gurmu, A.; Ainom, M.; Onyegam, E.; Xu, D.; Jawarani, D.; Fossum, J.; Banerjee, S.; Das, U.; Upadhyaya, A.; Rohatgi, A.; Wang, Q. *2012 38th Ieee Photovoltaic Specialists Conference (Pvsc)* **2012**, 1837.
(17) Jackson, P.; Hariskos, D.; Lotter, E.; Paetel, S.; Wuerz, R.; Menner, R.; Wischmann, W.; Powalla, M. *Prog Photovoltaics* **2011**, *19*, 894.
(18) Todorov, T. K.; Tang, J.; Bag, S.; Gunawan, O.; Gokmen, T.; Zhu, Y.; Mitzi, D. B. *Adv Energy Mater* **2013**, *3*, 34.
(19) Yella, A.; Lee, H. W.; Tsao, H. N.; Yi, C. Y.; Chandiran, A. K. *Science* **2011**, *334*, 1203.
(20) Burschka, J.; Pellet, N.; Moon, S.-J.; Humphry-Baker, R.; Gao, P.; Nazeeruddin, M. K.; Gratzel, M. *Nature* **2013**, *advance online publication*.
(21) Conibeer, G. *Mater Today* **2007**, *10*, 42.
(22) O’Regan, B.; Grätzel, M. *Nature* **1991**, *335*, 737.
(23) Kroon, J. M.; Bakker, N. J.; Smit, H. J. P.; Liska, P.; Thampi, K. R.; Wang, P.; Zakeeruddin, S. M.; Gratzel, M.; Hinsch, A.; Hore, S.; Wurfel, U.; Sastrawan, R.; Durrant, J. R.; Palomares, E.; Pettersson, H.; Gruszecki, T.; Walter, J.; Skupien, K.; Tulloch, G. E. *Prog Photovoltaics* **2007**, *15*, 1.
(24) Goldstein, J.; Yakupov, I.; Breen, B. *Sol Energ Mat Sol C* **2010**, *94*, 638.
(25) http://www.3gsolar.com/?page_id=53, 11.01.13; Vol. 2013.
(26) Raga, S. R.; Fabregat-Santiago, F. *Phys Chem Chem Phys* **2013**.
(27) Boschloo, G.; Hagfeldt, A. *Accounts Chem Res* **2009**, *42*, 1819.

(28) (a) Datta, J.; Bhattacharya, A.; Kundu, K. K. *B Chem Soc Jpn* **1988**, *61*, 1735(b) Nazeeruddin, M. K.; Kay, A.; Rodicio, I.; Humphrybaker, R.; Muller, E.; Liska, P.; Vlachopoulos, N.; Gratzel, M. *J Am Chem Soc* **1993**, *115*, 6382.

(29) Gratzel, M. *Accounts Chem Res* **2009**, *42*, 1788.

(30) Jennings, J. R.; Ghicov, A.; Peter, L. M.; Schmuki, P.; Walker, A. B. *J Am Chem Soc* **2008**, *130*, 13364.

(31) Zukalova, M.; Zukal, A.; Kavan, L.; Nazeeruddin, M. K.; Liska, P.; Gratzel, M. *Nano Lett* **2005**, *5*, 1789.

(32) Zhang, Q. F.; Myers, D.; Lan, J. L.; Jenekhe, S. A.; Cao, G. Z. *Phys Chem Chem Phys* **2012**, *14*, 14982.

(33) Gratzel, M. *Nature* **2001**, *414*, 338.

(34) (a) Hagfeldt, A.; Boschloo, G.; Sun, L. C.; Kloo, L.; Pettersson, H. *Chem Rev* **2010**, *110*, 6595(b) Leon, C. P.; Kador, L.; Peng, B.; Thelakkat, M. *J Phys Chem B* **2006**, *110*, 8723.

(35) Gonzalez-Valls, I.; Lira-Cantu, M. *Energ Environ Sci* **2009**, *2*, 19.

(36) Keis, K.; Lindgren, J.; Lindquist, S. E.; Hagfeldt, A. *Langmuir* **2000**, *16*, 4688.

(37) Cojocaru, L.; Olivier, C.; Toupance, T.; Hirsch, L., 2012; p FUEL.

(38) (a) Nazeeruddin, M. K.; Pechy, P.; Renouard, T.; Zakeeruddin, S. M.; Humphry-Baker, R.; Comte, P.; Liska, P.; Cevey, L.; Costa, E.; Shklover, V.; Spiccia, L.; Deacon, G. B.; Bignozzi, C. A.; Gratzel, M. *J Am Chem Soc* **2001**, *123*, 1613(b) Cao, Y. M.; Bai, Y.; Yu, Q. J.; Cheng, Y. M.; Liu, S.; Shi, D.; Gao, F. F.; Wang, P. *J Phys Chem C* **2009**, *113*, 6290.

(39) Constable, E. C.; Redondo, A. H.; Housecroft, C. E.; Neuburger, M.; Schaffner, S. *Dalton T* **2009**, 6634.

(40) Ito, S.; Miura, H.; Uchida, S.; Takata, M.; Sumioka, K.; Liska, P.; Comte, P.; Pechy, P.; Graetzel, M. *Chem Commun* **2008**, 5194.

(41) (a) Zhang, G. L.; Bala, H.; Cheng, Y. M.; Shi, D.; Lv, X. J.; Yu, Q. J.; Wang, P. *Chem Commun* **2009**, 2198(b) Yum, J. H.; Hagberg, D. P.; Moon, S. J.; Karlsson, K. M.; Marinado, T.; Sun, L. C.; Hagfeldt, A.; Nazeeruddin, M. K.; Gratzel, M. *Angew Chem Int Edit* **2009**, *48*, 1576(c) Xu, M. F.; Li, R. Z.; Pootrakulchote, N.; Shi, D.; Guo, J.; Yi, Z. H.; Zakeeruddin, S. M.; Gratzel, M.; Wang, P. *J Phys Chem C* **2008**, *112*, 19770.

(42) Nazeeruddin, M. K.; Zakeeruddin, S. M.; Humphry-Baker, R.; Jirousek, M.; Liska, P.; Vlachopoulos, N.; Shklover, V.; Fischer, C. H.; Gratzel, M. *Inorg Chem* **1999**, *38*, 6298.

(43) Wenger, B.; Gratzel, M.; Moser, J. E. *J Am Chem Soc* **2005**, *127*, 12150.

(44) Gratzel, M. *Inorg Chem* **2005**, *44*, 6841.

(45) O'Regan, B. C.; Durrant, J. R. *Accounts Chem Res* **2009**, *42*, 1799.

(46) Ito, S.; Murakami, T. N.; Comte, P.; Liska, P.; Gratzel, C.; Nazeeruddin, M. K.; Gratzel, M. *Thin Solid Films* **2008**, *516*, 4613.

(47) Wang, P.; Zakeeruddin, S. M.; Moser, J. E.; Nazeeruddin, M. K.; Sekiguchi, T.; Gratzel, M. *Nat Mater* **2003**, *2*, 402.

(48) Li, L. L.; Chang, C. W.; Wu, H. H.; Shiu, J. W.; Wu, P. T.; Diau, E. W. G. *Journal of Materials Chemistry* **2012**, *22*, 6267.

(49) (a) Khazraji, A. C.; Hotchandani, S.; Das, S.; Kamat, P. V. *J Phys Chem B* **1999**, *103*, 4693(b) Zakeeruddin, S. M.; Nazeeruddin, M. K.; Humphry-Baker, R.; Gratzel, M.; Shklover, V. *Inorg Chem* **1998**, *37*, 5251.

(50) Horiuchi, T.; Miura, H.; Uchida, S. *Chem Commun* **2003**, 3036.

(51) Ren, X. M.; Feng, Q. Y.; Zhou, G.; Huang, C. H.; Wang, Z. S. *J Phys Chem C* **2010**, *114*, 7190.

(52) Neale, N. R.; Kopidakis, N.; van de Lagemaat, J.; Gratzel, M.; Frank, A. J. *J Phys Chem B* **2005**, *109*, 23183.

(53) Kay, A.; Gratzel, M. *J Phys Chem-Us* **1993**, *97*, 6272.

(54) (a) Hara, K.; Dan-Oh, Y.; Kasada, C.; Ohga, Y.; Shinpo, A.; Suga, S.; Sayama, K.; Arakawa, H. *Langmuir* **2004**, *20*, 4205(b) Horiuchi, T.; Miura, H.; Uchida, S. *J Photoch Photobio A* **2004**, *164*, 29.

(55) Kay, A.; Gratzel, M. *Sol Energ Mat Sol C* **1996**, *44*, 99.

(56) Macht, B.; Turrion, M.; Barkschat, A.; Salvador, P.; Ellmer, K.; Tributsch, H. *Sol Energ Mat Sol C* **2002**, *73*, 163.

(57) Bai, Y.; Cao, Y. M.; Zhang, J.; Wang, M.; Li, R. Z.; Wang, P.; Zakeeruddin, S. M.; Gratzel, M. *Nat Mater* **2008**, *7*, 626.

(58) Gorlov, M.; Kloo, L. *Dalton T* **2008**, 2655.

(59) Huang, X. W.; Liu, Y. J.; Deng, J. Y.; Yi, B.; Yu, X. L.; Shen, P.; Tan, S. T. *Electrochim Acta* **2012**, *80*, 219.

(60) Snaith, H. J.; Moule, A. J.; Klein, C.; Meerholz, K.; Friend, R. H.; Gratzel, M. *Nano Lett* **2007**, *7*, 3372.

(61) Hamann, T. W.; Jensen, R. A.; Martinson, A. B. F.; Van Ryswyk, H.; Hupp, J. T. *Energ Environ Sci* **2008**, *1*, 66.

(62) Yu, Z.; Vlachopoulos, N.; Gorlov, M.; Kloo, L. *Dalton T* **2011**, *40*, 10289.

(63) (a) Wang, H. X.; Peter, L. M. *J Phys Chem C* **2012**, *116*, 10468(b) Liu, Y.; Hagfeldt, A.; Xiao, X. R.; Lindquist, S. E. *Sol Energ Mat Sol C* **1998**, *55*, 267.

(64) Kopidakis, N.; Neale, N. R.; Frank, A. J. *J Phys Chem B* **2006**, *110*, 12485.

(65) Wang, Z. S.; Sayama, K.; Sugihara, H. *J Phys Chem B* **2005**, *109*, 22449.

(66) Teng, C.; Yang, X. C.; Yuan, C. Z.; Li, C. Y.; Chen, R. K.; Tian, H. N.; Li, S. F.; Hagfeldt, A.; Sun, L. C. *Org Lett* **2009**, *11*, 5542.

(67) Oskam, G.; Bergeron, B. V.; Meyer, G. J.; Searson, P. C. *J Phys Chem B* **2001**, *105*, 6867.

(68) Wang, P.; Zakeeruddin, S. M.; Moser, J. E.; Humphry-Baker, R.; Gratzel, M. *J Am Chem Soc* **2004**, *126*, 7164.

(69) Daeneke, T.; Kwon, T. H.; Holmes, A. B.; Duffy, N. W.; Bach, U.; Spiccia, L. *Nat Chem* **2011**, *3*, 211.

(70) Nusbaumer, H.; Moser, J. E.; Zakeeruddin, S. M.; Nazeeruddin, M. K.; Gratzel, M. *J Phys Chem B* **2001**, *105*, 10461.

(71) Boschloo, G.; Haggman, L.; Hagfeldt, A. *J Phys Chem B* **2006**, *110*, 13144.

(72) Katoh, R.; Kasuya, M.; Kodate, S.; Furube, A.; Fuke, N.; Koide, N. *J Phys Chem C* **2009**, *113*, 20738.

(73) Zhang, C. N.; Huang, Y.; Huo, Z. P.; Chen, S. H.; Dai, S. Y. *J Phys Chem C* **2009**, *113*, 21779.

(74) Gratzel, M. *J Photoch Photobio A* **2004**, *168*, 235.

(75) Toivola, M.; Halme, J.; Miettunen, K.; Aitola, K.; Lund, P. D. *International Journal of Energy Research* **2009**, *33*, 1145.

(76) Lee, K.-M.; Chiu, W.-H.; Lu, M.-D.; Hsieh, W.-F. *J Power Sources* **2011**, *196*, 8897.

(77) Lei, B.-X.; Luo, Q.-P.; Yu, X.-Y.; Wu, W.-Q.; Su, C.-Y.; Kuang, D.-B. *Phys Chem Chem Phys* **2012**, *14*, 13175.

(78) Ito, S.; Ha, N. L. C.; Rothenberger, G.; Liska, P.; Comte, P.; Zakeeruddin, S. M.; Pechy, P.; Nazeeruddin, M. K.; Gratzel, M. *Chem Commun* **2006**, 4004.

(79) Kim, J. M.; Rhee, S. W. *J Electrochem Soc* **2012**, *159*, B6.

(80) Cha, S. I.; Kim, Y.; Hwang, K. H.; Shin, Y. J.; Seo, S. H.; Lee, D. Y. *Energ Environ Sci* **2012**, *5*, 6071.

(81) Huang, L. T.; Lin, M. C.; Chang, M. L.; Wang, R. R.; Lin, H. C. *Thin Solid Films* **2009**, *517*, 4207.

(82) Harikisun, R.; Desilvestro, H. *Sol Energy* **2011**, *85*, 1179.

(83) Kato, N.; Takeda, Y.; Higuchi, K.; Takeichi, A.; Sudo, E.; Tanaka, H.; Motohiro, T.; Sano, T.; Toyoda, T. *Sol Energ Mat Sol C* **2009**, *93*, 893.

(84) Tsubomura, H.; Matsumura, M.; Nomura, Y.; Amamiya, T. *Nature* **1976**, *261*, 402.

(85) (a) Matsumura, M.; Matsudaira, S.; Tsubomura, H.; Takata, M.; Yanagida, H. *Ind Eng Chem Prod Rd* **1980**, *19*, 415(b) Liska, P.; Vlachopoulos, N.; Nazeeruddin, M. K.; Comte, P.; Graetzel, M. *J Am Chem Soc* **1988**, *110*, 3686.

(86) Law, C.; Moudam, O.; Villarroya-Lidon, S.; O'Regan, B. *Journal of Materials Chemistry* **2012**, *22*, 23387.

(87) Enright, B.; Redmond, G.; Fitzmaurice, D. *J Phys Chem-Us* **1994**, *98*, 6195.

(88) Zhu, K.; Jang, S. R.; Frank, A. J. *Energ Environ Sci* **2012**, *5*, 9492.

(89) Mikoshiba, S.; Murai, S.; Sumino, H.; Kado, T.; Kosugi, D.; Hayase, S. *Curr Appl Phys* **2005**, *5*, 152.

(90) Zakeeruddin, S. M.; Nazeeruddin, M. K.; Humphry-Baker, R.; Pechy, P.; Quagliotto, P.; Barolo, C.; Viscardi, G.; Gratzel, M. *Langmuir* **2002**, *18*, 952.

(91) Hahlin, M.; Johansson, E. M. J.; Scholin, R.; Siegbabn, H.; Rensmo, H. *J Phys Chem C* **2011**, *115*, 11996.

(92) Pan, L.; Zou, J. J.; Zhang, X. W.; Wang, L. *J Am Chem Soc* **2011**, *133*, 10000.

(93) McNamara, W. R.; Milot, R. L.; Song, H. E.; Snoeberger, R. C.; Batista, V. S.; Schmuttenmaer, C. A.; Brudvig, G. W.; Crabtree, R. H. *Energ Environ Sci* **2010**, *3*, 917.

(94) Pechy, P.; Rotzinger, F. P.; Nazeeruddin, M. K.; Kohle, O.; Zakeeruddin, S. M.; Humphrybaker, R.; Gratzel, M. *J Chem Soc Chem Comm* **1995**, 1093.

(95) Law, C. H.; Pathirana, S. C.; Li, X. O.; Anderson, A. Y.; Barnes, P. R. F.; Listorti, A.; Ghaddar, T. H.; O'Regan, B. C. *Adv Mater* **2010**, *22*, 4505.

(96) Lu, H. L.; Lee, Y. H.; Huang, S. T.; Su, C. C.; Yang, T. C. K. *Sol Energ Mat Sol C* **2011**, *95*, 158.

(97) Jung, Y. S.; Yoo, B.; Lim, M. K.; Lee, S. Y.; Kim, K. J. *Electrochim Acta* **2009**, *54*, 6286.

(98) Vargas-Florencia, D.; Edvinsson, T.; Hagfeldt, A.; Furo, I. *J Phys Chem C* **2007**, *111*, 7605.

(99) Daeneke, T.; Uemura, Y.; Duffy, N. W.; Mozer, A. J.; Koumura, N.; Bach, U.; Spiccia, L. *Adv Mater* **2012**, *24*, 1222.

(100) Xiang, W. C.; Huang, F. Z.; Cheng, Y. B.; Bach, U.; Spiccia, L. *Energ Environ Sci* **2013**, *6*, 121.

(101) Boschloo, G.; Gibson, E. A.; Hagfeldt, A. *J Phys Chem Lett* **2011**, *2*, 3016.

Chapter 2: Theory

2.1 Introduction
2.2 Semiconductors
    2.2.1 Band structure
    2.2.2 Density of electrons
    2.2.3 Electron state density
    2.2.4 Electron state occupancy (Electron distribution)
    2.2.5 n-type Doping
    2.2.6 Quasi Fermi energy
    2.2.7 Trapping states
    2.2.8 Electron transport
2.3 Electrochemistry
    2.3.1 Metal/Electrolyte interface
    2.3.2 Surface charge
    2.3.3 Electrochemical reaction
    2.3.4 Mass transport
    2.3.5 Electron transfer
    2.3.6 Overpotential in a semiconductor
    2.3.7 Three electrode cell
    2.3.8 Measuring redox potential
    2.3.9 Cyclic Voltammetry
    2.3.10 Junction potential
2.4 Dye Sensitized Solar Cell operation
    2.4.1 In the dark
    2.4.2 Under illumination
        2.4.2.1 Short circuit
        2.4.2.2 Open circuit
2.5 Dye Sensitized Solar Cell performance
    2.5.1 IV curve
    2.5.2 IPCE
    2.5.3 Diffusion length
    2.5.4 Continuity equation
2.6 Techniques
    2.6.1 Infrared electron trapping density measurements

2.6.2 Open Circuit Voltage Decay (OCVD)
2.6.3 Frequency modulated techniques
2.6.3.1 Electrochemical Impedance Spectroscopy (EIS)
2.6.3.1.1 EIS for DSSCs
2.6.3.2 Intensity Modulated Photovoltage Spectroscopy (IMVS)
2.6.4 Surface tension and contact angle
2.6.5 Nanocalc
2.7 References

2.1 Introduction

In chapter 1, the general structure and basic working principles of the DSSC were introduced. Underlying topics important for understanding the DSSC are presented and a more detailed look is taken at the physical and chemical processes involved in dye cell operation. Theory relevant to the experimental techniques used in this chapter is also discussed.

2.2 Semiconductors

The semiconductor carries out several roles in the DSSC. It acts as a support for the sensitizing dye, enables charge separation at the dye|semiconductor interface and allows charge transport to the substrate. Semiconductors are complicated materials, and are discussed in detail below.

2.2.1 Band structure

To understand the band structure of a semiconductor it is useful to first consider the energy level diagram for a single atom or molecule. Each orbital has a discrete energy level resulting in set energy gaps between orbitals. The electron configuration of Si is $[Ne]3s^2 3p^2$ and the overlap of these orbitals results in $4sp^3$ hybrid orbitals. When two Si atoms are bonded, the interaction of the electron waveforms result in the formation of bonding and antibonding orbitals which are filled with electrons starting with the lowest energy orbital and obeying the Pauli exclusion principle. In the case of Si-Si, there are four bonding and four antibonding orbitals. Eight electrons are shared between these, meaning the bonding orbitals are all filled and the antibonding orbitals are unfilled. This results in a strong bond between the two atoms, and there is a large gap between filled and unfilled orbitals.

As more Si atoms are bonded together, further splitting of the orbital energy levels due to waveform interaction occurs, but there continues to be an energy gap between bonding and antibonding orbitals. In bulk silicon, it is assumed that there are essentially an infinite number of Si atoms, and the bonding and antibonding orbitals both form a continuum of energy levels (called a band)

separated by an energy gap (E_g). Within the bands, electrons can freely move between orbitals within the continuum, and will equilibrate to the lowest energy state. The two bands formed are usually termed the valence band (VB), which is the lower energy band and is (at 0K) completely filled with electrons and the conduction band (CB), which is the higher energy band and is (at 0K) completely unfilled with electrons. This is summarized in Fig 2.1. A metal has incomplete filling of a band at T = 0K allowing electrons to move in the band whereas a semiconductor has full bands at T = 0K. An insulating material is different from a semiconductor in that it has a larger E_g. A material is insulating if E_g is large enough that under the conditions in question, no electrons are promoted into the CB so there are no partially filled bands[1].

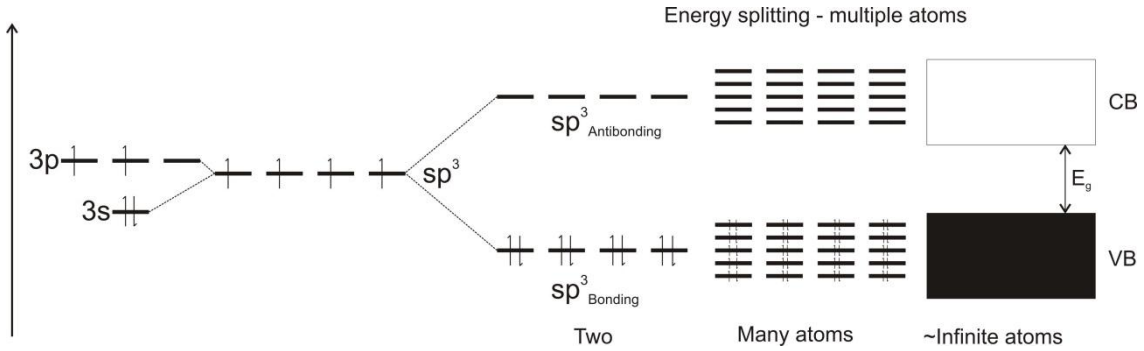

Fig 2.1 Origin of valence and conduction bands in bulk Si. Energy levels of 3s and 3p orbitals for a single atom on left hand side and hybridisation of orbitals to form sp^3 orbitals. In centre moving to right hand side showing formation of bonding and antibonding orbitals when two or more atoms are present and splitting of these levels to form a continuum when ~infinite atoms are present as in a bulk material.

2.2.2 Density of electrons

In many solar energy systems based on semiconductors the production, transport and transfer of both electrons and holes is important. In the DSSC electrons are injected into the semiconductor from the external sensitizer rather than generated by electron excitation within the semiconductor, therefore the photogenerated 'hole' is located externally to the semiconductor. Electrons will therefore be the main focus of this discussion into semiconductors.

To have an idea of the distribution of electrons within the semiconductor, electron densities can be calculated as a function of energy under different conditions. This gives a more detailed view of the bands that have been discussed above. In order to determine electron density, two parameters must be considered; the distribution of possible states an electron can occupy, and the occupancy of said states[2]. These can be calculated from first principals and to do so is outside the scope of this work, however the results of such calculations are briefly considered.

2.2.3 Electron state density

The density of electronic states can be determined by dividing the total volume in momentum space of all electronic states with the relevant momentum by the volume of a single state. Converting momentum to energy allows the number of states (N) as a function of energy to be calculated[2] as in equation 2.1[2]

$$N_{(E_e)} = \frac{8\pi V(2m_e^*)^{3/2}}{3h^3}(E_e - E_C)^{3/2} \quad \text{Equation 2.1}$$

where V is the volume of the semiconductor in question, m_e^* is the mass of an electron, h is the phase space volume per state, E_e is the electron energy and E_C is the conduction band energy.

2.2.4 Electron state occupancy (Electron distribution)

The Fermi distribution (f_e) (equation 2.2) satisfies several conditions including the Pauli exclusion principle and the minimisation of free energy and is used to define the electron distribution[2]

$$f_e(E_e) = \frac{1}{\exp\left(\frac{E_e - E_F}{kT}\right) + 1} \quad \text{Equation 2.2}$$

where E_F is the Fermi energy, k is the Boltzmann constant and T is the temperature. Based on this equation, it can be seen that when $E_e = E_F$, the value

of f_e is ½. This can also be expressed by saying that at the Fermi energy, the probability of finding an electron is a half.

By integrating the product of the electron state density and the electron state occupancy over the whole range of conduction band energies, the density of free electrons can be obtained.

2.2.5 n-type Doping

It is possible to modify the electronic properties of a semiconductor by doping. In the case of TiO_2, a small number of oxygen vacancies resulting in Ti^{3+} states leads to n-type doping without the need for additional dopants[3]. In the case of n-type doping, additional electronic states are created at energies slightly below the conduction band because of the difference in binding energies created in the semiconductor structure at doping sites. Because of the small difference in energy between the dopant sites and the conduction band, it does not require a lot of energy to donate electrons from these states to the CB, increasing the number of free electrons in the CB and so increasing the conductivity[2].

2.2.6 Quasi Fermi energy

In the non-equilibration case where electrons are promoted from the VB to the CB, there is a increase in the electron density and hole density which increases the Fermi energy describing the electrons, bringing it nearer to the CB and brings the Fermi energy describing holes nearer to the VB. To account for these effects two quasi Fermi energies are used. The electron quasi Fermi energy (nE_F) describes electron occupation of the CB and shallow donor states (see below) whereas the hole quasi Fermi energy (hE_F) describes electron occupation of the VB and shallow acceptor states. In the DSSC under illumination, electrons are injected into the semiconductor resulting in an increase in nE_F (section 2.4.2), however the hE_F remains relatively unchanged. The number of 'free' electrons (n_c), that is electrons in the CB, is described by equation 2.3 where N_C is the number of conduction band states.

$$n_c = N_C \exp\left(-\frac{E_C - nE_F}{k_B T}\right) \qquad \text{Equation 2.3}$$

When more free electrons are in the CB, nE_F will be raised relative to E_C. It can also be seen that for a given electron concentration, a change in E_C will result in a change in nE_F[2].

2.2.7 Trapping states

Nanoporous TiO_2 used in DSSCs has a very high surface area and is made up of a large number of individual particles sintered together. The result of this is that there are a large number of trap states which are thought to be physically located particularly at the surface and at the interface between particles[4] and energetically located in the band gap[5]. These have been observed primarily via spectroelectrochemical[5-6] methods and also through the effect of potential on photocurrent[4,7]. An electron located in a trap state is unable to travel through the film until it is thermally excited to the conduction band[8] and becomes free, meaning that trap states have a strong influence on electron mobility[8]. The precise nature of trap states has not yet been determined although several different possibilities have been suggested, including the presence of incompletely coordinated Ti atoms[6] or other defect states[9], or the coulombic interaction of electrons with species in the electrolyte[10].

The distribution of trap states has been suggested to show several features. Firstly there is evidence for an exponential distribution (g(E)) located energetically close to but below the conduction band[8,11] which follows the exponential profile described[12] in equation 2.4. Secondly a band at a specific energy approximately 0.6V below the conduction band has also been suggested[4,6].

$$g(E) = \frac{N_{t,0}}{k_B T_0} \exp - \left(\frac{E_C - E}{k_B T_0}\right) \text{Equation 2.4}$$

Here $N_{t,0}$ is the total trap density, T_0 is a characteristic temperature and E_C is the energy of the CB edge. The characteristic temperature describes the shape of the exponential distribution.

2.2.8 Electron transport

For a bulk semiconductor, contact with an electrochemically active material or solution results in band bending near to the surface. For the example of an n-doped semiconductor and an electrolyte solution containing a redox couple with a potential below the semiconductor Fermi energy, the equilibration of Fermi energy between the two materials will result in electrons flowing from the semiconductor to the redox couple, raising the redox Fermi energy ($E_{F,Redox}$) and lowering the semiconductor Fermi energy (E_F). A potential gradient across the Helmholtz layer will occur, with a negative charge on the electrolyte side and positive charge on the semiconductor near to the interface. In a bulk semiconductor, there is a low concentration of free charge carriers, and as a result the surface charge is not screened. This leads to the formation of a region containing excess positive charge because charge carriers near to the surface are depleted compared to the bulk. In terms of potential energy, this leads to 'band bending', where the energy of the conduction band near the surface is higher that in the bulk material[13]; the width across which this gradient occurs is called a depletion layer. This potential gradient will cause electrons generated near to the surface of the semiconductor to move away from the surface. Peter[14] points out that the movement of charge carriers is dependant on the free energy gradient, which encompasses both the potential energy gradient and also an entropic contribution; that of a concentration gradient. That is, charge carriers will also move from an area of high concentration to low concentration by diffusion.

The case of nanoporous TiO_2 based on an array of sintered nanoparticles is slightly different to that stated above. Peter[14] has calculated that for reasonable values of doping density and particles of 20nm radius, the band bending at each particle is fairly small. As each particle is mostly surrounded by electrolyte, the effect of the bending that does occur will be to help move electrons to the centre of the particle. This means that the movement of electrons to the substrate will be due to the concentration gradient[14]. Electron traps also have a significant effect on electron transport. Trapping is understood to occur on a timescale of pico to nanoseconds[10] and electrons will go through many trapping/detrapping events while travelling through a TiO_2 film. As a result, it is difficult to determine the

diffusion rate (D_0) of free electrons through a film, and generally an effective diffusion coefficient (D_n) is recorded[12b].

2.3 Electrochemistry

Electrochemistry is concerned with processes occurring which involve the transfer of electrons and typically result in a chemical change. To introduce the topic, it is common to describe what occurs when a metal is introduced into a liquid electrolyte and this approach will be taken here.

2.3.1 Metal/Electrolyte interface

The surface of a metal will typically have a different charge density from the bulk caused by the altered nature of the surface (e.g. terminating/dangling bonds) compared to the bulk material. On immersion into an electrolyte, ions and dipoles move to match and neutralise this charge and the resulting distribution of ions and charges along with the associated potential changes have been described by various models. The Grahame model is based on work from several previous models and also includes the idea of specifically adsorbed ions. This model will be described to summarise several ideas and is shown in Fig 2.2.

The Galvani potential ($\Delta\phi_{a/b}$)is the difference in potential between points in the bulk of two phases a and b. In the system of interest here, Φ_m is the surface charge on the metal electrode and Φ_s is the potential of the bulk electrolyte. The Galvani potential is the difference between these values as shown in Equation 2.5 and is also referred to as a potential drop.

$$\Delta\phi_{m/s} = \phi_m - \phi_s \quad \text{Equation 2.5}$$

The Grahame model helps rationalise the change in potential as a function of distance from the electrode and several particular regions can be defined. Firstly, when the electrode is introduced to solution, a number of ions with the opposite charge to the surface approach the surface based on electrostatic forces. The limit of approach is dependant on the solvation sphere surrounding the ions and a line drawn through the centre of the ions at their closest approach is termed the

Outer Helmholtz Plane (OHP); a large part of the potential is dropped across this distance. A second region is that between the OHP and the edge of the diffuse layer. This region contains a higher proportion of negatively charged counter ions than positive (as shown in Fig 2.2) with a ratio of negatively to positively charged ions that gradually changes to that of the bulk as the charge is screened further from the electrode. In this region ions are not generally bound to the surface. The diffuse layer thickness is the distance into solution over which the surface potential is completely dropped. The final region to be described is the Inner Helmholtz Plane (IHP). The IHP allows for the possibility that some ions can penetrate the solvent layer and directly adsorb to the surface of the electrode – the IHP defines a line through the centre of these ions.[15]

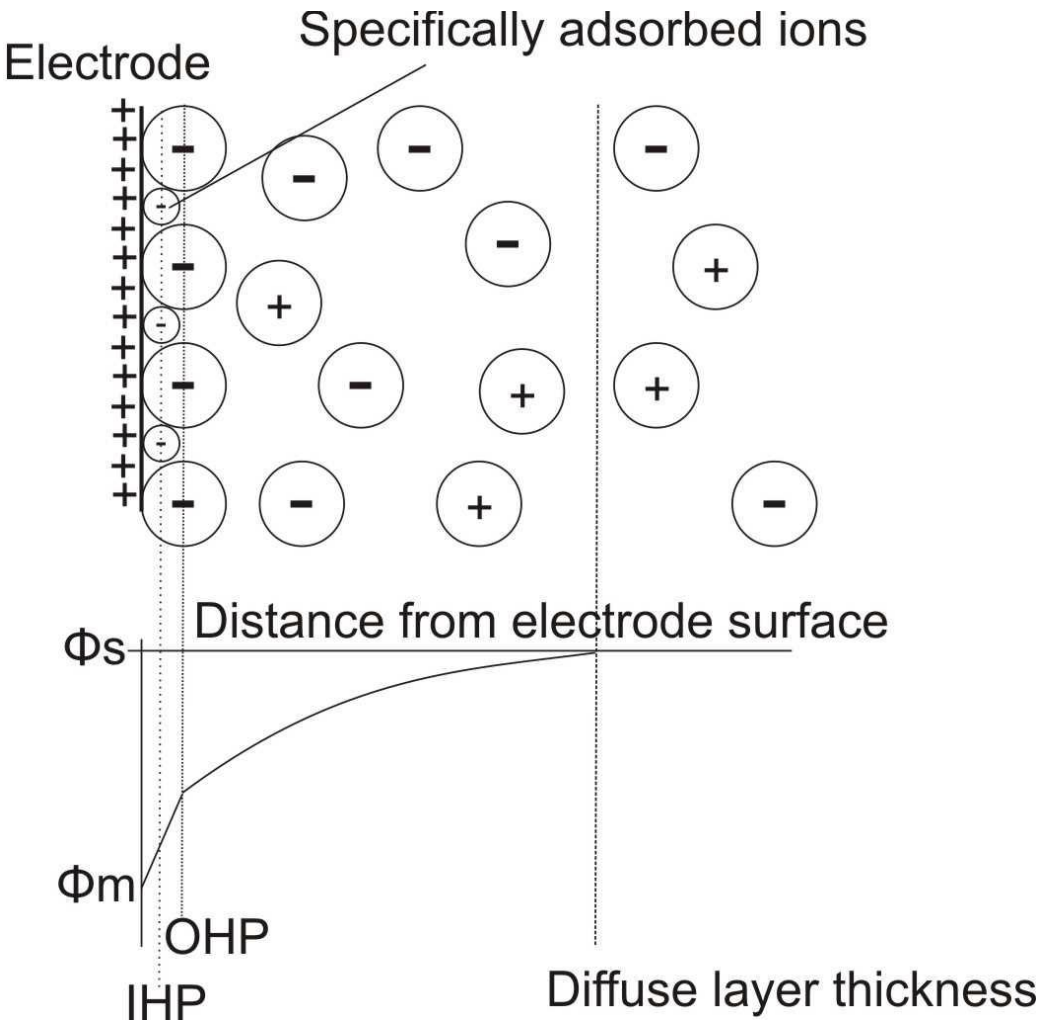

Fig 2.2 Grahame model of metal|electrolyte interface showing top) stylised ionic distribution as a function of distance from electrode surface and bottom) potential drop as a function of distance from electrode surface. Diagram based on picture in reference [15].

It can be seen that the electrochemical potential felt by a molecule in solution will depend on its separation from the electrode surface. Depending on the ionic strength of solution, the diffuse double layer thickness will change – a higher ionic strength will result in a thinner double layer. The surface potential of the metal can also be controlled externally and may change the double layer thickness.

2.3.2 Surface charge

As stated, ions in solution will move to neutralise the surface charge of a material upon it being placed in that solution. The extent to which this occurs will depend on the concentration of those ions and this can affect the surface charge. In water, H^+ and OH^- are the ions of most importance and the pH of the solution will alter the charge on the surface[1]. The 'point of zero charge' (pzc) is the point at which the surface charge is neutralised and this occurs at a specific pH for a given material. Below this pH, the increased concentration of H^+ causes a positive surface charge to develop whereas above it the lower concentration of H^+ and higher concentration of OH^- causes a negative surface charge to develop. This situation becomes more complicated when additional ions able to closely approach or adsorb to the surface are present, as these are also able to change the surface charge. The pzc is determined by the ionic potential (charge/radius) of the surface species and values of 6.2[16] (P25 TiO_2, Degussa), 6.0[17](anatase TiO_2) and ~5[18] have been measured for TiO_2 .

Changes in the surface charge will also have an effect on the position of the conduction band edge. By making the surface more positively charged the CB edge will shift to a more positive potential resulting in a change in the amount of band bending (see section 2.2.8).

2.3.3 Electrochemical reaction

Several steps can be identified in an electrochemical reaction process. Initially, the reactant will be in the bulk solution, from where it will diffuse to the electrode surface and in some cases molecules will adsorb to the surface.

Electron transfer can then occur which will be effected by the potential of the electrode. The product molecule can then diffuse away from the electrode. Two particular steps will be considered in more detail – electron transport and electron transfer.

2.3.4 Mass transport

Three particular mechanisms exist which result in the movement of ions through solution: Diffusion, convection and migration.

- Diffusion is the movement of species according to a concentration gradient and is described by Ficks laws. The driving force for this is entropy and molecules will move from high concentration regions to low concentration regions dependant on their diffusion constant which is influenced by parameters including molecule size and solvent viscosity.

- Convection is caused by mechanical forces acting on the molecules in solution. These include natural forces such as thermal gradients and induced forces such as those caused by bubbling gas into a solution.

- Migration is the movement of ions along an electric field gradient. In order to negate this effect, inert background electrolytes with high ionic strength can be used which minimize the diffuse double layer without undergoing electron transfer[15].

2.3.5 Electron transfer

In the context of electrochemistry, electron transfer generally involves either the transfer of an electron from an electrode to a redox active acceptor species, which is termed reduction and results in a cathodic current (equation 2.6), or the transfer of an electron from a redox active donor species to an electrode, which is termed oxidation and results in an anodic current (equation 2.7).

$$Fe^{3+}_{(aq)} + e^{-}_{(m)} \rightarrow Fe^{2+}_{(aq)}$$ Equation 2.6

$$Fe^{2+}_{(aq)} \rightarrow Fe^{3+}_{(aq)} + e^{-}_{(m)}$$ Equation 2.7

Electron transfer occurs via quantum tunnelling of electrons between the solution species and the electrode which occurs very quickly on a time scale of 10^{-15}-10^{-16}s, compared to nuclear vibrations of the solution species which occur on a time scale of around 10^{-13}s. As a result, the shape of the reactant and product (oxidised and reduced species in the case of a reduction) will not change over the period of electron transfer which follows the Frank-Condon principle[15]. Transfer of an electron is radiationless, so the initial state of the electron (e.g. Electron at E_F of electrode plus energy of oxidised species) must have the same energy as the resultant state (reduced species)[19]. For this to occur, the molecule being oxidised must become energetically excited and the reduced product will also be energetically excited immediately after electron transfer – this excited state is the transition state and will relate to a particular molecular geometry[15]. Transition state theory takes these considerations into account.

Assuming that both donor and acceptor species are present in a solution, both a cathodic and anodic current will flow at the electrode and the net current (i) measured will be the sum of these (equation 2.8)

$$i = FA(k_{ox}[R]_0 - k_{red}[O]_0) \qquad \text{Equation 2.8}$$

where F is the Faraday constant, A the electrode area, $k_{ox/red}$ the rate constant for oxidation/reduction and $[R/O]_0$ the concentration of reduced/oxidised species at the electrode surface. The effect of potential on these rate constants can be described which will enable helpful analysis to be made when performing electrochemical measurements. When a metal electrode is introduced to a solution containing some redox species, an equilibrium situation will be reached where the Fermi energy ($E_{F,Metal}$) of the metal is equal to the equilibrium potential (also called the Nernst potential) of the redox species. This potential will be based on the standard redox potential ($E^{\ominus}$) of the redox couple and the concentration of oxidised and reduced species in solution as shown in the Nernst equation (equation 2.9) where R is the gas constant, T the temperature and n the number of electrons transferred in the reaction.

$$E = E^{\ominus} - \frac{RT}{nF}\ln\left(\frac{[\mathrm{Red}]}{[\mathrm{Ox}]}\right)$$ Equation 2.9

At this point, the net current flowing across the electrode|solution interface is zero. In order to drive a redox process, an overpotential (η) is applied which is equal to E - E_e. Here E is the applied potential and E_e the equilibrium potential which is the potential at which there is no net current flow assuming no liquid junction potential contribution[19] (see section 2.3.10). If this is an increase in the energy of $E_{F,Metal}$, the additional potential is dropped across the double layer at the surface so the driving force for reduction of the species in solution increases. A decrease in $E_{F,Metal}$ results in the driving force for oxidation increasing. The effect on the current is described by the Butler-Volmer equation[19] (equation 2.10)

$$i = FAk^0\left([\mathrm{Ox}]_0 e^{\frac{-\alpha nF(E-E_e)}{RT}} - [\mathrm{Red}]_0 e^{\frac{(1-\alpha)nF(E-E_e)}{RT}}\right)$$ Equation 2.10

where k^0 is the standard rate constant (the rate constant at the potential where k_{ox} = k_{red}), $[Red/Ox]_0$ the concentration of reduced/oxidised species at the counter electrode surface, α the transfer coefficient and E the electrode potential[15].

2.3.6 Overpotential in a semiconductor

The situation for a semiconductor is not the same as for a metal electrode unless the semiconductor has a very high doping density. This is because there are now two regions where the potential can be dropped; the electronic double layer and the depletion layer.

If there is a low doping density such that the potential is dropped exclusively across the depletion layer upon application of an overpotential, there will be no change in the potential drop across the electronic double layer and the surface potential of the band is pinned (termed band edge pinning). This means there is no potential change at the surface of the semiconductor so k_{ox} and k_{red} are unaltered. In this case, the rate of a reaction will only change based on the

concentration of electrons and acceptor species[20] (see kinetic equation 2.19 in section 2.4.2.2).

If there is a high doping density or the applied overpotential moves the Fermi energy to a position within one of the bands then the high density of states allows increased charge movement so less potential is dropped across the depletion layer. In the extreme case no potential is dropped across this layer and it is all dropped across the electronic double layer. This situation is termed Fermi level pinning and results in the band edge moving as the Fermi energy is altered. In such a situation, changes in overpotential will effect electrochemical rate constants in a manner similar to metal electrodes. It is also possible to have a situation where part of the total overpotential is dropped in both these regions.

2.3.7 Three electrode cell

The three electrode cell is the set-up typically used to perform standard electrochemical measurements except in the case where currents are very low. A three electrode cell consists of a working electrode (WE), a counter electrode (CE) and a reference electrode (RE) submerged in a solution and connected as shown in Fig 2.3. Generally, the experiment is set up so that the reaction of interest occurs at the WE and the potential difference is applied relative to the RE. Current is measured between the WE and CE and a potentiostat controls the setup such that minimal current flows between the WE and RE.

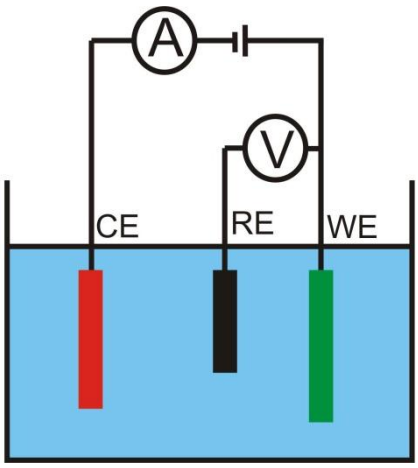

Fig 2.3 Three electrode electrochemical cell setup showing working, reference and counter electrodes in solution and circuit connections.

The rationale for using three electrodes is as follows. At any electrode introduced to a solution, there is a potential drop between the electrode potential and solution potential as described in section 2.3.1. In order to measure this potential difference a complete circuit is required, introducing the need for a second electrode. This will also have a potential drop at the surface and so the measured potential will be the sum of these drops:

$$E = (\phi_m - \phi_s) + (\phi_s - \phi_{ref})$$ Equation 2.11

where $(\phi_m - \phi_s)$ is the difference in potential between the working electrode (ϕ_m) and the bulk solution (ϕ_s) and $(\phi_s - \phi_{ref})$ is the difference in potential between the bulk solution (ϕ_s) and the reference electrode (ϕ_{ref}). The second electrode, the RE, is set up so as to have a constant potential drop and the potential of the WE can be set with respect to this. In the case where no current or very small currents flow, the potential drop at the reference electrode for a reference electrode showing ideal non-polarizable behaviour (where no charge is transferred at the electrode across a wide potential range) does not change from the situation where no current flows. However, when larger currents flow the potential drop changes and the reference electrode no longer has a constant current drop. When large currents are passed a further voltage drop due to the resistance of the solution to the passage of current becomes important. Termed the iR drop, this scales according to Ohms law (V=IR) and so complicates analysis. In order to accurately measure the cell potential even when large currents flow, the CE is introduced and the cell is controlled so that current flow is measured between this electrode and the WE. The current that flows between the WE and RE is minimal, so the potential drop at the RE is constant and any iR drop is minimal[15,19].

2.3.8 Measuring redox potential

It is possible to measure the Nernst potential of a redox couple in solution by introducing a WE and RE into the solution of interest and recording the potential between both electrodes.

2.3.9 Cyclic Voltammetry

In cyclic voltammetry (CV), the current is measured while the cell potential is scanned at a fixed rate from one value to another, then back to the first. To explain the data obtained by the technique, the simple case where a solution containing a redox couple that undergoes a reversible one electron transfer will be examined (equation 2.12), and features seen in the CV (Fig 2.4) will be considered.

$$\mathrm{Red} \rightleftharpoons \mathrm{Ox} + e^- \qquad \text{Equation 2.12}$$

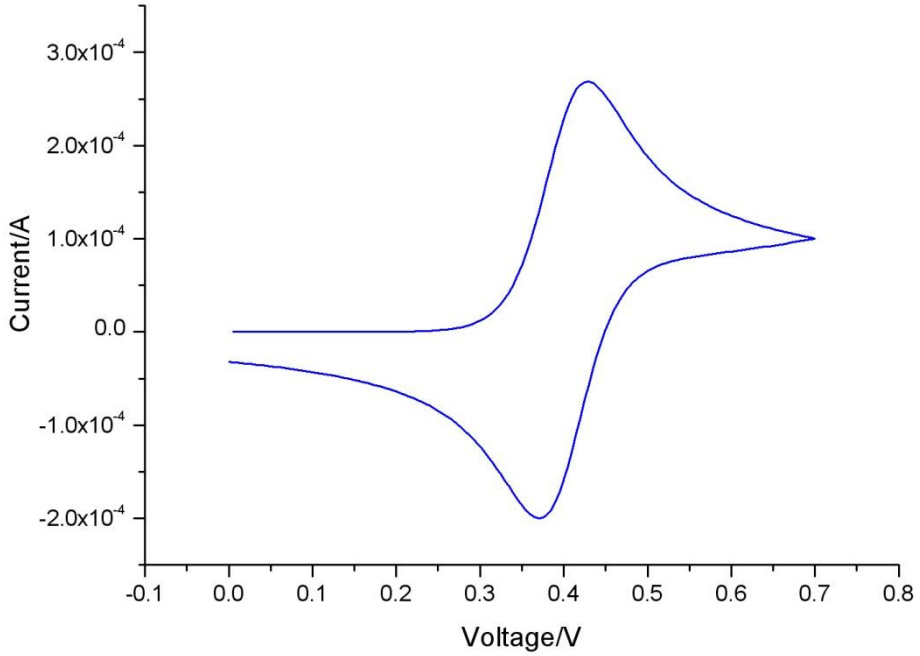

Fig 2.4 Simulated CV for a reversible one electron reaction with redox potential of 0.4V vs reference electrode, Scan rate 100 mVs^{-1}, [Red]=[Ox].

Initially, the potential is held such that the RE and WE are at the same potential. The WE potential is then swept positively at a constant scan rate up to 0.7V, before being swept back to 0V relative to the RE. It can be seen that initially no current is observed to flow, but that as the potential is increased a positive current flows which peaks and then decays to a level greater than the initial level. On the reverse scan the same effect is observed but the current flow is negative relative to the initial current.

In section 2.3.5, the current flowing was discussed in terms of both an anodic and cathodic component relating to the oxidation and reduction of solution species respectively. It was also observed that overpotential has an effect on the

current according to the Butler Volmer equation and this can be seen in the CV. As the overpotential is increased positively the rate of the oxidation reaction is increased relative to the reductive reaction resulting in a large anodic current. As the overpotential is made more negative the reverse occurs. When the kinetics of electron transfer are fast, equilibrium between the oxidised and reduced states continues as the potential is scanned, so the surface concentrations obey the Nernst potential[21]. The effect of mass transfer plays a significant role in causing the CV to take the shape observed. As species are depleted near to the electrode surface, a diffusion layer with concentrations of species below the bulk concentration is set up. As this gets thicker, the concentration gradient which causes species to diffuse to the electrode decreases. When this reaches a maximum the CV peak is observed; beyond this the concentration gradient decreases, limiting the current observed in the CV.

A large number of parameters can be obtained from analysis of the precise shape of a CV as described by equations such as the Cottrell equation. In this work CV has been used qualitatively. Of interest to this work is the Nernst potential of species in the solution or adsorbed onto the electrode. This can be estimated by determining $E_{1/2}$ which is the potential half way between the anodic and cathodic current peaks.

2.3.10 Junction potential

In equation 2.11, the measured potential was described in terms of the potential drop at the reference electrode and the potential drop at the working electrode. The iR drop was also introduced for cases when current flow is high. In the case where there is an interface in the system with different solutions on either side, for example at the glass frit in a reference electrode, there is an additional potential drop termed the liquid junction potential (LJP).

For junctions between liquids where the solvent is the same but the ionic species are different or at different concentrations, the LJP is caused by differences in the mobility of different species e.g. the cation and anion of a salt. The simplest example is that of a junction where the concentration of a salt is different on either side of the interface. The example given by Bard and Faulkner of two

solutions of HCl at different concentrations is used here[19]. In this situation there is a concentration gradient for both ionic species from the area of high concentration to that of low concentration. However, both ions have different mobility – H^+ mobility is higher – so H^+ diffuses faster into the dilute phase. This results in the dilute phase becoming positively charged relative to the concentrated phase so that a potential difference is built up between the two, producing an electric field which decreases the movement of H^+ and increasing the movement of Cl^- to the point where they cross the interface at the same rate. The potential difference built up by this process is the LJP. For this simple case the LJP can be modelled and calculated effectively as expressed by equation 2.13

$$E_j = \phi_\beta - \phi_\alpha = \frac{-RT}{F}\sum_i \frac{t_i}{z_i} d\ln a_i \quad \text{Equation 2.13}$$

where ϕ is the potential of phase α or β, t_i is the transference number for ion i, z_i is the charge on ion i and a is the activity coefficient of ion i. The transference number for an ion is the fractional contribution of that ion to the total conductivity of the solution and so depends on charge, mobility and concentration.

In most situations, the junction is a lot more complicated and different ions will be present on each side of the junction which can still be calculated reasonably well using the Henderson equation[19] (equation 2.14) when the solvent is the same on both sides.

$$E_j = \frac{\sum_i \frac{|z_i|u_i}{z_i}\left[C_i(\beta) - C_i(\alpha)\right]}{\sum_i |z_i| u_i \left[C_i(\beta) - C_i(\alpha)\right]} \frac{RT}{F} \ln \frac{\sum_i |z_i| u_i C_i(\alpha)}{\sum_i |z_i| u_i C_i(\beta)} \quad \text{Equation 2.14}$$

Here $C_i(\alpha)$ is concentration of ion i in phase α , $|z_i|$ is magnitude of charge on ion i and u_i is mobility of ion i. Applying this equation to an interface where a solution of 2 M LiI is in phase α and 3M KCl is in phase β, similar to the case expected when measuring the aqueous DSSC electrolyte with a SCE or Ag/AgCl reference electrode, a LJP of -5.3mV is determined. Mobility data for this calculation is based on literature values[19]: $u_{Li+} = 4.01\text{x}10^{-4}\text{cm}^2\text{s}^{-1}\text{V}^{-1}$, $u_{K+} = 7.619\text{x}10^{-4}\text{cm}^2\text{s}^{-1}\text{V}^{-1}$, $u_{I-} = 7.96\text{x}10^{-4}\text{cm}^2\text{s}^{-1}\text{V}^{-1}$, $u_{Cl-} = 7.912\text{x}10^{-4}\text{cm}^2\text{s}^{-1}\text{V}^{-1}$. Unfortunately a value for the

cation of the ionic liquid PMII used extensively in this work as the I^- source could not be found from the literature. However based on equation 2.15

$$u_i = \frac{|z_i|q}{6\pi\eta r_i} \qquad \text{Equation 2.15}$$

where q is the elementary charge, η is the solvent viscosity and r is the radius of ion i, it is possible to calculate u_{PMI+} as $2.29 \times 10^{-7} cm^2 s^{-1} V^{-1}$ based on an ionic radius of approximately 4Å and water viscosity of 1.002Pas[22]. This leads to a LJP value of -13.5mV. These values are fairly small, however larger LJP values can occur when a different solvent is present on either side of the liquid junction.

Calculating the LJP for junctions between immiscible liquids has additional complexity. In such cases, the difference in electrochemical potential or free energy of ions in the two solutions becomes very important, largely due to the difference in solubility. This can be estimated using equation 2.16

$$E_j = \phi_\beta - \phi_\alpha = -\frac{1}{z_i F}\left[\Delta G^{0_{\alpha\to\beta}}_{transfer,i} + RT\ln\left(\frac{a_i^\beta}{a_i^\alpha}\right)\right] \qquad \text{Equation 2.16}$$

where

$$\Delta G^{0_{\alpha\to\beta}}_{transfer,i} = \mu_i^{0_\beta} - \mu_i^{0_\alpha} \qquad \text{Equation 2.17}$$

where μ^0_i is the standard free energy of the species i in solution[19]. Measuring a LJP can be difficult as it adds an additional unknown term to the measurement of potential between two electrodes as shown in equation 2.18.

$$E = (\phi_m - \phi_s) + (\phi_s - \phi_{ref}) + (\phi_\beta - \phi_\alpha) \qquad \text{Equation 2.18}$$

Large E_j values of greater than 100mV have been determined for junctions between different solvents[23] which clearly has a significant influence on potential determination.

2.4 Dye Sensitized Solar Cell operation

A simple description of the operating principles of a dye cell was given in chapter 1. A fuller description of these will now be given and the various energy levels in the dye cell will be considered in greater detail.

2.4.1 In the dark

Most of the components of the dye cell have been previously described in chapter 1. When these are assembled, the energetics of the dye cell are those shown in the simplified diagram in Fig 2.5. The semiconductor has a conduction band and valence band as described previously, as well as a large number of trap states located in the band gap. When electrolyte is introduced, there is a negligible amount of band bending at the interface as described in section 2.2.8. In the dark, equilibration of Fermi energy across the cell sets the Fermi energy of the semiconductor at the Nernst potential of the redox couple. This also sets the Fermi energy of the conducting substrate and in doing so, depletion of electrons in the FTO results in band bending at the interface[14]. The addition of the dye to the surface can have an effect on the conduction band position. It has been seen that the adsorption of N719 onto TiO_2 shifts the CB positively by about 60-70mV[12a]. The reason suggested for this is that the two protons released by adsorption of dye change the surface charge of the TiO_2, causing the CB to drop[12a]. In the electrolyte, the redox Fermi energy is equal to the Nernst potential (equation 2.9) which will be affected by the relative concentrations of the species in solution. At the counter electrode, the Fermi energy is set by the equilibration of the redox Fermi energy and the Fermi energy in the metal.

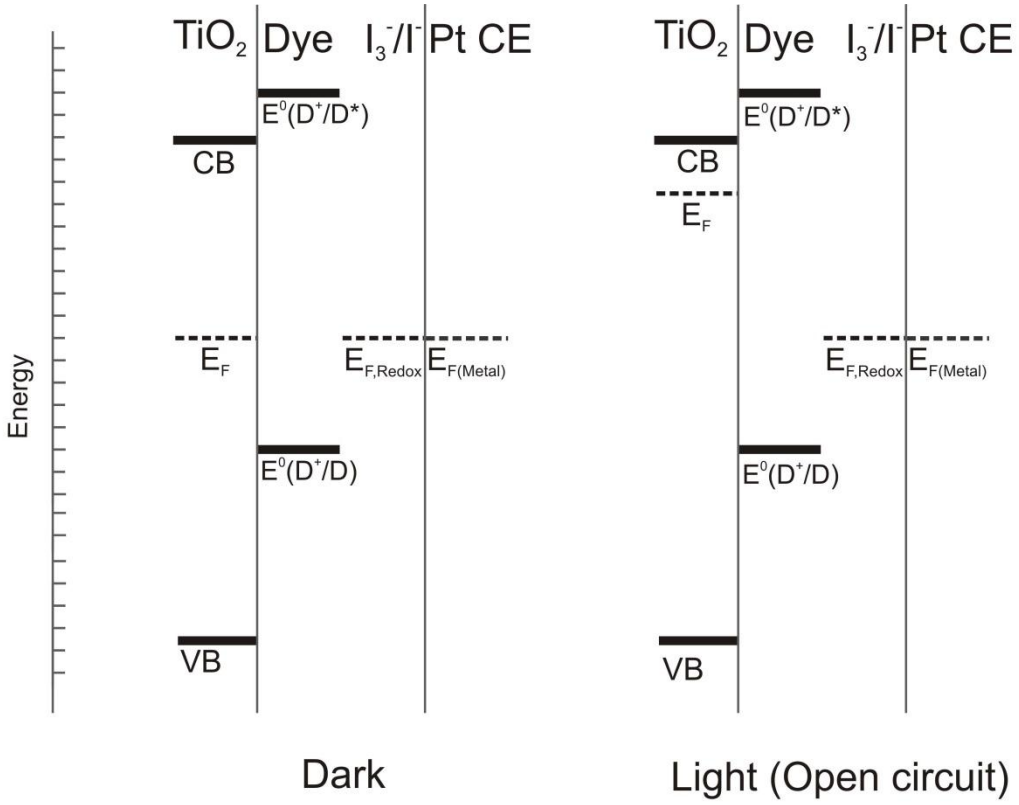

Fig 2.5 Energy level diagram for dye cell in dark and light conditions (at open circuit).

2.4.2 Under illumination

Upon visible illumination, photons are absorbed by dye molecules according to the absorption profile of the dye. The absorbed energy causes an electron to move to a higher energy level in the dye, from where it can be injected into the conduction band of the semiconductor. Depending on the external circuit conditions, different situations will occur in the semiconductor. Two limiting cases are considered: short circuit, where there is essentially no resistance between the photoanode and counter electrode in the external circuit, and open circuit, where the potential is set so that no net current flows in the external circuit.

2.4.2.1 Short circuit

The injection of electrons into the semiconductor causes an increase in the electron quasi Fermi energy nE_F at the semiconductor surface based on the increase in free electron concentration. The Fermi energy in the FTO substrate for the photoanode will be equal to that at the counter electrode i.e. the redox Fermi energy ($E_{F,Redox}$) plus the overpotential required for reduction of I_3^-

(scheme 2.1). The diffusion of injected electrons down the resulting concentration gradient in the TiO_2 results in an electron flux to the counter electrode and subsequent reaction with I_3^-. Providing there are no other limits, the flux of electrons due to the electron gradient at the point where the semiconductor meets the substrate will determine the current in the external circuit.

$$I_3^- + 2e^- \rightarrow 3I^-$$ Scheme 2.1[9,24]

At the counter electrode, the current density (j) that is able to flow can be described by the Butler Volmer equation[14,19] (equation 2.10) and so is dependant particularly on the standard rate constant for the reaction (k^0) and the diffusion of I_3^- to the surface. A certain overpotential ($\eta = E - E^0$) will be required to drive the reaction and the size of this will depend on the reaction rate constant. At the short circuit potential, the low position of the Fermi energy at the FTO|semiconductor interface and its 'sink' effect on electrons mean that the Fermi energy at the semiconductor|electrolyte interface is low compared to that under open circuit conditions. As a result, the longest electron lifetimes are obtained under these conditions because there is a lower driving force for loss mechanisms (which will be covered in more detail when describing open circuit conditions) to occur.

As a result of injecting an electron into the semiconductor, the dye molecule becomes oxidised. The mechanism for regeneration of dye by I^- is similar regardless of the external circuit potential, though this potential will affect the extent to which the dye is regenerated by this mechanism or direct recombination with injected electrons.

A suggested mechanism for dye regeneration is summarised by Boschloo et al[24-25] (scheme 2.2) and involves the production of the diiodide radical species.

$$D^+ + I^- \rightarrow (D\cdots I)$$

$$(D\cdots I) + I^- \rightarrow (D\cdots I_2^{-\bullet})$$ Scheme 2.2

$$\left(D\cdots I_2^{-\bullet}\right) \rightarrow D + I_2^{-\bullet}$$

$$I_2^{-\bullet} \rightarrow I_3^- + I^-$$

This means that the driving force for dye regeneration is based on the difference between the reduction potential for $I_2^{-\bullet}/I^-$ and D^+/D. After reduction of the dye, the I_3^- will diffuse down a concentration gradient to the counter electrode and react to produce I^-.

2.4.2.2 Open circuit

As the resistance in the external circuit between the electrodes is increased, the electron concentration at the Semiconductor|FTO interface is increased (Fig 2.5) which decreases the electron concentration gradient across the film. The increase in electron concentration in the film also increases nE_F in the film. The result of this is an increased reaction rate between electrons in the TiO_2 and either I_3^- or D^+ and for the reaction between electrons in the FTO and I_3^- (particularly if there is no blocking layer present) (scheme 2.3). As the concentration gradient becomes shallower the electron flux decreases, reducing the cell current. The open circuit condition will occur when the FTO nE_F is at an energy where the flux of electrons into the semiconductor (and FTO) directly matches the flux of electrons being lost through the mechanisms in scheme 2.3 at which point no net current will flow though the external circuit.

$$D^+ + e^-_{TiO_2} \rightarrow D$$

$$I_3^- + e^-_{TiO_2} \rightarrow I^- + I_2^{-\bullet} \qquad \text{Scheme 2.3}$$

$$I_3^- + e^-_{FTO} \rightarrow I^- + I_2^{-\bullet}$$

Despite the high concentration of I^-[14], it is expected that at high voltages the reaction between D^+ and electrons in the semiconductor will compete with the regeneration of dye by iodide[26]. The rate of the back reaction between I_3^- and electrons in the semiconductor depends on the rate constant for the reaction (k_{BR}), the electron concentration (n) and the I_3^- surface concentration (Equation 2.19). Determining the reaction order for n and I_3^- is not simple, and is complicated by the fact that electron transfer does not only occur from the CB (free electrons) but also from trapped states[27].

$$Rate_{BR} = k_{BR} n[I_3^-]_0 \qquad \text{Equation 2.19}$$

It is expected that under most cell operating conditions, band edge pinning will occur. This means that the increase in nE_F upon illumination will not alter k_{BR} but only have an influence on n.

2.5 DSSC Cell performance

There are a number of parameters that can be examined in determining cell performance. The simplest are the short circuit current density (J_{SC}), open circuit voltage (V_{OC}), fill factor (FF) and efficiency (η) and these can be determined from the IV curve which was introduced in chapter 1. Some others include the wavelength dependant incident photon to charge carrier efficiency (IPCE), electron diffusion length (L_n), electron lifetime of free electrons (τ_0) and electron diffusion constant (D_0). There are also a number of theoretical models for dye cells which seek to predict cell performance based on fundamental parameters.

2.5.1 IV curve

The IV curve has been introduced already in chapter 1 and now based on the following discussion it will be shown more clearly how the standard shape appears. The photocurrent response (j) can be considered as the sum of the light generated current and the dark current. Across the range of voltages used for a standard IV curve, the current generated by light is constant and equal to the short circuit current. The dark current varies according to potential and shows similar characteristics to that of a p-n diode having an 'on' voltage at a certain potential at which the reaction between I_3^- and e^-_{TiO2} begins to occur resulting in large cathodic currents. This can be described according to equation 2.20 as derived by Södergren et al[28]

$$j = qI_0(1-\eta_{inj}e^{-\alpha d}) - q\frac{D_0 n_c^0 d}{L_n^2}\left(e^{\frac{qU}{k_B Tm}} - 1\right) \qquad \text{Equation 2.20}$$

where I_0 is the light intensity, η_{inj} the electron injection efficiency, α the molar absorption coefficient, d the film thickness, D_0 the electron diffusion coefficient,

n_c^0 the free electron concentration in the dark, L_n the electron diffusion length (discussed in section 2.5.3), U the potential and m the diode non-ideality factor.

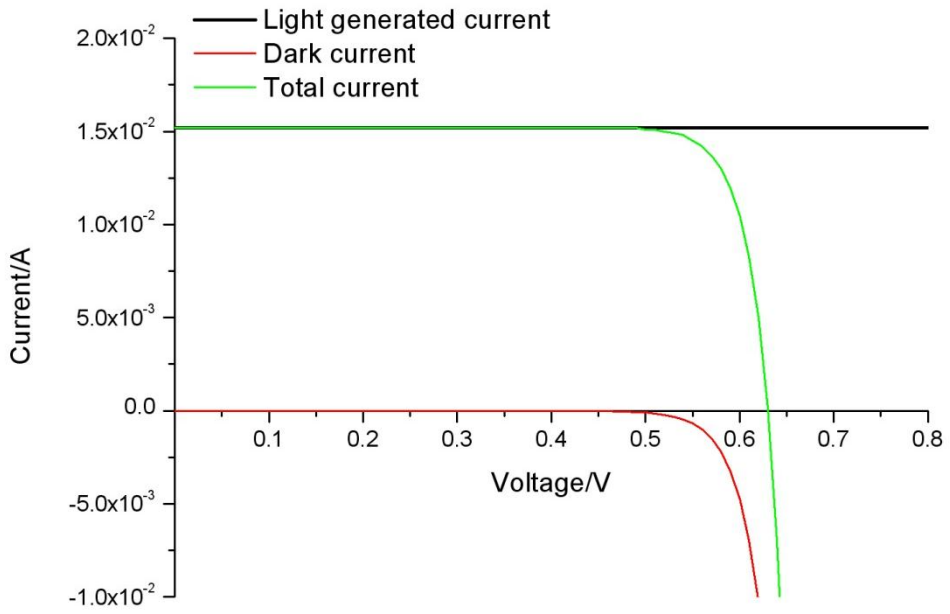

Fig 2.6 Simulated IV curves based on Equation 2.20 where $I_0 = 10^{18}$, $\eta_{inj} = 1$, $\alpha = 10^4$, $d = 10^{-5}$, $D_0 = 10^{-3}$, $n_c^0 = 10^{14}$, $L_n = 1.58 \times 10^{-1}$ and n = 1 showing contributions from dark and light generated current.

The simulated IV curve in Fig 2.6 has a very high fill factor. However, this is not always the case and there are several parameters which can reduce the fill factor. If the series resistance of the cell is high, this will dominate the response according to Ohms law (V=IR) resulting in a drop in fill factor. In the extreme case, the IV response will be a straight line between I_{SC} and V_{OC} with a slope equal to the resistance. If the kinetics at the counter electrode are slow, which could for example be caused by a dirty CE, the overpotential required for reaction will be high resulting in a decrease in fill factor, often seen as a 'z' curve. Two other factors that will alter the IV curve though not necessarily the fill factor are considered. The shunt resistance is the resistance to the reaction between I_3^- and e_{FTO}^- at the substrate and if this is low, the onset of the dark current will be at a lower voltage and reduce the V_{OC}. Cell non-ideality (m) is a complicated parameter linked to the reaction order for electrons and I_3^- in the reaction between them at the semiconductor interface, and the effect of this is shown in Fig 2.7.

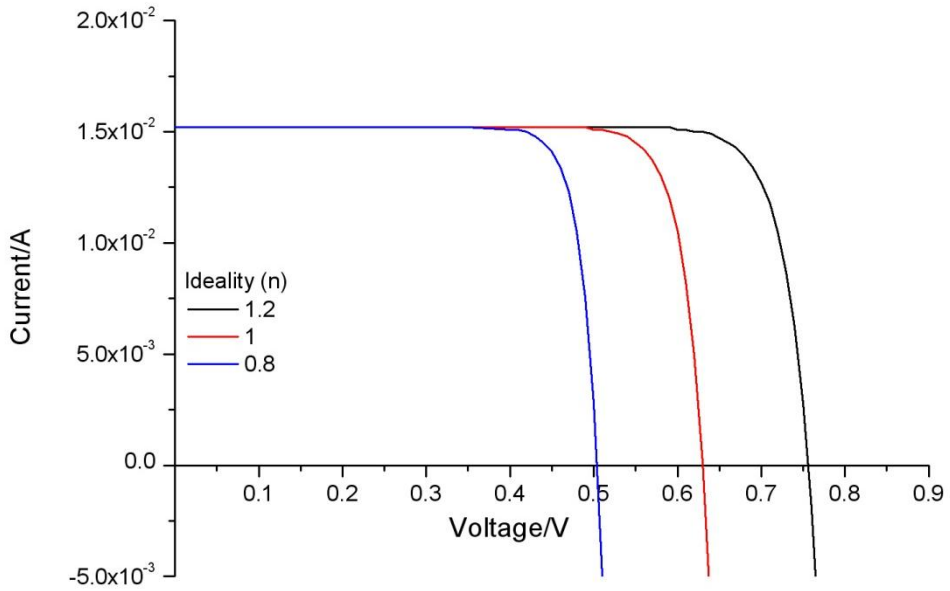

Fig 2.7 Simulated IV curves based on Equation 2.20 where $I_0 = 10^{18}$, $\eta_{inj} = 1$, $\alpha = 10^4$, $d = 10^{-5}$, $D_0 = 10^{-3}$, $n_c^0 = 10^{14}$, $L_n = 1.58 \times 10^{-1}$ and n is changed. The effect of m changing based on this model is to alter V_{OC}.

2.5.2 Incident photon to charge carrier efficiency (IPCE)

The incident photon to charge carrier efficiency measures the fraction of photons incident on a cell converted to current as a function of wavelength. The IPCE can be split into three additional parameters: wavelength dependant light harvesting efficiency ($\eta_{LH}(\lambda)$), electron injection efficiency (η_{inj}) and electron collection efficiency (η_{col}) as shown in equation 2.21[29].

$$IPCE(\lambda) = \eta_{LH}(\lambda) \times \eta_{inj} \times \eta_{col} \quad \text{Equation 2.21}$$

The light harvesting efficiency is dependant on the molar absorption coefficient of the dye and the wavelength dependence will follow the absorption profile of the dye. The absolute value will depend on the concentration of the dye – for example, if the film is thinner than the penetration depth of light at a certain concentration and wavelength, not all the light will be absorbed at that wavelength whereas if the concentration of dye is increased, more of the light will be absorbed. The electron injection efficiency will depend on the relative rates of electron injection and excited state deactivation (equation 2.22), either by quenching or excited state decay. Generally it is found that injection is very fast,

in the range of femto seconds[30] leading to values of η_{inj} close to one. These can be studied using techniques such as transient absorption spectroscopy[30].

$$\eta_{inj} = \frac{k_{inj}}{k_{deact} + k_{inj}}$$ Equation 2.22

The electron collection efficiency has also often been found to be close to one[29]. This parameter is the most complex to describe as it is based on the ability of an electron to travel from the point of injection through the semiconductor and to the electrode contact (at short circuit for IPCE). Therefore it is influenced primarily by the probability of reaction with I_3^- or D^+ and affected by trapping states.

2.5.3 Diffusion length

A factor that can be used to gauge the efficiency of electron collection is the ratio between the electron diffusion length and the film thickness (d)[31]. If this ratio is high, it implies that an injected electron has a high probability of reaching the contact before it is lost, indicating a high η_{col}: L_n/d ratios of 3 have been suggested to correlate to collection efficiencies of 98%[32]. Techniques that can be used to measure this will be considered in section 6.2.6. The parameter L_n can be described as the root of the product of the electron lifetime and the electron diffusion coefficient[32] (equation 2.23).

$$L_n = \left(D_0 \tau_0\right)^{1/2}$$ Equation 2.23

It has already been mentioned that these parameters cannot easily be obtained because of the influence of trap states on the electronic properties of the semiconductor. Work by Bisquert et al[12b] has shown that provided that $\partial n_t / \partial n_c >> 1$ (where n_t is number of trapped electrons, n_c is number of free (CB) electrons), that is provided trap relaxation is faster than the time scale of the process of interest (for example electron lifetime), the effective (measured) lifetime or diffusion constant (τ_n, D_n) can be related to that expected for free electrons (without the influence of trapping) according to equation 2.24 and 2.25:

$$\tau_n = \left(\frac{\partial n_t}{\partial n_c}\right)\tau_0$$ Equation 2.24

$$D_n = \left(\frac{\partial n_c}{\partial n_t} \right) D_0$$ Equation 2.25

As a result, L_n can still be determined (equation 2.26):

$$L_n = (D_0 \tau_0)^{1/2} = (D_n \tau_n)^{1/2}$$ Equation 2.26

Electron lifetime describes how long an electron will remain in the semiconductor film after injection before it is lost via recombination with I_3^- or D^+, assuming it is not collected at the contact. The diffusion constant describes the velocity at which an electron travels through the semiconductor film.

A further consequence of the condition $\partial n_t / \partial n_c >> 1$ is that the Fermi energy is related to both the Fermi-Dirac distribution for free electrons and the energy of the highest filled trap state.

2.5.4 Continuity equation

The continuity equation has been developed to describe the behaviour of a DSSC under steady state conditions. This equation contains three terms describing electron generation, diffusion to the substrate and loss at the semiconductor surface[14]

$$\frac{\partial n}{\partial t} = \eta_{inj} \alpha(\lambda) e^{-\alpha(\lambda)x} + D_n \frac{\partial^2 n_c}{\partial x^2} - \frac{n_c}{\tau_n} = 0$$ Equation 2.27

where α(λ) is the wavelength dependant absorption coefficient of the dye and x is the distance from the substrate. In order to solve this equation, the following boundary conditions are set.

$$n_{c,x=0} = n_c^0 e^{\frac{qU}{k_B T}}$$ Equation 2.28

$$\frac{dn_c}{dx} = 0 \text{ at } x = d$$ Equation 2.29

where n_c^0 is the free electron density in the dark and U is the photovoltage. From the solution of this equation it is possible to calculate a large number of parameters including electron density and photocurrent.

2.6 Techniques

2.6.1 Infra red electron density measurements

Infra red (IR) light has been used to measure the concentration of electrons (n) in TiO_2 films in a number of studies[12a,33]. Electrons in the film absorb light at IR wavelengths, resulting in a detectable change in the transmission of light (ΔT) through the film[33d] upon a change in the number of electrons present. This can be analysed according to the Beer-Lambert law to determine the number of electrons in the film[12a,33d] using (equation 2.30)

$$\frac{\Delta T}{T} = \sigma_n(\lambda) d \Delta n \quad \text{Equation 2.30}$$

where T is the initial transmission, $\sigma_n(\lambda)$ is the optical cross section of electrons as described below, d is the film thickness and Δn is the change in the number of electrons. For this analysis to be accurate, the wavelength dependant optical cross section of the electrons ($\sigma_n(\lambda)$), analogous to an absorption coefficient, must be determined by calibrating results versus another technique such as charge extraction[12a].

Expected free and trapped electron distributions can be modelled by using the following approach as shown by Nguyen et al[12a]. An approximation for the distribution of trap states is described above in equation 2.4. To determine the density of trapped electrons, the state distribution function multiplied by the occupancy probability function is integrated across all energies. A measurable property is the change in the number of trapped electrons between when the cell is in the dark and under illumination, so a useful expression can be given as

$$\Delta n_t = \int_{-\infty}^{\infty} f_{FD}^{light}(E) g(E) dE - \int_{-\infty}^{\infty} f_{FD}^{dark}(E) g(E) dE \quad \text{Equation 2.31}$$

The occupancy probability function is the Fermi-Dirac function, which, for example in the light, can be expressed as equation 2.32[12a].

$$f_{FD}^{light} = \frac{1}{1+\exp\left(\frac{E_C -_n E_F}{k_B T}\right)}$$ Equation 2.32

By applying the zero Kelvin approximation, this can be changed to a step function, and so equation 2.31 can be simplified to

$$\Delta n_t \approx \int_{\mathrm{E_{F,\,Redox}}}^{\mathrm{E_{F,\,Redox}} + \mathrm{U_{Photo}}} g(E)dE$$ Equation 2.33

Based on a solution of the continuity equation with appropriate boundary conditions, free electron profiles can be determined and according to equation 2.32, a quasi electron Fermi energy ($_nE_F$) profile can be calculated from this.

$$n_c = N_c \exp -\left(\frac{E_C -_n E_F}{k_B T}\right)$$ Equation 2.32

Here N_c is the number of CB states and n_c is the number of free electrons. One of the useful results of such a model is that it becomes clear that when using reasonable parameters, the number of trapped electrons is approximately four orders of magnitude higher than the number of free electrons. As such, measurements of Δn in equation 2.30 can be considered to be measures of trapped electrons, Δn_t.

Fig 2.8 demonstrates that a measurement of ΔT/T for an illumination pulse will provide information on a section of the trapped electron distribution between E_F in the dark (i.e. $E_{F,Redox}$) and the quasi Fermi energy of electrons in the light, but that there may be more electrons trapped in states energetically below the redox potential of the redox mediator.

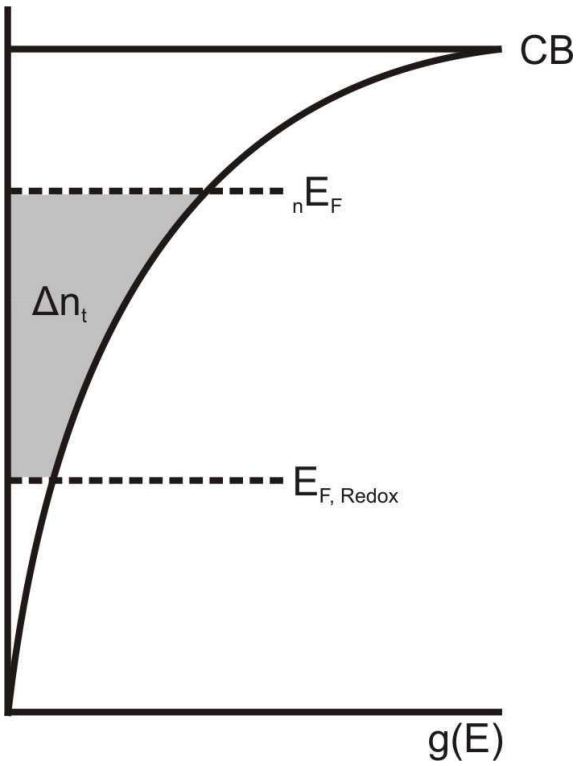

Fig 2.8[3] Representing trapped electrons measured by recording ΔT/T upon illumination. Curved line represents trapped electron density of states as described by g(E). Shaded area represent additional trap states filled upon illumination.

2.6.2 Open Circuit Voltage Decay (OCVD)

The open circuit voltage decay (OCVD) measurement involves measuring the open circuit voltage (V_{OC}) of a dye cell when a light pulse is applied and then switched off. The decay transient ($V_{OC}(t)$) can be used to obtain information such as the effective electron lifetime[34] (τ_n) and the characteristic temperature (T_0) describing the tail of the electron trap distribution[8]. Of particular interest in this work is τ_n, and the treatment of OCVD data to obtain this parameter as determined by Zaban et al[34] will be presented here.

Upon illumination, the number of free electrons in the cell (n) is determined by the balance between photon absorption and loss mechanisms such as recombination, assuming that η_{inj} is essentially one. This can be described as a rate equation

$$\frac{dn}{dt} = -U(n) + \alpha_{abs} I_0 \qquad \text{Equation 2.33}$$

where α_{abs} is the absorption coefficient of the dye, I_0 is the light intensity and U(n) is the rate of electron loss that is electron density dependant (equivalent to $Rate_{BR}$ in equation 2.19). In the (nonequilibrium) steady state case, dn/dt is equal to zero. At this point, V_{OC} is the difference between ${}_nE_F$ and $E_{F,Redox}$ and can be written as

$$V_{OC} = \frac{{}_nE_F - E_{F,\mathrm{Redox}}}{q} = \frac{k_B T}{q}\ln\left(\frac{n}{n_0}\right) \quad \text{Equation 2.34}$$

where e is the elementary charge and n_0 is the electron concentration in the dark. OCVD makes use of the fact that when illumination has been switched off, the generation term in equation 2.33 is no longer present and the transient change is only dependant on loss processes. As such, the change in free electron concentration can be described as

$$\frac{dn}{dt} = -U(n) \quad \text{Equation 2.35}$$

Zaban et al[34] go on to define the effective electron lifetime as

$$\tau_n^{-1} = -\frac{1}{n}\frac{dn}{dt} \quad \text{Equation 2.36}$$

where t is time which leads to

$$\tau_n = \frac{n}{U(n)} \quad \text{Equation 2.37}$$

for the case where recombination is linear.

The electron lifetime as a function of voltage can then be derived to give

$$\tau_n = -\frac{k_B T}{q}\left(\frac{dV_{OC}}{dt}\right)^{-1} \quad \text{Equation 2.38}$$

allowing $\tau_n(V_{OC})$ to be determined based on $V_{OC}(t)$ data. Rewriting equation 2.19 as the change in free electrons due to the reaction between electrons in the TiO_2 and I_3^- yields equation 2.39

$$\frac{dn}{dt} = -k_{br}[I_3^-]n \quad \text{Equation 2.39}$$

the solution of which is

$$n(t) = n(0)\exp(-k_{br}[I_3^-]t) = n(0)\exp\left(-\frac{t}{\tau}\right)$$ Equation 2.40

where

$$\tau = \frac{1}{k_{br}[I_3^-]}$$ Equation 2.41

assuming that the reaction between free electrons and I_3^- is first order with respect to $[I_3^-]$. Here the lifetime is equivalent to τ_0. As has been mentioned, the reaction between electrons and I_3^- is not necessarily linear[27b,35], that is (neglecting the reaction of electrons with D^+)

$$Rate_{BR} = -k_{BR}n^{\beta}[I_3^-]$$ Equation 2.42

where β is the reaction order for electrons. Zaban proposes that in the case where this parameter shows large changes as a function of voltage, equation 2.38 is no longer accurate and derives an alternative expression:

$$\tau_n^{-1} = -\frac{q}{k_B T}\frac{dV_{OC}}{dt} - \left(\frac{dV_{OC}}{dt}\right)^{-1}\frac{d^2V_{OC}}{dt^2}$$ Equation 2.43

Generally, equation 2.38 is used for analysis in this work.

It is also possible to determine the characteristic temperature of the trapped electron distribution through analysis of OCVD data. Walker et al[8] show that

$$\frac{dU_{Photo}(t)}{d\ln t} \approx -\frac{k_B T/q}{1 - T/T_0}$$ Equation 2.44

and so the gradient of a plot of the photovoltage decay as a function of ln(t) can be used to approximately determine this parameter.

2.6.3 Frequency modulated techniques

Various techniques exist which are based on the comparison between a modulated input applied to a system and the modulated response of that system. The modulation frequency of the signal applied to a system will tend to be varied allowing aspects of the system with differing response times to be analysed. The steady state input value about which the modulation occurs will also be varied, effecting the system response. Two such techniques used in this project are electrochemical impedance spectroscopy (EIS), which uses voltage as the input and current as the output, and intensity modulated photovoltage spectroscopy (IMVS) which uses light as the input and voltage as the output.

2.6.3.1 Electrochemical Impedance Spectroscopy (EIS)

Mathematical treatment of EIS is very complicated and is beyond the scope of this work. For significant treatments of this, the reader is directed to chapter 12 by Bisquert and Fabregat-Santiago in reference [3] and chapter 10 in reference [19]. Much of the theory presented in this section is based on these two sources. Here, some of the basics of the technique will be presented, and a standard equivalent circuit model for the DSSC introduced.

Fig 2.9 represents the input and output signals described earlier for an input potential (E) and an output current (I). Several particular features are of note; the magnitude of the signal (E or I) which is the peak height of the wave and the phase difference (Φ) which is the offset between the input and output waves. Mathematically, these can be expressed by equations 2.45 and 2.46

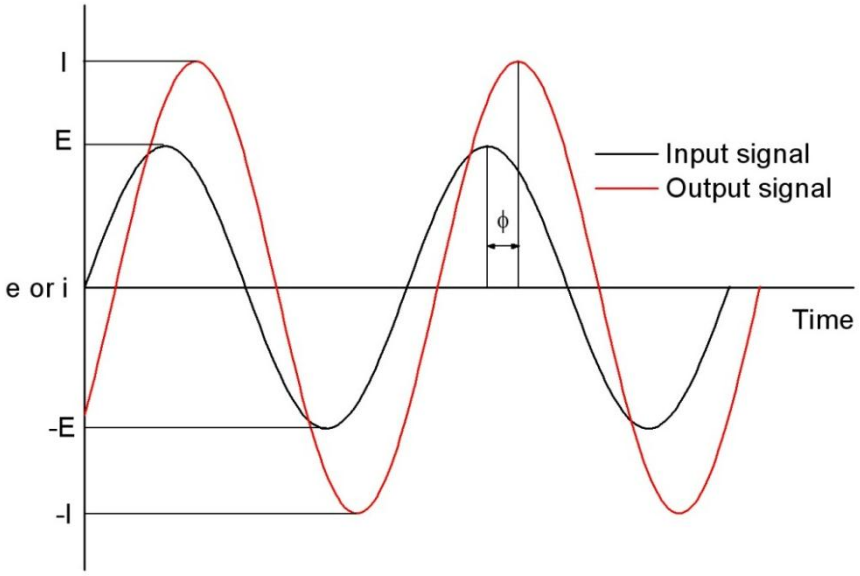

Fig 2.9 Representing modulated input and output signals and important wave characteristics including amplitude and phase.

$$\dot{E} = E\sin(\omega t) \qquad \text{Equation 2.45}$$

$$\dot{I} = I\sin(\omega t + \phi) \qquad \text{Equation 2.46}$$

where ω is the angular frequency, equal to the standard frequency, f, multiplied by 2π. These are often considered as phasors, denoted by the dot above E and I, which are rotating vectors and can be visualised as in Fig 2.10; phasors will be used whenever a modulated input or response is being considered.

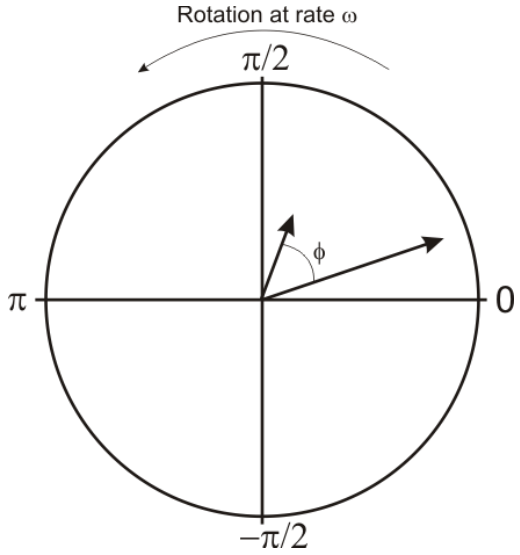

Fig 2.10 Phasor diagram for two rotating vectors with equal rotation frequency, different magnitude and constant phase shift.

Impedance (Z) is a vector quantity and is a measure of the ability of a circuit to resist the flow of current

$$Z = \frac{\dot{E}}{\dot{I}} \qquad \text{Equation 2.47}$$

In order to use this approach to analyse electrochemical systems in terms of impedance, different aspects of such systems can be modelled using equivalent circuits. These are model systems made up of circuit elements such as resistors and capacitors which show a similar impedance response to the electrochemical system. For example, in section 2.3.1 it was seen that on the introduction of an electrode to a solution, there is a build up of ions at the surface across which there is a potential drop but no charge transfer. This is very similar to the case of a capacitor where there are two oppositely charged conducting plates separated by a non-conducting dielectric layer, leading to a significant potential gradient between the plates but no charge transfer. As such, capacitors can be used to model the double layer at an electrode interface.

The simplest circuit element considered is that of the resistor. This can be related to real phenomenon such as the resistance of a wire in a circuit or the resistance across an interface to charge transfer. The current response to voltage for a resistor is described by Ohms law and when considered for a modulated input can be written using phasors as in equation 2.48.

$$\dot{E} = \dot{I}R \qquad \text{Equation 2.48}$$

Substituting in the phasors in equation 2.45 and 2.46, we obtain

$$\frac{E\sin(\omega t)}{I\sin(\omega t + \phi)} = R \qquad \text{Equation 2.49}$$

however in the case of a resistor, Φ is zero as the current response is instantaneous, so the response has a simple linear relationship and the impedance found by substitution with equation 2.47 is equal to the resistance

$$Z = R \qquad \text{Equation 2.50}$$

For a capacitor, the situation is slightly more complex. The current response for a capacitor is

$$i = C\frac{d\dot{E}}{dt}$$ Equation 2.51

When considering a modulating input this becomes

$$\dot{\mathrm{I}} = C\frac{dE\sin(\omega t)}{dt}$$ Equation 2.52

which can be simplified to

$$\dot{\mathrm{I}} = \omega CE\cos(\omega t)$$ Equation 2.53

which is equivalent to

$$\dot{\mathrm{I}} = \omega CE\sin(\omega t + \frac{\pi}{2})$$ Equation 2.54

Including the phasor for current allows the impedance to be determined (equation 2.55), however it is clear that the phase angle is now π/2. This means the impedance vector for a capacitor is at π/2 compared to a resistor

$$\frac{I\sin(\omega t + \phi)}{E\sin(\omega t + \frac{\pi}{2})} = \omega C = \frac{1}{Z}$$ Equation 2.55

It is also important to note that the response of a capacitor is frequency dependant due to the ω term whereas resistance will not change as a function of frequency.

At this point, it is useful to consider the impedance response in the complex plane. Where the phase angle is zero, as in the case of a resistor, the response is considered ‘real’ and is along the abscissa, when it is π/2 (90°) the response is

considered ‘imaginary’, denoted by j and is along the ordinate. For example, the impedance response of a capacitor is in fact

$$Z = \frac{1}{j\omega C} \qquad \text{Equation 2.56}$$

Mathematical analysis can be undertaken using complex exponentials in order to show the origin of the real and imaginary terms. This is based on the relationships below and will be demonstrated by deriving the total impedance response for a resistor and capacitor in series according to Kirchoffs laws as described below (equation 2.62).

$$A\cos(x+y) = Ae^{jx}e^{jy} \qquad \text{Equation 2.57}$$

$$Z(\omega) = Z_{\mathrm{Re}} - jZ_{\mathrm{Im}} \qquad \text{Equation 2.58}$$

The total Z for the system in Fig 2.12 is given as

$$Z_{tot} = Z_R + Z_C \qquad \text{Equation 2.59}$$

This can be written as a complex exponential based on the relationship in equation 2.57

$$Z_{tot} = \frac{Ee^{j\omega t}}{Ie^{j\omega t}e^{j\phi}} + \frac{Ee^{j\omega t}}{\omega CIe^{j\omega t}e^{j\phi}} \qquad \text{Equation 2.60}$$

in this case, $e^{j\omega t}$ cancels in both terms and Φ is zero in the first term and - π/2 in the second. E/I is equal to R in term one and equal to one in term two. The result is the expression

$$Z = R - \frac{j}{\omega C} \qquad \text{Equation 2.61}$$

where R is the real part and the j term the imaginary part. This could be plotted as in Fig 2.11 where the impedance vector can be described both in terms of a real and imaginary component as well as a magnitude and phase.

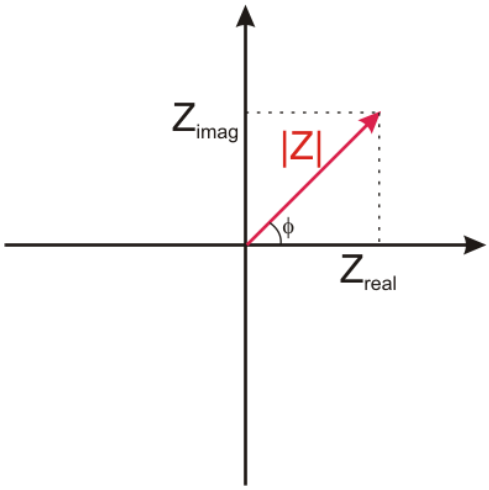

Fig 2.11 Impedance vector shown on a complex plot.

Combining circuit elements is important as electrochemical systems are complex. Combining elements follow Kirchoffs laws so in the case of a series combination (Fig 2.12), the total impedance is the sum of the individual components (Equation 2.62) whereas in a parallel combination the reciprocal of the total impedance is the sum of the reciprocals of the individual components (equation 2.63).

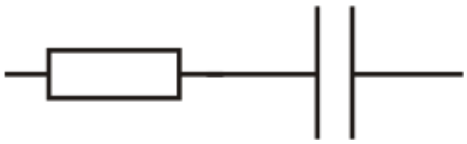

Fig 2.12 Series combination of resistor and capacitor

$$Z_{series} = Z_1 + Z_2 \qquad \text{Equation 2.62}$$

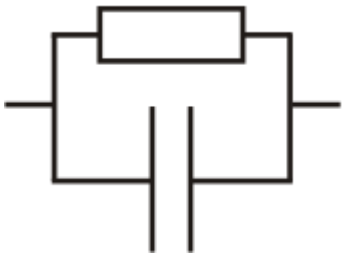

Fig 2.13 Parallel combination of resistor and capacitor

$$\frac{1}{Z_{Parallel}} = \frac{1}{Z_1} + \frac{1}{Z_2} \qquad \text{Equation 2.63}$$

A further example of a simple equivalent circuit system will be considered, that of a resistor connected in series with a resistor and capacitor connected in parallel. A real situation similar to this could be charge transfer across an interface, excluding the effects of diffusion in the electrolyte.

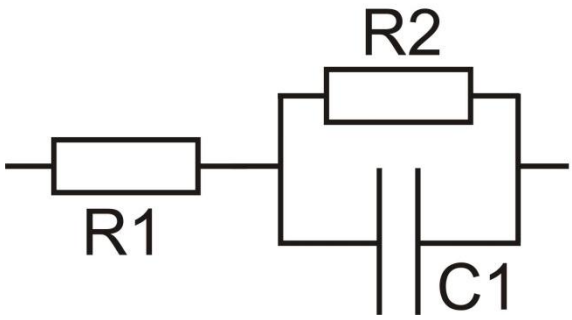

Fig 2.14 Combination of resistor in series with a resistor and capacitor in parallel.

$$Z = R_1 + \frac{R_2(1 - j\omega R_2 C)}{1 + \omega^2 R_2{}^2 C^2}$$ Equation 2.64

$$Z_{real} = R_1 + \frac{R_2}{1 + \omega^2 R_2{}^2 C^2}$$ Equation 2.65

$$Z_{imaj} = \frac{-\omega R_2{}^2 C}{1 + \omega^2 R_2{}^2 C^2}$$ Equation 2.66

The expected response in the complex plane is shown in Fig 2.15 and can be explained by considering the effect of frequency on the impedance response. R_1 is simple to analyse as it will remain constant at all frequencies and offsets the response at each frequency by R_1. At high frequency, Z_{real} tends to R_1 and Z_{imaj} tends to zero. However, at low frequency Z_{real} tends to R_1+R_2 whereas Z_{imaj} tends to zero. Intermediate frequency values produce the semicircle shown. There is a special case when $Z_{real} = R_1+(R_2/2)$ and $Z_{imaj} = -R_2/2$ as $\omega=1/RC$. These different features can be used to obtain system values directly from impedance data.

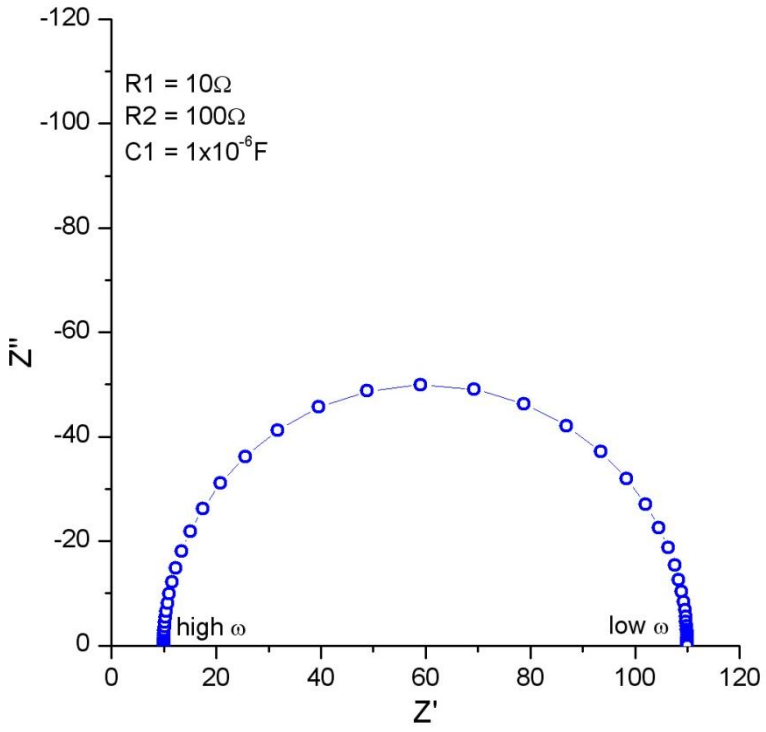

Fig 2.15 Impedance response for circuit diagram in Fig 2.14

Two further elements that are of importance in real systems and pertinent to modelling a DSSC are the Warburg element and the transmission line. The Warburg element is represented as 'W'. This element has a frequency dependant response and is used to represent diffusion of charge carriers through the electrolyte. The impedance response of the Warburg element is

$$Z_W = \frac{\sigma}{\omega^{1/2}} - \frac{j\sigma}{\omega^{1/2}} \qquad \text{Equation 2.67}$$

where σ is a parameter based on the diffusion coefficients and bulk concentrations of the oxidised and reduced species in solution. It can be seen that a signal based only on a Warburg element will have a slope of -1 and phase angle of 45° as both the real and imaginary response have the same magnitude and frequency response. In terms of frequency response, at high frequency the time scale of the potential change is too short to be influenced by diffusion effects and so the Warburg response becomes very small. Several variations of this element are used which have different responses at lower frequencies. The infinite or semi infinite variation is used where the depth of solution affected by the modulating signal is much smaller than the depth of available solution. In this

case the Warburg response show a large increase in Z'' with no change in Z' at a certain frequency. The finite Warburg ('W_S' in Fig 2.21) is used in the case where the penetration depth of the signal is similar or larger than the depth of solution, as is the case in DSSCs. In this case, a semi-circle is observed (Fig 2.16).

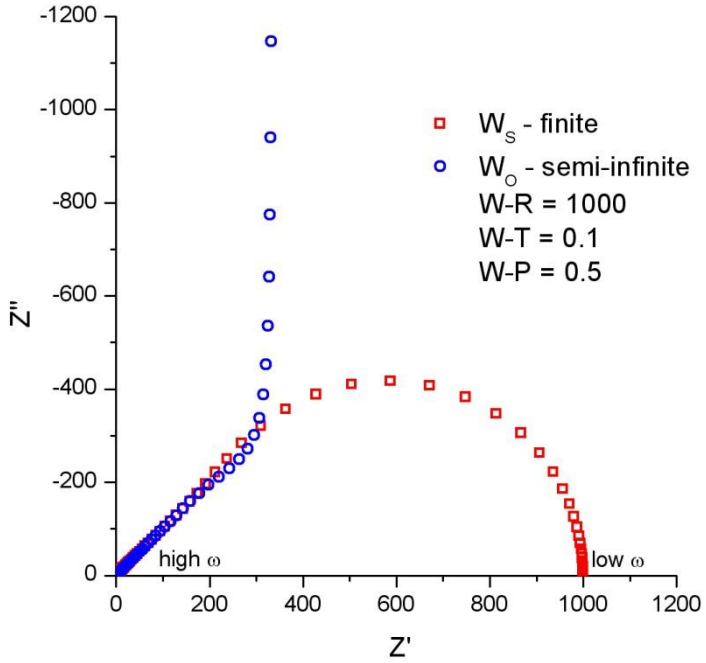

Fig 2.16 Expected impedance response for Warburg circuit element showing initial 45° slope and different high frequency behaviour depending on relative size of diffusion layer and solution depth.

A final element of importance when modelling DSSCs is that of the transmission line. This is a complex element made up of a large number of simpler elements often referred to as a distributed element. This is used to describe a system where spatial distribution is important; in the case of the dye cell, this is used to model processes occurring in the nanoporous TiO_2 and at its surface. In this case, charge transfer can occur at any point on the semiconductor surface, but electron transport to the substrate will vary depending particularly on the distance travelled by the electron. An equivalent circuit is shown in Fig 2.17. Here the resistance to electron transport is represented by a resistance (r_{trans}) and the charge transfer is an RC parallel circuit, where r_{CT} is the resistance to charge transfer and C_μ is the chemical capacitance. Chemical capacitance in this situation is not the same as double layer capacitance (at most cell potentials, see section 6.2.1.2) and is based on the charge in the film.

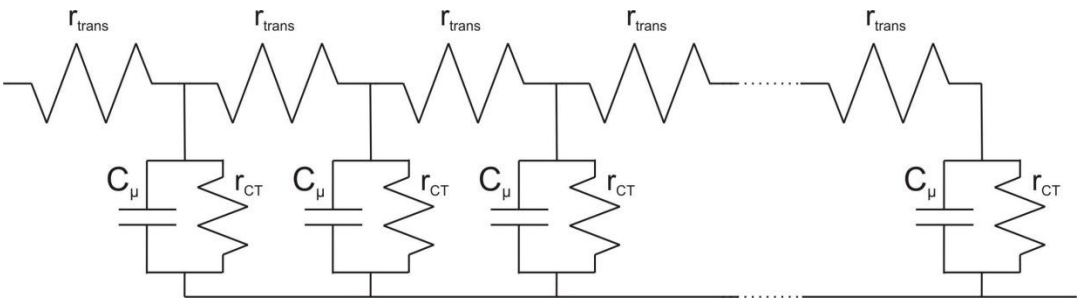

Fig 2.17 Transmission line model for electron diffusion and recombination

Fig 2.18 and 2.19 show the expected impedance responses for such an element (ignoring at this point other circuit elements that would be present to model all the mechanisms in a real cell) using different values for the resistance parameters. It can be seen that at high frequency the response is similar to that observed for a Warburg element and this feature is related to electron diffusion in the film. The semicircle at lower frequency is based on the parallel circuit between C_μ and R_{CT}, where R_{CT} is the macroscopic charge transfer resistance, related to r_{CT} by

$$R_{CT} = \frac{1}{LA(1-p)} r_{CT} \qquad \text{Equation 2.68}$$

where L is the film thickness, A is film area and p is film porosity – the denominator being equal to the film volume.

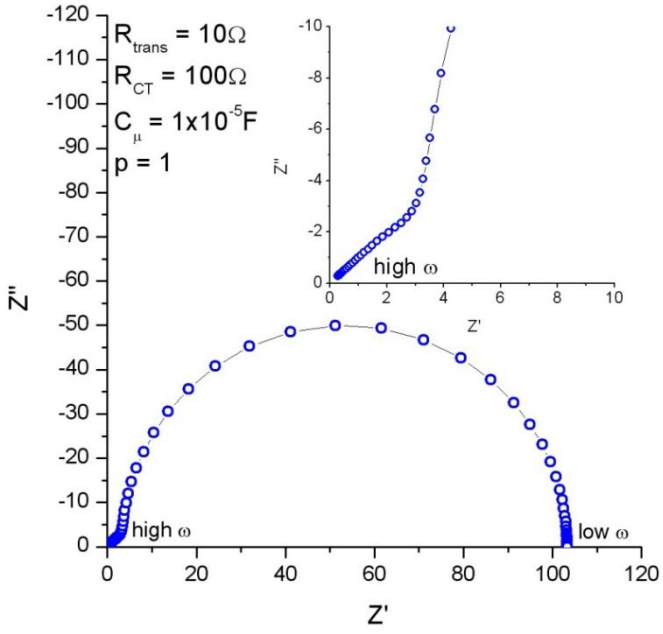

Fig 2.18 Modelled impedance response for transmission line shown in Fig 2.17 Parameters are set to represent slow recombination i.e. electron transport has a much lower resistance than back reaction.

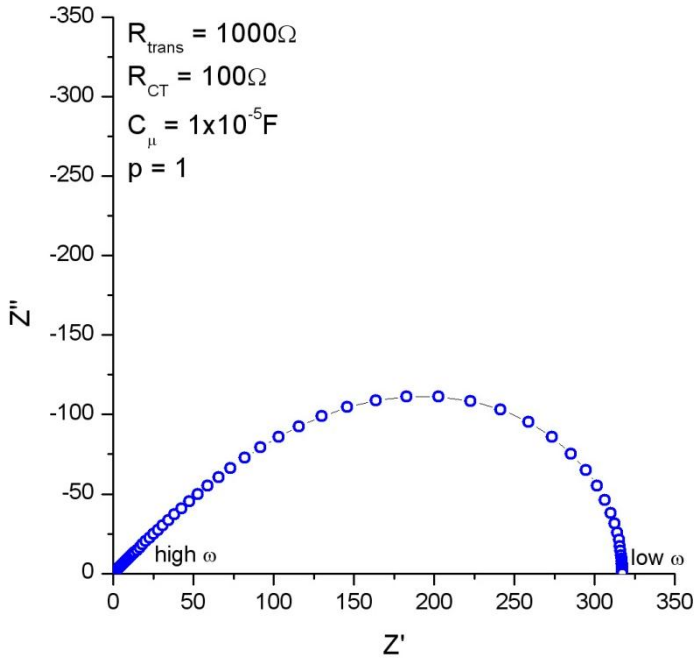

Fig 2.19 Modelled impedance response for transmission line shown in Fig 2.17 Parameters are set to represent fast recombination i.e. back reaction has a much lower resistance than electron transport.

In Fig 2.18, the case is presented where the recombination reaction is slow, so the ratio R_{CT}/R_{trans} is high. In Fig 2.19, the case where the recombination reaction is fast is shown so R_{CT}/R_{trans} is low. Practically, real systems do not always follow ideal models, and often elements known as Constant phase elements are introduced in place of capacitors. These have a power law dependence on frequency, and result in a depressed semicircle as shown in Fig 2.20. However, these elements must be used cautiously as fitting with them leads to values for which the physical cause is not clear.

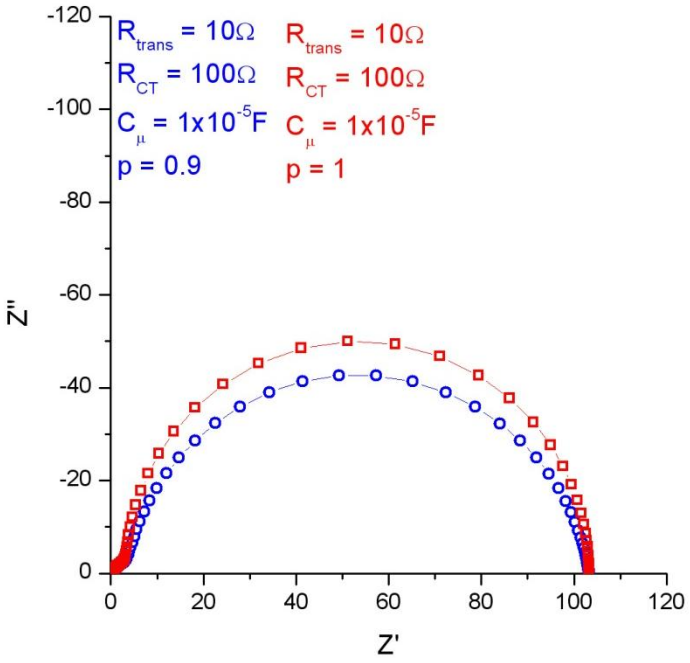

Fig 2.20 Showing effect of using constant phase element in place of capacitor in transmission line shown in Fig x15. Blue trace uses CPE with p = 0.9.

2.6.3.1.1 EIS for DSSCs

The transmission-line model developed by Bisquert[36] and Fabregat-Santiago et al[37] is typically used as an equivalent circuit for a standard liquid based DSSC. This model (Fig 2.21), which applies to liquid based DSSCs at intermediate cell potentials, consists of five circuit elements. However, these can be broken down further, particularly in the case of DX1.

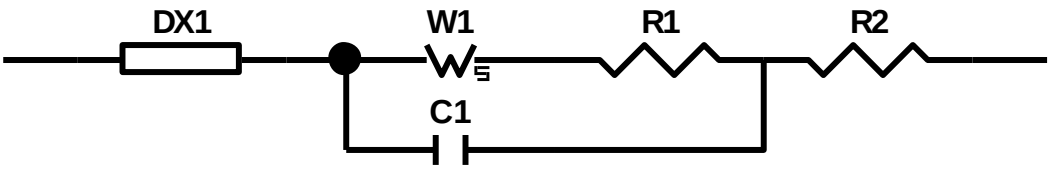

Fig 2.21 Equivalent circuit model for DSSC.

R_2 is the series resistance, which accounts for resistance in the cell contacts and external circuit. R_1 and C_1 relate to the counter electrode, and are the resistance to charge transfer and the double layer capacitance. W_1 is the Warburg impedance for charge transport in solution and DX1 is a distributed element and

accounts for electron transport in the nanoporous TiO_2 and electron transfer at the semiconductor|dye/electrolyte interface.

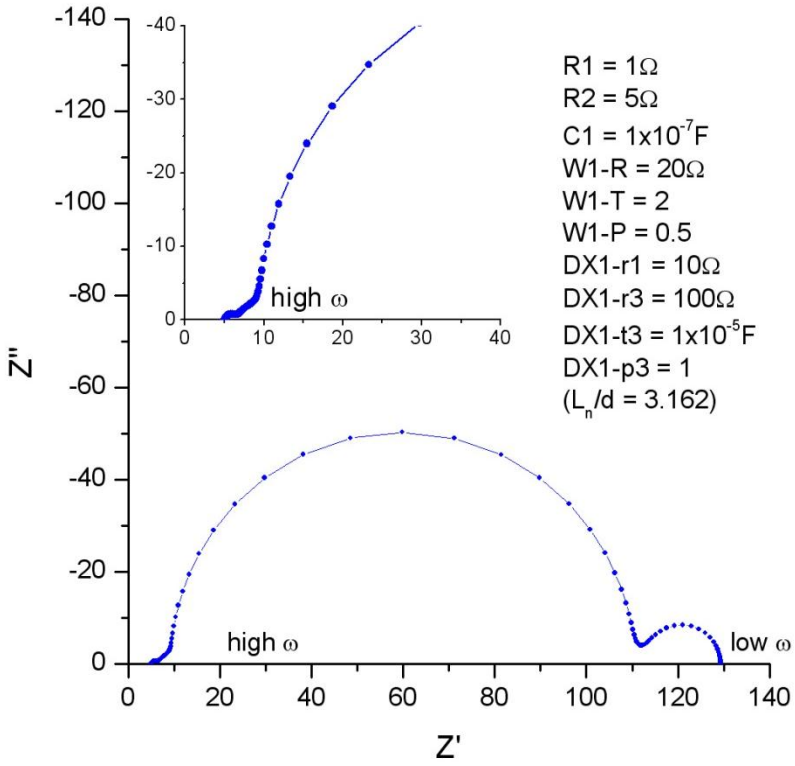

Fig 2.22 Simulated impedance spectra for DSSC using equivalent circuit model shown in Fig 2.21. Fitting parameters are as shown.

The plot shown in Fig 2.22 is that simulated for this model. The signal offset is due to the series resistance, the small semicircle at high frequencies is due to charge transfer at the counter electrode, the 45° line and subsequent semicircle are linked to the semiconductor response and the final semicircle is due to the finite Warburg.

2.6.3.2 Intensity Modulated Photovoltage Spectroscopy (IMVS)

Intensity modulated photovoltage spectroscopy (IMVS) is another technique where the oscillating response to an oscillating input is used to determine cell parameters. In this case, the cell is held under open circuit conditions and the voltage response to an incident illumination of oscillating intensity is recorded. This illumination is modulated (AC) around a steady value (the DC value) and the modulation is kept small to ensure a linear voltage response. The value of the

DC illumination may be altered to determine the effect of light intensity on the voltage response[3].

By holding the cell at open circuit, current flow through the external circuit is prevented and the effect of modulating the illumination is to modulate the Fermi energy in the semiconductor, resulting in an oscillating change in the back reaction rate. The time it takes for this response will depend on the rate at which electron loss mechanisms occur and this will be reflected in the phase angle between the input and output signal. Plotting the response on the complex plane in a manner similar to impedance should result in a semicircle with a positive real and negative imaginary axis (Fig 2.23) where the high frequency intercept is at the origin and the low frequency intercept is at the photovoltage value corresponding to the maximum photovoltage increase induced by the AC illumination. The frequency at which the semicircle is at a minimum corresponds to the reciprocal of the effective electron lifetime (equation 2.69) and so this technique can be used to determine this parameter.

$$2\pi f_{\min} = \frac{1}{\tau_n} \qquad \text{Equation 2.69}$$

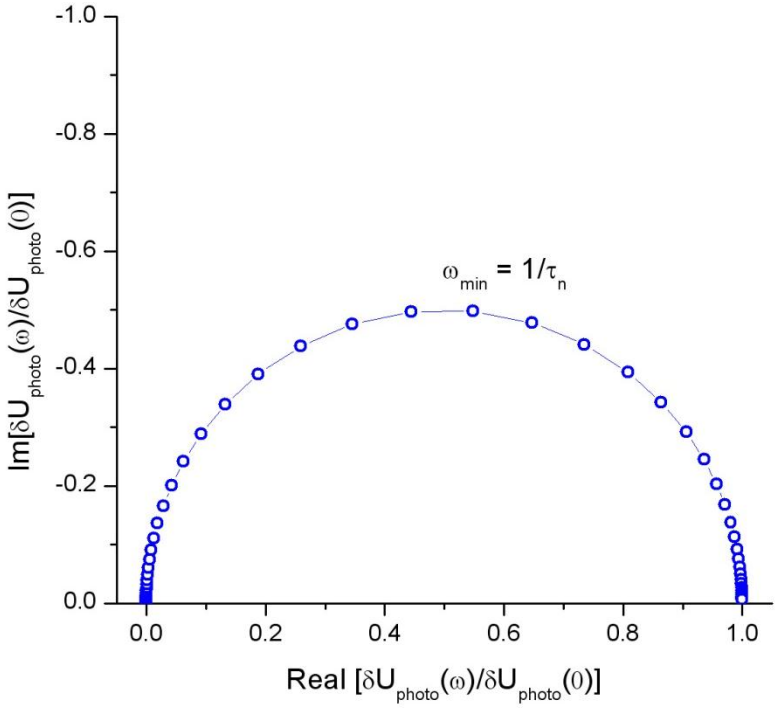

Fig 2.23 Showing simulated IMVS response normalised to DC response.

2.6.4 Surface tension and contact angle

It is well known that in the absence of other forces, liquids will tend to form a perfect sphere. This is because a sphere is the shape that has the smallest surface area for a given volume of material. Minimising this surface area is required in order to minimise the energy of the system as molecules at a surface have a greater energy than molecules in the bulk. This is a result of the disruption of intermolecular (IM) forces at the surface; in the bulk, molecules are stabilised by other molecules around them; at the surface the molecules are not surrounded so the stabilisation is less resulting in a higher energy. When placed on a surface, the shape of a droplet of liquid will be different depending on the strength of IM forces between molecules in the liquid and between liquid and surface molecules. By using water as the liquid, analysis of the droplet shape can be used to determine the relative hydrophobicity of different materials. In particular, the angle at which the edge of a droplet touches a surface is measured; this is called the contact angle (Fig 2.24). Analysis of contact angles is based on the following equation

$$\cos\theta_C = \frac{\gamma_{sg} - \gamma_{sl}}{\gamma_{\mathrm{lg}}} \qquad \text{Equation 2.70}$$

where γ_{sg} is the solid-gas interfacial free energy, γ_{sl} is the solid-liquid interfacial free energy and γ_{lg} is the liquid-gas interfacial free energy. The higher the contact angle, the more hydrophobic the surface because the internal IM forces (cohesive) in water are stronger than those between water and the surface molecules (adhesive)[1].

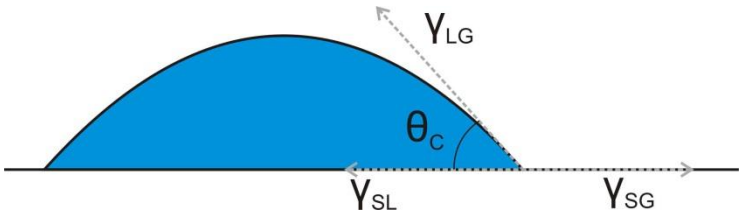

Fig 2.24 Showing contact angle and relevant interfaces. The blue area represents the water drop and the bottom line represents the surface.

2.6.5 Nanocalc

Interferometry can be used to determine the thickness of thin films and in this work the nanocalc system which illuminates normal to the film was used.
The basis for this measurement is the interference between light reflected from the front and back of the film. The phase difference in the reflected waves produces an interference pattern which, in the case of thin films, is largely dependant on the film thickness[38]. This can be analysed to determine the thickness of the thin film being measured.

2.7 References

(1) Atkins, P. W.; Atkins, P. W. P. c.; De Paula, J. *Atkins' Physical chemistry*; 7th ed. / Peter Atkins, Julio de Paula. ed.; Oxford University Press: Oxford, 2002.

(2) Würfel, P. D. *Physics of solar cells : from principles to new concepts*; Wiley-VCH: Weinheim, 2005.

(3) Kalyanasundaram, K. *Dye-sensitized solar cells*; CRC Press: Boca Raton, Fla., 2010.

(4) Boschloo, G. K.; Goossens, A. *J Phys Chem-Us* **1996**, *100*, 19489.

(5) Berger, T.; Anta, J. A.; Morales-Florez, V. *J Phys Chem C* **2012**, *116*, 11444.

(6) Redmond, G.; Fitzmaurice, D.; Graetzel, M. *J Phys Chem-Us* **1993**, *97*, 6951.

(7) Hoyer, P.; Weller, H. *J Phys Chem-Us* **1995**, *99*, 14096.

(8) Walker, A. B.; Peter, L. M.; Lobato, K.; Cameron, P. J. *J Phys Chem B* **2006**, *110*, 25504.

(9) Hagfeldt, A.; Boschloo, G.; Sun, L. C.; Kloo, L.; Pettersson, H. *Chem Rev* **2010**, *110*, 6595.

(10) Peter, L. *Accounts Chem Res* **2009**, *42*, 1839.

(11) Salvador, P.; Hidalgo, M. G.; Zaban, A.; Bisquert, J. *J Phys Chem B* **2005**, *109*, 15915.

(12) (a) Nguyen, T. T. O.; Peter, L. M.; Wang, H. X. *J Phys Chem C* **2009**, *113*, 8532(b) Bisquert, J.; Vikhrenko, V. S. *J Phys Chem B* **2004**, *108*, 2313.

(13) Zhang, Z.; Yates, J. T. *Chem Rev* **2012**, *112*, 5520.

(14) Peter, L. M. *Phys Chem Chem Phys* **2007**, *9*, 2630.
(15) Fisher, A. C. *Electrode dynamics*; Oxford University Press: Oxford, 1996.
(16) Preocanin, T.; Kallay, N. *Croat Chem Acta* **2006**, *79*, 95.
(17) Parks, G. A. *Chem Rev* **1965**, *65*, 177.
(18) Yu, Z.; Vlachopoulos, N.; Gorlov, M.; Kloo, L. *Dalton T* **2011**, *40*, 10289.
(19) Bard, A. J.; Faulkner, L. R. *Electrochemical methods : fundamentals and applications*; 2nd ed. ed.; John Wiley: New York ; Chichester, 2001.
(20) Peter, L. M. *J Solid State Electr* **2013**, *17*, 315.
(21) Compton, R. G.; Banks, C. E. *Understanding voltammetry*; 2nd ed. ed.; Imperial College Press: Singapore ; London, 2011.
(22) Haynes, W. M.; Bruno, T. J.; Lide, D. R. *CRC handbook of chemistry and physics*; 94th ed., 2013-2014 / editor-in-chief, W.M. Haynes ; associate editor, Thomas J. Bruno ed.; CRC: Boca Raton, Fla. ; London, 2013.
(23) (a) Kolthoff, I. M.; Thomas, F. G. *J Phys Chem-Us* **1965**, *69*, 3049(b) Kotocova, A. *Chem Zvesti* **1980**, *34*, 56.
(24) Boschloo, G.; Hagfeldt, A. *Accounts Chem Res* **2009**, *42*, 1819.
(25) Boschloo, G.; Gibson, E. A.; Hagfeldt, A. *J Phys Chem Lett* **2011**, *2*, 3016.
(26) Haque, S. A.; Tachibana, Y.; Klug, D. R.; Durrant, J. R. *J Phys Chem B* **1998**, *102*, 1745.
(27) (a) Gonzalez-Vazquez, J. P.; Oskam, G.; Anta, J. A. *The Journal of Physical Chemistry C* **2012**(b) Bisquert, J.; Cahen, D.; Hodes, G.; Ruhle, S.; Zaban, A. *J Phys Chem B* **2004**, *108*, 8106.
(28) Sodergren, S.; Hagfeldt, A.; Olsson, J.; Lindquist, S. E. *J Phys Chem-Us* **1994**, *98*, 5552.
(29) Hamann, T. W.; Jensen, R. A.; Martinson, A. B. F.; Van Ryswyk, H.; Hupp, J. T. *Energ Environ Sci* **2008**, *1*, 66.
(30) Wenger, B.; Gratzel, M.; Moser, J. E. *J Am Chem Soc* **2005**, *127*, 12150.
(31) Dunn, H. K.; Peter, L. M. *J Phys Chem C* **2009**, *113*, 4726.
(32) Jennings, J. R.; Ghicov, A.; Peter, L. M.; Schmuki, P.; Walker, A. B. *J Am Chem Soc* **2008**, *130*, 13364.
(33) (a) Rothenberger, G.; Fitzmaurice, D.; Gratzel, M. *J Phys Chem-Us* **1992**, *96*, 5983(b) Franco, G.; Gehring, J.; Peter, L. M.; Ponomarev, E. A.; Uhlendorf, I. *J Phys Chem B* **1999**, *103*, 692(c) Oregan, B.; Gratzel, M.; Fitzmaurice, D. *Chem Phys Lett* **1991**, *183*, 89(d) Neale, N. R.; Kopidakis,

N.; van de Lagemaat, J.; Gratzel, M.; Frank, A. J. *J Phys Chem B* **2005**, *109*, 23183.

(34) Zaban, A.; Greenshtein, M.; Bisquert, J. *Chemphyschem* **2003**, *4*, 859.

(35) Duffy, N. W.; Peter, L. M.; Rajapakse, R. M. G.; Wijayantha, K. G. U. *J Phys Chem B* **2000**, *104*, 8916.

(36) Bisquert, J. *J Phys Chem B* **2002**, *106*, 325.

(37) (a) Fabregat-Santiago, F.; Garcia-Belmonte, G.; Bisquert, J.; Zaban, A.; Salvador, P. *J Phys Chem B* **2002**, *106*, 334(b) Fabregat-Santiago, F.; Bisquert, J.; Garcia-Belmonte, G.; Boschloo, G.; Hagfeldt, A. *Sol Energ Mat Sol C* **2005**, *87*, 117.

(38) Graham-Smith, F.; King, T. A. *Optics and photonics : an introduction*; Wiley: Chichester, 2000.

Chapter 3: Experimental

3.1 Introduction

3.2 DSSC fabrication

3.3 Film thickness

3.4 Current-voltage (IV) curves

3.5 IPCE

3.6 OCVD

3.7 IMVS

3.8 EIS

3.9 Electrochemistry

3.10 IR

3.11 pH

3.12 Redox potential

3.13 Contact angle

3.14 UV/Vis

3.1 Introduction

In this chapter experimental details that are common for more than one chapter are given. Some additional details are given in individual chapters when they are only relevant to those chapters.

3.2 DSSC fabrication

Unless otherwise stated, all chemicals were used as supplied. TiO_2 films for dye uptake and desorption measurements were deposited on FTO glass (Hartford or Aldrich, TEC 15) or microscope slides (Sail Brand, 7101). FTO glass (Hartford or Aldrich, TEC 15) was used as the photoanode substrate for DSSCs. Cleaning glass involved two 15mins sonication steps in DECON 90 (Decon) with heating to 80°C, then 15mins sonication in Milli-RO water (In-house), then 15mins sonication in isopropanol (Fisher, LRG) at 80°C and a final 15mins sonication in ethanol (Fisher, ARG). Glass was then dried with N_2. A layer of TiO_2 nanoparticles was then deposited onto this substrate by the doctor blade technique – 'magic tape' (Scotch) was used to mark out a 1cm wide strip on the glass, and TiO_2 paste (Dyesol, DSL 18NR-T) was applied. The film was then sintered at 500°C for 30mins (in air) in a lab furnace (Elite, custom furnace). Films were dyed by submerging in the dye being studied; usually either N719 ([Ru(2,2'-bipyridyl-4,4'-dicarboxylic acid $)_2(NCS)_2$]: 2 tetra-*n*-butylammonium) (Dyesol) or Z907 ($RuLL'(NCS)_2$ (L=2,2'-bipyridyl-4,4'-dicarboxylic acid; L'=4,4'-dinonyl-2,2'-bipyridine)) (Dyesol) solution ($3x10^{-4}$M in a 1:1 t-butanol (Sigma-Aldrich, 99.7%):acetonitrile (Fisher, HPLC) solvent) overnight (~16hours) in blacked out containers. Dye desorption was achieved using a known amount of 0.1M KOH (Sigma, ACS >85%) solution in Milli-RO water.

DSSCs were made using a variation of the following procedure. To prepare the photoanode, FTO glass was cleaned as described above, then a blocking layer of TiO_2 was applied to the conducting side of the glass by spray pyrolysis on a hot plate at 400°C using a solution of 0.2M diispropoxytitanium bis(acetylacetonate) (Aldrich) in isopropanol. A layer of TiO_2 nanoparticles was then deposited onto this as above. Several variations to this technique are discussed in the results section. The most common method involved using a

single layer of tape, and depositing TiO_2 paste twice, with a heating step at 100°C in between the applications. Variants included depositing only a single layer, or depositing a single layer using two thicknesses of tape. When a scattering layer (DYESOL, WER2-O) was used, this was deposited onto the original TiO_2 layer using the doctor blade method. When the $TiCl_4$ treatment was used, this involved putting the sintered film into a 33mM solution of $TiCl_4$ (Fluka, puriss. >99.0%) in water (MILLI-RO) for 30mins at 70°C and then resintering at 500°C for 30mins. Films were then dyed as above in a solution of the dye being studied (N719, Z907, D35 ((E)-3-(5-(4-(Bis(2',4'-dibutoxybiphenyl-4-yl)amino)phenyl)thiophen-2-yl)-2-cyanoacrylic acid) or Z105 ([Ru(4,4'-Me_2-2,2'-bipy)(4'-PO_3H-terpy)(NCS)) in 1:1 t-butanol:acetonitrile solution or ethanol for Z105, usually at a concentration of 0.3mM. In some cases coadsorbates were also adsorbed onto the film at this point including bis-(3, 3-dimethyl-butyl)-phosphinic acid (DINHOP) (Dyesol), Deoxycholic acid (DCA) (Aldrich), 11-hydroxyundecyl-1-phosphinic acid (HUPA) (Aldrich) and bis(hydroxymethyl)phosphinic acid (HMPA) (Aldrich); these were typically at $1x10^{-3}$M concentration in the same solvent as the dye. Dimensions of the active area were usually 1cm x 1cm. To make the cathode, two 0.6mm diameter holes were drilled into FTO glass (Aldrich, TEC 7) which was then cleaned as described above. Pt was deposited by dropping several drops of $5x10^{-3}$M hexachloroplatinate (Aldrich, 99.995%) solution in isopropanol on the conductive side of the glass. This was then heated at 390°C for 15mins. To assemble the cell, a hot-melt SURLYN (Sol aronix, SX1170-25PF) gasket was used, and once the two sides were sealed together, a small quantity of electrolyte was introduced through the drilled holes. This varied as described in the text, the most common system consisting of 0.05M I_2 (Aldrich, 99.999%), 2M 3-propyl-1-methylimidazolium iodide (PMII) (Alfa Aesar or Merck) or LiI (Aldrich), 0.1M guanidine thiocyanate (GSCN) (Fluka, ≥99%) and 0.5M tert-butylpyridine(Aldrich, 99%) in either an 85:15 acetonitrile:valeronitrile (Aldrich) solvent or a water solvent with 1vol% Triton X-100 (BDH or Sigma Aldrich). The open back holes were sealed using SURLYN and a piece of coverslip glass (SLS). Finally, a layer of silver conductive paint (RS Components) was applied to the two electrodes to reduce series resistance. Surfactants other than Triton X-100 that were used included hexadecyltrimethylammonium bromide (CTAB) (Aldrich) and sodium dodecyl sulphate (SDS) (Aldrich). Buffer solutions were prepared using

potassium dihydrogen phosphate (Sigma Aldrich) and potassium hydrogen phthalate (Sigma Aldrich) in water and pH adjusted using HCl (Fisher, LRG) and NaOH (Aldrich). Ionic strength was kept constant using KCl (Aldrich).

3.3 Film thickness

Film thickness was measured with a reflectometer (Ocean Optics, Nanocalc-XR) equipped with a UV-VIS-NIR light source. Equipment control and data analysis were performed using the nanocalc software package. Non-conductive glass was used as the reference material. The thickness of the different layers of the dye cell was determined by initially measuring the simplest system (FTO on glass substrate) with the nanocalc system programmed to measure a single layer, then incrementally building up the system being measured (blocking layer on FTO on glass, nanoporous TiO_2 on blocking layer on FTO on glass). Thickness was determined based on the closest match of the theoretical waves calculated in nanocalc to the measured waves, generally values were close to the expected values based on standard literature or commercial data.

3.4 Current-voltage (IV) curves

IV curves were measured while cells were under illumination from one of two solar simulators; a TS Space Systems solar simulator equipped with a 200W metal halide lamp and internal AM1.5 filter and calibrated against a Si reference cell (Fraunhofer ISE, RS-OD-4) to 1 sun illumination, and a Müller Elektronic Optik solar simulator equipped with a Xenon lamp (Müller Elektronic Optik, ELL 1000), using AM1.5 filter (Abet-Technologies, 11056-1 AM1.5G) and calibrated against a separate Si reference cell (Czibula & Grundmann, RS-0D-1). Cells were not masked. IV curves were recorded on one of two potentiostats (Keithley, 2601A Sourcemeter or in-house build system). To vary light intensity, the cell position was altered relative to the light source and metal mesh filters were placed between the light source and the cell. Temperature was not controlled.

3.5 IPCE

IPCE measurements on full cells were taken using a setup consisting of a light source (Bentham IL1 Illuminator), monochromator (Bentham TMc300), amplifier and lock-in amplifier (Stanford Research Systems, SR830 DSP). Light was focussed onto the cell being measured using lenses and the spot size was smaller than the cell area. The lenses and cell were housed in a dark faraday cage. A diagram of the setup is shown in figure 3.1. Chopping was not employed due to the slow response time of DSSCs so the lock-in amplifier only recorded a DC current. However, measurements (not presented here) taken using chopped excitation light (low frequency) and a bias light resulted in a similar IPCE response. A delay time of 1s between readings was used to allow the DSSC to equilibrate after each step. After each measurement set a calibrated photodiode was used to determine the illumination intensity for the experimental conditions; this was positioned at the same point relative to the light source as the cell being measured.

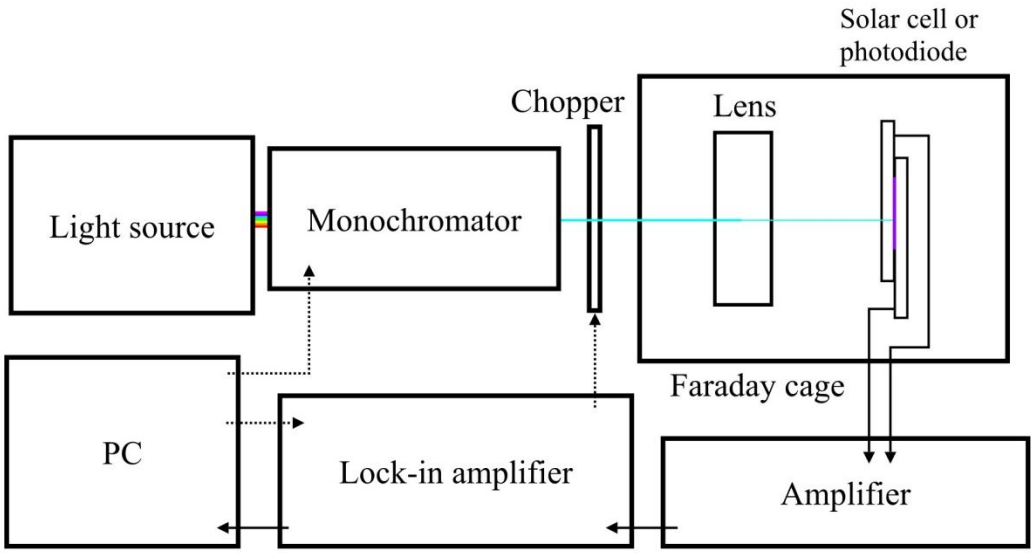

Fig 3.1 Experimental setup for IPCE measurements. DSSC is shown in diagram, for illumination intensity calibration this is replaced with a calibrated photodiode. Multi-coloured line represents white light, blue line represents single wavelength light, thin black solid lines represent measurement connections, dotted black lines represent control connections.

3.6 OCVD

A DSSC was connected to an oscilloscope (Tektronix TPS 3012) via a high impedance buffer amplifier and a low-noise pre-amplifier (Stanford Research Systems, SR560) which filtered out signal noise above 30Hz. A short (≈2s) light pulse from a green LED (530nm) controlled by an LED driver attached to a waveform generator (Hi-Tek Instruments, 2791366 PPRI) was applied to the DSSC, and the photovoltage decay measured against time. Resulting voltage vs time data was analysed according to equation 2.38. A diagram of the setup is shown in figure 3.2.

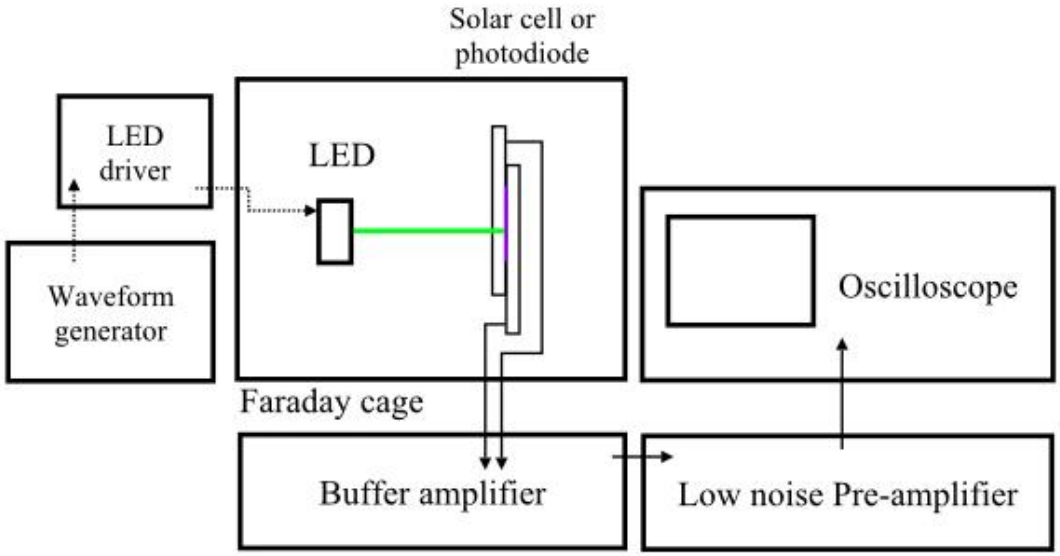

Fig 3.2 Experimental setup for OCVD measurements. DSSC is shown in diagram, for illumination intensity calibration this is replaced with a calibrated photodiode. Green line represents single wavelength light which could be controlled using neutral density filters if required, thin black solid lines represent measurement connections, dotted black lines represent control connections.

3.7 IMVS

A green LED (530nm) controlled by an LED driver was used to illuminate DSSCs at different DC illumination intensities. The light was modulated with a modulation depth of 10%, and the frequency of this was controlled by a frequency response analyzer (Solatron, SI 1250), which also measured the photovoltage response via measuring the output of a high impedance buffer amplifier connected to the

cell. A diagram of the setup is shown in figure 3.3. Typical frequency ranges used were between 2000 to 0.01Hz. The frequency response analyzer was controlled using a PC equipped with the Zplot and Zview software.

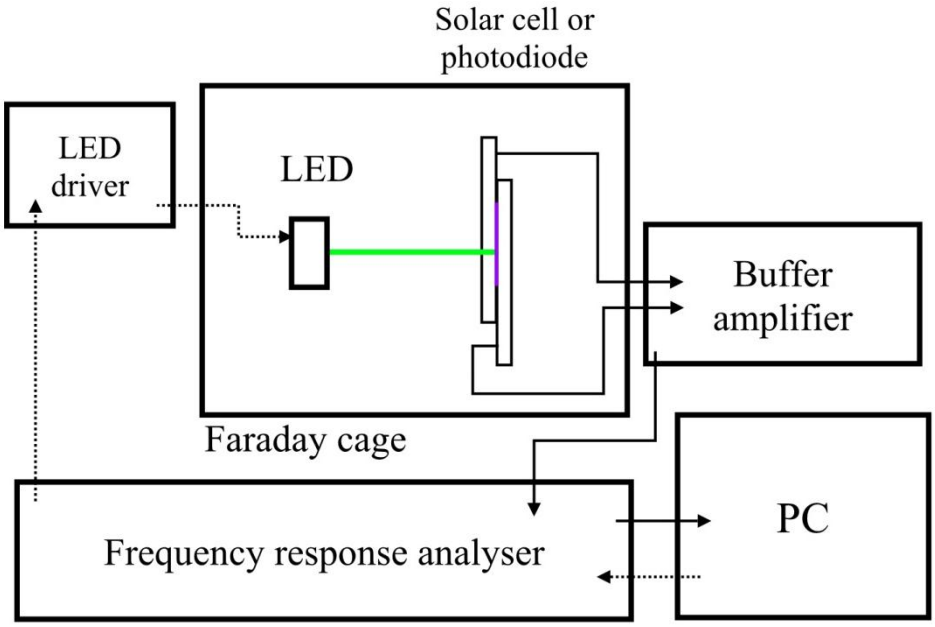

Fig 3.3 Experimental setup for IMVS measurements. DSSC is shown in diagram, for illumination intensity calibration this is replaced with a calibrated photodiode. Green line represents single wavelength light which could be controlled using neutral density filters if required, thin black solid lines represent measurement connections, dotted black lines represent control connections.

3.8 EIS

A DSSC was connected to a potentiostat (Solatron, SI 1287) controlled by a frequency response analyzer (Solatron, SI 1250), operated by a PC with the Zplot software installed. The DC potential of the cell was set either by a green LED (530nm) controlled by an LED driver where the illumination intensity was changed using neutral density filters, or directly by the potentiostat. The potential applied to the cell was modulated by 10% and the current response measured. Analysis of impedance data was done using the programmes ZView and ZPlot. A diagram of the setup is shown in figure 3.4.

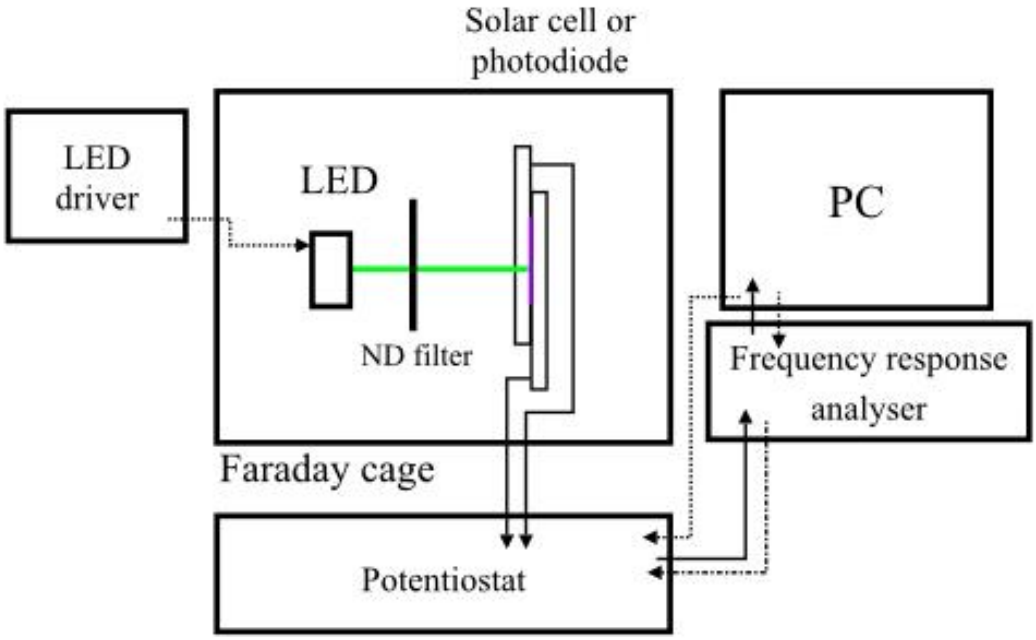

Fig 3.4 Experimental setup for EIS measurements. DSSC is shown in diagram, for illumination intensity calibration this is replaced with a calibrated photodiode. Green line represents single wavelength light, thin black solid lines represent measurement connections, dotted black lines represent control connections. Dashed dotted line represents frequency reference signal used to set the modulation frequency of the potential applied by the potentiostat across solar cell.

3.9 Electrochemistry

Several electrochemical measurements were performed. These were controlled by one of two potentiostats (Autolab, PGSTAT30 or Autolab, μAutolab FRA2 Type III) and run using Autolab General Purpose Electrochemical System (GPES) software. Reference electrodes were typically Ag/AgCl (3M KCl) (World Precision Instruments, DRIREF-2) or Saturated Calomel Electrode (SCE) (Radiometer analytical, Ref 401) and counter electrodes were typically Pt foil or Pt wire.

3.10 IR

A green (530nm) or blue (470nm) LED controlled by a waveform generator (Hi-Tek Instruments, 2791366 PPRI) was used to vary the illumination intensity incident on the DSSC. An infra red LED (1550nm or 950nm) with a small amplitude (30mA) oscillation at a frequency of 9.4kHz set by a lock-in amplifier (Stanford Research Systems, SR850 DSP) superimposed on a 45mA DC signal

set by a LED driver was shone constantly onto the cell. The response measured by an InGaAs photodiode placed behind the cell was fed via a low resistance amplifier (FEMTO, DLPCA-200) into the lock-in amplifier, then via a low noise pre-amplifier (Stanford Research Systems, SR560) with a 3Hz cutoff filter into an oscilloscope (Tektronix, TDS 3012). At the same time, the open circuit voltage or short circuit current of the cell were also measured on the oscilloscope via a low resistance amplifier (FEMTO, DLPCA-200) for short circuit conditions, or high impedance buffer amplifier for open circuit conditions. A longpass filter (Edmund Optics, RG1000) with a cutoff wavelength of 1000nm was placed between the cell and detector to minimize any effect from the green/blue LED on the detector (Figure 3.5).

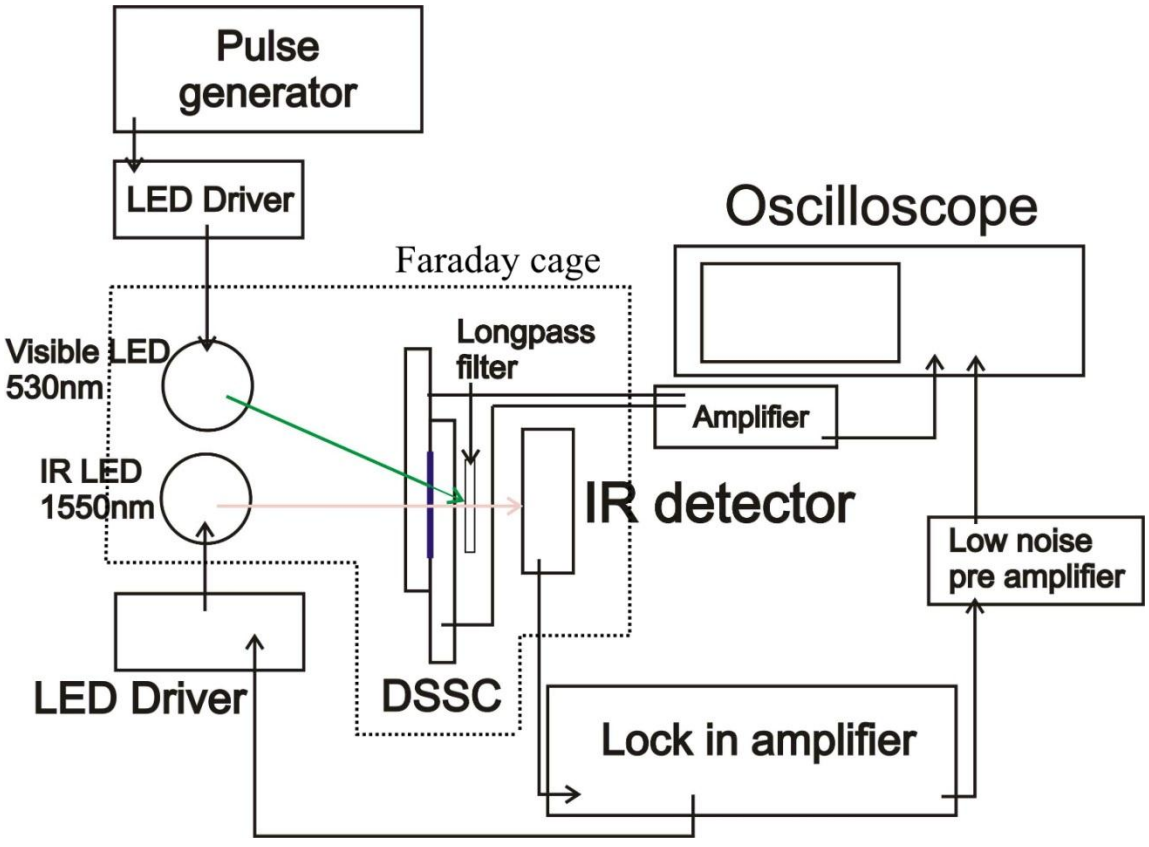

Fig 3.5 Experimental setup for IR measurements when visible light pulse is used. Coloured lines represent single wavelength light from LED, dotted line marks all equipment contained in faraday cage, black lines represent electrical connections (both measurement and control).

3.11 pH

pH measurements were performed on a Jenway Model 3505 pH meter. This was calibrated against buffered pH standards (Sigma, Reference standard – pH4, 7, 10). Measurements were taken at room temperature and recorded once a steady signal was observed.

3.12 Redox potential

Redox potentials were measured in two electrode mode by connecting a digital Voltmeter (DVM) (Iso-tech, IDM91E) to a reference electrode and a platinised FTO coated substrate, simulating the counter electrode in a DSSC. These were submerged in the electrolyte solution of interest and the potential recorded once the system had stabilized. Measurements were taken at room temperature.

3.13 Contact angle

Contact angles were recorded using a contact angle goniometer (Veho, Discovery VMS-004 Deluxe) controlled by photographic capture software (Veho, Microcapture). The surface to be measured was placed on a flat plate parallel to the ground and the camera was placed so that the substrate|air interface was clearly visible in photographs. A drop of water was placed on the surface and a picture taken from which the contact angle was determined using ImageJ software.

3.14 UV/Vis

UV/Vis measurements were performed on a UV/Vis spectrometer (Varian, Cary 50 Probe) controlled by the supplied software. Beam path is parallel to the ground. Scan rate used was 600 nm/min and scans were usually made from 800nm to 400nm. Generally quartz cuvettes were used to minimise background absorption below 400nm. In all cases, scans are background corrected. Both liquid and solid samples were measured as described in results chapters. Solid samples were mounted in a vertical holder. In some cases, such as for the spectroelectrochemical measurements found in section 8.3.2, solid samples were

held in a cuvette containing electrolyte; in this case, the back of the glass sample was placed touching the quartz cuvette vertical wall and the background was of a non-dyed FTO-npTiO_2 sample.

Chapter 4: Optimization of aqueous dye sensitized solar cells

4.1 Introduction
4.2 Results
    4.2.1 Initial testing; general observations
    4.2.2 Electrolyte variations; use of additives with ionic liquid
    4.2.3 Cell filling and nanoporous TiO_2 wetting
        4.2.3.1 Surfactants – Triton X-100
        4.2.3.2 Filling technique
        4.2.3.3 UV treatment
    4.2.4 Coadsorbates
    4.2.5 Dye
4.3 Conclusions
4.4 References

4.1 Introduction

As discussed in chapter 1, one of the problems facing DSSCs fabricated using electrolytes based on organic solvents is that of water ingress and solvent egress over time. The presence of water in a DSSC is close to unavoidable if cells are fabricated in air[1] and it has been shown that over time water concentration can increase in DSSCs as water penetrates through the cell sealing material[2]. It has also been suggested that electrolyte evaporation could be a problem at higher temperature operating conditions[3]. Generally, water has been shown to reduce cell performance[1,4] but this observation tends to be made for systems that are optimized for other solvent systems. Optimizing a cell for aqueous solvents rather than looking at problems caused by water ingress to cells optimized for organic solvents may lead to improvements in the DSSC. As water is likely to be present in DSSCs unless high cost measures are taken to prevent it, the development and optimization of a system based around an electrolyte where water is the main solvent is worthwhile. The benefits of developing a working aqueous cell include negating the problems discussed above while potentially reducing the electrolyte cost.

The work in this chapter looks at beginning the process of optimizing cells which have water as a significant component of the electrolyte. Much work to date[5] has focussed on cells which have a small addition of water to the electrolyte whereas the focus here is on using electrolytes where water is the main solvent. This chapter highlights some of the issues that became apparent as these devices were made, and how they were overcome. It was found that cell filling and semiconductor wetting was a significant problem. Filling techniques that involved heating were developed to improve cell filling. The effect of coadsorbates and UV light on surface hydrophobicity and hence cell filling were also examined; using coadsorbates did increase hydrophobicity but not cell performance. Additives such as 4-tert-butylpyridine and guanidine thiocyanate were found to improve cell performance and Z907 was found to be the most effective dye from several that were tested.

4.2 Results

The objective of the work presented in this chapter was to produce optimized DSSCs that contained electrolytes made with water as the primary solvent. In order to provide a relevant comparison point to the aqueous cells the IV curve for an optimized cell made using an acetonitrile/valeronitrile electrolyte produced in the same lab as the aqueous cells is shown in Fig 4.1. As a result of cell optimizations discussed below, the best efficiency obtained for an aqueous DSSC was 3.5% as shown in Fig 4.2.

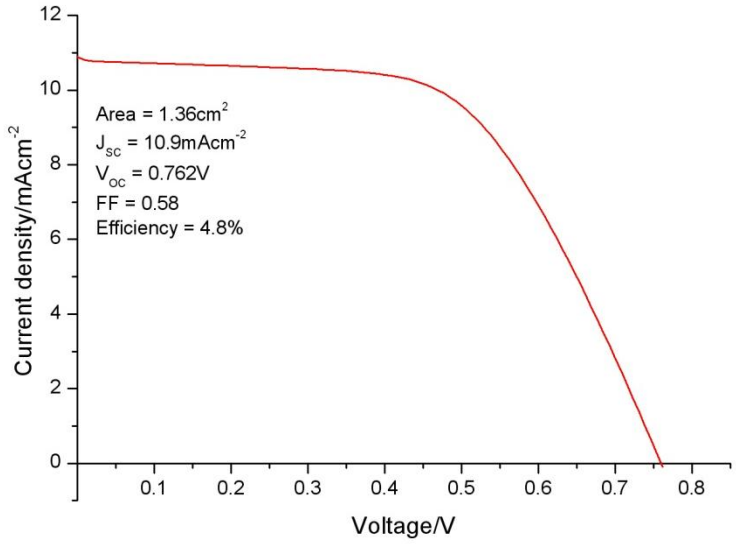

Fig 4.1 IV curves for standard acetonitrile/valeronitrile DSSC. Electrolyte contains 0.6M PMII, 0.03M I_2, 0.1M GITC, 0.5M tBP, TiO_2 dyed with 0.3mM N719. Photoanode has blocking layer and doctor bladed TiO_2, no scattering layer or $TiCl_4$ treatment. Illumination AM1.5 1sun, cell performance 4.8%.

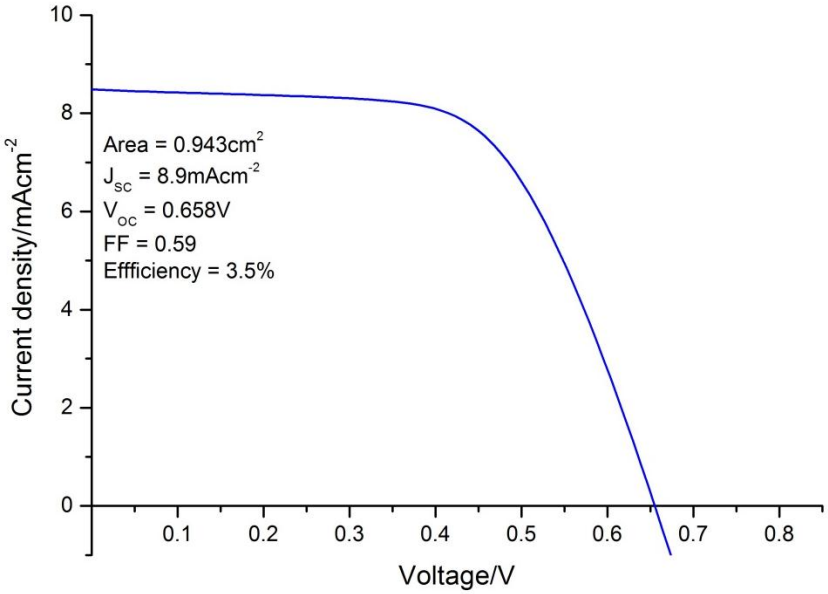

Fig 4.2 Highest efficiency aqueous DSSC produced in this work under AM1.5 1 sun illumination. Cell filled using aqueous electrolyte containing 2M PMII, 0.1M GSCN, 0.5M tBP, 0.05M I_2 and 1% Triton X-100, TiO_2 dyed with 0.3mM Z907.

4.2.1 Initial testing; general observations

Generally, state of the art DSSCs are produced using optimized electrolytes containing a number of performance enhancing additives. However, these additives also complicate the analysis of a cell and so at the beginning of this work cells were made with electrolyte systems containing only I_2, an I^- source and water. The aim of this was to start with a simple system and increase the complexity of the electrolyte gradually in order to understand the effect of each component. Several variations were made to these simple cells which will be briefly considered, but generally it was found that these cells had very poor performance.

Firstly, cells were made using electrolytes that contained either LiI or PMII as the I^- source (Fig 4.3). When using PMII, the cell fill factor dropped to almost zero though the short circuit current was similar to that with LiI. Based on the theory in section 2.5.1, this could be linked to a drop in the light generated current or an increase in the dark current response. Unfortunately dark current data is not available; however the shape of the decay from this initial I_{SC} is quite different to the normal decay expected for the dark current. It seems more likely that the IV shape seen is caused by decay in the light generated current from the initial value to zero. This is likely to be caused either by complete depletion of I_3^- at the counter electrode or poor dye regeneration at the semiconductor, which could occur if the electrolyte did not permeate effectively into the pores. This second effect is important as in many cases the filling of cells with aqueous electrolyte was found to be problematic, as was permeation of electrolyte through the nanoporous film. In order to attempt to improve electrolyte filling, the surfactant molecules CTAB and SDS (Fig 4.4) were added to the electrolyte but with no beneficial effect.

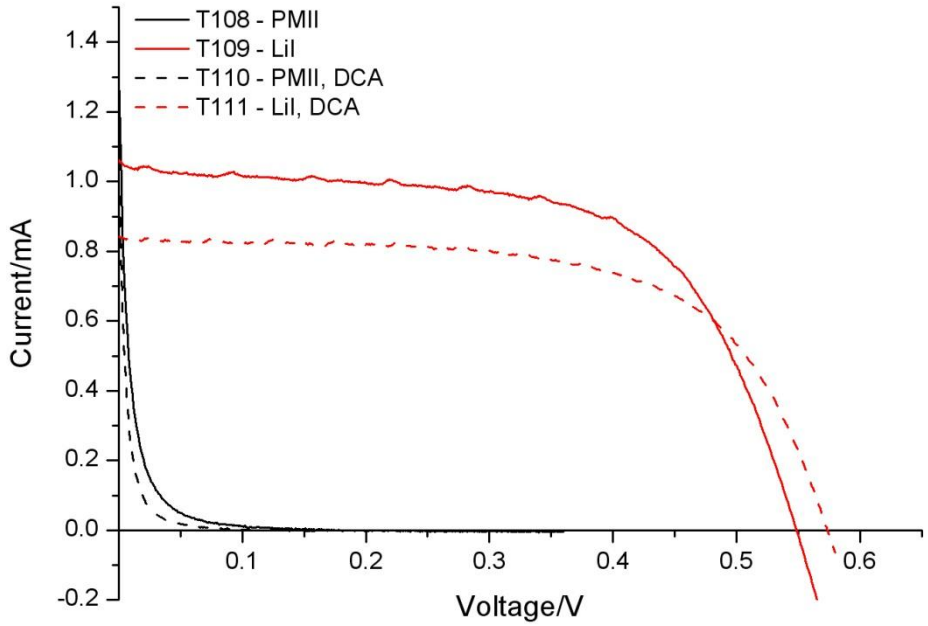

Fig 4.3 IV curves measured under 1 sun AM 1.5 illumination for cells made using simple electrolyte containing 0.05M I_2 and either 0.6M LiI or 0.6M PMII in water. Films were dyed in 0.3mM N719 overnight and the coadsorbate DCA (1mM) where indicated.

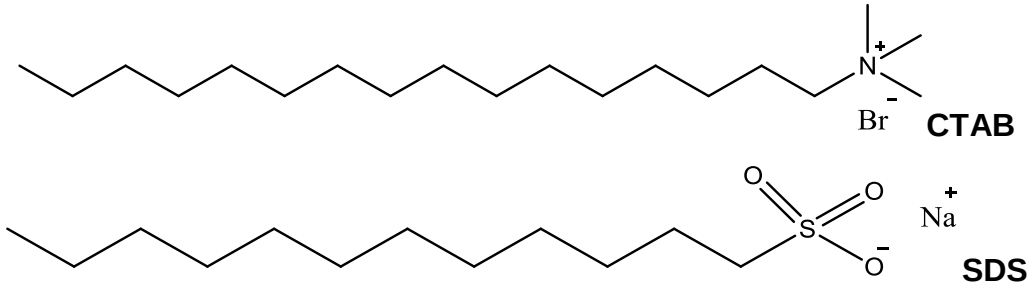

Fig 4.4 Hexadecyltrimethylammonium bromide (CTAB) and sodium dodecyl sulphate (SDS) surfactants.

Having seen the effect of changing the I^- source, the concentration of I^- was changed. It is apparent in Fig 4.5 that increasing the LiI concentration results in an increase in I_{SC} and a decrease in V_{OC}. A likely explanation for this is that Li^+ adsorbs onto the TiO_2 surface, decreasing the surface dipole resulting in a positive shift in the CB potential and this occurs to a greater extent at higher concentrations. Such a shift would be expected to increase the photocurrent due to the increased driving force for electron injection as has been seen in conventional DSSCs [6] and could also decrease the photovoltage by lowering nE_F. The effect of changing the initial I_2 concentration was also examined but no clear trends emerged.

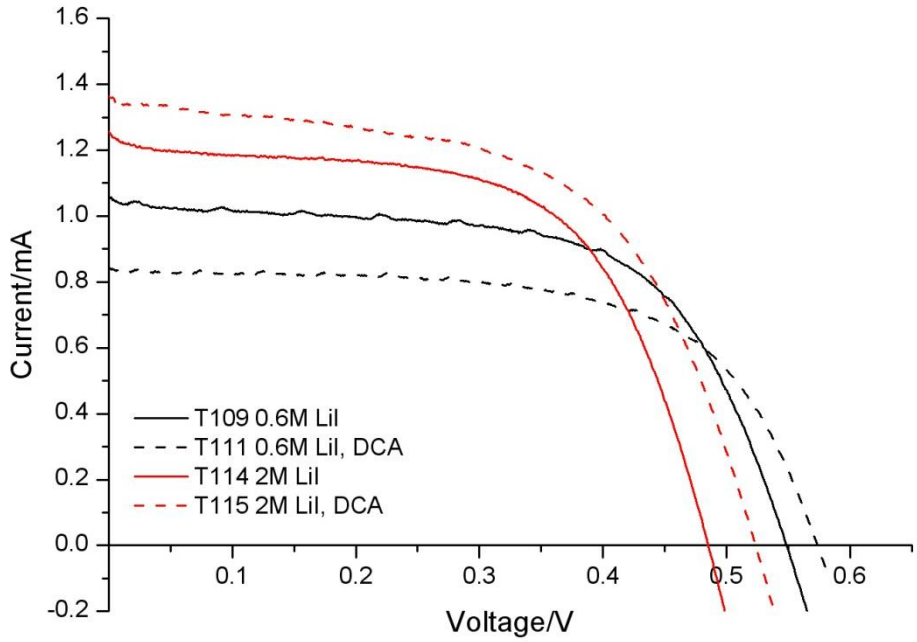

Fig 4.5 IV curves measured under 1 sun AM 1.5 illumination for cells made using simple electrolyte containing I_2 and either 0.6M or 2M LiI in water. Films were dyed in 0.3mM N719 overnight and the coadsorbate DCA (1mM) was added where indicated.

The dye used was also found to influence cell performance. When using a simple electrolyte, the current produced by cells made using the hydrophobic Z907 dye was typically an order of magnitude smaller than that produced by cells made using N719. However, it was also observed that over time cells made using N719 decoloured, suggesting that the dye was desorbing from the surface. Fig 4.3 also shows that adding coadsorbate molecules such as deoxycholic acid (DCA) (Fig 4.6) to the dyeing bath has some effect on aqueous dye cells and this will be considered in detail in section 4.2.4.

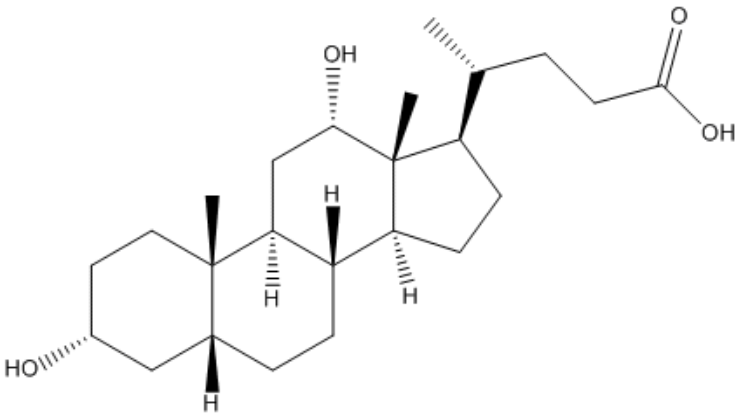

Fig. 4.6 Deoxycholic acid coadsorbate.

These simple variations show that water based cells can work and that by changing the materials used to make the cell the performance can be improved. However, the electrolytes used resulted in cells with very low performance when compared to Fig 4.1; this is likely to be due at least in part to poor cell filling as was observed in some cases. If, as suggested, part of the reason cells made using PMII have such a low fill factor is that poor wetting/cell filling results in poor dye recombination, then it is useful to observe that this can be improved to some degree by changing the components of the electrolyte. In the next section, a more complex electrolyte will be considered.

4.2.2 Electrolyte variations; use of additives with ionic liquid

Having initially tested a simple system, an aqueous electrolyte system that had been found to be effective in the literature was examined[7]. In this section, it is shown that this electrolyte is more effective than those considered previously and some reasons for this are examined.

Law et al[7] demonstrated that an electrolyte containing 2M PMII, 0.1M GSCN, 0.5M tBP and 0.05M I_2 along with 1 vol% of the surfactant Triton X-100 (Fig 4.7) in water could be used to make DSSCs with efficiencies up to 2.4%. This electrolyte composition was examined as a comparison to that used earlier and was adopted as the standard electrolyte for cells made in the rest of this work. It was observed that the components of this electrolyte did not dissolve in each other completely, and some phase separation tended to be seen between components (Fig 4.8) particularly after being left to stand for a period of time. This may contribute to problems of cell filling which are considered in section 4.2.3 and has been identified as contributing to photocurrent limitations as discussed in chapter 8.

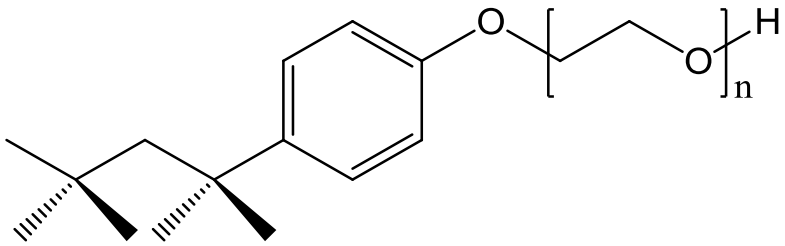

Fig 4.7 Triton X-100, the surfactant used in aqueous electrolytes. No. of repeating polyethylene oxide units is approximately 9.5 on average.

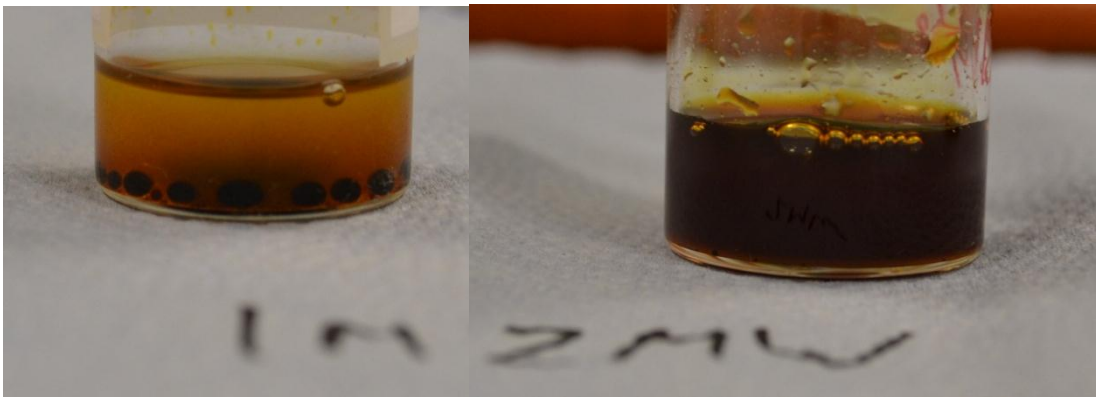

Fig 4.8 Photo on left shows standard aqueous electrolyte (0.05M I_2, 0.1M GSCN, 0.5M tBP and 1% Triton X-100 in water) containing 1M PMII, photo on right containing 2M PMII. Close inspection of 2M case shows incomplete dissolution of some components.

IV curves for cells made using this electrolyte are shown in Fig 4.9 and may be compared with IV curves from cells containing no additives and 2M LiI shown in Fig 4.10. It can be seen that while the cells made with the Z907 dye barely functioned with the simple LiI electrolyte, they are now comparable with those made with N719 both in terms of photocurrent and photovoltage. It is also apparent that the initial photocurrent has increased significantly for both dyes, though the shape of the IV curves for cells in Fig 4.10 are unusual. In the case of Z907 dyed cells, the change in performance is large and suggests that some process within the cell that was barely functioning with the simple electrolyte has now been turned ‘on’. One possibility is that electron injection was very poor in the previous case, resulting in a low photocurrent. A more likely possibility is linked to electrolyte permeation into the semiconductor: Z907 is a more hydrophobic dye than N719 and it is likely that the wetting/pore filling by aqueous electrolyte was less effective. This would result in limited dye regeneration and therefore a lower rate of electron injection in a manner similar to that discussed regarding PMII/LiI earlier. If this explanation is correct, it would suggest that the composition of the more complicated electrolyte aids the wetting/pore filling of electrolyte in the cell. This may be due to molecules like Triton X-100 and tBP acting as surfactants and reducing the interfacial energy between water and the TiO_2 surface. A second possibility is that the excited state energy level position compared to the CB is different for the two dyes such that injection is less

favourable for Z907 in the simple electrolyte case, and changes to these energy levels caused by the additives allow injection to occur.

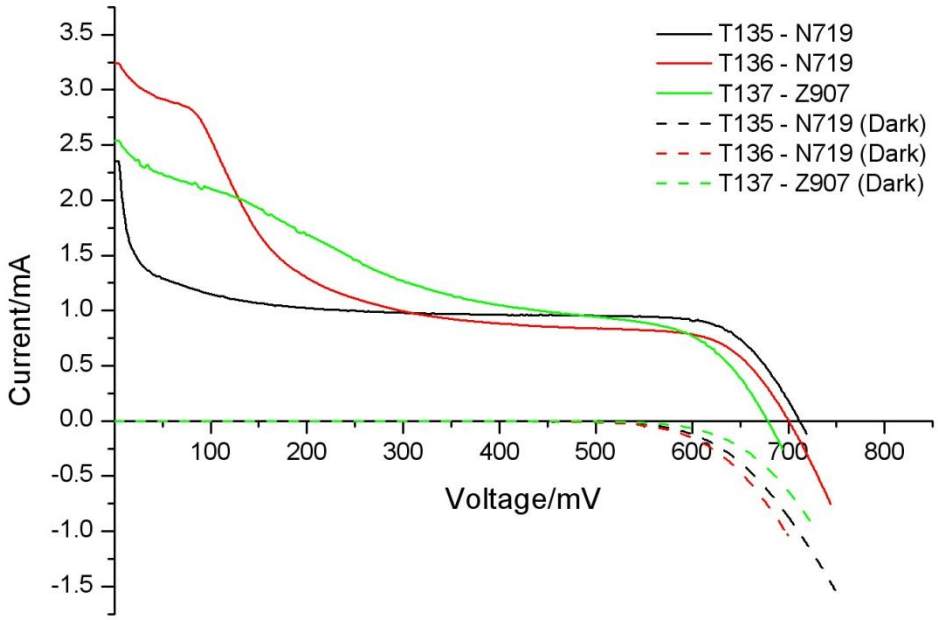

Fig 4.9 IV curves measured under 1 sun AM 1.5 illumination comparing water cells made using standard electrolyte (2M PMII, 0.1M GSCN, 0.5M tBP, 0.05M I_2 and 1% Triton X-100 in water) for different dyes. Note that current is not corrected for area. Unusual shape of IV curves is discussed in the text and in section 8.3.4.

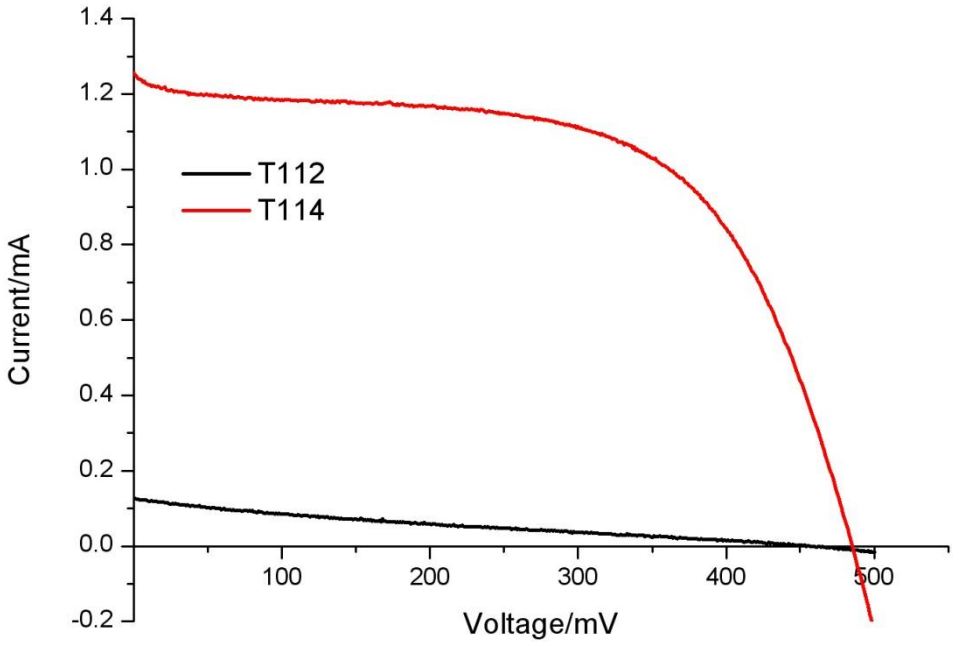

Fig 4.10 IV curves measured under 1 sun AM 1.5 illumination comparing water cells made using simple aqueous electrolyte (0.05M I_2 & 2M LiI) for T112 (Dyed with 0.3mM Z907) and T114 (Dyed with 0.3mM N719) containing no surfactant. Note that current is not corrected for area.

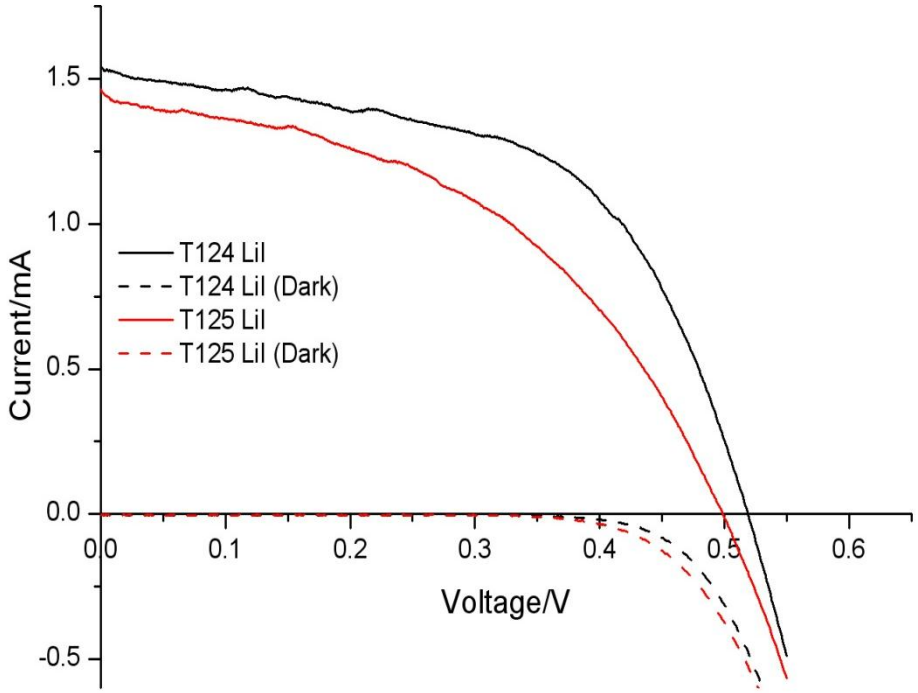

Fig 4.11 IV curves measured under 1 sun AM 1.5 illumination for cells made using simple electrolyte containing 0.05M I_2 and 2.5M LiI in water. Films dyed in 0.3mM N719 with 1mM DCA coadsorbate. The two cells measured are replicates. Note that current is not corrected for area.

It is also seen that there are improvements in the photovoltage and dark current onset when the more complicated electrolyte is used (Fig 4.11 vs Fig 4.9). The additives used are expected to have an effect both on the CB position and the reaction between I_3^- and electrons in the semiconductor as reported elsewhere. GSCN has been shown to cause the CB potential to shift positively and to decrease the reaction between I_3^- and electrons[8], while tBP has been shown to increase V_{OC} in other systems by 280 mV, due to a negative CB potential shift and a decrease in the same reaction[4].

Finally it is noted that the shape of the IV curves with the more complex electrolyte is unusual showing initially high current which is not maintained as the voltage increases and in some cases small peaks in the photocurrent. Generally, these peaks that occur between 100 and 200 mV are not seen in subsequent data. However, the initial high photocurrent and decay are observed elsewhere and will be discussed in greater detail in section 8.3.4.

This section confirms that changes can be made to the aqueous electrolyte resulting in cells that function more efficiently. It is seen that additives improve several of the cell performance parameters and several reasons for this are suggested. It has also been observed that changing the electrolyte has markedly increased the performance of cells made with the Z907 dye. Based on the greater stability of this dye in water, it is used as the standard dye in the rest of this work. The problem of TiO_2 wetting and cell electrolyte filling has again been seen to be important and this will be considered in further detail in the next section.

4.2.3 Cell filling and nanoporous TiO_2 wetting

One of the major problems in trying to produce aqueous DSSCs was found to be cell filling. In many cases it could be seen that on introduction of electrolyte via the filling holes only a fraction of the cell area would be filled initially although over time this would improve slightly. Linked to this is the problem of pore filling, which is harder to measure. It is possible for the gap between semiconductor and counter electrode to be filled but many pores to still be dry. Observing the degree of electrolyte filling on the substrate side of the TiO_2 film gives an indication that some pores have been filled, but doesn't guarantee all have. The main problem caused by incomplete wetting of the semiconductor is that I^- cannot get to D^+ after electron injection where electrolyte is not present and so dye regeneration via oxidation of I^- cannot occur. This makes the net electron injection efficiency of dye molecules in these areas zero as in order to inject again they must be reduced by an electron in TiO_2. The importance of wetting has also been highlighted in work by Law et al[9].

Whereas electrolytes made using acetonitrile wet a dyed TiO_2 surface very effectively, contact angles when water was used tended to be significantly higher. This is particularly due to the differences in the interfacial energy between the solvent and the surface. The interface (liquid|surface or liquid|gas) which has the lower energy will be favoured, and if interactions between the liquid and the surface are low, this will result in a higher contact angle and poorer wetting. For the dyed surfaces used here, there is poor interaction between the surface and water leading to the high contact angles and poor wetting behaviour observed.

In this section several alteration are considered which specifically aim to improve cell filling and semiconductor wetting.

4.2.3.1 Surfactants – Triton X-100

The effect of surfactant concentration in the electrolyte was first considered with a view to improve mixing between the different liquid components (Water, PMII, tBP) in the electrolyte and to decreasing the surface|liquid interfacial energy. Surfactant molecules are amphiphilic in nature having both a hydrophobic and hydrophilic part. When added to a liquid such as water they concentrate at the surface to allow the hydrophobic moiety to be out of contact with the water, disrupting IM interactions near to the surface and decreasing the interfacial energy. This effect can lower the interfacial energy for different interfaces e.g. Liquid|liquid, liquid|solid, liquid|gas, and using surfactants is anticipated to improve cell wetting.

Having seen little effect in initial tests with CTAB and SDS, Triton X-100 which has been used effectively in other work was examined in further detail[7]. Concentrations of 1, 2, 3, 4, 5 and approximately 10vol% were examined in electrolytes containing 2M PMII, 0.05M I_2, 0.1M GSCN and 0.5M tBP. I_2 was not visibly very miscible up to 2%, above this more I_2 started to dissolve. When about 10vol% was included, all the I_2 dissolved. When using these electrolytes to fill cells it was seen that filling improved as the Triton concentration increased. It was also noticed that for the 3% case there was some desorption of dye from around the holes; this effect is considered in greater detail in section 7.2.2. Initially, the cell made using 3% Triton gave the best performance, but this changed when the cells were left overnight and the 1% Triton case was later found to give the best performance (Fig 4.12). At higher concentrations it can be seen that the fill factor decreases and this may be caused by Triton X-100 adsorbing onto the counter electrode surface and reducing the charge transfer rate constant. Most of the cells could be seen to improve overnight and in this case it seems possible that this is due to the electrolyte permeating the pores more effectively after being left for a period of time. Based on these results a Triton X-100 concentration of 1% was considered to be optimum, though cell performance was not high.

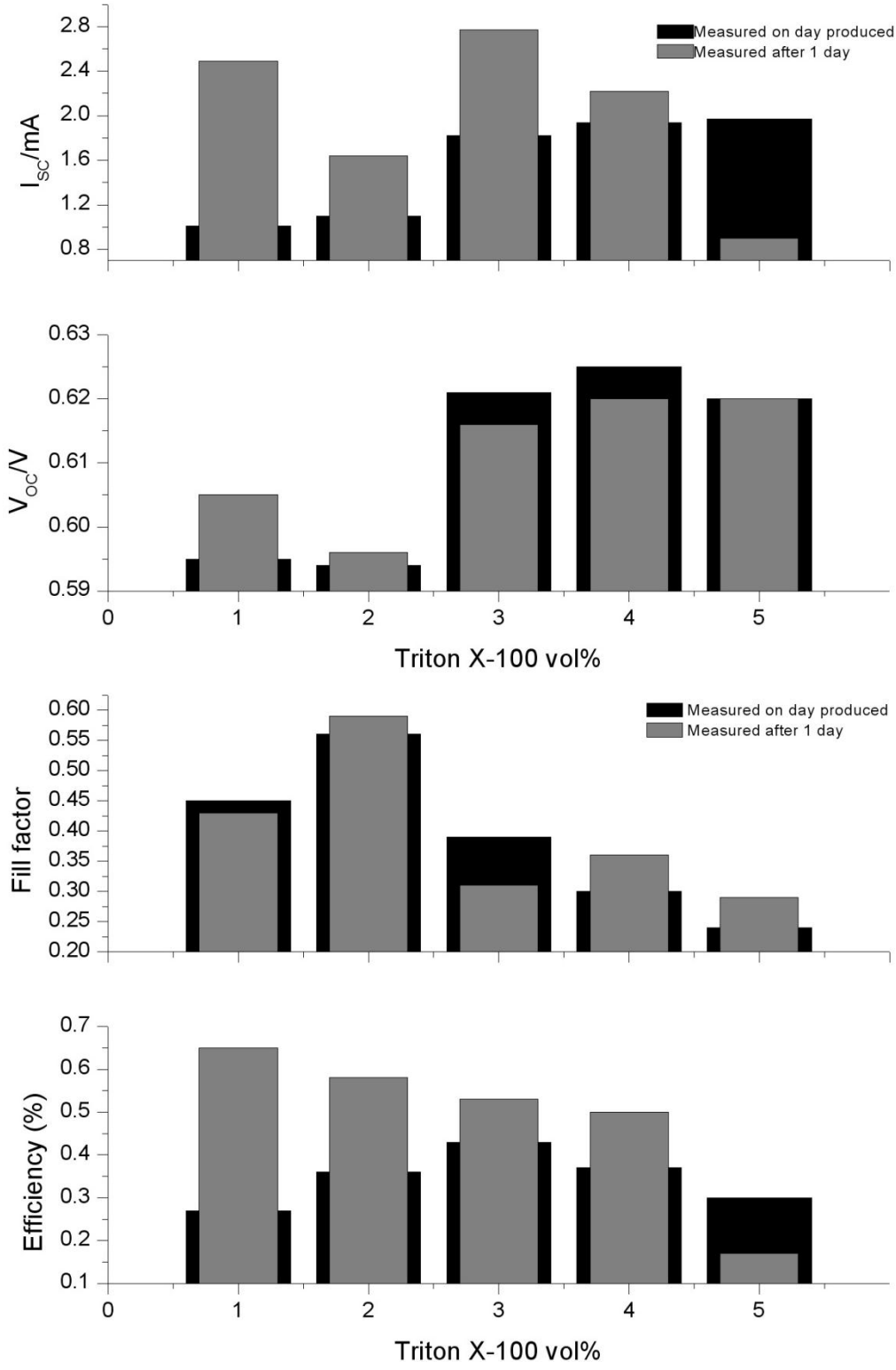

Fig 4.12 IV characteristics summary for dye cells measured under 1 sun AM 1.5 illumination made using different Triton X-100 surfactant concentrations in the aqueous electrolyte containing 2M PMII, 0.05M I_2, 0.1M GSCN and 0.5M tBP, dyed in 0.3mM Z907. A general improvement is observed in cell performance when left overnight and at this point the lowest concentration of surfactant was found to give the best cell performance.

4.2.3.2 Filling technique

Heating the cells during the filling step was tested as it was thought this would improve agitation of the electrolyte within the cell and so aid electrolyte permeation into the cell. Initial results using this method showed greatly improved filling and cell performance compared to previous results on similar cells (Fig 4.13) and so further work was done to try and optimize this technique. Several temperatures were examined and two methods were examined; where electrolyte was added after heating had finished and where electrolyte was added before heating was started (table 4.1). Electrolyte was added after heating the cell for the first set in order to minimise evaporation of volatile components. This was found to be ineffective, so it was added before and during the heating process. Generally, as the temperature was increased, the electrolyte permeation improved slightly. Further filling improvement was observed when the cell was first heated while under vacuum, then the room pressure was restored. However this did not cause cell performance to improve (Fig 4.13).

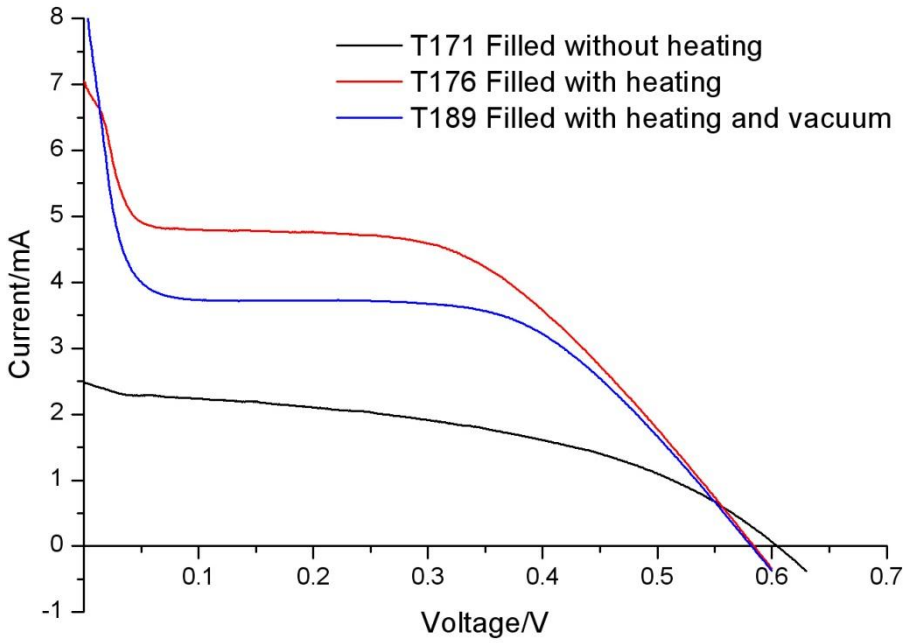

Fig 4.13 IV curves for cells measured under 1 sun AM 1.5 illumination made using the same electrolyte (2M PMII, 0.05M I_2, 0.1M GSCN and 1% Triton X-100 in water) filled with and without heating during the vacuum filling step. Cell made without heating, η = 0.3%, cell made with heating η = 1.5%, cell made with heating and vacuum η = 1.3%

Table 4.1: Visual examination of extent of cell filling when electrolyte was added at different temperatures before and after heating step

Temperature/°C	**Filling result when drop added at end of heating step**	**Filling result when drop added at beginning of heating step**
41-49	Space between WE and CE filled, poor film penetration	Space between WE and CE filled, some film penetration
62-69	As for 41-49	As above, slightly improved film penetration
75-88	As for 41-49	As above, slightly improved film penetration
100-110	As for 41-49	As above, slightly improved film penetration
134-151	No electrolyte went into film	As above, better film penetration

In order to improve cell filling, this technique was generally adopted, involving placing a drop of electrolyte onto each filling hole then heating the cell to 80°C under vacuum for approximately 20 seconds before releasing the pressure to introduce the electrolyte to the cell. Cells were then left under vacuum for a further period of approximately 30 seconds.

4.2.3.3 UV treatment

An alternative approach to improving electrolyte permeation into the film is to change the wetting properties of the semiconductor surface. This was examined in several ways including using coadsorbates (section 4.2.4) and treating the surface with UV light which is covered in this section.

It has been found that treatment of thin films of amorphous and polycrystalline TiO_2 with UV light can cause such surfaces to become superhydrophilic with negligible contact angles[10]. Gao et al have suggested that changes in the capping groups attached to Ti at the surface[11] induced by UV light adsorption play a significant part in the process. They suggest that holes generated by the excitation of electrons when TiO_2 absorbs UV light can cause the oxidation of

organic contaminants near the surface[11] which may also have an effect on hydrophobicity. The aim of this investigation was to determine if a UV treatment prior to dye adsorption could similarly be used to increase the wetability of the TiO_2 surface and so improve aqueous electrolyte wetting within the porous structure.

Two sets of TiO_2 films were made then treated with different intensities of UV light; strong (Mercury Xenon lamp >50W) and mild (254nm, ≤12W). These were then dyed and made into DSSCs. Each set was compared to a control cell which was not exposed to UV light. Figs 4.14 & 4.15 show initially low contact angles before UV treatment or dyeing processes take place. After the initial UV treatment it can be seen that there is a small drop in contact angle as might be expected based on the above discussion. When the dye was added the contact angle increased to a similar value regardless of the strength of the UV light used to treat the film. This value was higher than that for the undyed film, but similar to the dyed film that wasn't treated with UV before dyeing. It is therefore apparent that the dye has a more significant effect on the wettability than the UV surface treatment.

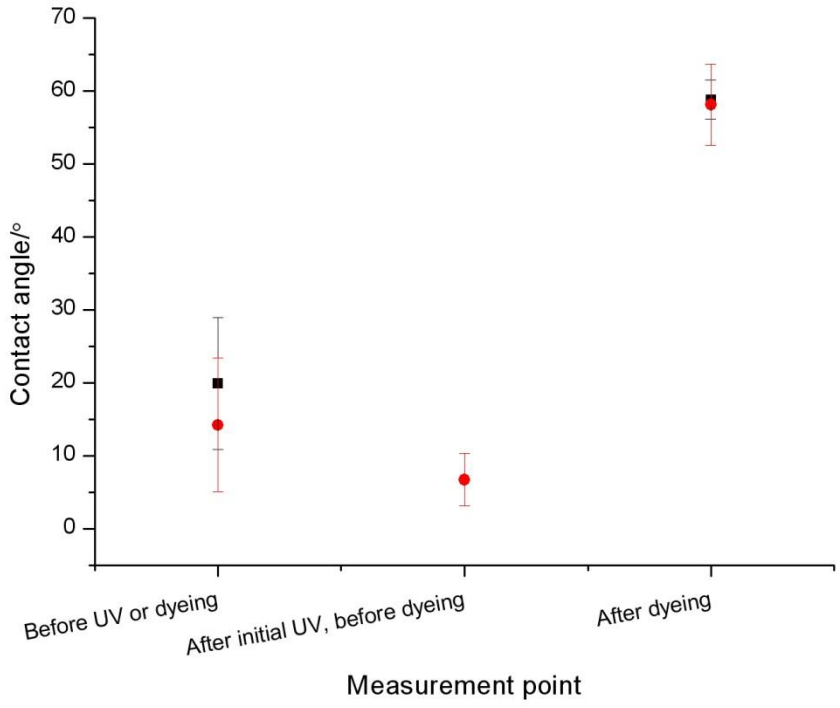

Fig 4.14 Contact angle measurements of water drop on nanoporous TiO_2 film. Effect of mild UV treatment and dyeing (set 1). Black squares - Control measurements (no UV treatment), red circles - mild UV treatment before dyeing cell.

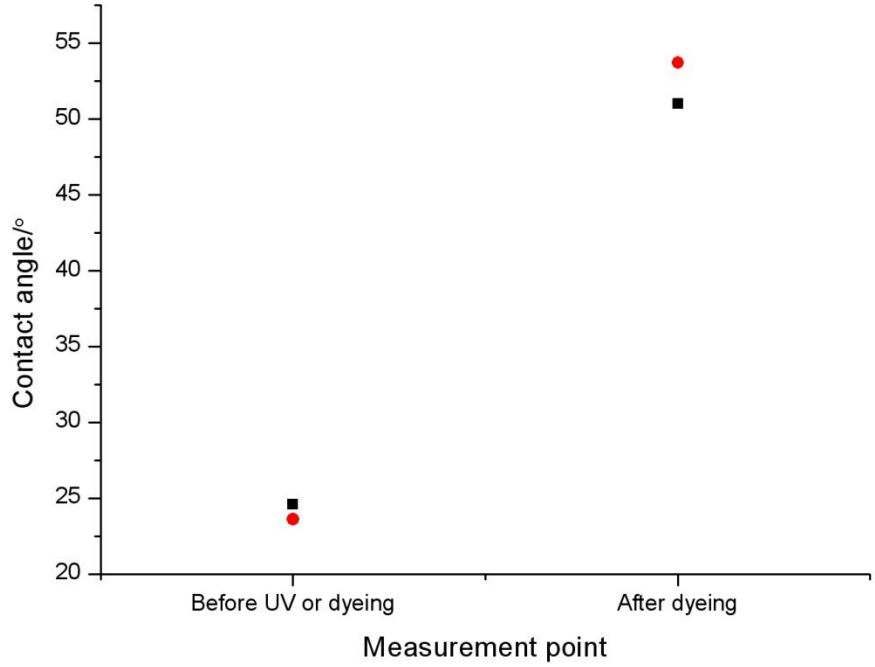

Fig 4.15 Contact angle measurements of water drop on nanoporous TiO_2 film. Effect of strong UV treatment and dyeing (set 2). Black squares - control measurements (no UV treatment), red circles - strong UV treatment immediately prior to dyeing.

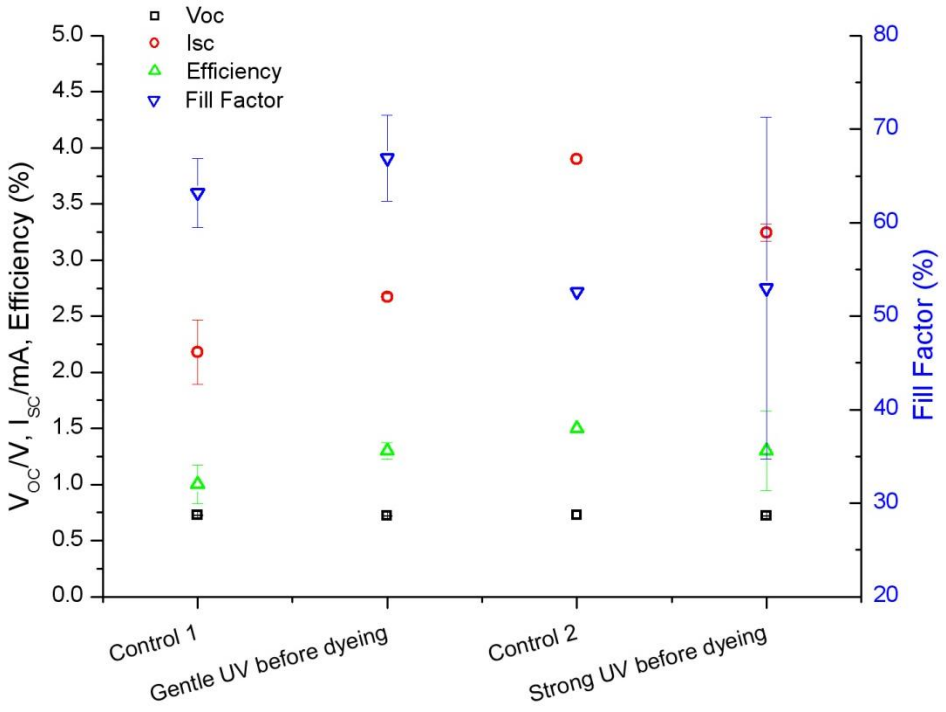

Fig 4.16 Summary of the effect of UV light during production on final cell IV performance. Black open squares - open circuit voltage, red open circles - short circuit current, green open upward pointing triangles - efficiency, blue open downward pointing triangles - fill factor. Set one are first two cells, set two are second two cells.

Fig 4.16 shows that neither treatment with strong or mild UV light has a significant consistent effect on cell performance, again suggesting that any changes made by UV light to the semiconductor surface are negated by the effect of the dye.

4.2.4 Coadsorbates

On the basis of the UV measurements above, it is apparent that the wetting properties of the material were influenced more significantly by adsorbed molecules than the semiconductor surface treatment implying that the 'surface' interacting with water to effect wetting is primarily that of the adsorbed molecules. This is in line with calculations shown in appendix A demonstrating that a monolayer of dye is adsorbed onto the semiconductor surface. A second approach to improving the wetting properties of the dyed semiconductor is to modify this effective surface using coadsorbate molecules which have been introduced in section 4.2.1. These molecules have been used effectively in improving DSSC performance for other electrolyte and dye systems for various reasons which have included decreasing the reaction between I_3^- and electrons in the semiconductor, altering the surface charge of the semiconductor and decreasing aggregation behaviour[12]. In this section the effect of using different coadsorbates is examined in terms of cell performance and wetting.

The effect of coadsorbates was measured for cells produced where the photoanode consisted of a double layer of TiO_2 (~10 μm) with a scattering layer made up of larger particles (150-250 nm) applied on top. These films were then treated with $TiCl_4$ before being resintered. Four different coadsorbates that were expected to vary in terms of their hydrophilic properties were tested. These were bis-(3, 3-dimethyl-butyl)-phosphinic acid (DINHOP), Deoxycholic acid (DCA), 11-hydroxyundecyl-1-phosphinic acid (HUPA) and bis(hydroxymethyl)phosphinic acid (HMPA) (Fig 4.17). In particular, HMPA was expected to be the most hydrophilic due to its hydroxyl groups whereas DINHOP was expected to be the most hydrophobic due to its bulky alkyl groups.

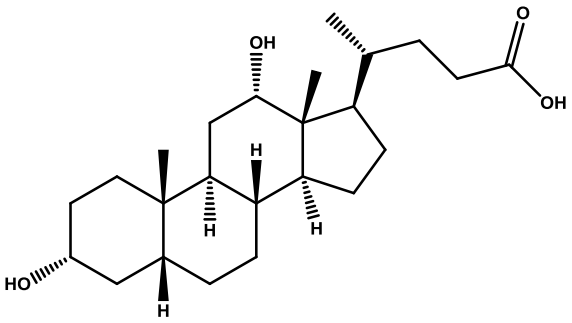

DCA

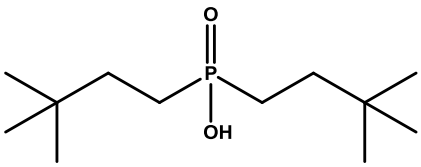

DINHOP

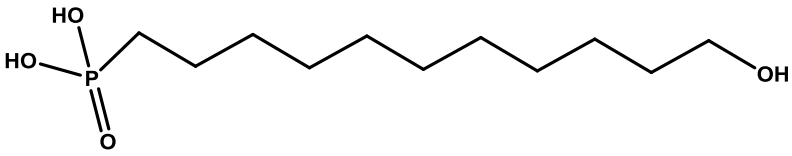

HUPA

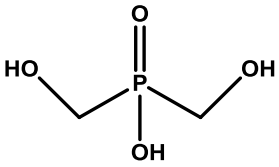

HMPA

Fig 4.17 Deoxycholic acid (DCA), bis-(3, 3-dimethyl-butyl)-phosphinic acid (DINHOP), 11-hydroxyundecyl-1-phosphinic acid (HUPA) and bis(hydroxymethyl)phosphinic acid (HMPA) coadsorbates.

Fig 4.18 shows UV/Vis data for films made as described and then dyed with and without coadsorbates. The peak at around 530nm is the dye absorption maximum. It is clear for all the films with coadsorbates that there is reduced absorption, implying lower dye coverage suggesting that coadsorbates compete with dye for binding sites. The variation between coadsorbates can be rationalized as follows. The coadsorbates split into two types based on binding group. Three of the coadsorbates – DINHOP, DPA and HMPA – are analogues of phosphinic acid. These tend to bind more strongly to TiO_2 than carboxylic acid groups[13] (as in DCA) and so it is reasonable to expect them to replace some of the dye on the surface, with the concurrent drop in photocurrent. DCA does not have such strong binding due to its carboxylic acid binding group[13], but as it was adsorbed at the same time as the dye it also competes for some of the space on the surface. Because DCA has a carboxylic acid binding group and hence the weakest binding of the coadsorbates, it competes the least with the dye hence

the smallest dye reduction. The three phosphinic acid coadsorbates can be compared in terms of steric and electronic factors. HUPA is similar in size to HMPA though with a long thin alkyl group which is unlikely to be a large barrier to dye adsorption in its near vicinity. However, HUPA has an additional electron withdrawing hydroxyl group attached to the phosphorus which is likely to weaken the bonding of the coadsorbate to titania, leading to a slightly increased dye coverage compared to HMPA. DINHOP has two bulky alkyl groups which have both a steric effect in reducing dye coverage and a small electron donating effect, which may slightly strengthen coadsorbate bonding to TiO_2.

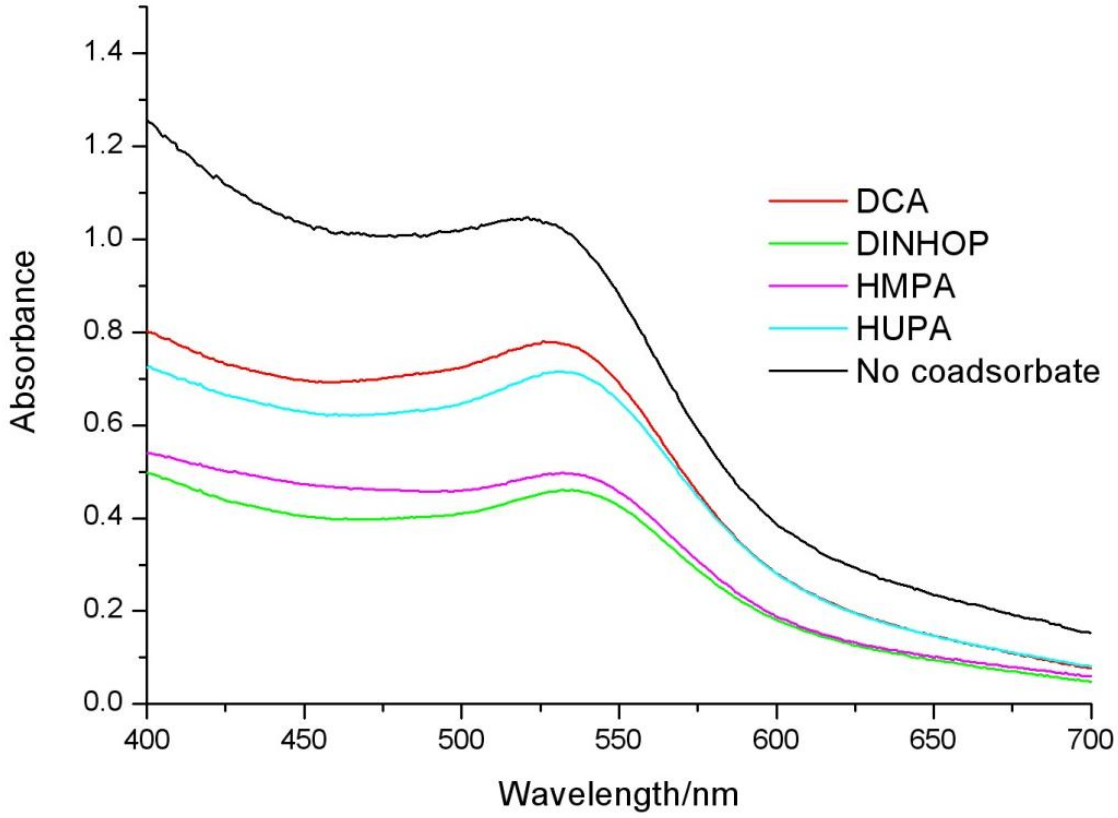

Fig 4.18 UV/Vis spectrum for films dyed with Z907 and different coadsorbates. Films dyed in 0.3mM Z907 and 1.2mM coadsorbate.

The contact angles for water droplets placed on films made in the same way and then dyed with and without coadsorbates are shown in Table 4.2, and changes in dye coverage help to account for some of the contact angle variations.

Table 4.2: Contact angles measured for cells with different coadsorbates.

Adsorbents	**Contact angle/°**
None	28
Z907	137
Z907 + HUPA	122
Z907 + DCA	109
Z907 + DINHOP	108
Z907 + HMPA	59

The contact angle results first of all again highlight the high hydrophobicity of the dye film when compared to the clean TiO_2 surface. It can also be seen that the coadsorbates reduce this by varying amounts. The changes can be understood in terms of both the amount of dye/coadsorbate on the surface and the relative hydrophilicity of the different coadsorbates, determined by their structure. The small variation in contact angle for HUPA is likely due to the relatively high amount of dye still on the surface but the alkyl group may also have some shielding effect, making it rather than the hydroxyl group the important factor in determining the effect of the molecule on the hydrophobicity. DCA probably has a greater effect at increasing hydrophilicity based on its higher surface coverage. DINHOP gives an unexpected result in that it appears to be largely hydrophobic, and only have a small coverage, and may be an erroneous result. Finally, HMPA greatly improves hydrophilicity and this is largely due to its hydrophilic nature, based on three polar hydroxyl groups coupled with reduced dye coverage. It is clear that the wetting properties can be affected by altering the coadsorbates bound to the TiO_2 surface.

These molecules also have an effect on cell performance. Figs 4.19 & 4.20 summarize the results for the different coadsorbates. Photocurrent is lower in the cells made using coadsorbates by 3.4 – 6.2mAcm^{-2}. There is not a direct correlation between the amount of dye coverage as measured by UV/Vis (assuming film thickness is constant), the contact angle and the photocurrent. However, it is intriguing that the DINHOP coadsorbate gives the highest photocurrent, particularly as it appears to result in the lowest dye coverage.

A variation in photovoltage can also be seen as shown in fig 4.19 & 4.20. All of the coadsorbates used give some improvement to this voltage, with variation between 25 and 60mV. As mentioned earlier, similar changes have previously been assigned as due to both conduction band movement and a variation in the rate of the reaction between I_3^- and electrons in the semiconductor[14].

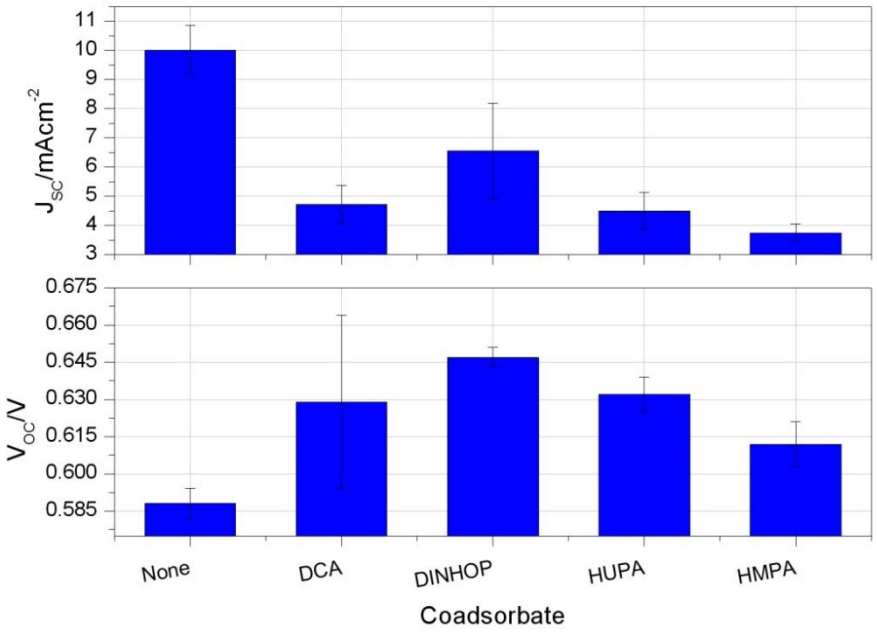

Fig 4.19 Summary of current density and open circuit voltage for water cells containing 2M PMII, 0.05M I_2, 0.1M GSCN, 0.5M tBP and 1% Triton X-100 dyed in 0.3mM Z907 with different coadsorbates. Measured under 1 sun AM 1.5 illumination.

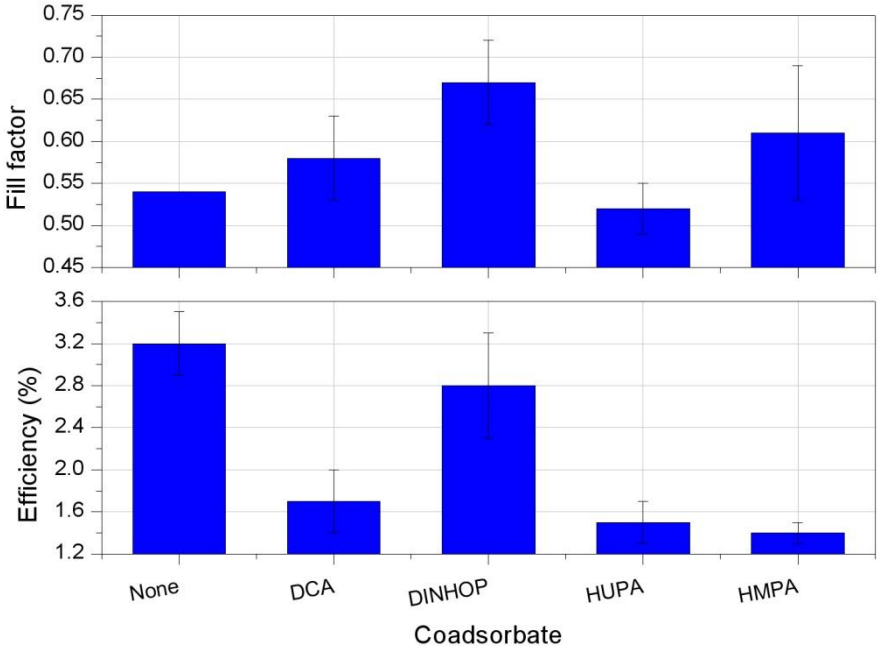

Fig 4.20 Summary of fill factor and efficiency for water cells containing 2M PMII, 0.05M I_2, 0.1M GSCN, 0.5M tBP and 1% Triton X-100 dyed in 0.3mM Z907 with different coadsorbates. Measured under 1 sun AM 1.5 illumination.

Fig. 4.21 shows representative electron lifetime vs V_{OC}, and a clear shift can be seen between the different cells. Unfortunately charge density data is not available for these measurements so several assumptions need to be made to make a comparison. Assuming that E(I_3^-/I$^-$) is at the same potential for each dye/coadsorbate composition, and that the distribution of trap states and CB position is the same in all the different cells, it is expected that a given cell voltage will correspond to the same charge density in each cell. It is unlikely that the redox potential will be largely affected by the coadsorbates, however there may be some changes to CB position and surface states distribution due to the adsorption of the acidic binding groups. If however the assumptions made are correct, the implication of this data is that the coadsorbates have a different effect on the rate of reaction between semiconductor electrons and I_3^-. For example, at higher voltages DINHOP gives the highest effective electron lifetime explaining why the highest V_{OC} values were obtained with it as coadsorbate.

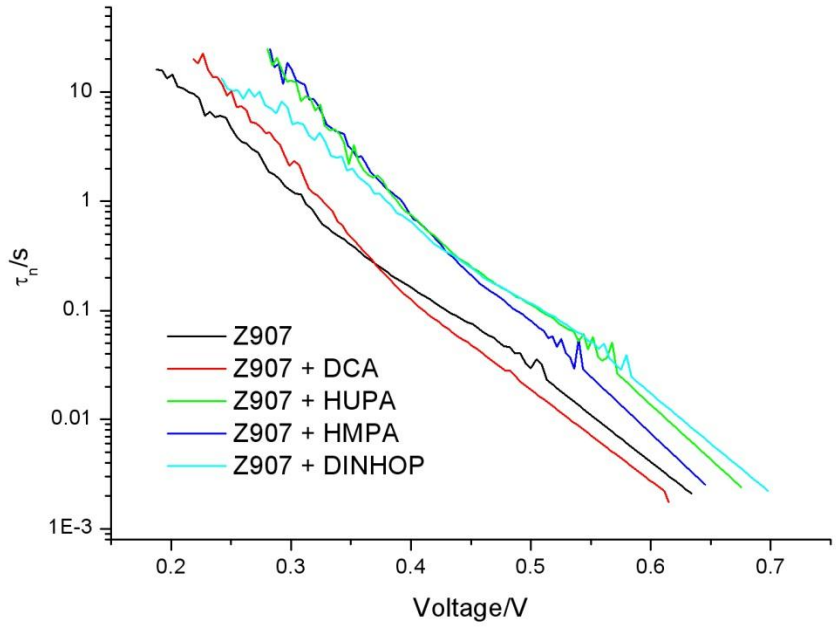

Fig 4.21 Representative electron lifetime measured using OCVD as a function of voltage for cells dyed in 0.3mM Z907 with a variety of different coadsorbates. Aqueous electrolyte contained 2M PMII, 0.05M I_2, 0.1M GSCN, 0.5M tBP and 1% Triton X-100.

This section has shown that while coadsorbates do indeed have an effect on the wetting properties of the semiconductor, this does not translate directly into improvements in cell performance, partly because there is less dye adsorbed

onto the surface. It is possible that further variations may give an improvement and other work looking at further coadsorbates has shown that they can lead to improvements in cell performance[9]. Of the coadsorbates tested, cells made with DINHOP had the highest performance.

4.2.5 Dye

An obvious outcome of using water as the main solvent in a dye cell rather than acetonitrile is that the environment the sensitizer is in is significantly changed. It has already been seen that when using the complex aqueous electrolyte system described above, Z907 is a more effective dye than N719. It has also been seen that in some cases dye desorption occurs, and this will be considered in more detail elsewhere (sections 5.3.3.4 and 7.2.2). In the development of DSSCs that use organic electrolyte solvents, relative energy level positions have been optimized to produce high efficiency; any changes to these levels in water is likely to reduce this optimization. As an example, it has been noted by Boschloo et al[15] that the redox potential of the $I_2^{-\bullet}/I^-$ redox couple, understood to be the main species involved in dye regeneration is approximately 250mV more positive in water than acetonitrile. This may decrease dye regeneration, though it is not clear if the liquid junction potential was accounted for in these measurements. Energy levels differ between dyes, so changing the dye can be used to tune this alignment. Use of an aqueous electrolyte is also seen to lead to photocurrent limits induced by slow I_3^- diffusion as considered in further detail in chapter 8. By studying a number of different dyes and optimizing these different parameters it should be possible to find a sensitizer that is very suitable for use in water. The sensitizer was not the main focus of this project; however two dyes other than Z907 and N719 were examined. The electrolyte used for these measurements contained 2M PMII, 0.05M I_2, 0.1M GSCN, 0.5M tBP and 1% Triton X-100.

D35 (Fig 4.22) is a metal free organic dye which has achieved efficiencies of up to 6.7% with a cobalt redox couple[16] with a high V_{OC} of 0.9V. The aim of examining this dye was to look for changes that might be expected due to its energy levels being at different values compared to Z907. Z105 (Fig 4.23) was one of the first dyes to be made that uses a phosphonic acid binding group[17]. This dye was examined to determine whether binding via the phosphonic acid to

TiO_2, which is expected to be stronger than the binding of carboxylic acid to TiO_2, would make it more effective than other dyes in water.

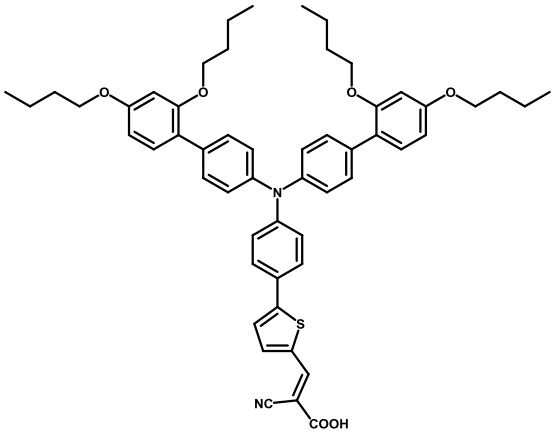

Fig 4.22 Dye D35

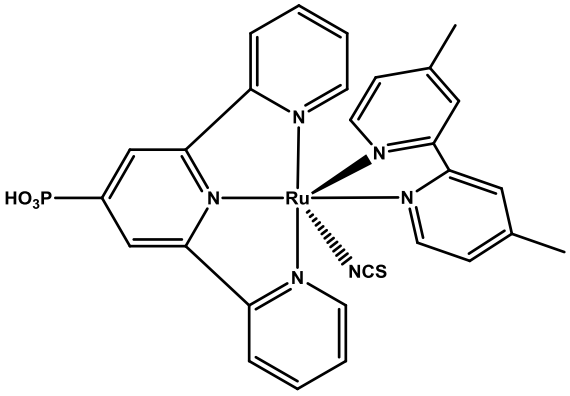

Fig 4.23 Dye Z105

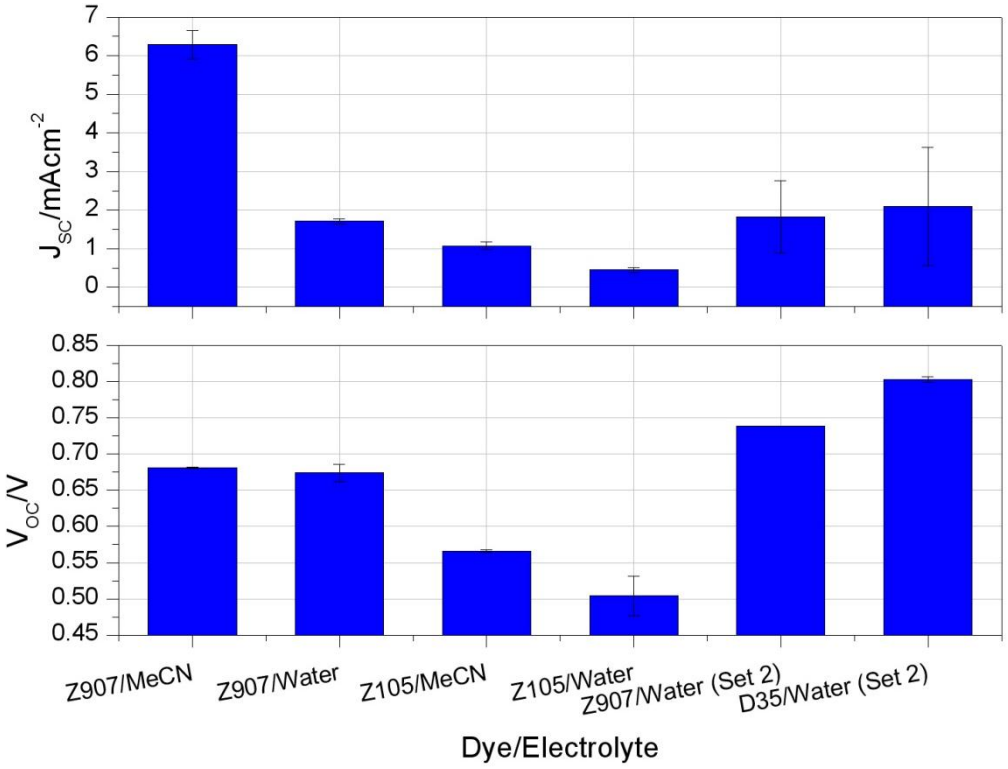

Fig 4.24 Current density and open circuit voltage for DSSCs made using acetonitrile and water solvents with 0.3mM Z907, Z105 or D35 dye. Note that because the cells dyed with Z105 and D35 were produced in separate batches, they are considered as two sets, each of which had its own Z907 comparison cell. All cells contained 2M PMII, 0.05M I_2, 0.1M GSCN, 0.5M tBP and water cells contained 1% Triton X-100, whereas acetonitrile cells contained 15% (with respect to acetonitrile) valeronitrile solvent. Cells measured under 1 sun AM 1.5 illumination.

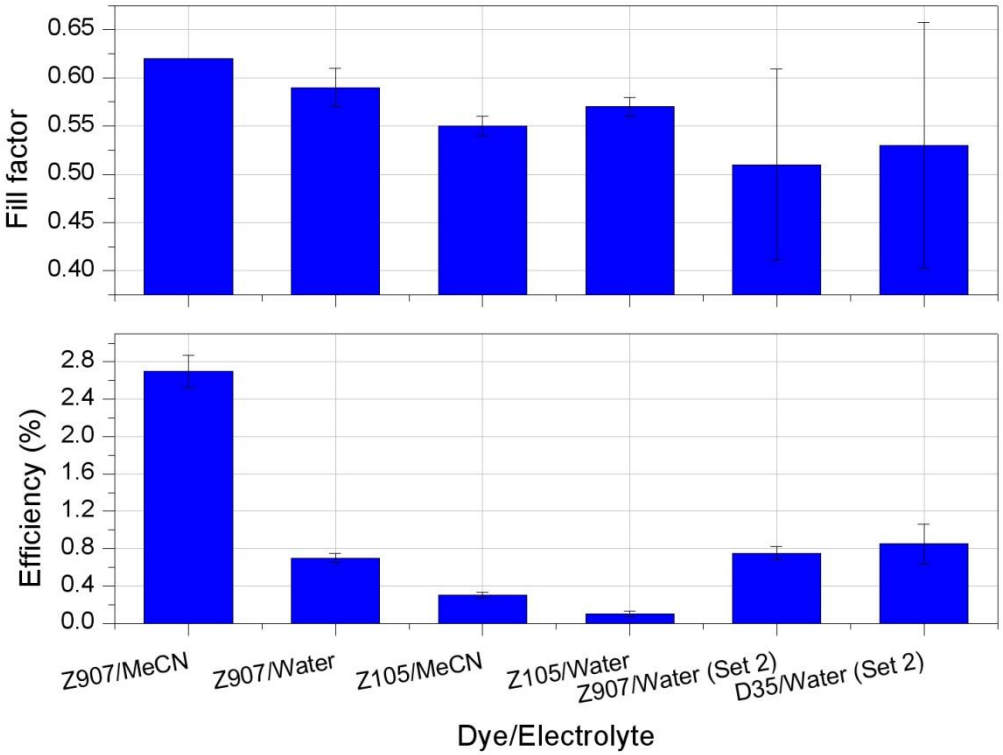

Fig 4.25 Fill factor and cell efficiency for DSSCs made using acetonitrile and water solvents with 0.3mM Z907, Z105 or D35 dye. Note that because the cells dyed with Z105 and D35 were produced in separate batches, they are considered as two sets, each of which had its own Z907 comparison cell. All cells contained 2M PMII, 0.05M I_2, 0.1M GSCN, 0.5M tBP and water cells contained 1% Triton X-100, whereas acetonitrile cells contained 15% (with respect to acetonitrile) valeronitrile solvent. Cells measured under 1 sun AM 1.5 illumination.

The two dyes were examined separately and compared to Z907, IV curve results are summarised in fig 4.24 & 4.25. When compared to cells made using the Z907 dye in acetonitrile electrolyte, the performance of Z105 was poor whereas D35 was comparable.

In water, cells made with Z105 had a significantly lower photocurrent and IPCE compared to Z907 (Fig 4.26) which may indicate that electron injection is poor through the phosphonic acid group in this dye, though other groups have been able to achieve IPCE values over 0.7 for semiconductor films dyed with this compound when measured in organic solvents[17]. Photovoltage was also reduced, which could be due to various factors including poor electron injection and slow dye regeneration by the redox couple which would result in greater losses via the reaction between electrons in the semiconductor and D^+. The fill

factor was stable, but the overall efficiency was very low. On this basis, Z105 is not a suitable dye for water cells. It would be informative to do a similar analysis using the Z955 dye, which is an analogue of the Z907 dye utilising phosphonic acid binding groups[18].

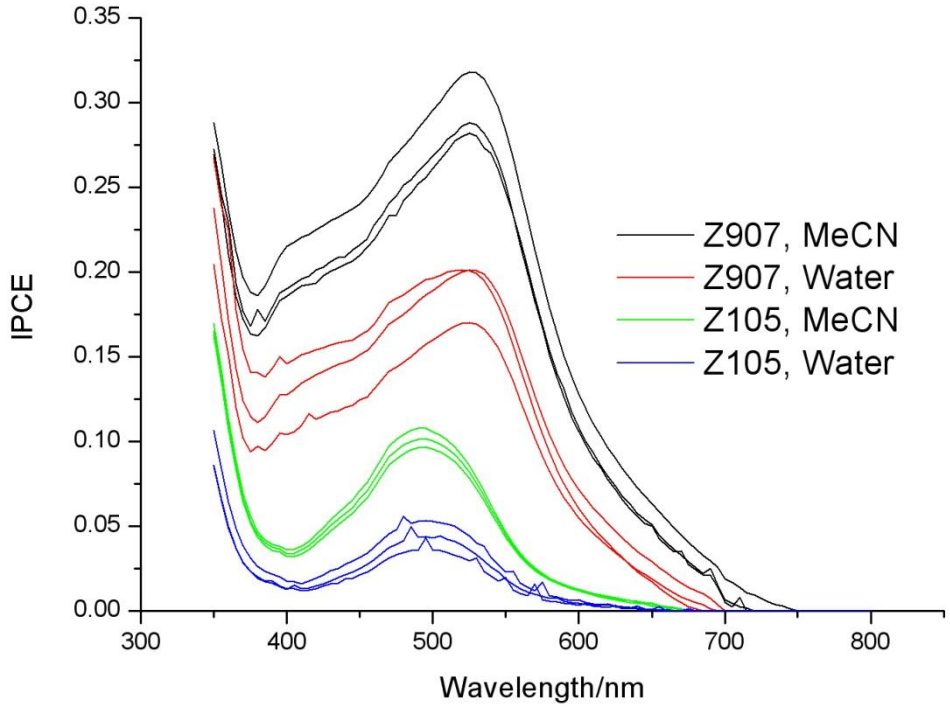

Fig 4.26 IPCE spectra for DSSCs dyed with 0.3mM Z907 or Z105. All cells contained 2M PMII, 0.05M I_2, 0.1M GSCN, 0.5M tBP and water cells contained 1% Triton X-100, whereas acetonitrile cells contained 15% (with respect to acetonitrile) valeronitrile solvent.

D35 produced a similar photocurrent to the equivalent Z907 cell (Set 2 in Fig 4.24 & 4.25) but its photovoltage was approximately 50mV higher. In acetonitrile, $E_0(D/D^+)$ for D35 is 1.04V vs NHE[16], approximately 0.15V below that for Z907[19]. Assuming this variation is similar in water, it means there is a greater potential difference between this and the redox potential of the redox mediator which should result in faster dye regeneration for D35 based on the increased overpotential for this reaction. This will be significant if a redox couple with a redox potential more positive than that for I_3^-/I^- is used. Regarding photovoltage, D35 has only one carboxylate binding group compared to two on Z907 which may lead to a reduced surface acidity and a raised CB which would increase the cell voltage. It is also possible that the large size of D35 helps to decrease the reaction between I_3^- and semiconductor electrons. The fill factor was similar for

both sensitizers but D35 gave slightly better efficiency. Both sensitizers showed a limited photocurrent and D35 had a slightly higher limit, which may be linked to its size. It would be useful to perform further analysis on this dye, however due to material constraints this was not possible.

This section sets out some of the important parameters that need to be addressed by altering the dye used when making aqueous DSSCs and suggests that D35 may be a candidate for further study regarding aqueous DSSCs.

4.3 Conclusions

A large number of DSSCs containing an aqueous electrolyte have been produced with several variations in materials and fabrication method. It has been shown that the efficiency of cells made with such an electrolyte can be improved through the use of additives though problems were encountered relating to cell electrolyte filling and semiconductor wetting. Heating the cell while filling was found to aid electrolyte permeation and increase cell performance. The effect of the concentration of the surfactant Triton X-100 was examined and 1vol% was found to produce the most efficient cells. When UV light was used to alter the TiO_2 surface and improve wettability it was found that this effect was negated by the hydrophobicity of the dye; however, using different surfactants did alter the contact angle between water and the surface though this did not lead to an improvement in cell performance largely because the coadsorbate molecules were seen to compete with dye molecules for surface binding sites. Z907 was found to be the most effective dye in terms of performance and stability, though in some low efficiency cells D35 was found to match this and production of additional cells made with this dye would be of interest.

4.4 References

(1) Sumita, M.; Sodeyama, K.; Han, L. Y.; Tateyama, Y. *J Phys Chem C* **2011**, *115*, 19849.

(2) Macht, B.; Turrion, M.; Barkschat, A.; Salvador, P.; Ellmer, K.; Tributsch, H. *Sol Energ Mat Sol C* **2002**, *73*, 163.

(3) Hinsch, A.; Kroon, J. M.; Kern, R.; Uhlendorf, I.; Holzbock, J.; Meyer, A.; Ferber, J. *Prog Photovoltaics* **2001**, *9*, 425.

(4) Nazeeruddin, M. K.; Kay, A.; Rodicio, I.; Humphrybaker, R.; Muller, E.; Liska, P.; Vlachopoulos, N.; Gratzel, M. *J Am Chem Soc* **1993**, *115*, 6382.

(5) (a) Liu, Y.; Hagfeldt, A.; Xiao, X. R.; Lindquist, S. E. *Sol Energ Mat Sol C* **1998**, *55*, 267(b) Zhu, K.; Jang, S. R.; Frank, A. J. *Energ Environ Sci* **2012**, *5*, 9492(c) Lu, H. L.; Shen, T. F. R.; Huang, S. T.; Tung, Y. L.; Yang, T. C. K. *Sol Energ Mat Sol C* **2011**, *95*, 1624.

(6) Jennings, J. R.; Wang, Q. *J Phys Chem C* **2010**, *114*, 1715.

(7) Law, C. H.; Pathirana, S. C.; Li, X. O.; Anderson, A. Y.; Barnes, P. R. F.; Listorti, A.; Ghaddar, T. H.; O'Regan, B. C. *Adv Mater* **2010**, *22*, 4505.

(8) (a) Kopidakis, N.; Neale, N. R.; Frank, A. J. *J Phys Chem B* **2006**, *110*, 12485(b) Zhang, C. N.; Huang, Y.; Huo, Z. P.; Chen, S. H.; Dai, S. Y. *J Phys Chem C* **2009**, *113*, 21779.

(9) Law, C.; Moudam, O.; Villarroya-Lidon, S.; O'Regan, B. *Journal of Materials Chemistry* **2012**, *22*, 23387.

(10) Wang, R.; Hashimoto, K.; Fujishima, A.; Chikuni, M.; Kojima, E.; Kitamura, A.; Shimohigoshi, M.; Watanabe, T. *Nature* **1997**, *388*, 431.

(11) Gao, Y. F.; Masuda, Y.; Koumoto, K. *Langmuir* **2004**, *20*, 3188.

(12) (a) Khazraji, A. C.; Hotchandani, S.; Das, S.; Kamat, P. V. *J Phys Chem B* **1999**, *103*, 4693(b) Zakeeruddin, S. M.; Nazeeruddin, M. K.; Humphry-Baker, R.; Gratzel, M.; Shklover, V. *Inorg Chem* **1998**, *37*, 5251(c) Ren, X. M.; Feng, Q. Y.; Zhou, G.; Huang, C. H.; Wang, Z. S. *J Phys Chem C* **2010**, *114*, 7190(d) Kay, A.; Gratzel, M. *J Phys Chem-Us* **1993**, *97*, 6272.

(13) Young, K. J.; Martini, L. A.; Milot, R. L.; Snoeberger, R. C.; Batista, V. S.; Schmuttenmaer, C. A.; Crabtree, R. H.; Brudvig, G. W. *Coordin Chem Rev* **2012**, *256*, 2503.

(14) Neale, N. R.; Kopidakis, N.; van de Lagemaat, J.; Gratzel, M.; Frank, A. J. *J Phys Chem B* **2005**, *109*, 23183.

(15) Boschloo, G.; Gibson, E. A.; Hagfeldt, A. *J Phys Chem Lett* **2011**, *2*, 3016.

(16) Feldt, S. M.; Gibson, E. A.; Gabrielsson, E.; Sun, L.; Boschloo, G.; Hagfeldt, A. *J Am Chem Soc* **2010**, *132*, 16714.

(17) Pechy, P.; Rotzinger, F. P.; Nazeeruddin, M. K.; Kohle, O.; Zakeeruddin, S. M.; Humphrybaker, R.; Gratzel, M. *J Chem Soc Chem Comm* **1995**, 1093.

(18) Wang, P.; Klein, C.; Moser, J. E.; Humphry-Baker, R.; Cevey-Ha, N. L.; Charvet, R.; Comte, P.; Zakeeruddin, S. M.; Gratzel, M. *J Phys Chem B* **2004**, *108*, 17553.

(19) Giribabu, L.; Singh, V. K.; Vijay Kumar, C.; Soujanya, Y.; Gopal Reddy, V.; Yella Reddy, P. *Advances in OptoElectronics* **2011**, *2011*, 8.

Chapter 5: Spatially resolved measurements of dye sensitized solar cells

5.1 Introduction
5.2 Experimental
5.3 Results
    5.3.1 Photocurrent mapping repeatability
    5.3.2 Low resolution photocurrent mapping comparing water and acetonitrile DSSCs
    5.3.3 Higher resolution photocurrent mapping and transmission mapping
        5.3.3.1 AC5 (Acetonitrile cell, filled by vacuum without heating)
        5.3.3.2 W4 (water cell, filled under vacuum but with no heat)
        5.3.3.3 W5 (water cell, vacuum filling with heating)
        5.3.3.4 Dye desorption
5.4 Conclusions
5.5 References

5.1 Introduction

It has been noted already (section 4.2.3) that problems related to cell electrolyte filling when water is the main solvent lead to a reduction in cell performance. In some cases, there were visible 'dry' areas within the cell which are expected to significantly reduce photocurrent though this effect is difficult to measure quantitatively. A method that can give some information on the relationship between electrolyte filling and photocurrent is spatially resolved photocurrent mapping. Although information about pore filling cannot be obtained on the nanoscale, larger scale inhomogeneities can be observed, and their local effect on photocurrent determined.

Photocurrent mapping has been used previously to examine the effect of damage and pressure on a cell[1], reasons for cell degradation[2] and dye stability[3]. A variation on this technique is that of visible transmission mapping, which can give information on the 2D dye coverage. Only one other use of transmission mapping for DSSCs has been found in the literature, where Barkschat *et al.* used a video camera in order to measure light transmission through a dyed film[3]. One practical difficulty in attributing changes in local current density to electrolyte filling is compensating for any dye inhomogeneity across the cell, or any effects on the dye caused by the addition of electrolyte. If the dye coverage can be measured separately, then these effects can be examined, and a better picture of what is occurring in the cell obtained. Transmission measurements reported in this chapter allow the dye coverage to be measured in this way at a qualitative level, and so account for electrolyte induced variations.

In this chapter two experiments are presented. In the first, two sets of DSSCs were made with different types of electrolyte - water based and acetonitrile based. In all other respects the DSSCs were identical. 2D photocurrent maps of these cells were measured and compared. In the second set of experiments, three cells were examined at different stages in their production by both transmission mapping and photocurrent mapping. It is seen that in some but not every case there is very clear dye desorption near to electrolyte filling holes, particularly in water cells. Varying degrees of photocurrent homogeneity are also observed,

showing that there are clear differences between cells fabricated in the same way.

5.2 Experimental

Cells were made as described in chapter 3. For the first photocurrent mapping experiment in section 5.3.2, electrolyte filling of the water cells involved heating to 80°C while under vacuum in order to aid the electrolyte permeation, whereas for acetonitrile/valeronitrile, only vacuum was used. The cells were dyed with 0.3mM Z907 and the electrolyte consisted of 2M PMII, 0.05M I_2, 0.5M tBP and 0.1M GSCN. The water cells also contained 1% triton X-100. The cell composition is summarized in table 5.1 and table 5.2. For the second experiment, after dyeing the films a transmission map was obtained. Cells were then sealed and filled by one of two techniques – W4 (water) & AC5 (acetonitrile) were filled by the vacuum technique, while W5 (water) was filled by vacuum and heating to 80°C. Photocurrent maps were then measured. Finally, these cells were taken apart, aided by brief heating (~100°C) after which a second transmission measurement was taken. For spatially resolved photocurrent mapping measurements, the solar cells were mounted on stepper-motor-driven translation stages so that the cell could be moved in two orthogonal directions. These directions were also orthogonal to the axis of an optical beam from a 532 nm laser diode (10 mW) illuminating the cell. Neutral density filters were used to adjust the laser power reaching the sample and microscope lenses were used to focus the beam to 50 micron diameter spot sizes. The laser beam was mechanically chopped (MC2000, ThorLabs) at 3Hz when measuring photocurrent maps – this was determined to be the fastest chop rate that allowed the cell to reach steady state conditions – and at 20Hz when measuring transmission maps. The photocurrent was amplified by a large dynamic range amplifier (Melles Griot) and rectified by a digital lock-in (Stanford Research SR830). A DC white light bias (halogen lamp) was used to illuminate the whole cell during mapping experiments to avoid resistive losses due to electron trapping at the TiO_2. The setup is shown in Fig 5.1. Intensity was kept constant within both of the two experiments (i.e. cells Set 1: AC1 – AC4 & W1 – W3 and Set 2: AC5, W4 and W5), but was not kept the same between them, mainly due to the positional variations that were required in the two slightly differing setups,

particularly in the case of transmission measurements. A similar setup was used for high-resolution optical transmission mapping. In this case, a stationary calibrated Si photodiode (ThorLabs) was placed below the sample to measure variations in the transmitted light power while the sample was moved by the translation stage. No bias light was used when measuring the transmission. Laser stability and the frequency response of the investigated solar cells was measured using a multichannel oscilloscope (Tektronik, DPO4104B). Low resolution maps were measured with a 400 μm step size and high resolution maps with a 160 μm step size. As such, the measurements do not record data from the whole film. However, a gradual transition between features in individual maps demonstrates that useful data representing real film and cell characteristics is being obtained from the experiment.

Table 5.1: Summary of cell characteristics before laser mapping measurements were taken.

Cell	Solvent	I_{sc} / mA	V_{oc} / V	Fill Factor / %	η / %	Average η
AC1	MeCN/BuCN	6.4	0.665	64	2.9	
AC2	MeCN/BuCN	4.7	0.631	63	2.1	2.4±0.4
AC3	MeCN/BuCN	4.5	0.672	67	2.3	
W1	Water/Triton X-100	6.5	0.661	64	2.9	
W2	Water/Triton X-100	6.7	0.662	65	3.1	2.8±0.4
W3	Water/Triton X-100	4.6	0.692	67	2.4	

Table 5.2: Summary of cell characteristics after laser mapping photocurrent measurement.

Cell	Solvent	I_{sc} / mA	V_{oc} / V	Fill Factor / %	η / %	Average η
AC1	MeCN/BuCN	10.5	0.680	42	3.0	
AC2	MeCN/BuCN	5.6	0.659	52	1.9	2.4±0.5
AC3	MeCN/BuCN	4.9	0.695	64	2.2	
AC4	MeCN/BuCN (leaked)	3.4	0.688	58	1.4	
W1	Water/Triton X-100	6.9	0.704	59	2.9	
W2	Water/Triton X-100	6.8	0.704	63	3.0	2.8±0.3
W3	Water/Triton X-100	5.8	0.713	51	2.4	

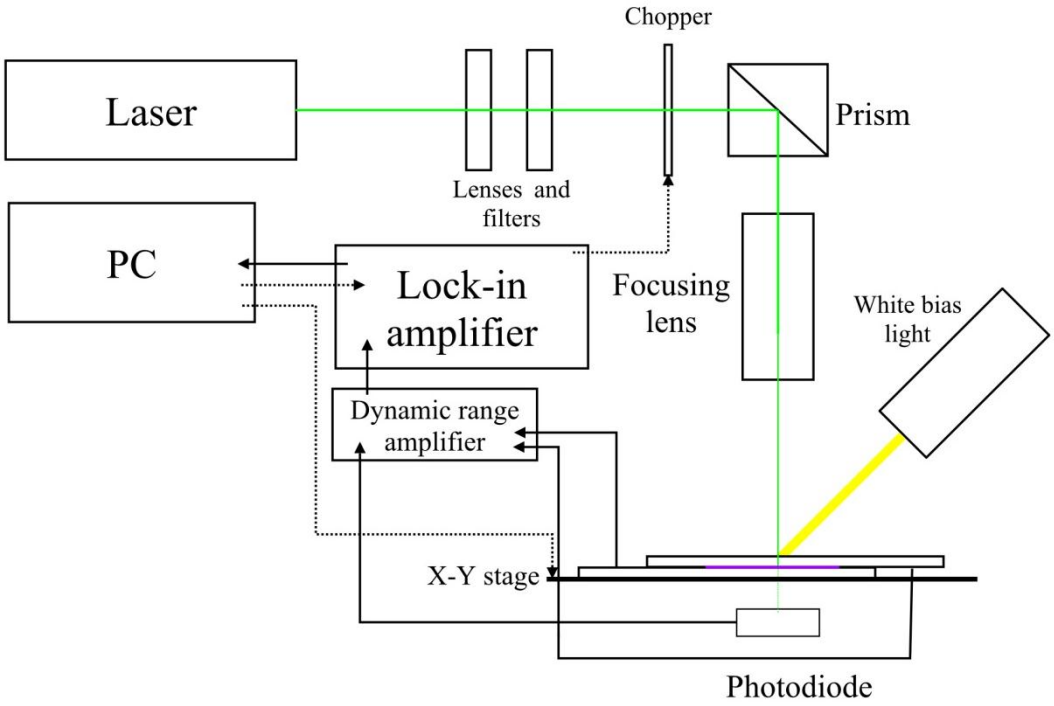

Fig 5.1 Experimental mapping setup. For photocurrent maps only the photocurrent of the cell is measured, for transmission maps only the photodiode response is measured. Black lines represent electrical connections, dotted black lines represent control connections, coloured lines represent light beams.

5.3 Results

5.3.1 Photocurrent mapping repeatability

Before measurements could be taken, the repeatability of the analysis technique needed to be determined. Photocurrent maps taken for this purpose used a step size of 400 µm giving a resolution of 625 measurement points per square centimeter, which will be called 'low' resolution. In all cases the blue areas of zero photocurrent around the edges of the plots represent areas where no TiO_2 was present.

A number of repeats were measured on one cell containing an acetonitrile based electrolyte to determine if there was any change between measurements (Fig 5.1 & 5.2). There was some deterioration of the cell photocurrent performance over multiple readings, particularly when measurements were taken immediately after one another. The performance tended to recover a little when the cells were stored in the dark for one hour but did not return to initial values within this period (e.g. Fig 5.2 c->d, e->f), and a similar response was seen when the cells were kept in the dark overnight (fig 5.2 f->g).

IV curves taken before and after photocurrent mapping (tables 5.1 and 5.2) showed similar performance changes for both types of cells. After the measurements, photocurrent and voltage both increased while fill factor decreased resulting in essentially unchanged efficiencies. A detailed understanding of these effects is beyond the scope of this work but a possible explanation is suggested based on the work of Listorti *et al.*[4] who examined the effect of light soaking on dye cells. It is possible that the illumination incident on the cell from the bias and laser light led to a lowering in the conduction band (CB) of the semiconductor and subsequent increase in electron injection and photocurrent. Listorti *et al.* also saw a reduction in the recombination reaction between semiconductor electrons and I_3^-, negating the expected drop in photovoltage due to changes in CB position and this may also partly explain the direction of the change in photovoltage observed here. The drop in fill factor could be explained by an increase in internal resistance. Macht *et al.* noted that loss of iodine occurring in the electrolyte under illumination can lead to an

increase of internal resistance and that this loss of iodine is favored at increased temperature[2] – the cell temperature was not controlled in these experiments. The large changes in fill factor observed here may be due to localized heating effects from the 50 µm diameter laser spot. Interestingly, the cell used for degradation analysis (cell measured seven times, Fig. 5.2 and 5.3) showed the largest increase in photocurrent, the smallest increase in photovoltage and the greatest decrease in fill factor of all the cells measured, which would be consistent with having a greater negative change to CB potential compared to the other cells, and the largest increase in internal resistance, both of which could result from the increased exposure to light the cell received.

There are a number of large discrepancies between consecutive scans in the form of step changes in the recorded photocurrent, which do not change in any consistent manner. This was considered to be an experimental artifact. The fact that the variation was a constant step change suggested that an effect such as a small variation in laser intensity at the cell surface, possibly caused by temperature variations in the laser, or small vibrations which altered the beam path length was the cause of this. Laser stability was initially excluded by measuring the laser output for prolonged times and confirming that no significant variations occurred. However, it was discovered a long time after the experiment was completed that the laser output intensity was affected when the power supply wire was disturbed, leading to the step changes observed. As the photocurrent changes appear as a step change in the measured values and are not reproduced between measurements it is generally easy to notice them and to disregard them in the data interpretation. However it makes quantitative analysis of the experiment very difficult.

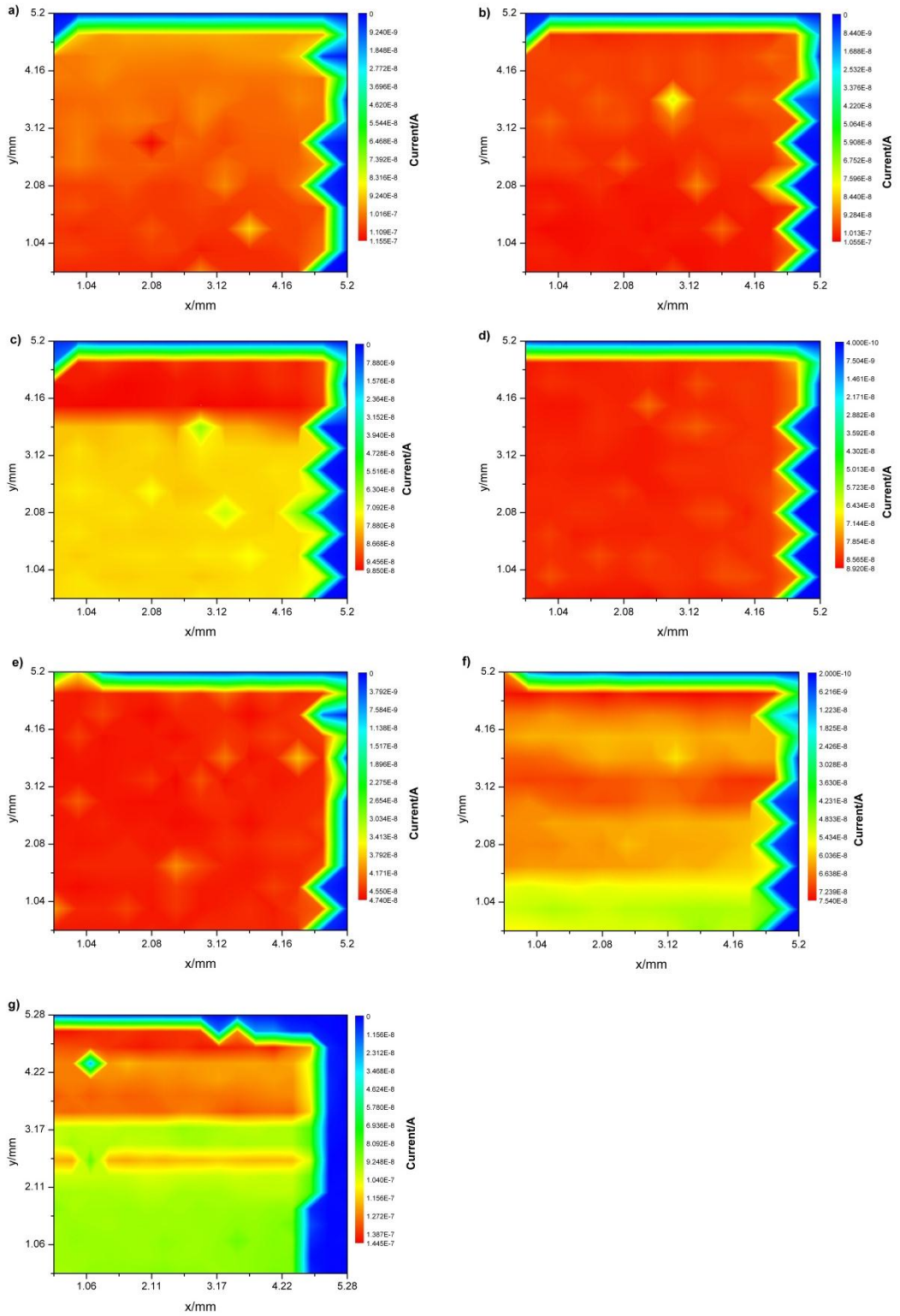

Fig 5.2 Repeatability testing of photocurrent measurements taken on acetonitrile cell AC1. Scaled to emphasize local features a) – f) low resolution (400 μm step size) g) high resolution (160 μm step size). A) Initial reading, b) Measured immediately after a), c) Measured immediately after b), d) Cell kept in dark for one hour after previous reading (c), e) Cell kept in dark for one hour after previous reading (d), f) Cell left in dark overnight after previous reading, g) Cell left in dark overnight after previous reading.

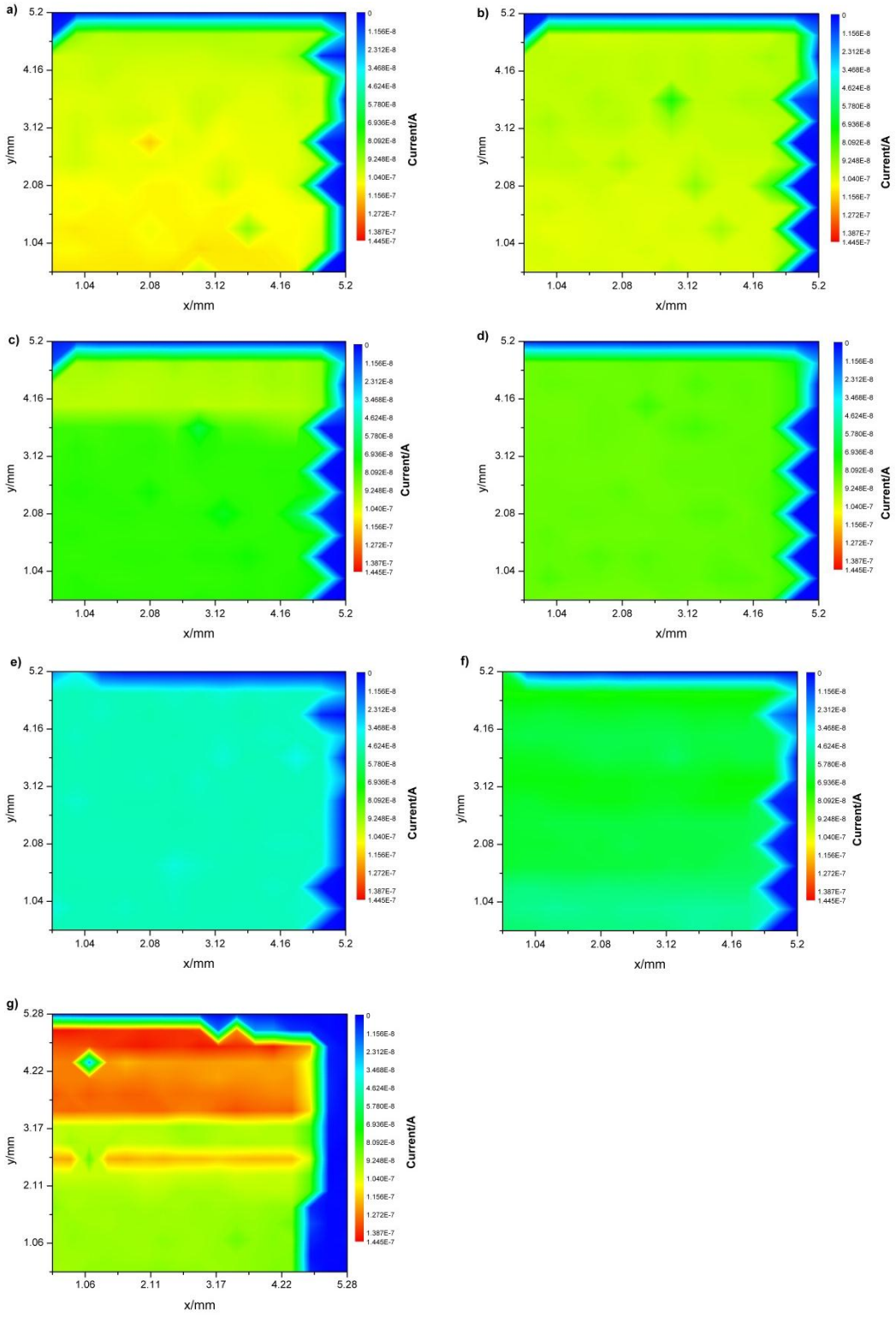

Fig 5.3 Repeatability testing of photocurrent measurements taken on acetonitrile cell AC1. Scaled to emphasize variation between readings features a) – f) low resolution (400 µm step size) g) high resolution (160 µm step size). a) Initial reading, b) Measured immediately after a), c) Measured immediately after b), d) Cell kept in dark for one hour after previous reading (c), e) Cell kept in dark for one hour after previous reading (d), f) Cell left in dark overnight after previous reading, g) Cell left in dark overnight after previous reading.

5.3.2 Low resolution photocurrent mapping comparing water and acetonitrile DSSCs

Photocurrent maps of six cells on the same intensity scale (relative to the maximum current) are shown in Figure 5.4, where it can be seen that there are no obvious differences between the water and acetonitrile based cells. One cell in each batch has a lower photocurrent across the whole cell, and in both cases (AC3 and W3), this corresponds to a lower overall photocurrent from the IV curve. However, this link does not appear to account for the lower total photocurrent seen for AC2 which has a higher photocurrent over most of the film, though it is not completely homogeneous. One possible hypothesis that has not been taken further at the time of writing is that the photocurrent maximum is limited by the lowest performing part of the cell – if for example there are defects in the film which allow the reaction between electrons in the TiO_2 or FTO and I_3^- to increase. However, it is thought that this would be more likely to reduce the V_{OC} than the I_{SC}. A way to study this phenomenon in more detail would involve integrating the photocurrent produced across the cell area and comparing this with the output I_{SC}. This could then be compared with a theoretical value determined by assuming output at each point was the minimum value obtained and integrating using this value. This measurement is made difficult in this situation by the variation in laser output seen in the maps obtained.

Figure 5.5 shows the same current maps scaled individually for each cell, making the inhomogeneities in the photocurrent maps clearer. The acetonitrile cells all showed slightly higher efficiencies in one corner. In the case of the water cells, W1 was essentially homogeneous and W3 showed only a slight increase in photocurrent in the bottom right hand corner whereas the photocurrent produced by W2 was very inhomogeneous, being significantly higher in one corner.

Miettunen *et al.*[5] saw a decrease in cell performance as they moved further from the electrolyte filling hole in their cells which they attributed to a decrease in local tert-butyl pyridine (tBP) concentration as it was adsorbed strongly to the surface. A similar pattern is not observed in these measurements, with corners of high photocurrent sometimes corresponding to the filling holes and sometimes not (areas of higher photocurrent labeled A-D). In addition all cells were filled from

two holes (two 0.6 mm diameter filling holes, a drop of electrolyte placed on each hole, filled under vacuum) and there was no clear pattern of higher photocurrent under both holes. This suggests that, in contrast to Miettunen, variation in current in these cells was not due to local adsorption of electrolyte species – it is noted that the electrolyte composition, dye used and TiO_2 production conditions and thickness are not exactly the same between this work and the work of that group. Finally there was no definite evidence of poor cell filling in the water cells (heat and vacuum filled), however it is noted that W2 shows the greatest variation across the cell and it is possible that this is due to better electrolyte filling into the area centered around 'B'. Plots of photocurrent versus illumination intensity (Figure 5.6) suggest that there is no diffusion limitation occurring at least up to the photocurrents produced by these cells.

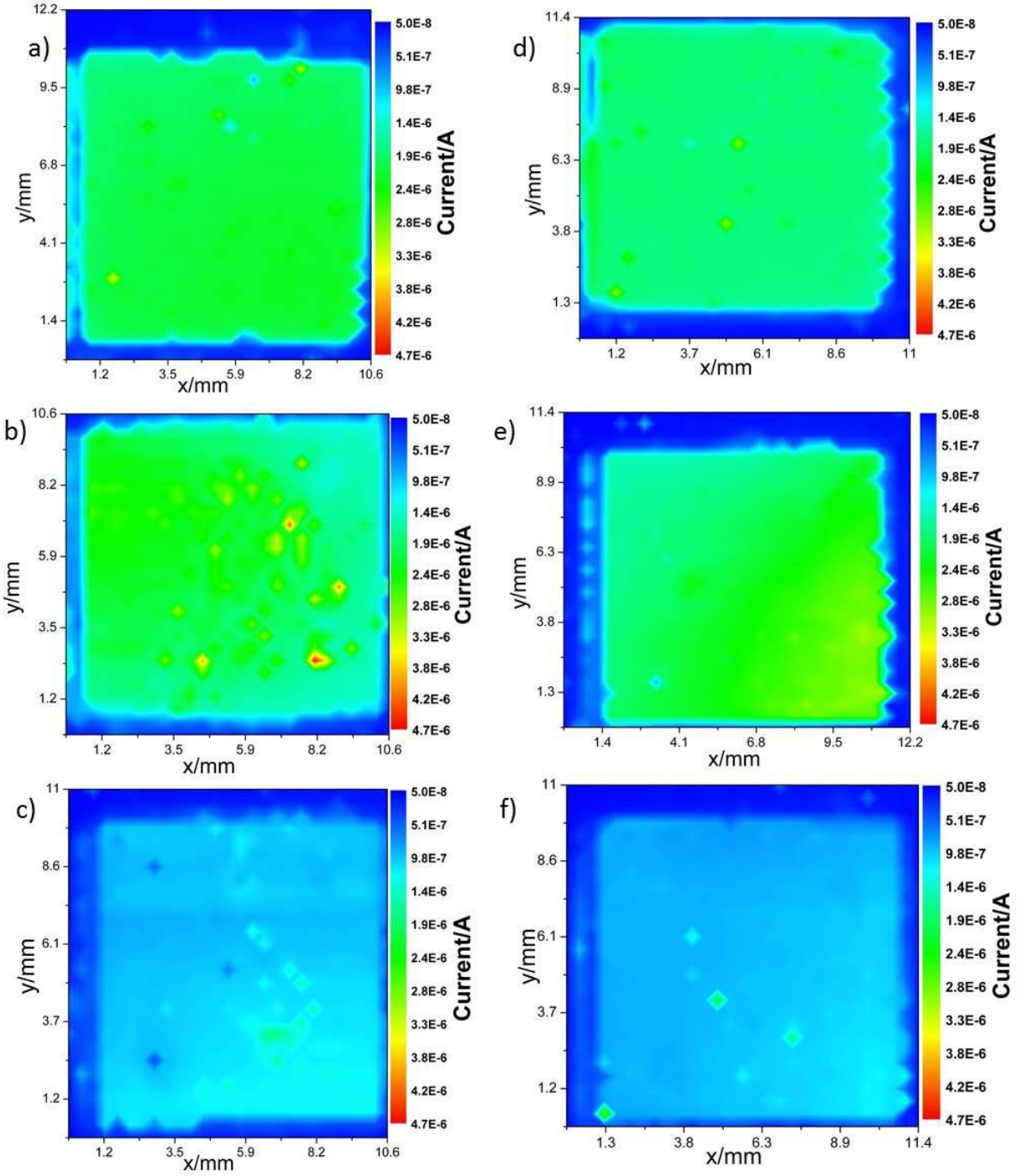

Figure 5.4 Photocurrent maps for three cells using acetonitrile based electrolyte a) AC1, b) AC2, c) AC3 and three cells using water based electrolyte d) W1, e) W2 and f) W3. Photocurrent is measured on the same intensity scale for each map in order to compare between cells. Filling holes are located in the bottom left and top right corners of each cell.

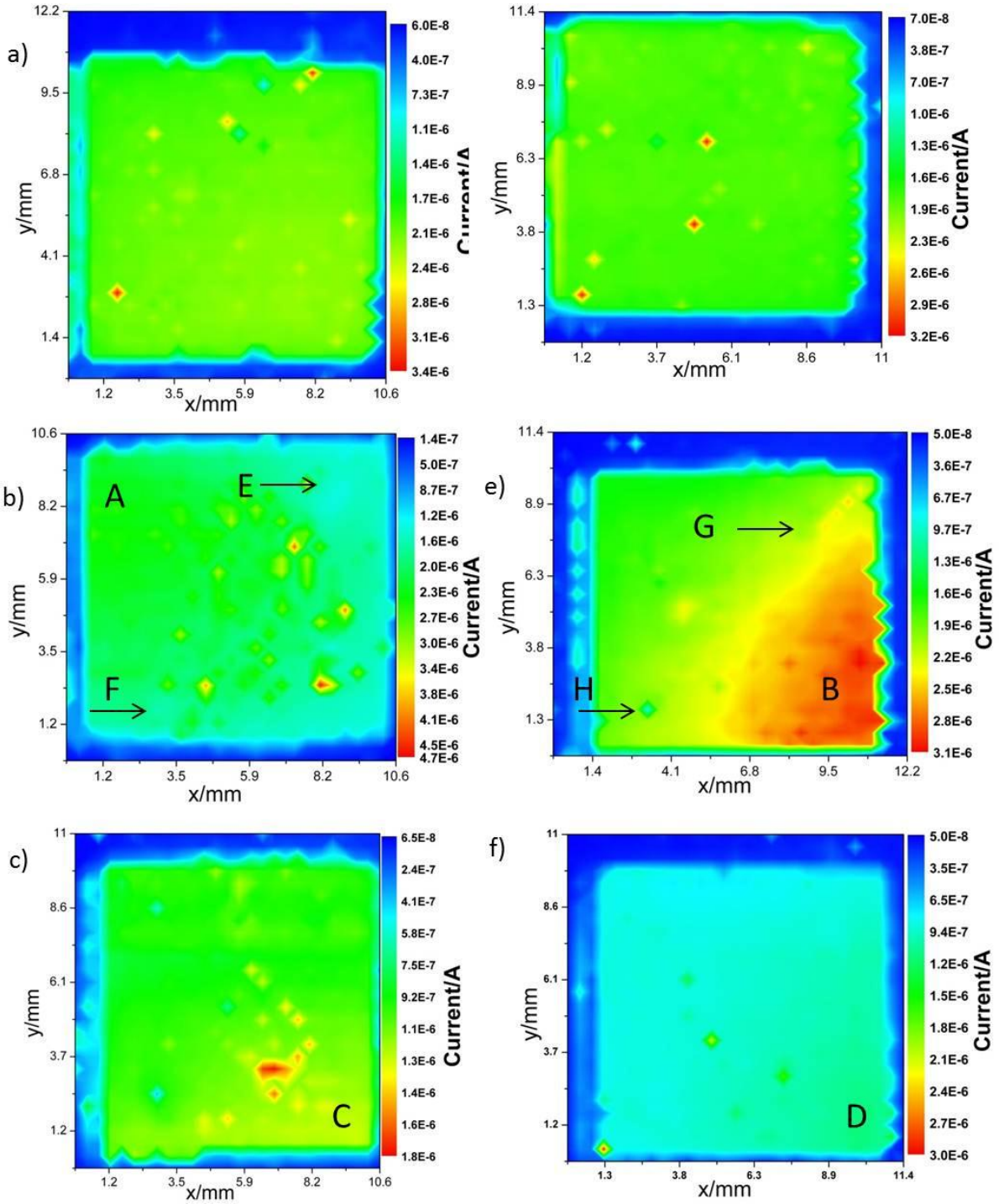

Figure 5.5 Photocurrent maps for three cells using acetonitrile based electrolyte a) AC1, b) AC2, c) AC3 and three cells using water based electrolyte d) W1, e) W2 and f) W3. Photocurrent is measured on a different scale for each map in order to emphasize features within each cell. Filling holes are located in the bottom left and top right corners of each cell and cold spots adjacent to the filling holes have been marked by black arrows where observed.

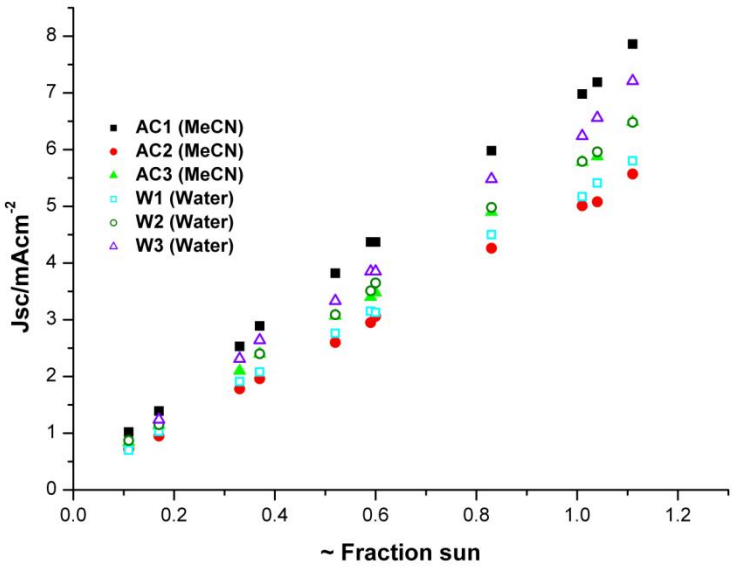

Figure 5.6 Photocurrent response for cells made using electrolyte containing water or acetonitrile as solvent as a function of light intensity. Light source has attached AM1.5 filter. Readings for the same solvent are replicates.

In several cells localized spots of lower photocurrent were seen directly under the filling holes (just visible in AC2 and W2, marked E,F,G and H in Fig 5.5) which will be discussed in more detail later. Transmission mapping suggests that small differences in photocurrent could have been due to the local dye distribution in the film.

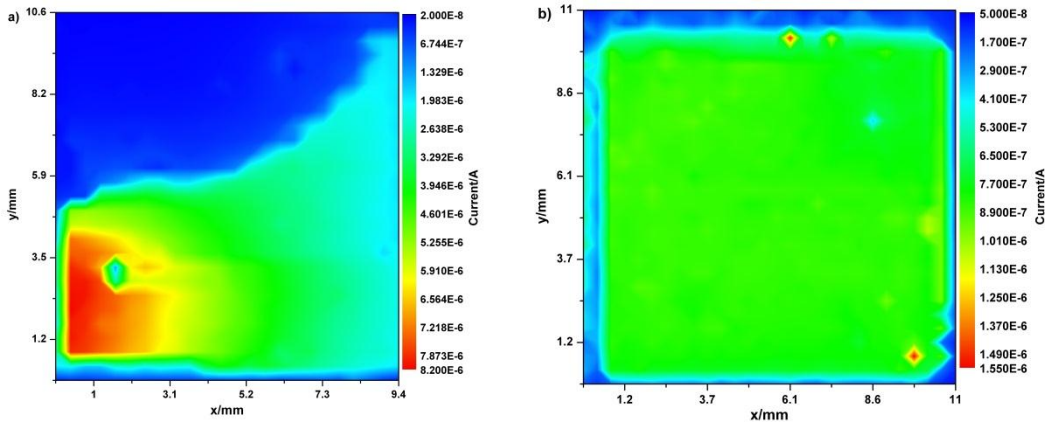

Fig. 5.7 Photocurrent maps for cells a) AC4 (acetonitrile) and b) W4 (water). Data not presented in main sections as both cells leaked at a point within the experiment. In the case of AC4, this was before the photocurrent map was obtained, and this is very clear in the graph shown – the leak was mainly via the filling hole which was located in a position corresponding to the top right corner of the map shown. In the case of W4, the leak occurred before IV measurements were taken.

In Fig 5.7 an acetonitrile cell is shown where some electrolyte leaked out of the cell. It can be seen that there are large variations in photocurrent due to loss of electrolyte which correlate to a visual inspection of the cell. This is also reflected in the overall photocurrent. It is expected that a cell that didn't fill well would show a similarly stark variation between filled and unfilled area.

It is more difficult to analyze the small spots of low/high photocurrent seen on many of the cells. Areas of reduced photocurrent may be due to dust particles or film imperfections. Small areas of high photocurrent may also be due to local differences in the TiO_2 films. The main conclusion from this section is that no clear differences between the two sets of cells were observed and that overall, cells showed a homogeneous photocurrent output.

5.3.3 Higher resolution photocurrent mapping and transmission mapping

Three DSSCs were investigated in more detail using transmission mapping and high resolution photocurrent mapping. Transmission mapping was carried out on the photoanodes before they were assembled into cells (Figure 5.8), photocurrent maps were obtained (Figure 5.9) and finally transmission maps were measured again for the same anodes after the cells were disassembled (Figure 5.10). Transmission mapping was used to investigate whether variations in dye coverage or TiO_2 film thickness were responsible for the areas of high and low photocurrent in the DSSC. High resolution photocurrent mapping was carried out using a step size of 160 µm giving 3906 data points/cm^2, and data was normalized with respect to the maximum transmission seen through the glass, which is white in Fig 5.8 and 5.10. Three cells were measured: AC5 containing an acetonitrile based electrolyte, W4 containing a water based electrolyte that was introduced under vacuum at room temperature and W5 containing a water based electrolyte introduced into the cell using both vacuum and heating at ~80°C. When interpreting transmission maps, bear in mind that lower transmission relates to higher dye coverage, so areas that are darker blue have a greater amount of dye in the beam pathway.

As noted in section 5.4.1, clear horizontal lines appeared (e.g. Figure 5.9(c)), separating areas of apparent variation in photocurrent. These lines are not seen

in lower resolution (faster) scans (Figure 5.11) of the same cells and appear then disappear between sequential high resolution readings; the reason for these lines is discussed in the repeatability section and is due to the experimental technique rather than variations in the cell.

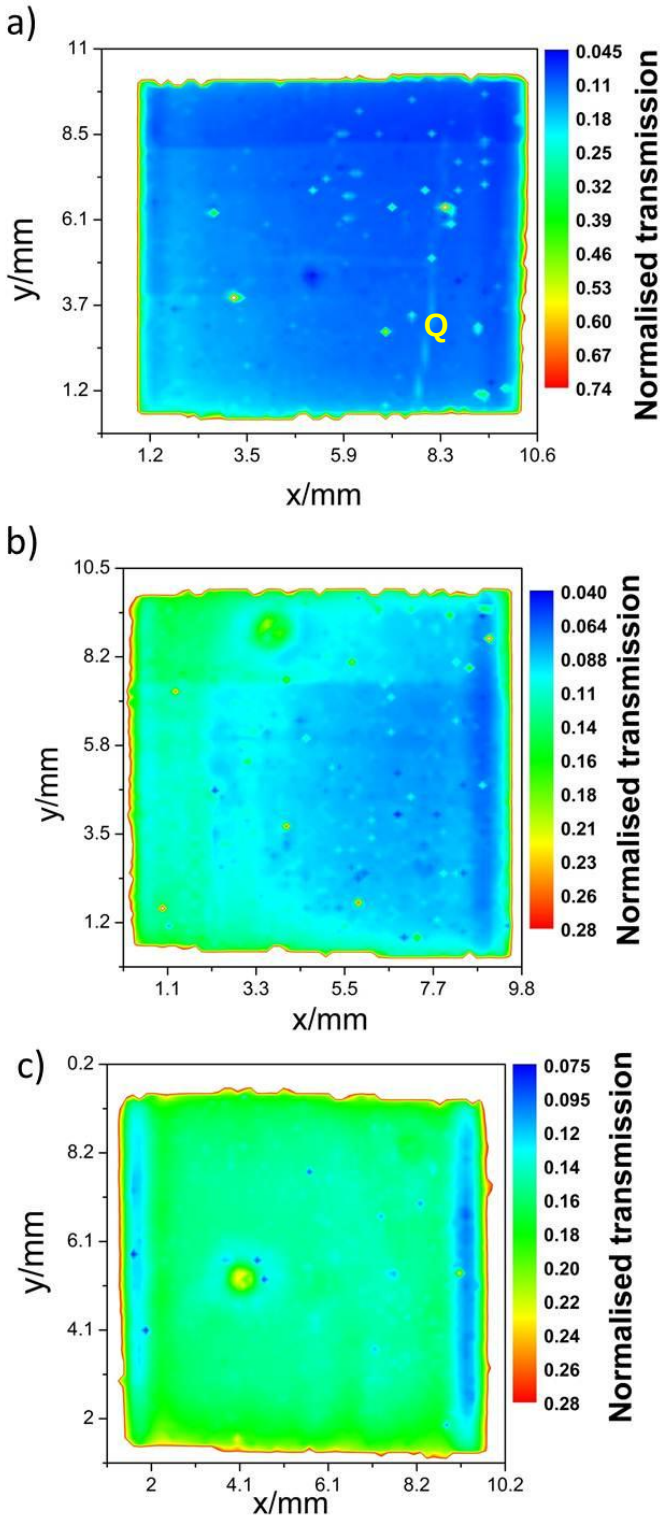

Figure 5.8 Transmission maps for dyed films (0.3mM Z907) before making into cells. Made into the following cells a) AC5 (acetonitrile), b) W4 (water) and c) W5 (water). Note that for transmission maps, blue represents lowest transmission and so the greatest amount of dye.

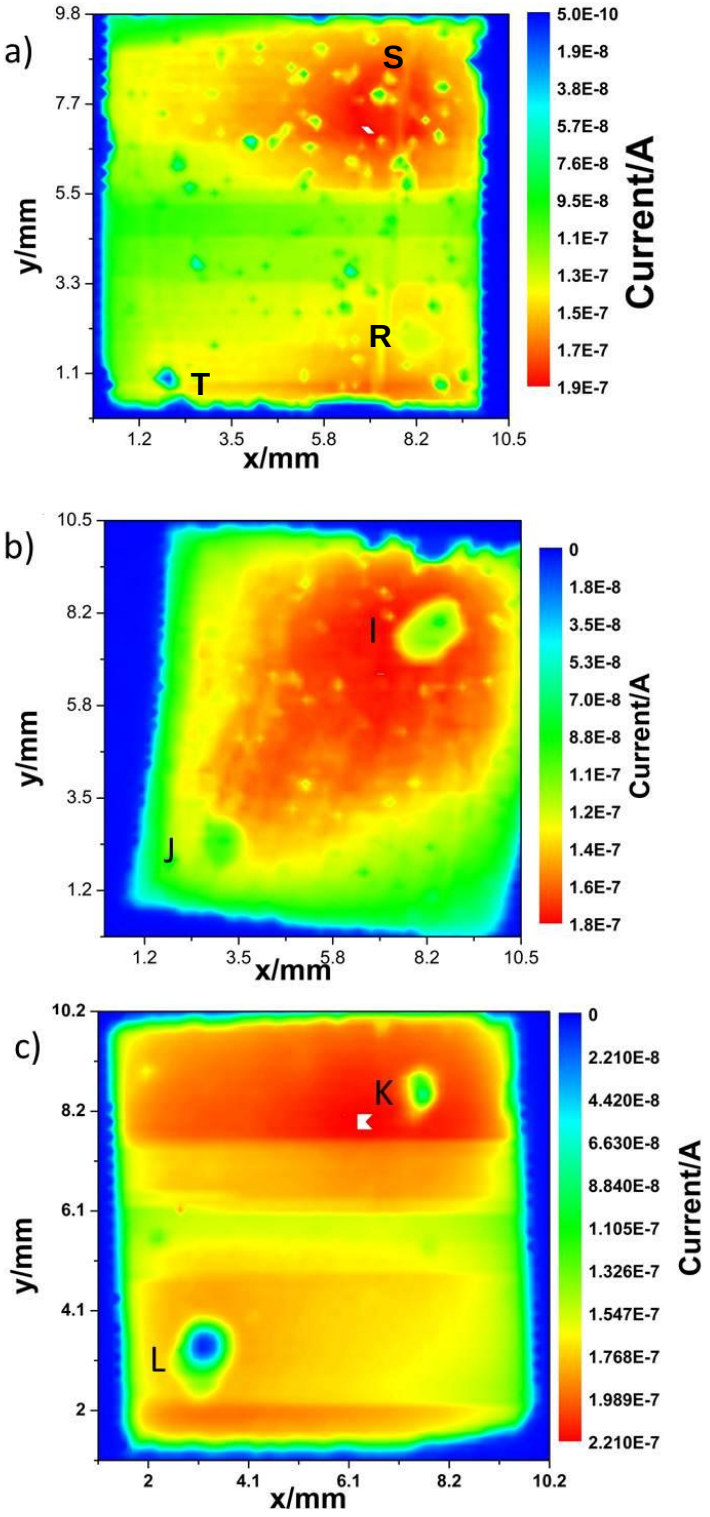

Figure 5.9 Photocurrent maps for cells a) AC5 (Acetonitrile, filled with only vacuum), b) W4 (Water, filled with only vacuum) and c) W5 (Water, filled with vacuum and heating). The positions of the filling holes and the corresponding cold spots are indicated by the letter I-L.

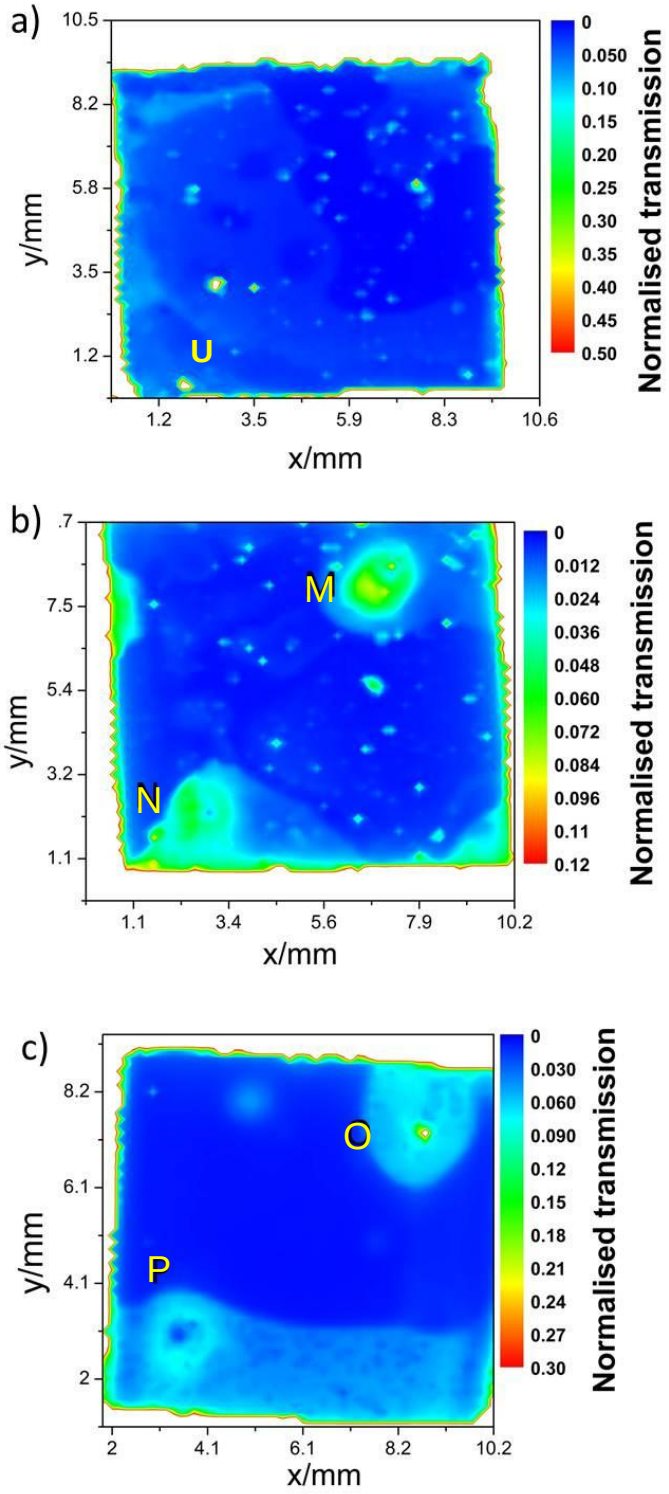

Figure 5.10 Transmission maps for dyed films after taking cells apart. Taken from the following cells a) AC5 (Acetonitrile, filled with only vacuum), b) W4 (Water, filled with only vacuum) and c) W5 (Water, filled with vacuum and heating). Note that for transmission maps, blue represents lowest transmission and so the greatest amount of dye.

5.3.3.1 AC5 (Acetonitrile cell, filled by vacuum without heating)

An area of high photocurrent was observed at the top of this cell (visible on the high resolution scan, figure 5.9(b), and on a low resolution scan, figure 5.11(a)). The area of enhanced photocurrent may correspond to an area of higher dye coverage seen in the first transmission map (figure 5.8(a)) however this feature looks similar to the step changes mentioned for photocurrent, so this is unlikely. The transmission map is reasonably homogeneous, with a general slight increase in dye coverage going from left to right on the film. One other notable feature is a scratch on the right hand side, which can also be seen in the photocurrent map. Interestingly this does not show up in the final transmission map.

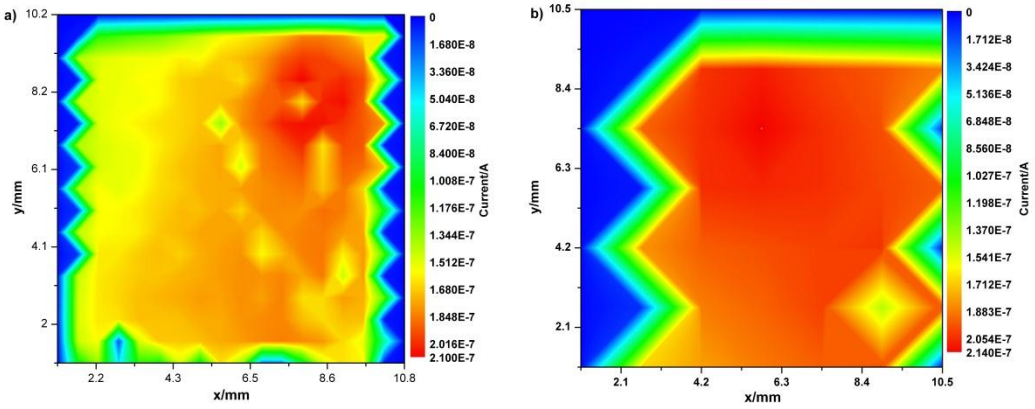

Fig. 5.11 Low resolution photocurrent maps for the cells a) AC5, 600 µm step size and b) W5, 1500 µm step size. The step variation in photocurrent observed in Figure 5.9 is not seen in either of these maps, strongly suggesting it is due to variation, possibly caused by vibration, in the high resolution long time experiments.

The step changes seen in the photocurrent map make comparison of the centre of the cell with the top and bottom of it difficult. However, what is apparent is that there is a region of higher photocurrent near to one of the filling holes (Fig 5.9, S), and it appears that the right side of the cell has a slightly higher photocurrent than the left. This can be linked to the increase in dye coverage seen in the transmission map, though does not correlate completely. This suggests a second factor is involved which relates to the electrolyte. However, the nature of this factor is unknown. It is interesting that this variation was not significantly seen in the first set of acetonitrile cells measured at low resolution, which may mean the

TiO_2 thickness and so dye coverage was more consistent for those cells. It is noted that the photocurrent produced by those cells was higher. Further measurements of cells at higher resolution are required to determine the extent of the electrolyte effect. The spot of low photocurrent in the bottom left corner (Fig 5.9, T, Fig 5.10, U) also shows up in the second transmission map (Fig 5.10(a)), and may correlate to damage caused to the film in the cell making process.

5.3.3.2 W4 (water cell, filled under vacuum but with no heat)

The photocurrent map (Figure 5.9(a)) shows an area of high photocurrent that spreads out from the filling hole (Fig 5.9, I). Transmission mapping (Figures 5.8(a)) shows an area of lower transmission (higher dye coverage) on the right side of the film. The photocurrent map does not show any features that corresponded with the initial transmission map suggesting that the photocurrent map is dominated by the distribution of the electrolyte. This cell was filled at room temperature under vacuum; the photocurrent map suggests that cell filling was relatively poor under these conditions and may have limited the cell performance. It is interesting to note that there are two clear areas of low photocurrent under the filling holes (Fig 5.9, I & J) and it can be seen from Figure 5.10(a) that the dye has been desorbed from the area of the photoanode under these holes. This effect can also be seen visually (Fig. 5.12), and is discussed in more detail below.

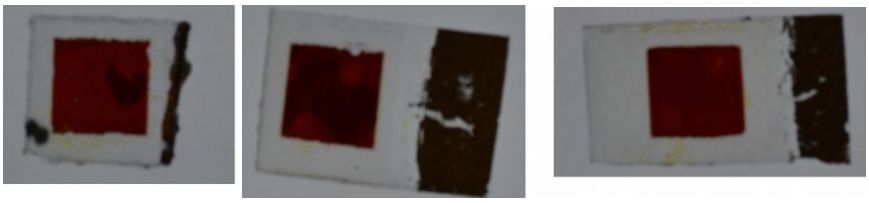

AC4 W4 W5

Fig. 5.12 Photographs of dyed TiO_2 from cells W4, AC4 and W5 after taking them apart.

5.3.3.3 W5 (water cell, vacuum filling with heating)

The current map for W5 (Figure 5.9(c)) suggests homogeneous current densities across the cell area. The horizontal lines showing areas of apparent differences in photocurrent are artifacts of the measurement and disappear when lower

resolution scans are taken (Figure 5.11(b)). The better homogeneity observed for this cell (and for cells W1 and W3 above) compared to W4 was attributed to better electrolyte penetration because the cell was filled at 80^{o}C under vacuum. This agitates the electrolyte within the cell during the filling process, improving permeation. Cell W2 (Fig 5.5e) showed inhomogeneity however, showing that the technique is not always completely effective. Again two areas of low photocurrent were measured under the filling holes and corresponded to areas of low dye coverage in the final transmission maps (Figure 5.10(c) K and L).

5.3.3.4 Dye desorption

Two possible explanations can be considered for the decrease in dye coverage near to the filling holes in the water cells. One is that there is no platinized counter electrode due to the drilled out filling hole at this point, which may limit the local I^- production and lead to dye desorption. The second is that some part of the electrolyte filling process causes dye desorption near to the filling hole.

Several reasons stand against the first explanation. Diffusion of a species follows a random pathway, and so a diffusion front is spherical except where intercepted by a barrier to the diffusing species. Thus, I^- will be supplied to the dyed TiO_2 directly below the filling hole from areas further away (and similarly I_3^- produced by oxidized dye will be able to diffuse to an active part of the counter electrode). The viscosity of water is higher than acetonitrile, meaning diffusion constants are lower. This may partly explain why, with the exception of AC4 which is anomalous on the basis of electrolyte leakage, the reduced photocurrent below filling holes was only observed clearly for water cells. However, it does not explain why dye desorbs from the surface. Even if I^- levels dropped underneath the filling hole, any dye that was not regenerated by I^- would usually be reduced by electrons from TiO_2 rather than breaking down. Finally in some water cells loss of dye has been observed by eye during electrolyte filling and before an IV curve was measured.

The second explanation could be related to tBP (see section 7.2.2). The basic molecule tBP increases the pH of the aqueous solution, which lowers the dye binding equilibrium constant. If tBP is itself able to adsorb onto TiO_2[6], tBP

concentration will then decrease in solution so the pH will decrease. Over time the tBP concentration would therefore decrease, which could explain why dye desorption only occurs near to the holes. The mechanism for this process is discussed in more detail in section 7.2.2.

Calculations were done to try to determine if this was a reasonable explanation. Assuming that the gap between the two electrodes was 25 μm (thickness of the spacer), the TiO_2 film was 10 μm and 50 % porous and the area into which electrolyte can go is 1 cm x 1 cm, then the volume of the gap between the two electrodes is $1.5x10^{-6}$ dm^3. The concentration of tBP in the electrolyte was 0.5 M, so a total of $7.5x10^{-7}$ mol should have been added into the cell. Analysis of the photocurrent map for W5 shows that the loss in photocurrent around the holes happens over 2.3 % of the total cell area. Based on dye coverage results described in appendix A, the total dye coverage is taken as $1.22x10^{-4}$ $molcm^{-3}$. This means that, assuming all dye molecules are desorbed in the areas in question, $2x10^{-9}$ mol of dye were desorbed (the actual value will be slightly lower as not all the dye was desorbed in these areas). This would mean that for the solution to be completely depleted of tBP by the edge of the low photocurrent areas, 375 tBP molecules would need to be adsorbed for each desorption of one dye molecule. It seems unlikely that this many tBP molecules could adsorb in the place of one dye molecule. However, for the effect observed to occur, the solution does not need to be depleted of tBP, rather the pH needs to decrease to the point where the dye binding equilibrium constant is higher than that for tBP. It is shown in chapter 7 that the pH for an electrolyte containing 0.5 M tBP is 6.85 but without tBP is 5.43, corresponding to a difference in $[H^+]$ of $3.574x10^{-6}$ M. If it is assumed that $[H^+]$ changes linearly in this regime with tBP concentration, then this means that $1.4x10^5$ mol of tBP are required to increase the amount of H^+ in solution by 1 mol. If 375 molecules of tBP are adsorbed per desorbed dye molecule then the pH will drop to 5.43. However, it is more realistic that only a few tBP molecules of tBP will adsorb per desorbed dye molecule. If it is assumed that 3 tBP molecules adsorb per desorbed dye molecule, then the bulk pH is calculated to change to 6.77. Without knowing the precise dependence of dye binding on pH, it is difficult to say if this is a large enough drop to stop the dye desorption seen further from the filling hole. However, this seems to be a very small change and it is suggested that additional factors may also be important in

producing the increased dye desorption near to the filling hole. One example of this would be if the high flow rate of electrolyte near the hole compared to in other points in the film increased the rate of dye desorption. It is noted that the phenomenon of dye desorption near to the filling holes does not appear clearly in all of the water cells in this chapter though it has been observed in some cases in other water cells. This suggests that the precise electrolyte makeup or filling process may have an effect on the dye desorption observed, and may indicate that only a small difference in pH can produce this effect. An experiment examining the effect of changing the flow rate of electrolyte addition could shed further light on this process.

5.4 Conclusions

It can be concluded that the lower efficiency of water based DSSC is at least partially due to dye instability with dye desorption occurring close to the filling holes even when using the hydrophobic dye Z907. The development of efficient water stable dyes may be an effective way to increase the solar conversion efficiencies of water based DSSCs. Finding an alternative for tBP which increases V_{OC} without causing dye desorption seems to also be important.

By measuring both photocurrent maps and transmission maps it has been possible to decouple dye and film thickness effects from variations caused by electrolyte across the DSSC surface. It has also been seen that an aqueous electrolyte filling method which involves heating the cell while under vacuum leads to improved electrolyte filling.

Finally the majority of DSSC are characterized by reporting photocurrents and efficiencies that are an average from the whole cell area; the results reported here show that the non-homogeneity of cell photocurrents must be taken into account when optimizing cells. It is also apparent that there are often differences between cells made in a similar way.

It is noted that a significant proportion of the work presented in this chapter has been published in reference [7].

5.5 References

(1) Scott, M. J.; Woodhouse, M.; Parkinson, B. A.; Elliott, C. M. *J Electrochem Soc* **2008**, *155*, B290.

(2) Macht, B.; Turrion, M.; Barkschat, A.; Salvador, P.; Ellmer, K.; Tributsch, H. *Sol. Energy Mater. Sol. Cells* **2002**, *73*, 163.

(3) Barkschat, A.; Moehl, T.; Macht, B.; Tributsch, H. *Int J Photoenergy* **2008**.

(4) Listorti, A.; Creager, C.; Sommeling, P.; Kroon, J.; Palomares, E.; Fornelli, A.; Breen, B.; Barnes, P. R. F.; Durrant, J. R.; Law, C.; O'Regan, B. *Energ Environ Sci* **2011**, *4*, 3494.

(5) Miettunen, K.; Halme, J.; Lund, P. *Electrochem Commun* **2009**, *11*, 25.

(6) Boschloo, G.; Haggman, L.; Hagfeldt, A. *J Phys Chem B* **2006**, *110*, 13144.

(7) Risbridger, T. A. G.; Castro, F. A.; Cameron, P. J. *The Journal of Physical Chemistry C* **2012**, *116*, 22253.

Chapter 6: Comparing dye sensitized solar cells made with aqueous and acetonitrile-based electrolytes

6.1 Introduction
6.2 Results
    6.2.1 Electrochemical Impedance Spectroscopy: Relative conduction band position estimation
        6.2.1.1 Conductivity
        6.2.1.2 Chemical capacitance
    6.2.2 Electrochemical Impedance Spectroscopy: Counter electrode charge transfer
    6.2.3 Electron lifetime
    6.2.4 Cell non-ideality
    6.2.5 Iodide concentration variation
    6.2.6 Electron diffusion length
6.3 Conclusions
6.4 References

6.1 Introduction

The production of DSSCs has commonly utilised electrolytes that have an organic liquid such as acetonitrile[1] or 3-methoxypropionitrile[1a,2] as the solvent as discussed in chapter 1. In order to gain a better understanding of aqueous DSSCs it is useful to compare them to such a system which is known to show good performance. In this chapter, cells made using acetonitrile/valeronitrile and aqueous electrolytes are compared. Energy levels, electron trap distributions and electron lifetimes are examined as is the non-ideality factor. The effect of I^- concentration is examined in terms of Nernst potentials and cell response. Electron diffusion length is also discussed.

It is seen that aqueous DSSCs produce a lower photocurrent compared to acetonitrile cells but a similar photovoltage. It is found that conduction band positions are unchanged between cells made with the two different solvents and that the electron trap distribution is also similar. Evidence is seen suggesting that the measured E(I_3^-/I^-) values may be different to the actual values and that results make the most sense if it is assumed that E(I_3^-/I^-) is the same in both solvents. Cell non-ideality is found to be similar regardless of the electrolyte solvent, suggesting that non-ideality is not due to surface states but rather to fundamental properties of the semiconductor. It is observed that increasing the concentration of the I^- source results in a decrease in V_{OC} which is most strongly influenced by the change in the Nernst potential of the redox couple. Lower concentrations of I^- resulted in improved V_{OC} but problems with phase separation prevented concentrations below 2M being used. Similarities in electron diffusion length suggest that the electron collection efficiency is unchanged by the solvent.

6.2 Results

In order to examine the effect of solvent on cell parameters, several sets of cells were fabricated differing only in terms of the electrolyte solvent used; acetonitrile/valeronitrile or water. Cells were dyed with Z907 and the standard electrolyte contained 2M PMII, 0.1M GSCN, 0.5M tBP and 0.05M I_2 unless stated otherwise. An example of a simple IV curve comparison between cells produced that differ only in electrolyte solvent is shown in Fig 6.1.

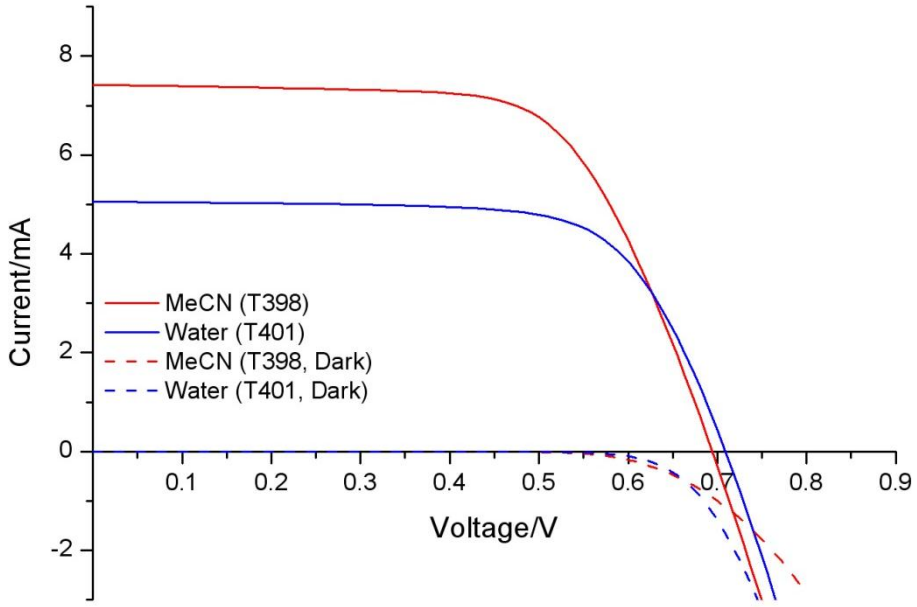

Fig 6.1 IV curves measured under 1 sun AM1.5 illumination for cells dyed with 0.3mM Z907 filled with electrolyte containing 2M PMII, 0.1M GSCN, 0.5M tBP and 0.05M I_2. T398 uses 85:15 acetonitrile:valeronitrile solvent, T401 uses water and 1vol% Triton X-100. T398 η = 3.4%, T401 η = 2.5%.

The main difference observed is that the short circuit current production is higher in the acetonitrile cell; the other IV parameters are similar. The dark current onset is in a similar position for both cells. This suggests that the main differences between aqueous and acetonitrile cells are linked to the light generated current. It is noted that in most cases the cells produced were made with electrolytes that optimized the water cell performance, such as high PMII concentration. These were not optimum conditions for the acetonitrile cells so comparison cells were generally not as efficient as would otherwise be expected. Optimized 1 cm^2 acetonitrile cells made alongside the comparison cells produce efficiencies of up to 5% (Fig 4.1).

Two other cells designated T183 (MeCN) and T201 (Water) were analyzed in detail and IV characteristics for these are recorded in table 6.1. These two cells were optimized towards their respective electrolyte solvent and so PMII concentration is higher in the water cell T201 (2M PMII) than in the acetonitrile cell T183 (0.6M PMII). The effect of PMII concentration is considered in more detail in section 6.2.5. IPCE measurements taken with no bias light for these cells are shown in Fig 6.2; these show similarity between the two systems, though the photocurrent onset is at a slightly lower energy in water which may correspond to small shifts in the energy levels in the dye likely due to differences in solvent stabilization.

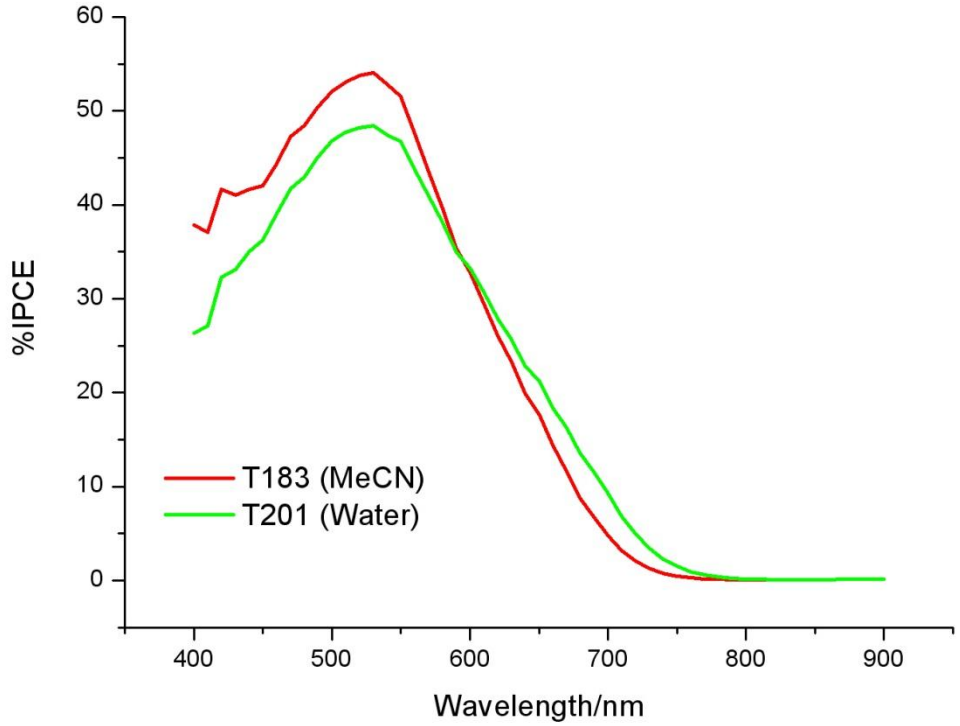

Fig 6.2 IPCE spectra for cells T183 (acetonitrile/valeronitrile) and T201 (water). Cells dyed with 0.3mM Z907, electrolyte contained 0.1M GSCN, 0.5M tBP, 0.05M I_2 and 0.6M (acetonitrile/valeronitrile, T183) or 2M (water, T201) PMII.

Table 6.1: IV performance summary for an acetonitrile and water based cell.

Cell	**J_{SC}/mAcm^{-2}**	**V_{OC}**	**FF**	**Efficiency (%)**
T183 (MeCN)	10.8	0.753	0.67	3.8
T201 (Water)	8.2	0.667	0.55	3.0

6.2.1 Electrochemical Impedance Spectroscopy: Relative conduction band position estimation

Electrochemical Impedance Spectroscopy (EIS) has often been used in the analysis of DSSCs. As described in section 2.6.3.1, a number of parameters can be determined relating to electron transfer and transport as well as capacitance information relating to charge storage. In this section measurements are taken which are used to estimate the relative conduction band position and relative electron trap distributions (g(E)) in different electrolyte solvents. Examples of raw EIS data are shown in appendix E.

6.2.1.1 Conductivity

Measurements of conductivity (σ_n) based on charge transport resistance (R_{trans}) can be made and used to estimate relative conduction band positions. Conductivity can be calculated from impedance data using equation 6.1

$$\sigma_n = \frac{L}{A(1-p)R_{trans}} \quad \text{Equation 6.1}$$

where L is film thickness, A is film area, p is porosity and R_{trans} is charge transport resistance[3]. In this case, L was set as 10 μm for each film and p was 0.5. Bisquert et al show that, assuming constant electron mobility for free electrons in the conduction band with respect to potential, this conductivity depends only on the number of free electrons (n_c) according to the expression[4]

$$\sigma_n = \frac{q^2}{k_B T} n_c D_0 \qquad \text{Equation 6.2}$$

where q is the elementary charge, k_B the Boltzmann constant, T the temperature and D_0 the diffusion coefficient of free electrons. Based on the relationship between free electrons, conduction band (free electron) states (N_C) and the difference between Fermi energy (E_F) and the conduction band position (E_C),

$$n_c = N_C \exp\left(\frac{E_F - E_C}{k_B T}\right) \quad \text{Equation 6.3}$$

conductivity can be described by

$$\sigma_n = \sigma_0 \exp\left(\frac{E_F - E_C}{k_B T}\right) \quad \text{Equation 6.4}$$

where σ_0 is a constant[3]. As a result, it is possible to estimate the relative position of the conduction band edge by comparing absolute Fermi energy at a set conductivity value, assuming similar free electron state distributions.

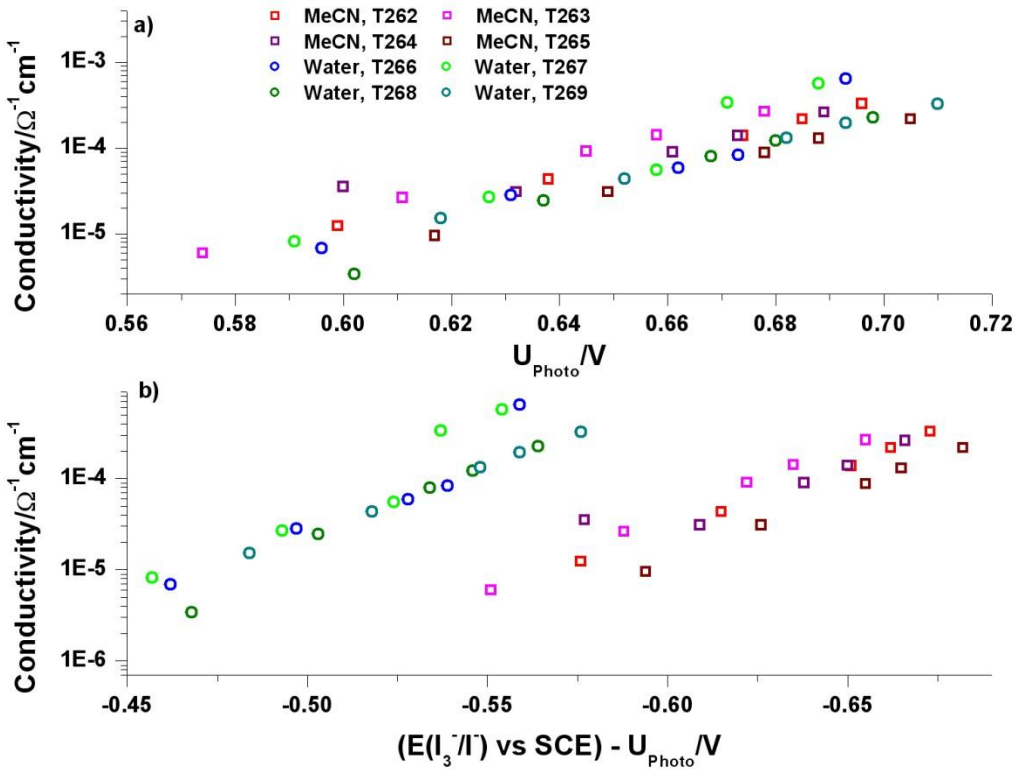

Fig 6.3 Conductivity vs a) voltage and b) nE_F as calculated in equation 6.6 for several cells containing water or acetonitrile/valeronitrile based electrolyte. Data points calculated using equation 6.1 from charge transport resistance determined by EIS, cell thickness was 10 µm, porosity was 0.5.

Fig 6.3 shows conductivity data as a function of cell voltage and of quasi electron Fermi level (nE_F). Applying the above analysis indicates that the CB is 100mV more positive in water than in acetonitrile. However, it can be seen in table 6.2 that the V_{OC} does not alter significantly between the two types of cells. Such a change in CB would be expected to cause at least some constant change in nE_F and subsequently cell voltage between the two types of cells unless the reaction between electrons in TiO_2 and I_3^- altered in a manner that produced an equal and opposite change in nE_F; this seems highly unlikely. The value of nE_F is determined based on equation 6.5 & 6.6 (showing electron quasi Fermi energy in terms of energy (6.5) and in terms of potential (6.6))

$$nE_F = E_{F,\mathrm{Redox}} + qU_{Photo} \quad \text{Equation 6.5}$$

$$\frac{nE_F}{q} = E(\mathrm{I_3^-/I^-}) - U_{Photo}$$ Equation 6.6

where $E_{F,Redox}$ is the Fermi energy in the dark and equal to the redox potential, U_{Photo} is the photovoltage (equivalent to V_{OC}) and $E(\mathrm{I_3^-/I^-})$ is the redox potential of the I_3^-/$\mathrm{I^-}$ redox couple. For the standard electrolyte used containing 2M PMII, the measured redox potential of I_3^-/$\mathrm{I^-}$ is 0.017V vs SCE in acetonitrile and 0.122V vs SCE in water. These values are similar to those recorded by Law et al[5] for a similar system where the solvents MPN and water were used (which did not appear to take the liquid junction potential into account). In addition, the liquid junction potential (LJP) expected at the MeCN|Water interface in the reference electrode frit when measuring species in acetonitrile with an aqueous reference electrode has been found to be between 40mV[6] and 100mV[7]. If such a difference is correct, it would mean that the actual difference in redox potential between the two solvents is between 145-205mV, which would be expected to have a significant effect on nE_F. It seems exceedingly unlikely that such a difference would not result in some variation in the photovoltage. Furthermore, the solvent is not directly involved in the reduction of I_3^- to $\mathrm{I^-}$ at the counter electrode. Therefore the only reason the potential of the redox couple might be expected to change is if the solubility of the species in the different solvents was large enough to significantly change the concentration of the oxidised and reduced species in solution, altering the potential according to the Nernst equation. Based on equilibrium constants for the equilibrium $I_2 + I^- \rightleftharpoons I_3^-$ in the two solvents and the subsequent calculated concentrations of I_3^- and $\mathrm{I^-}$, the expected changes in the Nernst potential from the standard potential were calculated (Appendix B & C) and found to be 92.1mV in acetonitrile and 91.7mV in water.

In light of these arguments it is unlikely that the measured difference in the redox potential between the two solvents is due to real variation in the redox potential. Measurement of the LJP is difficult and has not been done in this work. However it is possible that in the relatively complicated electrolyte system used, a LJP different to that recorded in the above papers is found at the reference electrode frit, particularly as there were often miscibility problems between the different electrolyte components in water. However, a full reason as to why such a

probable discrepancy between the measured redox potential and the actual redox potential occurred is not known and a study seeking to understand this further would be a useful continuation of this work. From hereon the redox potential is assumed to be the same in both solvents. This means that the voltage difference between cells measured in the two solvents is equivalent to the nE_F difference between the cells.

Analysis of the conductivity data using this assumption is shown in Fig 6.3a and shows that the position of the CB does not alter for cells made using the two different solvents.

Table 6.2 IV characteristics measured under 1 sun AM1.5 illumination for cells T262 – T269 dyed in 0.3mM Z907 filled with standard electrolyte containing 2M PMII and acetonitrile/valeronitrile or aqueous solvent.

Cell T26# (Solvent)	J_{SC}/mA	V_{OC}/V	FF	η/%
2 (MeCN)	7.9	0.690	0.73	4.0
3 (MeCN)	6.5	0.673	0.73	3.2
4 (MeCN)	6.2	0.679	0.72	3.0
5 (MeCN)	6.2	0.679	0.72	3.0
6 (Water)	3.8	0.664	0.74	1.9
7 (Water)	5.9	0.669	0.74	2.9
8 (Water)	5.8	0.682	0.73	2.9
9 (Water)	5.0	0.694	0.75	2.6

6.2.1.2 Chemical capacitance

The chemical capacitance c_μ of a cell can be determined as a function of cell potential by altering the illumination intensity when measuring an impedance response and is expected to describe the exponential trap distribution g(E) below the conduction band as a function of potential[3] according to equation 6.7

$$c_\mu^{traps} = q^2 \int_{-\infty}^{E_{Fn}} \frac{dg}{dE} = q^2 g(E_{Fn}) \quad \text{Equation 6.7}$$

where E_{Fn} is the Fermi energy. It has been shown previously that three regions can be expected in a plot of capacitance versus potential which will be dominated by different capacitances[3]. At low potentials capacitances due to the blocking layer and counter electrode have the greatest effect and result in a low gradient. Intermediate potentials give the highest gradient and are dominated by the chemical capacitance. At very high potentials the capacitance tends to the Helmholtz capacitance at the semiconductor|electrolyte interface.

The data shown in Fig 6.4 matches with that expected for chemical capacitance, showing an exponential variation with potential in both cells, matching the expected build up of charge with potential. When voltage is plotted as a function of capacitance there is no offset between the two plots and the gradient is the same. When assuming the redox potential is the same in both solvents as discussed above, this implies that the trap distribution g(E) is very similar for both solvents.

It was shown in Table 6.1 that for the cells measured in Fig 6.4 there was however a significant voltage difference. This is discussed below in section 6.2.5 and is explained as largely due to the effect of the difference in PMII concentration between the two cells on the redox potential rather than any relative shift in g(E) between the two types of cells.

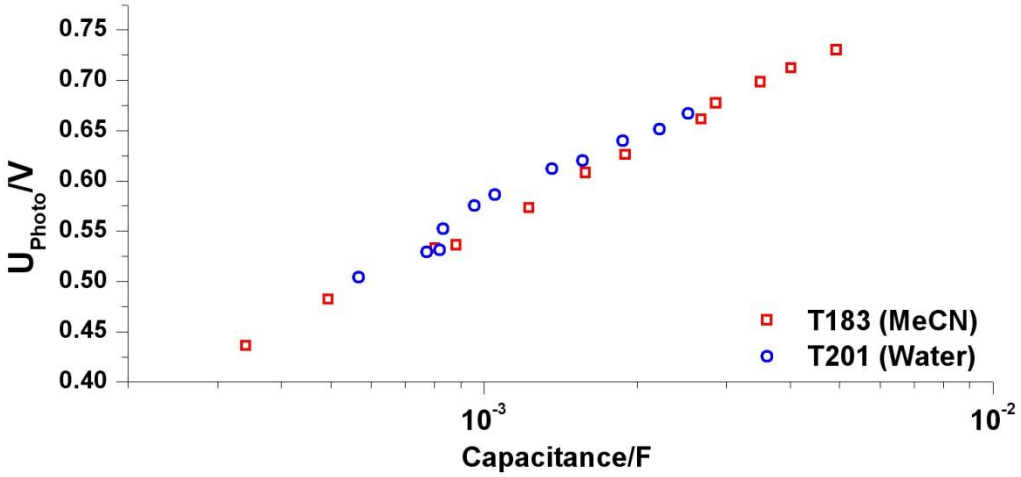

Fig 6.4 Voltage vs capacitance measured by EIS for cells containing acetonitrile (0.6M PMII) and water (2M PMII) based electrolyte. Showing logarithmic increase in capacitance with Fermi energy for acetonitrile and water cell. Exponential change strongly suggests that data points in this potential range are dominated by chemical capacitance.

Similarities in the shape of g(E) between cells made with the two different solvents are also implied based on the values of characteristic temperature T_c obtained in the analysis of open circuit voltage decay behaviour. In acetonitrile, T_c was found to be 749K whereas in water a value of 714 K was recorded. However, there was some variation between cells for both solvents.

6.2.2 Electrochemical Impedance Spectroscopy: Counter electrode charge transfer

It is possible that there would be some change in the rate at which the reaction between I_3^- and e^-_{Pt} occurs at the counter electrode for cells made with different solvents. The most likely reason this would occur is not based on the solvent itself but on the slight change in additives i.e. the use of Triton X-100 in aqueous cells. This is a reasonably large polymeric molecule (Fig 4.7) which could slow down electron transfer if it is strongly adsorbed onto the platinum cathode. Fig 6.5 shows the resistance to charge transfer at the counter electrode (R_{Pt}) based on EIS measurements for cells at a number of PMII concentrations. R_{Pt} is very low and is the same between water and acetonitrile within error. This implies that the reaction at the counter electrode is not effected by the change in solvent or use of Triton X-100.

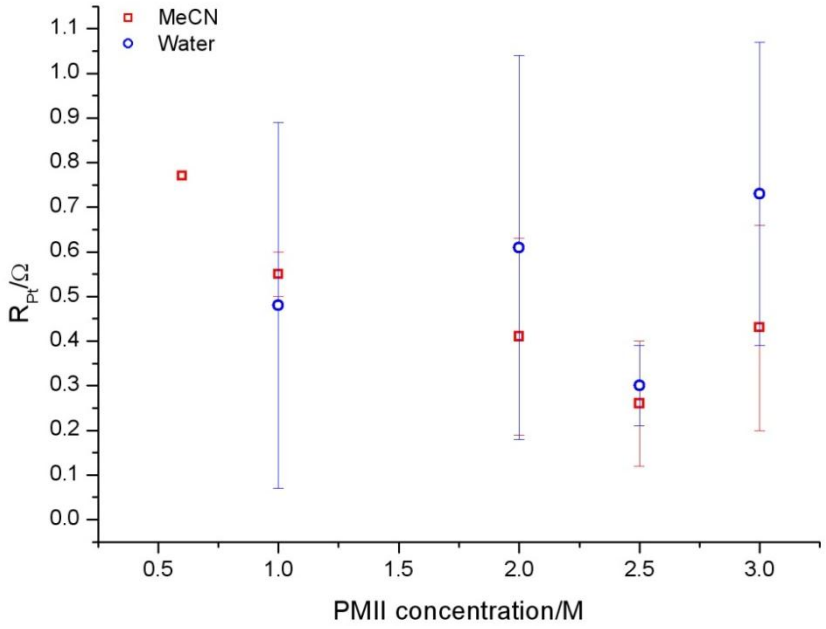

Fig 6.5 Effect of solvent and PMII concentration in the electrolyte on charge transfer at the counter electrode of Z907 cells based on fitting of EIS data to DSSC model. Cells contained 0.1M GSCN, 0.5M tBP, 0.05M I_2 and in the water cells 1% Triton-X100.

6.2.3 Electron lifetime

The extent to which recombination losses at the semiconductor or substrate interface occur will affect the performance of a DSSC. Electron lifetime (τ_0) data gives an indication of the degree to which loss mechanisms are occurring by indicating how long an injected electron will remain in the semiconductor before it is lost via recombination with D^+ or I_3^-. In this work the effective electron lifetime (τ_n) is measured using either open circuit voltage decay (OCVD) or intensity modulated photovoltage spectroscopy (IMVS) and good agreement was seen between the two techniques.

As described in the theory section, the rate of the back reaction between electrons in the semiconductor and I_3^- in the electrolyte follows the rate law shown in equation 6.8

$$Rate_{br} = k_{br} n[I_3^-] \quad \text{Equation 6.8}$$

where k_{br} is the reaction rate constant and n is the number of free electrons[8]. Reaction order with respect to free electrons is not usually one as shown in non-ideality plots in section 6.2.4, probably because electron transfer is not only from the conduction band[9]. Equation 6.8 shows that at higher free electron densities, the rate of the back reaction will be faster assuming the same $[I_3^-]$. In order to be able to compare between systems, it is therefore important to plot τ_n as a function of electron density. Electron density was not able to be obtained in this work; however based on the analysis described above useful comparisons can still be made from lifetime data as a function of voltage according to the following argument. In previous sections it has been concluded that the position of the CB does not change substantially when changing from acetonitrile to water. Furthermore, it has been seen that the trapped electron distribution g(E) is similar in cells made with both solvents. Due to the fast equilibrium between trapped and free electrons, nE_F corresponds to the highest energy filled trap state and so in this situation for a given cell voltage, the electron density will be the same in both types of cell.

Fig 6.6 shows the effective electron lifetime as a function of voltage measured using IMVS. It can be seen that cells made with both solvents show a very similar

response across the voltage range measured. The same similarity is observed for lifetime plots measured using OCVD (Fig 6.7). At high voltages the electron lifetime is low. This is because the electron density is high and because nE_F is high. This means that the activation energy (E_A) for excitation of trapped electrons to the conduction band is low so detrapping/trapping occurs more often. Therefore more free electrons are available for the reaction with I_3^-. As nE_F decreases and the charge density decreases, E_A increases and so the effective electron lifetime increases. The implication of the similarity in the plots for the different cell types is that the recombination behaviour is similar in cells made with both types of solvent. Altering the solvent in this way does not appear to significantly change the rate constant for the back reaction. Fig 6.8 shows the charge transfer resistance for the reaction between e^-_{TiO2} and I_3^- measured using EIS. It can be seen that the gradient of the plots is again similar, though they are separated by the difference in V_{OC}. As will be discussed below, this is probably due to the effect of PMII on the redox potential. On that basis this plot also shows that the rate of the reaction between e^-_{TiO2} and I_3^- as a function of free electron density also does not change significantly between the two types of cells.

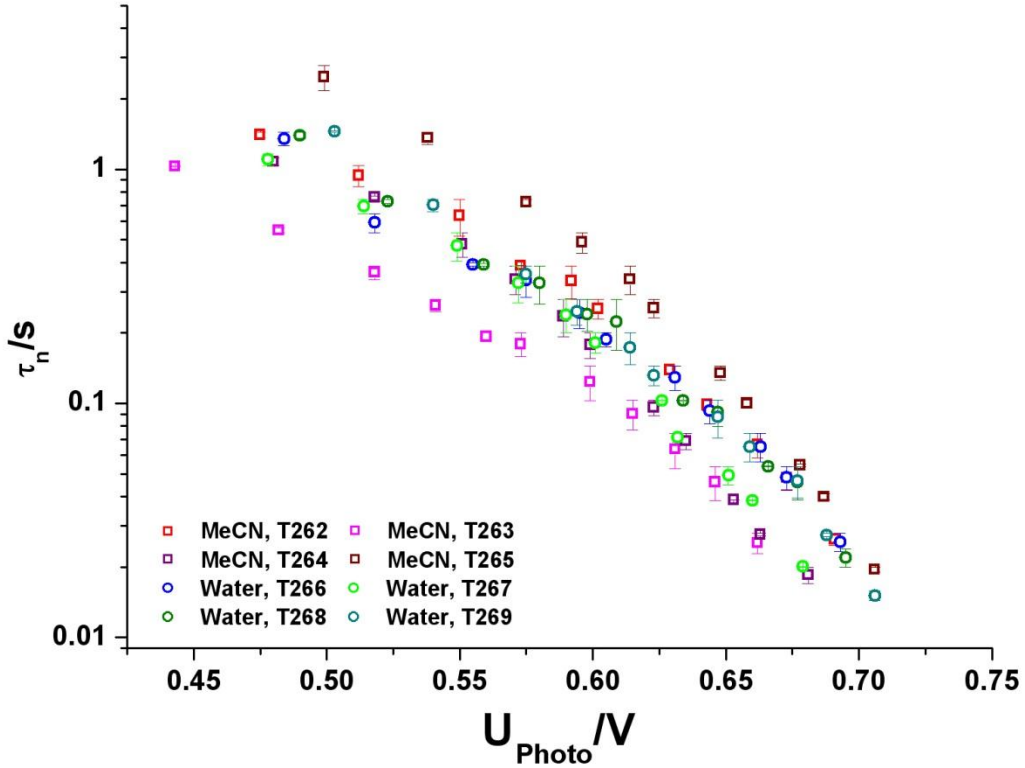

Fig 6.6 Comparing electron lifetime as a function of voltage for cells filled with electrolyte based on acetonitrile/valeronitrile (T262-265) and water (T266-269) solvents. Results taken from IMVS data. Error bars based on experimental uncertainty.

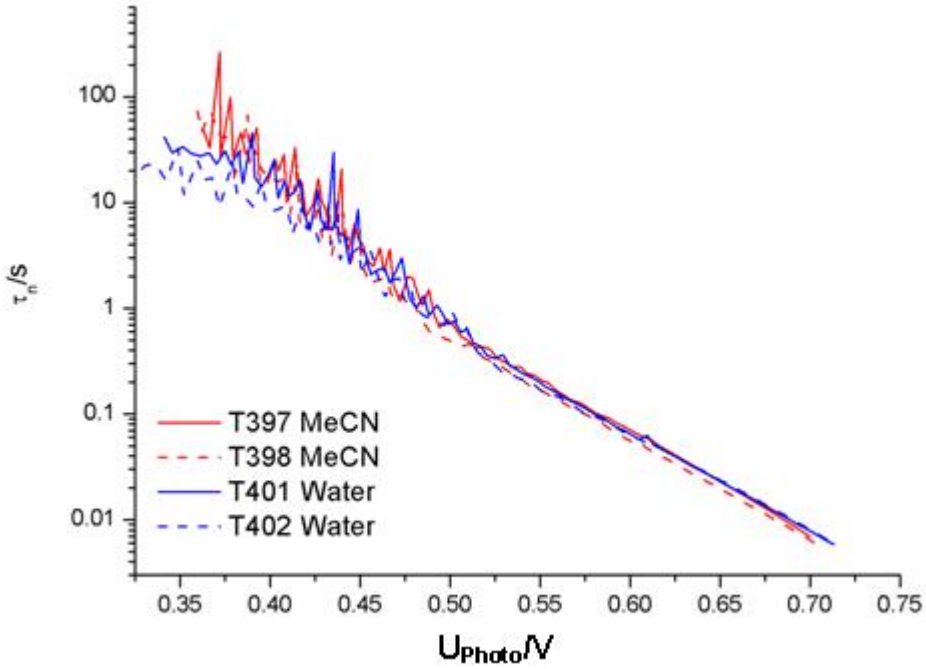

Fig 6.7 Comparison of electron lifetime as a function of photovoltage between Z907 cells filled with acetonitrile and water based electrolytes. Dashed lines are for replicate cells. Data calculated from OCVD. Experimental noise seen at lower voltages.

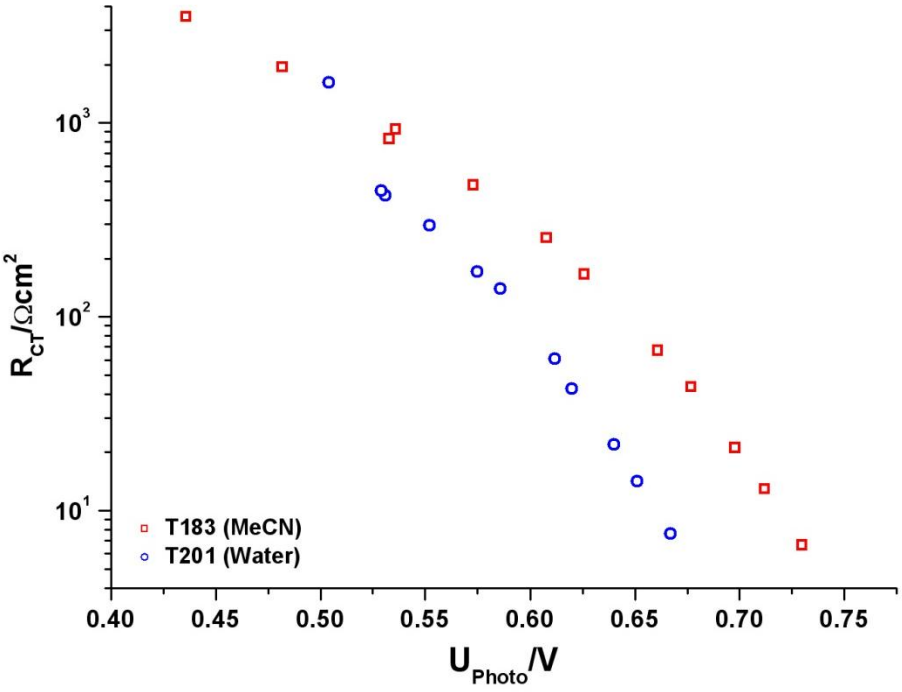

Fig 6.8 Charge transfer resistance measured using EIS for Z907 cells containing acetonitrile/valeronitrile (T183) and water (T201) as electrolyte solvent. Raw EIS data fitted using DSSC equivalent circuit model and plotted as a function of voltage.

6.2.4 Cell non-ideality

DSSCs have nearly always been observed to show non-ideal behaviour in terms of photovoltage response to light intensity. Based on Boltzmann statistics for free electron concentration, electron recombination from the conduction band to species in the electrolyte is expected to follow equation 6.9 with a non-ideality factor (m) of 1

$$\frac{dU_{Photo}}{d\log I_0} = \frac{2.303 m k_B T}{q} \qquad \text{Equation 6.9}$$

where k_B is the Boltzmann constant, T is temperature and q is the elementary charge. However, this is not usually observed, and non-ideality factors tend to be greater than 1[9-10], with values up to 2 being recorded[11]. One possible explanation is that electron recombination does not only occur via conduction band electrons. Salvador et al[12] observed several regions with different gradients in plots of photovoltage vs log light intensity when measuring dye cells. They explained this by suggesting that the state in which the reacting electron came from (CB state or one of two types of trap state), which was dependant on potential, altered the recombination properties. However, the effect was later shown by Cameron et al[13] to be due to reactions at the substrate when no TiO_2 blocking layer was present. In the case where such a blocking layer was present they showed that the non-ideality factor was constant over a wide illumination range (10^{12} - 10^{17} $cm^{-2}s^{-1}$).

The non-ideality values observed in Fig 6.9 are similarly constant over the measured illumination range. The non-ideality factor for both types of cell is 1.19, similar to that obtained in the work by Cameron et al[13] where the cell with a blocking layer gave a non-ideality factor of 1.25. The similarity between the two types of cell is of particular interest. Generally, recombination via some type of surface state is suggested as the reason for non-ideality[14]. However, it is unlikely that the surface of the TiO_2 will be the same for cells made with the two different solvents. Water is likely to adsorb onto the surface and higher proton concentration is likely to also make a difference. This suggests that the non-ideality is actually due to a property fundamental to the TiO_2 and not due to the surface. As seen in section 6.2.1.2 there is evidence that the distribution g(E) of

trap states is similar between the two solvents, which may suggest that the non-ideality is due to reaction of electrons in non-surface based trap states with I_3^- which could occur via electron tunnelling.

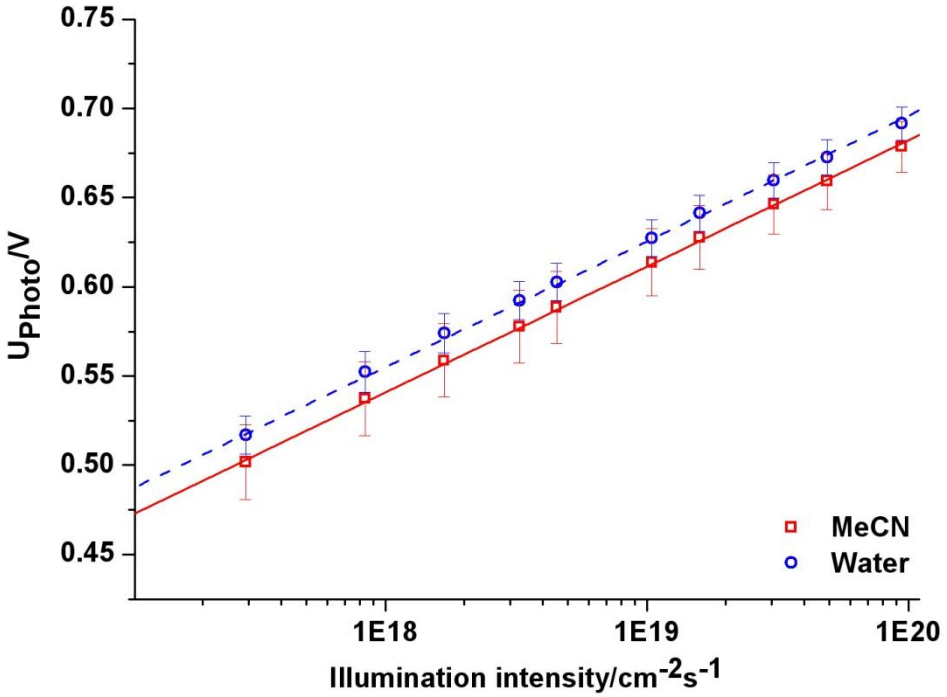

Fig 6.9 Open circuit voltage as a function of light intensity for cells dyed with 0.3mM Z907 and containing acetonitrile/valeronitrile (T262-T265) and water (T266-T269) as electrolyte solvent, PMII concentration 2M. For acetonitrile/valeronitrile cells: slope = 70.4 mV/decade, m = 1.2; for water cells: slope = 70.7 mV/decade, m = 1.2. Error bars based on n = 4 cells.

6.2.5 Iodide concentration variation

In previous sections, the change in the measured redox potential between the electrolytes made with acetonitrile or water has been discussed and it was suggested that the actual difference in redox potential between the two types of solvents was minimal. Presuming that this is indeed the case then results show that for cells made with otherwise identical electrolytes, the conduction band position remains at the same potential and recombination is similar resulting in the similar photovoltages obtained. However, when comparing cells made with different PMII concentrations there was a difference in V_{OC}. The effect of PMII concentration was examined to determine its effect on the cell performance and in an attempt to further optimize cell performance; the results of this are shown in this section.

Based on the Nernst equation, expected values for the redox potential of the I_3^-/I$^-$ couple were calculated and are compared to the actual measured values as a function of PMII concentration (fig 6.10). These calculations are based on literature equilibrium constants for similar I_2/I$^-$ concentrations and measured standard potentials from a simpler I_2/LiI system containing no additives (appendix C). To calculate these values it was assumed that the activity of the redox species was constant across the concentration range in question, however it is possible that at higher concentrations this was not the case. Actual E(I_3^-/I$^-$) values were measured potentiometrically in a two electrode setup vs Ag/AgCl using a platinum coated FTO slide as the working electrode. For both solvents, the values from the electrolyte used in the DSSCs are at significantly offset potentials compared to the calculated values. This may be due to differences between the simple electrolytes that standard potentials were based on, and the actual electrolytes used in measurements and cells. However, the gradient is very similar between the real and calculated cases, implying that the redox couple in the electrolyte follows Nernstian behaviour, with the redox potential dropping linearly with the exponential increase in PMII concentration.

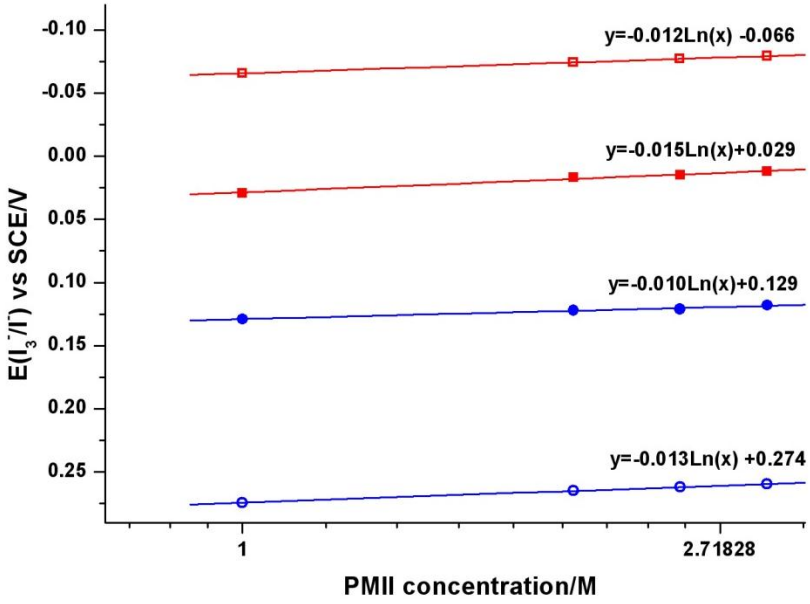

Fig 6.10 – Measured and calculated (appendix C) E(I_3^-/I$^-$) variation with PMII concentration within the electrolyte. Showing measured values for acetonitrile solvent (filled red squares), calculated values for acetonitrile solvent (open red squares), measured values for water solvent (filled blue circles) and calculated values for water solvent (open blue circles). Calculations are shown in appendix B & C.

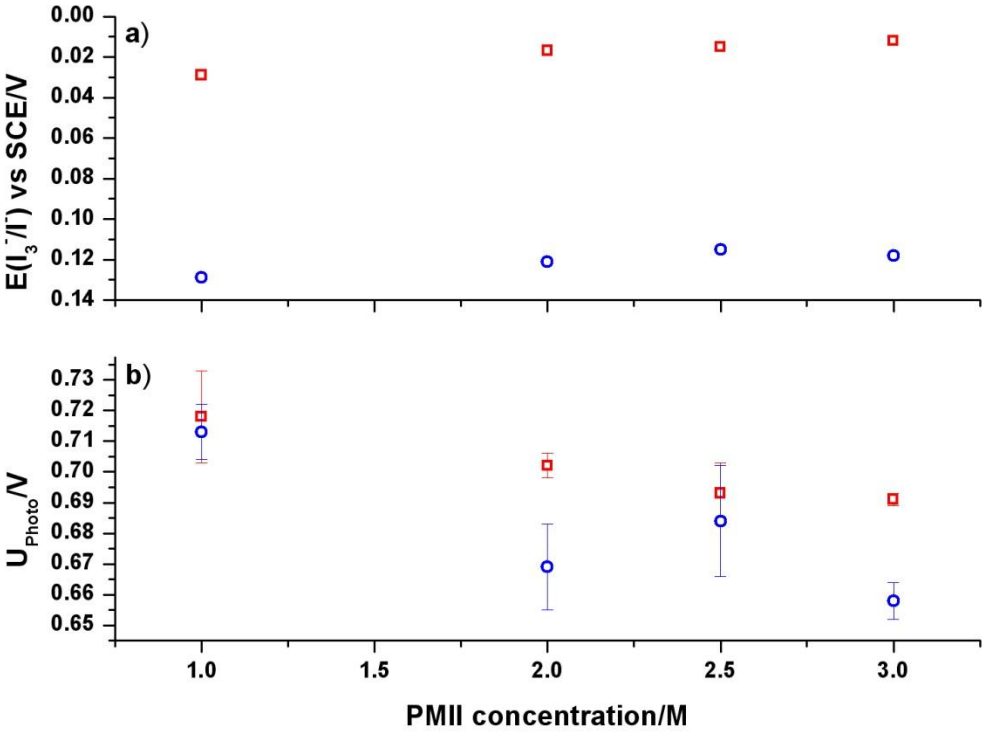

Fig 6.11 a) Measured redox potential, b) photovoltage under 1 sun AM1.5 illumination as a function of PMII concentration in the electrolyte. Red open squares are for acetonitrile solvent and blue open circles are for water solvent. When error bars are present, n=3.

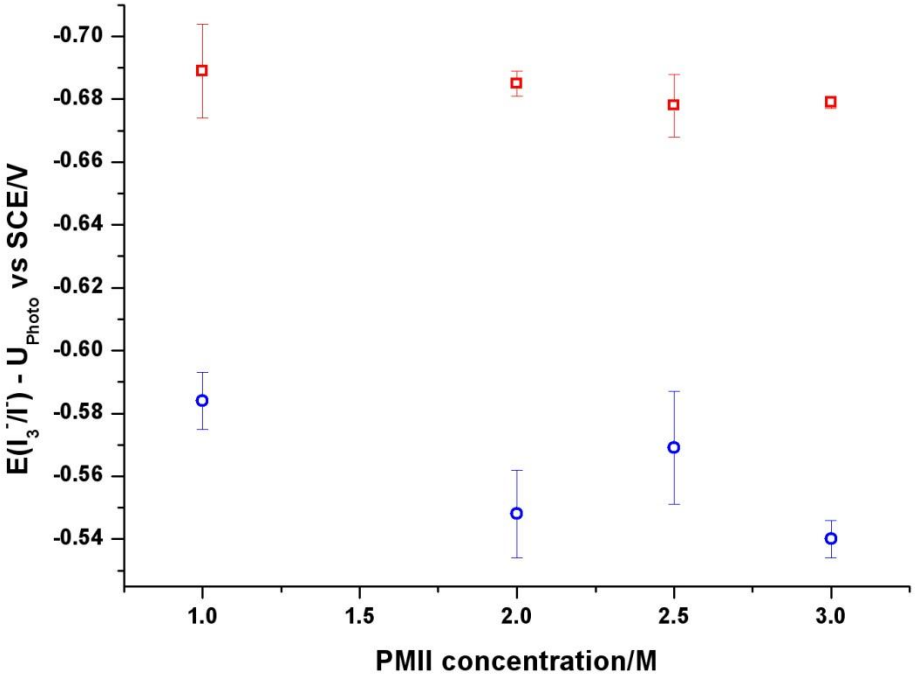

Fig 6.12 Fermi energy (calculated based on equation 6.6) as a function of PMII concentration for cells measured under AM1.5 1 sun illumination. Cells made with Z907 filled with electrolyte containing acetonitrile as solvent (Red open squares) and water as solvent (Blue open circles). Error bars are based on n=3 repeats.

Values of the measured redox potential, photovoltage and calculated nE_F are shown in fig 6.11 and 6.12 as a function of PMII concentration. As a result of the increasing energy of the redox potential and decreasing photovoltage, calculations show that the position of nE_F is only changed slightly with increasing PMII concentration in both water and acetonitrile. Over the concentration range 1.0 – 3.0 M examined nE_F drops by ~10 mV in MeCN and 40 mV in water. An explanation for this can be made by considering several parameters. Fig 6.13 shows a slight shift in the positions of the conductivity slopes as a function of PMII concentration that approximately follows the change in V_{OC} as described for the cells measured in table 6.3. The values are given as a function of nE_F as calculated from redox potential and V_{OC} data. Though the actual difference between the redox potential in the two different solvents may be minimal, within the same solvent it is expected that the redox potential change is real particularly as it follows the expected Nernst potential changes. This implies that there is a slight positive CB shift as PMII concentration increases.

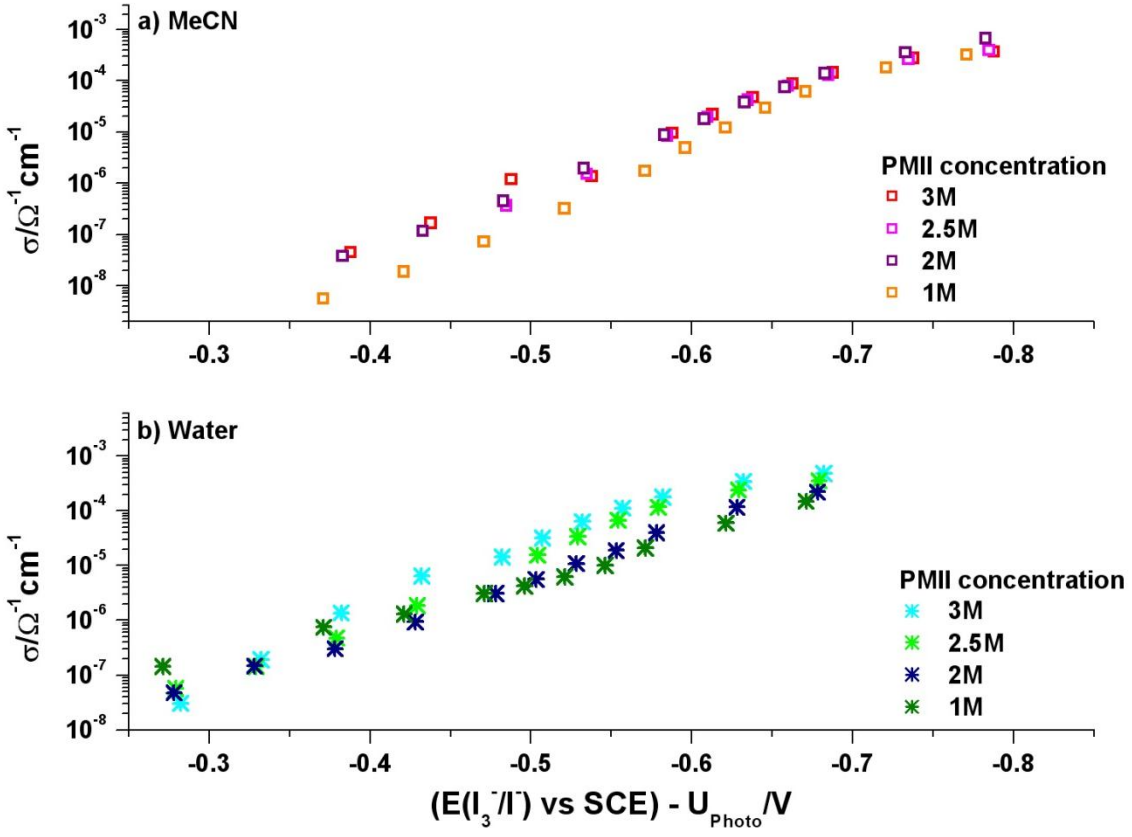

Fig 6.13 Conductivity vs nE_F for several water and acetonitrile/valeronitrile cells with varying PMII concentrations in the electrolyte. Cells made with Z907, electrolytes contain 0.1M GSCN, 0.5M tBP, 0.05M I_2 and 1%Triton-X100 in the water cells.

Table 6.3 Measured redox potential and V_{OC} (measured under 1 sun AM1.5 illumination) for cells containing 0.1M GSCN, 0.5M tBP, 0.05M I_2 and different concentrations of PMII in the aqueous or acetonitrile/valeronitrile electrolyte. Water cells also contained 1% Triton-X100.

Cell Solvent/PMII concentration/M	Measured redox potential vs SCE/V	Voc/V
MeCN / 3	0.012	0.701
MeCN / 2.5	0.015	0.695
MeCN / 2	0.017	0.706
MeCN / 1	0.029	0.727
Water / 3	0.118	0.663
Water / 2.5	0.121	0.693
Water / 2	0.122	0.68
Water / 1	0.129	0.714

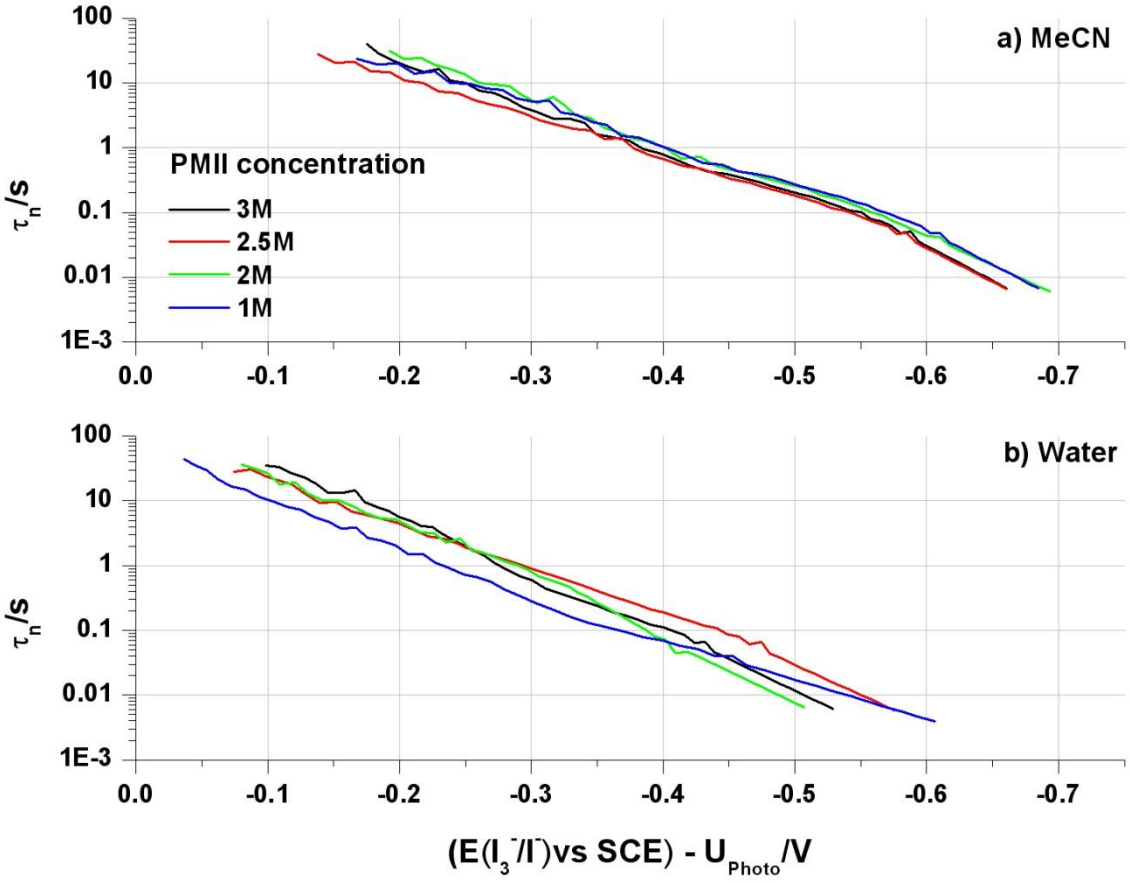

Fig 6.14 Electron lifetime vs nE_F (calculated from equation 6.6) at various PMII concentrations for cells containing 0.1M GSCN, 0.5M tBP and 0.05M I_2 based on a) acetonitrile/valeronitrile, b) water as solvent. Water cells also contained 1% Triton-X100.

Fig 6.14 shows that the electron lifetime dependence on nE_F does not appreciably change as a function of PMII concentration and Fig 6.15 shows no change in the ideality factor as a function of PMII, implying that the electron distribution and recombination do not change at different PMII concentrations. This suggests that the main change in V_{OC} is caused by the change in the redox potential though a slight shift in CB may occur as well. In these results and some of those below (e.g. Fig 6.16 & 6.17) a shift in voltage of ~40 mV is seen for a difference in PMII concentration of 1.4 M (between 0.6M and 2M in acetonitrile). This is the same difference in PMII concentration as that between the cells T183 and T201 made with different solvents for which a difference in V_{OC} of 86mV was observed. This confirms that the difference in redox potential is a large part of the reason for the difference in potential between the two cells.

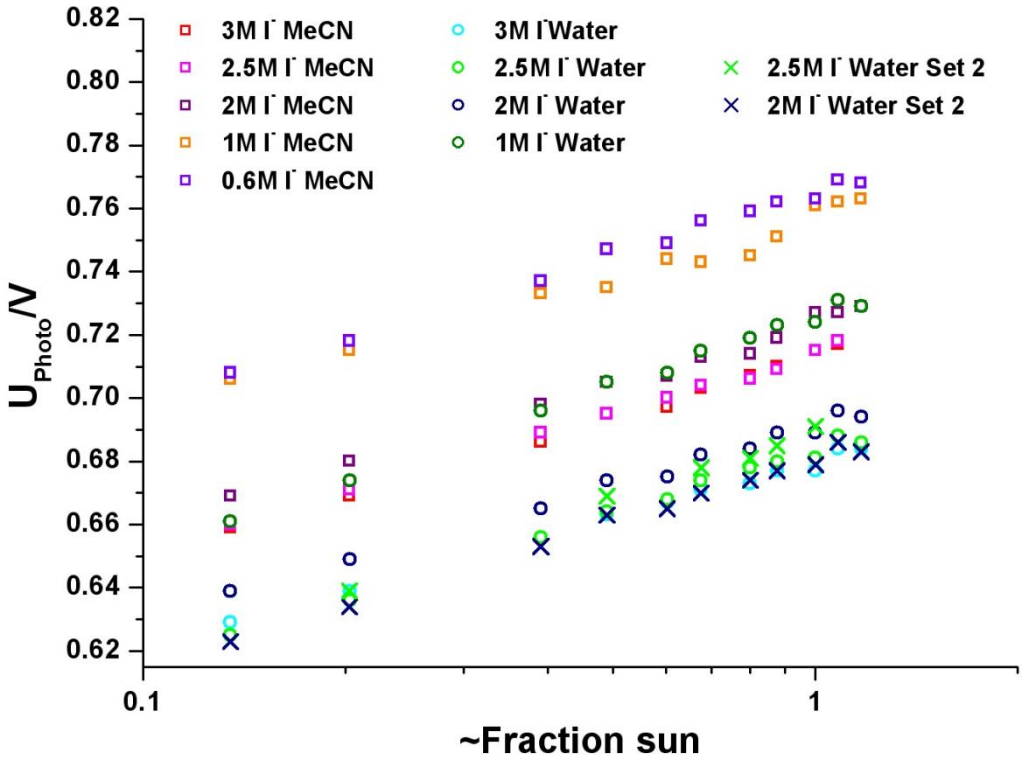

Fig 6.15 Ideality for Z907 cells containing acetonitrile or water based electrolyte with varying quantities of PMII (T322-T353) along with 0.1M GSCN, 0.5M tBP and 0.05M I_2. Water cells also contained 1% Triton-X100.

In terms of the cell performance, photovoltage is the main parameter changed by the variation in PMII concentration as shown in Fig 6.16 & 6.17. The short circuit current remains approximately constant, as do the fill factor and efficiency. In acetonitrile, the short circuit current is slightly higher at low PMII concentrations,

and as the voltage is also higher it seems that this lower concentration should be used to achieve the best cell performance. In water cells the voltage is also highest at low PMII concentrations largely related to the redox potential as discussed above. However, for the aqueous electrolyte system used significant problems relating to phase separation become apparent at low concentration, making this improvement route difficult to implement. The voltage produced is lowest at high PMII concentrations and it was also observed that after a certain period large crystals of an unknown material were formed in the stored electrolyte solutions. These are both reasons why a high PMII concentration should not be used, though phase separation was less of a problem. As such, 2M PMII has generally been used as the optimum concentration for water cells. It is useful to note from this that the V_{OC} can be adjusted by changing the I^- concentration.

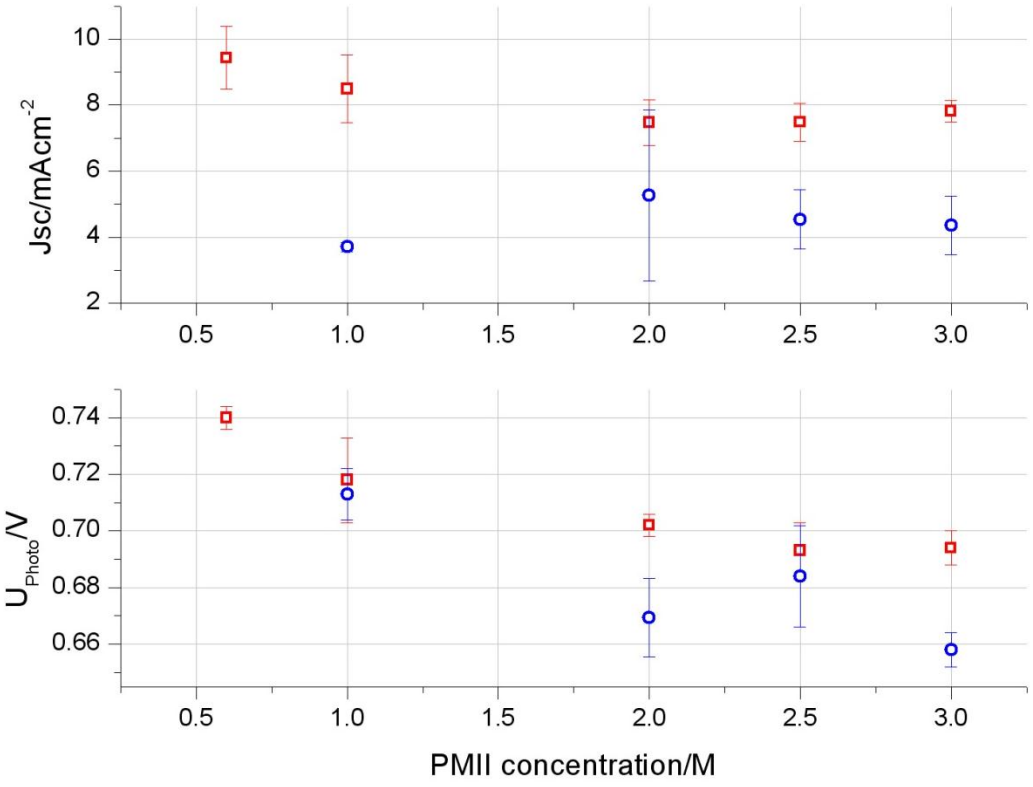

Fig 6.16 Cell performance summary for cells measured under AM1.5 1 sun illumination; Jsc and Voltage as a function of PMII concentration for cells filled with standard electrolyte containing acetonitrile solvent (red open squares) or water solvent (blue open circles). Error bars based on n=3 repeats.

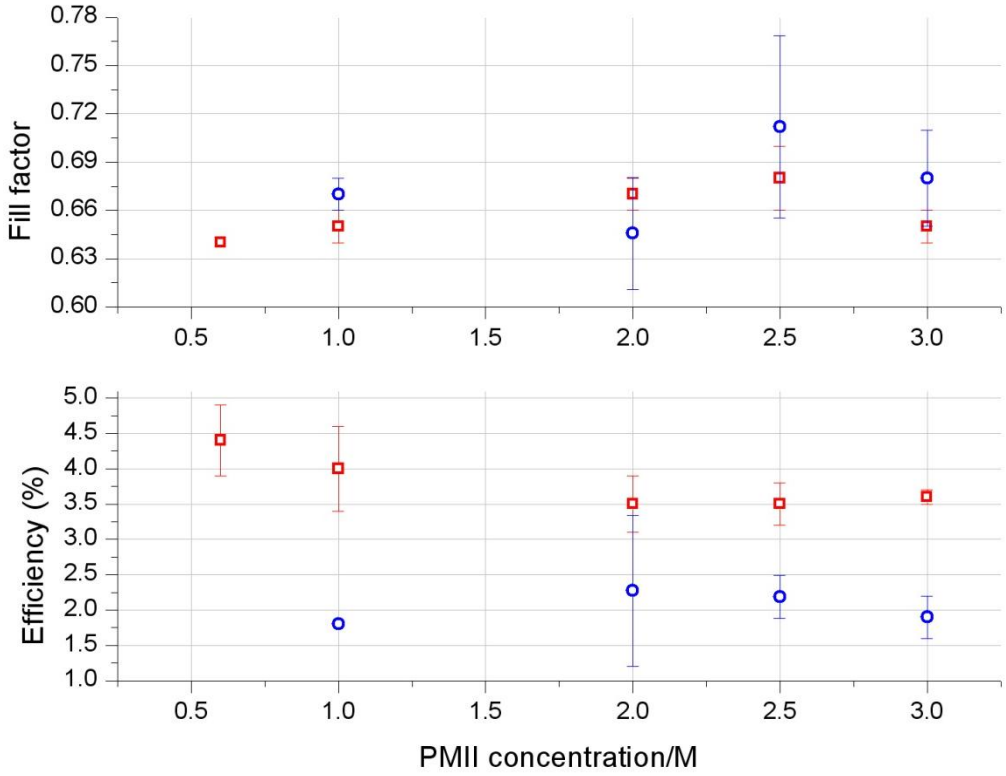

Fig 6.17 Cell performance summary for cells measured under AM1.5 1 sun illumination; Fill factor and efficiency as a function of PMII concentration for cells filled with standard electrolyte containing acetonitrile solvent (red open squares) or water solvent (blue open circles). Error bars based on n=3 repeats.

6.2.6 Electron diffusion length

Electron diffusion length (L_n) is a property based on the ability of the semiconductor to transport charge effectively without losses and can give an indication of the electron collection efficiency (η_{col}). The results presented here are calculated from EIS measurements based on the following relationship[3]

$$\frac{L_n}{d} = \left(\frac{R_{CT}}{R_{trans}} \right)^{1/2} \quad \text{Equation 6.10}$$

where R_{CT} is the charge transfer resistance at the semiconductor included in the distributed element in the DSSC model (Section 2.6.3.1.1), R_{trans} is the transport resistance in the same element and d is the film thickness. Results are shown as the ratio L_n/d so normalised for film thickness.

Fig 6.18 shows relatively similar trends for cells made using the two different solvents though the L_n/d ratio is low. This suggests that electron collection is similar for cells made with both types of solvent when the electrolyte has otherwise the same composition. This implies that the solvent does not greatly interfere or alter loss or transport mechanisms (assuming as before that the actual redox potential has not changed). It would be useful to obtain alternative L_n measurements which can be done using for example the IMVS and IMPS (Intensity modulated photocurrent spectroscopy) techniques to obtain τ_n and D_n, correcting these to be at the same Fermi energy and then using equation 2.26 to calculate L_n. These were attempted, however IMPS data for these cells was difficult to interpret as there were large additional signals not accounted for in current models so accurate values could not be obtained.

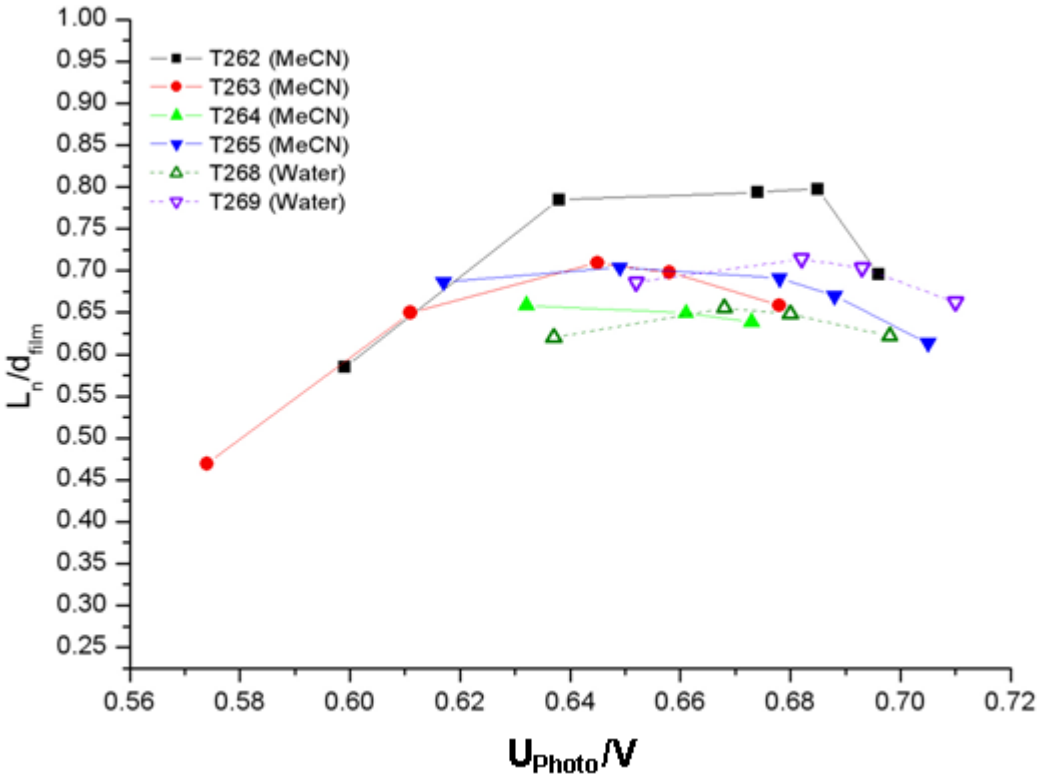

Fig 6.18 Comparing diffusion length/film thickness as a function of cell photovoltage for Z907 cells filled with electrolyte containing acetonitrile/valeronitrile (T262-T265) or water (T266-T269) as solvent. Electrolyte contained 0.1M GSCN, 0.5M tBP and 0.05M I_2. Water cells also contained 1% Triton-X100. Cells made with the same solvent are replicates.

Regarding the data presented here, it is important to consider the reason for such low values of L_n/d and possible consequences. Typical values are around

5[11] to 10[15] and values of 3 or above are required for a collection efficiency of 98%[11]. The most significant practical difficulty in this project was found to be the production of consistently good TiO_2 films and film quality varied for an unknown reason. In some cells the value of L_n/d was significantly longer – up to 6, but in other cells such as those shown in Fig 6.18 this value was very low. It is thought that this was linked to the quality of the TiO_2 films produced. In particular this makes the analysis of EIS results more difficult as the shape of the impedance response changes to a certain degree, so the fitting is more difficult or invalid. In particular this may affect the analysis of Fig 6.3 relating to changes in CB position. The conclusions drawn from that data set assume that the conductivity values obtained from EIS were correct.

6.3 Conclusions

In this chapter it has been shown that the main difference between acetonitrile and aqueous DSSCs is in the short circuit current. Evidence has been seen suggesting that the measured $E(I_3^-/I^-)$ values may be different to the actual values and that a number of results make the most sense if it is assumed that $E(I_3^-/I^-)$ is the same in both solvents. When this has been taken into account it is seen that the conduction band position is similar between cells made with the two solvents. Similarly, the trap distribution and electron lifetime response as a function of charge have been found to show no significant difference between cells made with the two solvents. This is in line with the fact that the open circuit voltage was very similar when the concentration of the various electrolyte components was the same between the two types of cells. The non-ideality factor was also found to be very similar for both types of cell suggesting that loss mechanisms are not linked to surface states but rather to some fundamental property of the TiO_2, which could be linked to trapping states. It was seen that increasing the PMII concentration reduced the open circuit voltage due primarily to changes to the Nernst potential and a PMII concentration of 2M was found to be optimal. Finally it was seen that the diffusion length dependence on voltage was fairly similar between the two types of cell implying that the electron collection was similar; however in many cases the diffusion length was low which may have implications for the data analysis.

6.4 References

(1) (a) Yu, Z.; Vlachopoulos, N.; Gorlov, M.; Kloo, L. *Dalton T* **2011**, *40*, 10289(b) Hagfeldt, A.; Boschloo, G.; Sun, L. C.; Kloo, L.; Pettersson, H. *Chem Rev* **2010**, *110*, 6595.

(2) (a) Nguyen, T. T. O.; Peter, L. M.; Wang, H. X. *J Phys Chem C* **2009**, *113*, 8532(b) O'Regan, B. C.; Durrant, J. R. *Accounts Chem Res* **2009**, *42*, 1799.

(3) Kalyanasundaram, K. *Dye-sensitized solar cells*; CRC Press: Boca Raton, Fla., 2010.

(4) Bisquert, J.; Vikhrenko, V. S. *J Phys Chem B* **2004**, *108*, 2313.

(5) Law, C. H.; Pathirana, S. C.; Li, X. O.; Anderson, A. Y.; Barnes, P. R. F.; Listorti, A.; Ghaddar, T. H.; O'Regan, B. C. *Adv Mater* **2010**, *22*, 4505.

(6) Murray Jr, R. C.; Aikens, D. A. *Electrochim Acta* **1976**, *21*, 1045.

(7) Kotocova, A. *Chem Zvesti* **1980**, *34*, 56.

(8) Peter, L. M. *Phys Chem Chem Phys* **2007**, *9*, 2630.

(9) Gonzalez-Vazquez, J. P.; Oskam, G.; Anta, J. A. *The Journal of Physical Chemistry C* **2012**.

(10) Fisher, A. C.; Peter, L. M.; Ponomarev, E. A.; Walker, A. B.; Wijayantha, K. G. U. *J Phys Chem B* **2000**, *104*, 949.

(11) Jennings, J. R.; Ghicov, A.; Peter, L. M.; Schmuki, P.; Walker, A. B. *J Am Chem Soc* **2008**, *130*, 13364.

(12) Salvador, P.; Hidalgo, M. G.; Zaban, A.; Bisquert, J. *J Phys Chem B* **2005**, *109*, 15915.

(13) Cameron, P. J.; Peter, L. M.; Hore, S. *J Phys Chem B* **2005**, *109*, 930.

(14) (a) Walker, A. B.; Peter, L. M.; Lobato, K.; Cameron, P. J. *J Phys Chem B* **2006**, *110*, 25504(b) Bisquert, J.; Cahen, D.; Hodes, G.; Ruhle, S.; Zaban, A. *J Phys Chem B* **2004**, *108*, 8106.

(15) Dunn, H. K.; Peter, L. M. *J Phys Chem C* **2009**, *113*, 4726.

Chapter 7: Influence of pH on the behaviour of aqueous dye sensitized solar cells

7.1 Introduction
7.2 Results
    7.2.1 Effect of pH on cell performance
    7.2.2 Effect of 4-tert-butylpyridine on cell performance
    7.2.3 Transient infrared measurement of electrons
        7.2.3.1 Open circuit voltage transients
        7.2.3.2 Short circuit current transients
        7.2.3.3 Water cell IR response model
        7.2.3.4 Continuity equation modelling of trapped electrons under short circuit/open circuit conditions
7.3 Conclusions
7.4 References

7.1 Introduction

Having considered some of the effects on a DSSC of moving from an acetonitrile to an aqueous electrolyte, the water cell itself is now considered in more detail. One of the key differences between water and acetonitrile is the proton concentration which is significantly higher in water due to the disassociation of H_2O into H_3O^+ and OH^-. Other work has looked at the effect of water concentration[1] and pH on dyed TiO_2 nanoparticles[2] and undyed TiO_2 films[3]. Cells where acids and bases have been added to the organic solvent-based electrolytes[4] have also been studied. In this chapter the effect of pH is considered on complete DSSCs that utilise electrolytes containing water as the primary solvent.

The effect of pH on cell IV characteristics is investigated and it is seen that the cell voltage increases with pH, and that photocurrent decreases with pH. This is attributed to changes in the CB energy. The effect of the additive tBP has also been studied and it is seen that this primarily changes the pH. Dye adsorption is found to be dependant on pH, limiting the usable pH range for DSSCs. Finally, analysis of transient infrared measurements is presented. It is seen that depending on the wavelength used, electrons in different parts of the cell can be measured. IR transients of water and acetonitrile cells are compared and it is seen that water cells display markedly different behaviour which is attributed to proton intercalation into the TiO_2 film. It is also seen that this behaviour alters as a function of pH and a model is proposed explaining this behaviour.

7.2 Results

7.2.1 Effect of pH on cell performance

In water, it is possible to measure and control the pH – something that is more problematic in aprotic organic solvents like acetonitrile[5]. Changes in pH are expected to have a number of effects on the dye cell, so understanding this property is important. Controlling pH effectively in an aqueous DSSC could be a way to tune the CB energy level to give optimised performance.

Firstly, the effect of pH on dye was examined. It has been observed in previous experiments that many dyes will desorb from TiO_2 under basic conditions and so a simple visual inspection of the effect of pH on TiO_2 films dyed in Z907 was undertaken. Table 7.1 shows that at pH values above 9 there is a visible discolouration of the film as dye is desorbed. It is possible that some dye desorption is also occurring at pH values lower than this that could not be observed visually on the time scale of the experiment. In the investigation of DSSC properties with pH carried out here, no measurements were done above pH 7.5 to prevent dye desorption.

Table 7.1: Effect of pH on dye desorption upon immersion in aqueous HCl solution for several minutes from TiO_2 film initially dyed in 0.3mM Z907 overnight. pH adjusted with NaOH(aq).

pH	**Effect on Z907 dyed film**
2.1	No effect
6	No effect
7	No effect
8	No effect
9	No effect
10	Marginal discolouring
11	Slight discolouring
12	Obvious discolouring
13	Obvious discolouring

In chapter 2, the concept of surface charge and the zero point charge (zpc) were introduced. Literature values for the zpc of anatase TiO_2 tend to be around pH6[6], though values of 5[7] – 7.5[8] have been reported. Assuming that H^+/OH^- are the only potential determining species, the surface charge will be positive below the pzc (~pH6) and negative above the pzc. The anchoring group for Z907 is a carboxylate group which is negatively charged so binding is much less likely when the pH is above the zpc. In the case above where dye is already bound to the surface there will be a pH dependant amount of desorption/re-adsorption which will depend on the value of the binding constant. At higher pH values, the rate at which dye binds to the surface will be lower due to the increased repulsion and the increased OH^- concentration is likely to lead to increased dye desorption as the base catalyses hydrolysis of the ester linkage. As mentioned above, this will result in an overall decrease in the amount of dye on the surface.

It was found that accurately controlling the pH in a standard DSSC electrolyte was a non-trivial problem. Initially, a set of cells were made containing standard electrolytes (2M PMII, 0.05M I_2, 0.5M tBP, 0.1M GSCN, 1% Triton X-100 in water) where buffer solutions made using potassium hydrogen phthalate and potassium hydrogen phosphate along with low concentrations of HCl were used to adjust the pH. However, it was found upon measurement that the pH of this electrolyte was difficult to perturb using these solutions. Both GSCN and tBP are basic compounds and at the concentration at which they are used in the electrolyte they prevented any significant pH changes. As a result, all pH values in the initial test were within 1 unit of each other, ranging from pH 7.2 – 6.4. Cell performance as a function of electrolyte pH is summarised in Fig. 7.1. Data from this set show that there is minimal change in cell performance in this pH region using the buffered cells, and there is a significant variation in cell performance for each pH as shown by the large error bars.

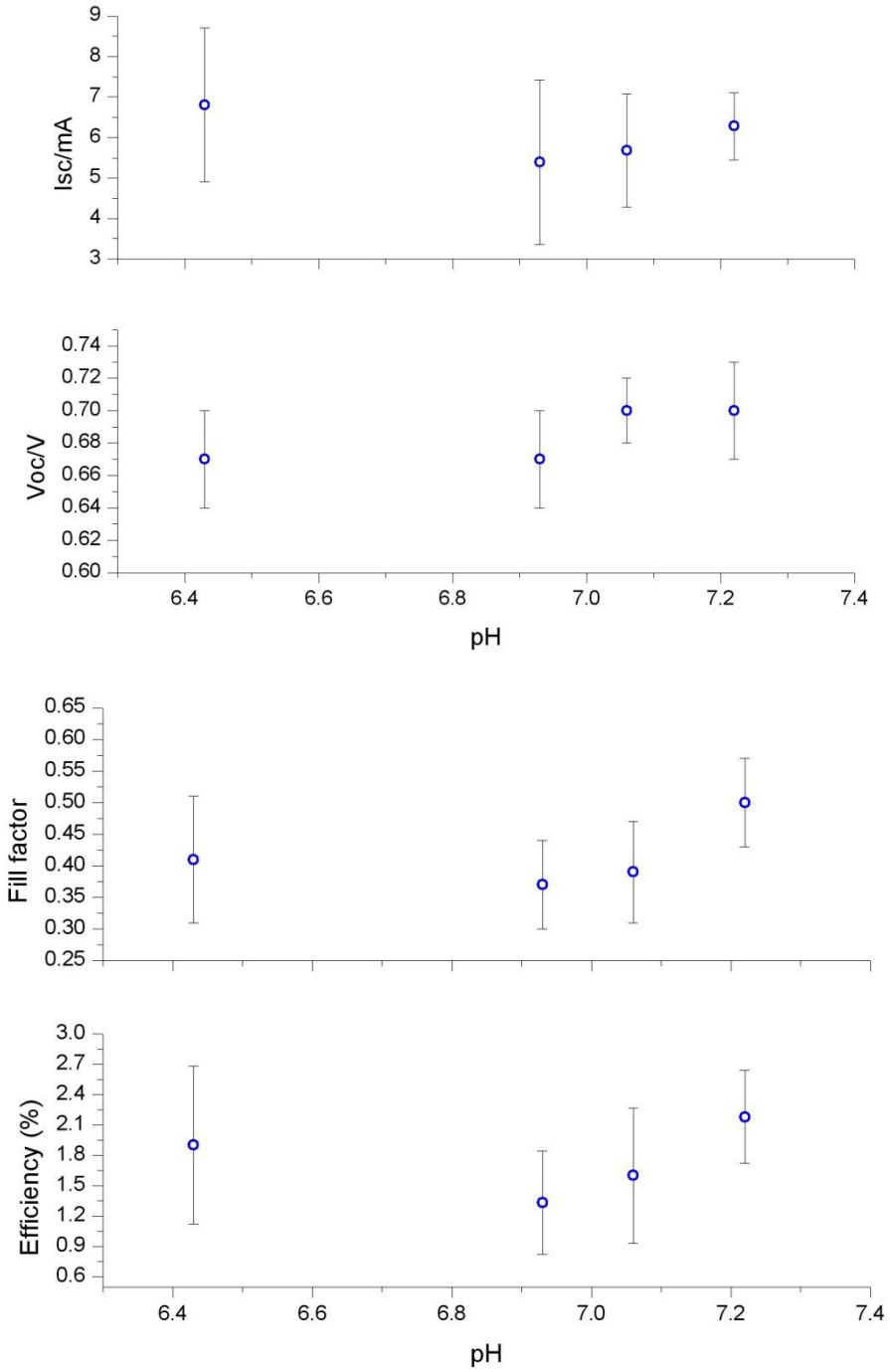

Fig. 7.1 IV performance summary for cells measured under 1 sun AM1.5 illumination. Cells dyed in 0.3mM Z907 and contain aqueous electrolyte (2M PMII, 0.05M I_2, 0.1M GSCN, 0.5M tBP and 1% Triton X-100) adjusted to different pH values using phosphate or phthalate buffer solutions. Error bars are based on n=3 repeats.

Adding HCl at reasonably high concentrations was found to be more effective at changing the electrolyte pH and allowed cells with a pH range from 5 to 7.5 to be investigated. Cells in this set contained the electrolyte additives tBP and GSCN

with the exception of the cells with a pH of 5.43 which contained no tBP. IV parameters for these cells are shown in Fig 7.2.

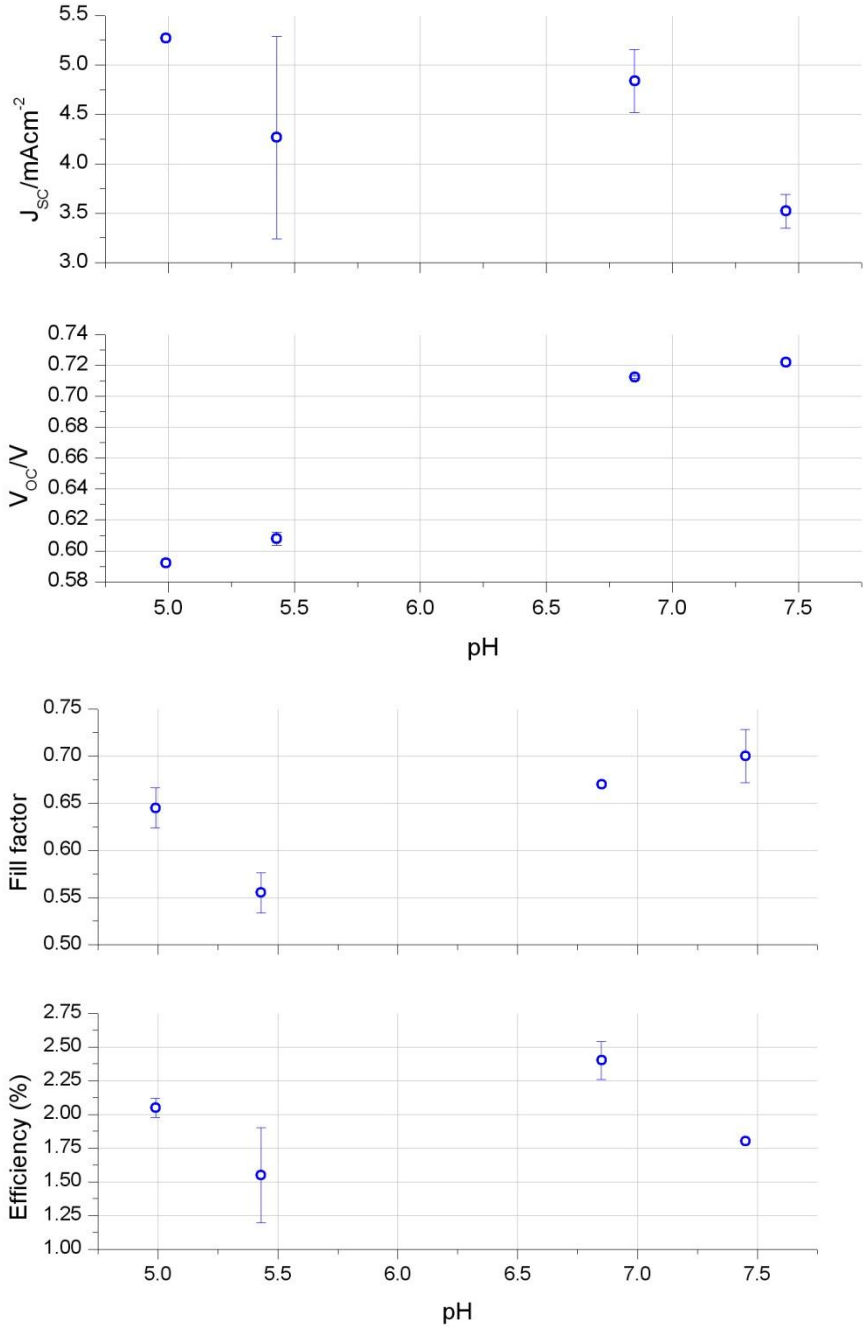

Fig 7.2 IV performance summary for cells measured under 1 sun AM1.5 illumination. Cells dyed in 0.3mM Z907 and contain aqueous electrolyte (2M PMII, 0.05M I_2, 0.1M GSCN, 0.5M tBP and 1% Triton X-100) adjusted to different pH values using HCl. Note that cell at ~pH5.4 contains no. Error bars based on n=2 repeats.

It can be seen from Fig 7.2 that, as for the previous data set, pH has no large effect on fill factor or overall efficiency. However, there is a linear relationship

between cell voltage and electrolyte pH and there may be an inverse relationship between pH and J_{SC}, though large error bars in this measurement make this harder to determine.

The relationship between voltage and pH is interesting for several reasons. Firstly, it is independent of tBP; as noted all the cells used here were made with tBP except for the ones at pH 5.43, however this does not alter the linear relationship. This implies that in the water cell the effect of tBP on pH is what causes any tBP related changes. Secondly, the gradient of the V_{OC} change is 57mV/pH unit in Fig 7.2 and similar to this in Fig 7.1 though with greater error. It has been found by Enright et al[3a] that the flat band potential of TiO_2 changes by 60mV/pH unit due to the adsorption and desorption of H^+. This implies that the change in V_{OC} observed in the aqueous DSSC as a function of pH is due to this change in CB position and suggests that the Nernst potential of the redox couple does not change. However, when measurements of the redox potential were taken as shown in fig 7.3, there was some change in the redox potential. If cells at pH 5.43 (no tBP) are neglected, the change in redox potential is 12mV/pH unit. The reaction occurring at the counter electrode is $I_3^- + 2e^- \rightarrow 3I^-$ which does not involve any protons, so the Nernst potential should therefore depend only on $[I^-]$ and $[I_3^-]$. The small changes could be due to differences in LJP as changing the proton concentration is expected to alter the LJP. The influence of tBP is considered below.

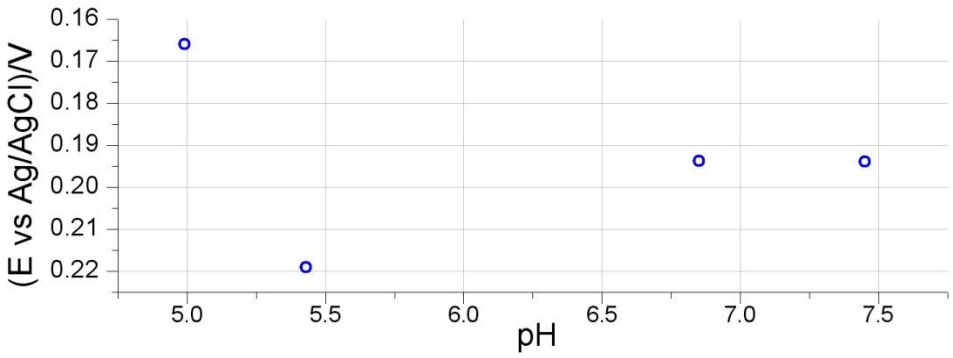

Fig 7.3 Redox potential for water based electrolyte/cells (2M PMII, 0.05M I_2, 0.1M GSCN, 0.5M tBP and 1% Triton X-100) as a function of measured electrolyte pH. pH 5.4 is measured for electrolyte containing no tBP. Cell pH adjusted with HCl.

A change in CB position with pH would also explain the decrease in J_{SC} observed as a function of pH. As the CB energy level increases with increasing pH, the driving force for electron injection decreases which reduces the measured photocurrent.

This section shows that the main effect of pH on cell IV parameters is to change the CB position by 57mV/pH unit which is in agreement with other studies focussing on TiO_2 films[3a]. This change results in an increase in V_{OC} and a decrease in J_{SC} with increasing pH, resulting in unchanged cell efficiency. These conclusions are based on the assumption that changes in the measured redox potential with pH are due to changes in LJP.

7.2.2 Effect of 4-tert-butylpyridine on cell performance

In the previous section two cells without tBP were included. Leaving out tBP from the electrolyte resulted in a decrease in pH which altered cell potential. TBP has often been used in DSSCs as a performance enhancing additive and is considered now in greater detail.

Four sets of two cells were produced that were identical apart from electrolyte composition; two sets used a standard acetonitrile electrolyte, one containing and one without tBP; the remaining two sets used a standard aqueous electrolyte, again one containing and one without tBP. The cells were labelled T397-T404 and are summarised in Table 7.2 with IV curve results shown in Fig 7.5.

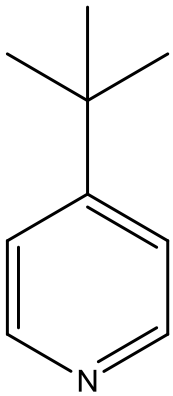

Fig 7.4 tert-Butyl Pyridine

Table 7.2: Materials, pH, redox potential and IV performance (measured under 1 sun AM1.5 illumination) summary for cells made using different solvents and with and without tBP adjusted to different pHs.

Cell	Solvent/tBP	pH	Redox potential vs Ag/AgCl/V	I_{SC}/mA	V_{OC}/V	FF	Efficiency (%)
T397	MeCN/tBP	-	0.089	6.99	0.687	0.62	3.1
T398	MeCN/tBP	-	0.089	7.42	0.697	0.64	3.4
T399	MeCN/No tBP	-	0.093	7.02	0.651	0.65	3.1
T400	MeCN/No tBP	-	0.093	6.67	0.657	0.59	2.6
T401	Water/tBP	6.85	0.193	5.06	0.713	0.67	2.5
T402	Water/tBP	6.85	0.193	4.61	0.712	0.67	2.3
T403	Water/No tBP	5.43	0.219	4.99	0.611	0.54	1.8
T404	Water/No tBP	5.43	0.219	3.54	0.605	0.57	1.3
T406	Water/tBP	7.45	0.194	3.64	0.722	0.68	1.8
T407	Water/tBP	7.45	0.194	3.4	0.722	0.72	1.8
T408	Water/tBP	6.96	0.192	0.44	0.691	0.98	0.3
T409	Water/tBP	6.96	0.192	0.34	0.705	1.13	0.3
T410	Water/tBP	4.99	0.166	5.27	0.592	0.66	2.1
T411	Water/tBP	4.99	0.166	5.27	0.592	0.63	2

The most obvious effect of tBP was to cause a large increase in photovoltage of around 100mV in water and 50mV in acetonitrile. There is no change in J_{SC} caused by tBP but a small increase in fill factor in water; overall cell efficiency tended to be slightly higher. It was also noticed that tBP usually improved electrolyte filling. When tBP was present, there was in some cases desorption of dye near the filling holes which did not occur when this was not present.

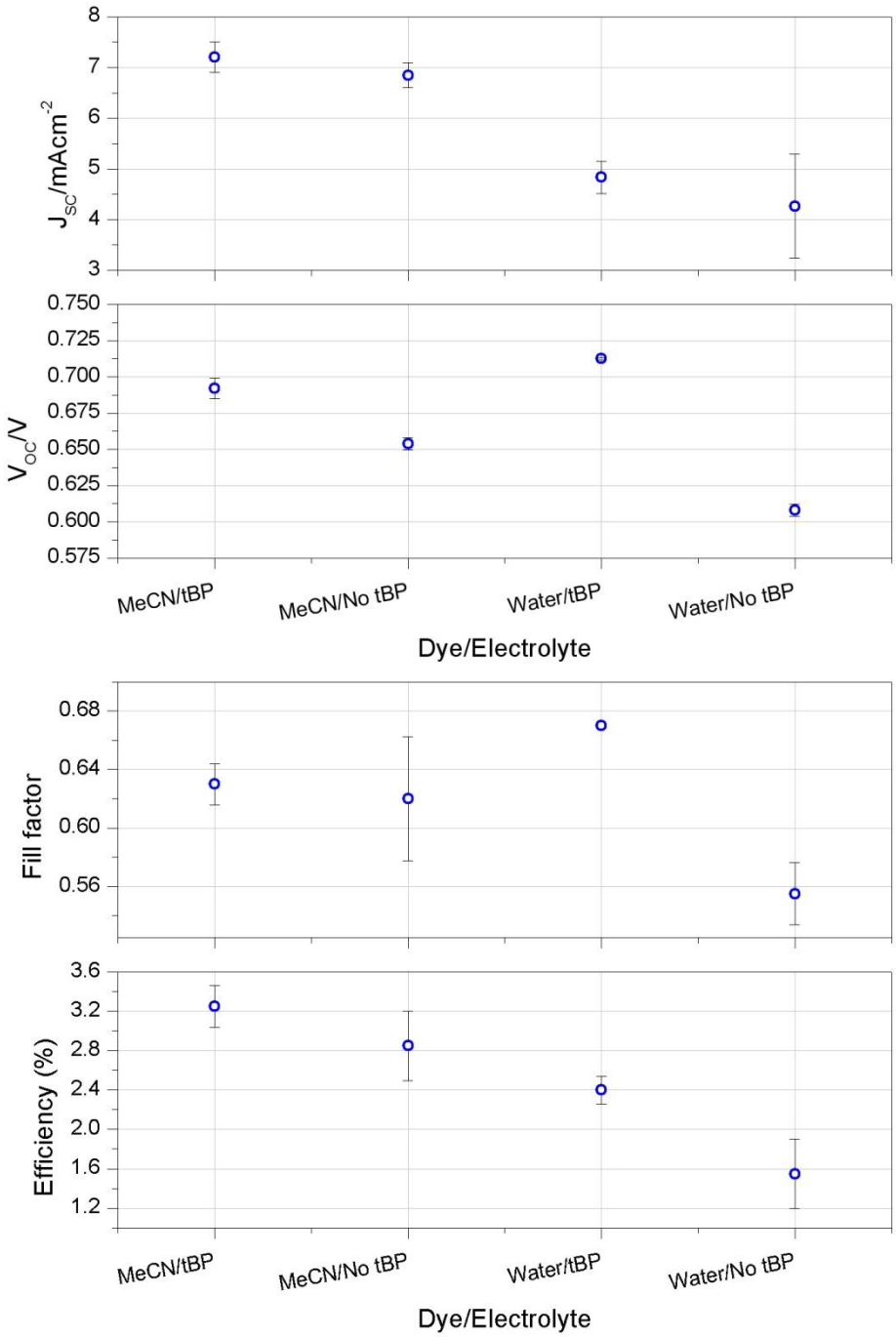

Fig 7.5 IV performance summary measured under 1 sun AM1.5 illumination for cells dyed in 0.3mM Z907 and containing electrolyte (2M PMII, 0.05M I_2, 0.1M GSCN and 0.5M tBP. 1% Triton X-100 in aqueous cells) made with either acetonitrile/valeronitrile or water as the solvent and with and without tBP. Error bars are based on n=2 repeats.

TBP is a weakly basic molecule in water and the pK_a of its conjugate acid is 5.76. For the aqueous DSSCs described in Fig 7.5, the cells made using electrolyte containing tBP have a pH of 6.85 and the cells made using electrolyte without tBP have a pH of 5.43 showing that one of the effects of adding tBP to water is to

reduce the H^+ concentration in solution - the equilibrium for tBP and H^+ is shown in fig 7.6. When tBP is present in the water electrolyte (pH 6.85), it is therefore primarily in its basic form unless additional acid is introduced to the solution.

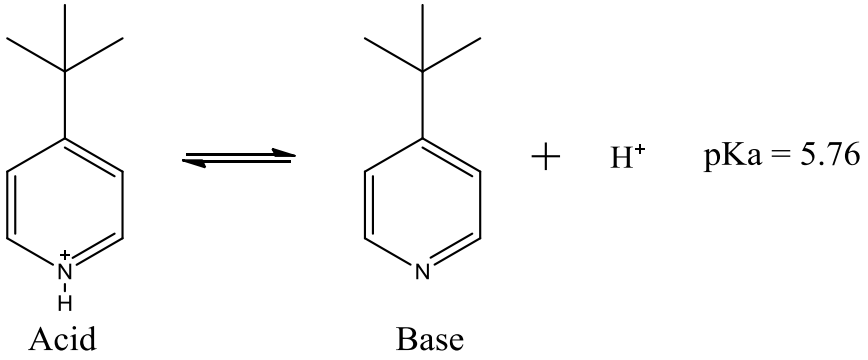

Fig 7.6 Acid base equilibrium for conjugate acid and basic form of tBP

The effect of tBP can be explained In line with previous literature[9]. On addition of tBP, the H^+ concentration is decreased in the bulk and will decrease at the surface as a result. This causes the conduction band to move to a higher energy as a result of the change in surface charge as seen in the previous section. This will result in an increased V_{OC} as the electron quasi Fermi energy moves to higher energies. The effect is more pronounced in water than acetonitrile, which may be due to the higher H^+ concentration in water.

It has also been suggested that tBP can adsorb onto TiO_2, directly influencing surface charge and blocking the surface to reduce the reaction between electrons in the TiO_2 and I_3^-[10]. This will be most likely when in its basic form, where the nitrogen lone pair can directly interact with the TiO_2. Such a blocking effect could be a second reason for an increase in photovoltage, though as seen in Fig 7.2 above, the linear 57 mV/pH unit increase in voltage observed regardless of the presence of tBP strongly suggests that the pH effect is dominant. Unfortunately charge data is not available for these cells, and so electron lifetime as a function of charge cannot be plotted which would give a clearer indication of the blocking effect of tBP in water and would be a useful experiment for future study in this area.

The adsorption of tBP onto TiO_2 could also be linked to the desorption of dye observed close to the filling hole upon introduced of electrolyte to the cell in some

cases; if tBP adsorbs to the surface, then it is likely to occupy dye binding sites. A possible scenario is as follows. As discussed earlier, a small amount of dye desorption/adsorption is ongoing in solution. When electrolyte is initially introduced to the cell through the filling hole this process can occur and tBP in its basic form can adsorb onto binding sites where dye has desorbed. The resulting drop in tBP concentration decreases the pH of the electrolyte and the surface charge becomes more positive which increases the equilibrium binding constant for dye. This would result in dye desorption occurring only near the filling hole.

In this section the effect of tBP on the DSSC has been considered in greater detail. It has been suggested that the change in pH and subsequent change in CB position are primarily responsibly for the change in voltage with and without tBP. The effect of tBP adsorption to the TiO_2 has been suggested to be more important in terms of competing with dye adsorption than in blocking the reaction between e^-_{TiO2} and I_3^-.

7.2.3 Transient infrared measurement of electrons

Measurements so far have concentrated on non-equilibrium steady state behaviour such as the open circuit voltage under illumination. Now, transient behaviour will be considered based on infra red measurements of electrons. In particular, the behaviour of water cells when illuminated for a period of time will be examined and compared with that for acetonitrile cells. The effect of pH on the observed response will be considered and a model explaining the behaviour suggested.

In this technique, infra red light is used to determine the density of electrons in TiO_2. As the measurement is optical and therefore disconnected from the electronic properties of the cell, it is possible to control and measure the potential of the cell at the same time. By locking into a modulating IR signal it is also possible to apply bias illumination to the cell. Transients were taken for a number of different cell conditions that gave insight into cell behaviour under operating conditions.

7.2.3.1 Open circuit voltage transients

Transients for cells held under open circuit conditions are first considered and shown in Fig 7.7 and 7.8. Upon illumination with green light (530nm), the photovoltage response quickly reaches a steady state value, corresponding to the nE_F/q potential at which the rate of electron injection is equal to the rate of electron losses. When the light is turned off, the voltage response is a decay equivalent to that observed for OCVD measurements, corresponding to the loss of electrons in the semiconductor via reaction with D^+ or I_3^-. Upon illumination, the transmission of the cell decreases primarily due to the additional electrons in the photoanode which absorb IR light according to the optical cross section. When illumination is turned off, the response increases back to the original value as the number of electrons in the photoanode decreases. The voltage and transmission response of both cells is mostly similar, though in water the transmission response when the light is turned off is initially fast, then becomes significantly slower when the transmission has returned to approximately one fifth of the illumination induced change. A scenario explaining this behaviour is as

follows. It has been shown in work by Halverson et al[1] and Lyon et al[3b] that protons can intercalate into TiO_2 from water in the electrolyte at low voltages (0.2-0.4V), and that increasing the water content increases the density of intercalated protons. Interestingly, Halverson et al showed this process to be irreversible, whereas Lyon et al showed it to be reversible which may be due to the higher cell potentials used by Halverson et al. The intercalation mechanism was given as:

$$Ti^{IV}O_2 + e^- + H^+ \rightleftharpoons Ti^{III}(O)(OH) \qquad \text{Equation 7.1}$$

The result of this intercalation was to generate a shallow trap level in which electrons had a longer residence time than in traps described by the exponential distribution g(E) resulting in increased diffusion rates[1]. For the cell measured in Fig 7.8, the water content is around 50vol% which is greater than the water content shown to be required for the intercalation and subsequent generation of shallow trap state to occur[1]. In this case it is expected that proton intercalation has occurred, resulting in a shallow trap state as described. The origin of the ΔT/T signal will be considered in detail below; for the purpose of this description it is enough to say that it is linked to the electron concentration in TiO_2 and FTO, therefore the decrease in signal corresponds to an increase in electrons and the increase in signal is linked to the loss of electrons. The slower change in the signal in Fig 7.8 compared to Fig 7.7 supports the idea that a shallow trap state as described above has been produced according to the following argument. Initially when the light is turned off, electron diffusion to recombination sites is fast resulting in the initial increase in ΔT/T. In water, the change in signal then slows considerably, which can be explained if electron transport is now limited by slow detrapping. In contrast, the signal in Fig 7.7 in acetonitrile increases quickly to the original dark value when the light is turned off. Trap states produced by proton intercalation as described above are expected to produce this behaviour. It is also noted that in some cases, acetonitrile cells had a similar offset; in the Halverson paper the effect of H^+ intercalation could be clearly seen at water concentrations of 1vol%, though data is not given between 0 and 1vol%. Typical values for the water content of acetonitrile are around ≤0.3vol%[11], and it is probable that the effect observed in some acetonitrile cells is linked to the water content.

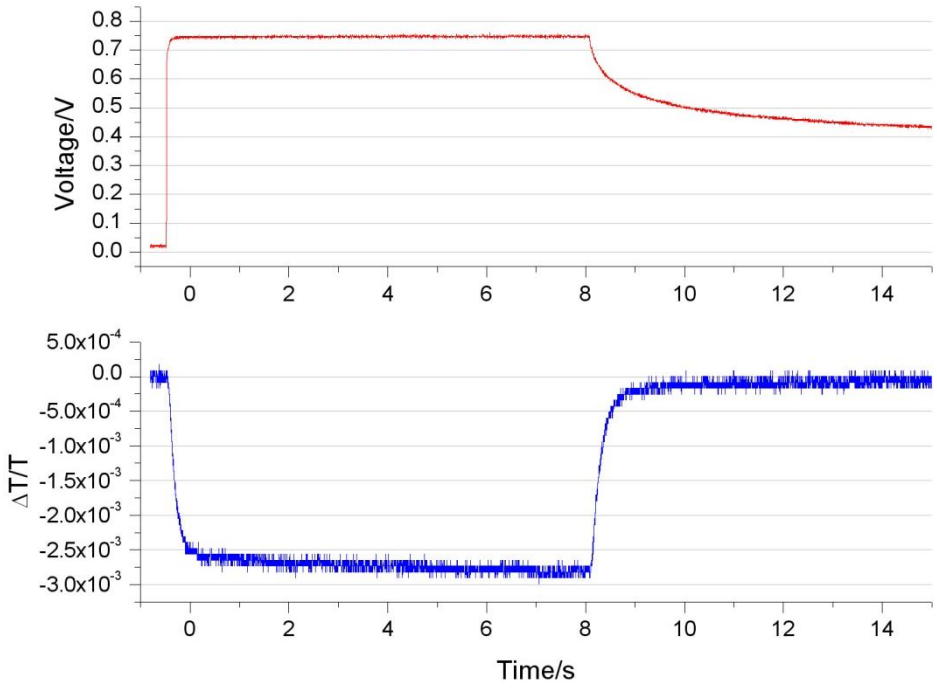

Fig 7.7 Voltage (red) and ΔT/T (blue) transient response of acetonitrile/valeronitrile cell (T183, dyed in 0.3mM Z907, electrolyte contained 0.6M PMII, 0.05M I_2, 0.1M GSCN and 0.5M tBP) under open circuit condition upon green light (530nm) illumination at t=0. IR wavelength = 1550 nm. Light on at ~ t = 0, light off at ~ t = 8 s.

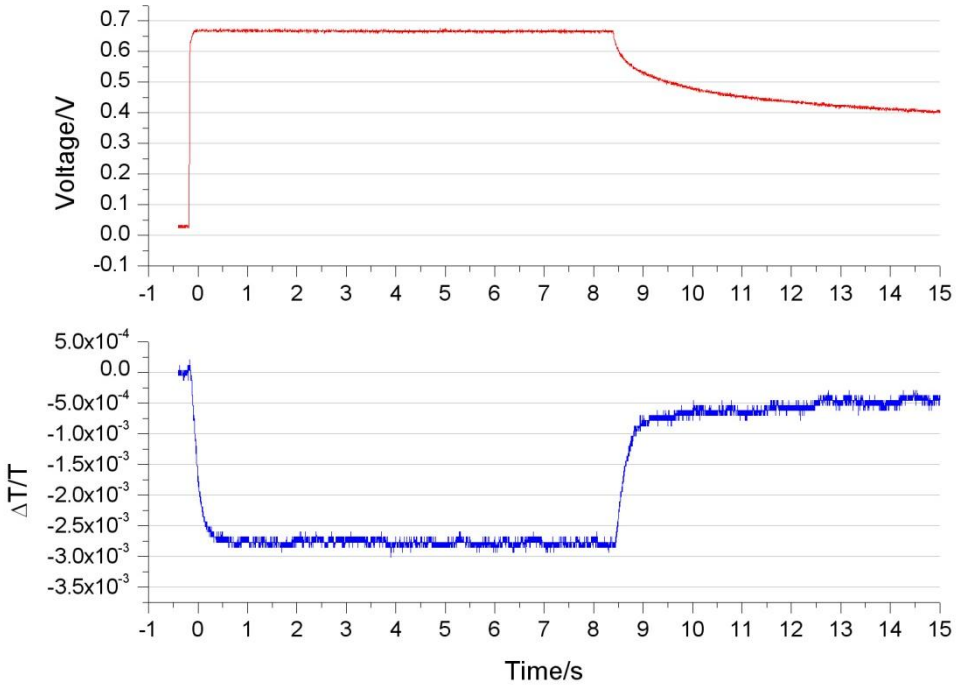

Fig 7.8 Voltage (red) and ΔT/T (blue) transient response of water cell (T201, dyed in 0.3mM Z907, electrolyte contained 2M PMII, 0.05M I_2, 0.1M GSCN, 0.5M tBP and 1% Triton X-100) under open circuit condition upon green light (530nm) illumination at t=0. IR wavelength = 1550 nm. Light on at ~ t = 0, light off at ~ t = 8.5 s.

7.2.3.2 Short circuit current transients

Significantly different behaviour is observed between water and acetonitrile cells when measured under short circuit conditions as shown in (Fig 7.9 & 7.10). For both cells, the current quickly increases upon illumination until it reaches a steady state value. In the acetonitrile case the transmission decreases to a steady value whereas in water an initial decrease in transmission is followed by a slower increase until a steady state is reached. This is likely to mean that two different processes are being measured which have different time constants and which oppose each other in terms of their effect on the transmission signal.

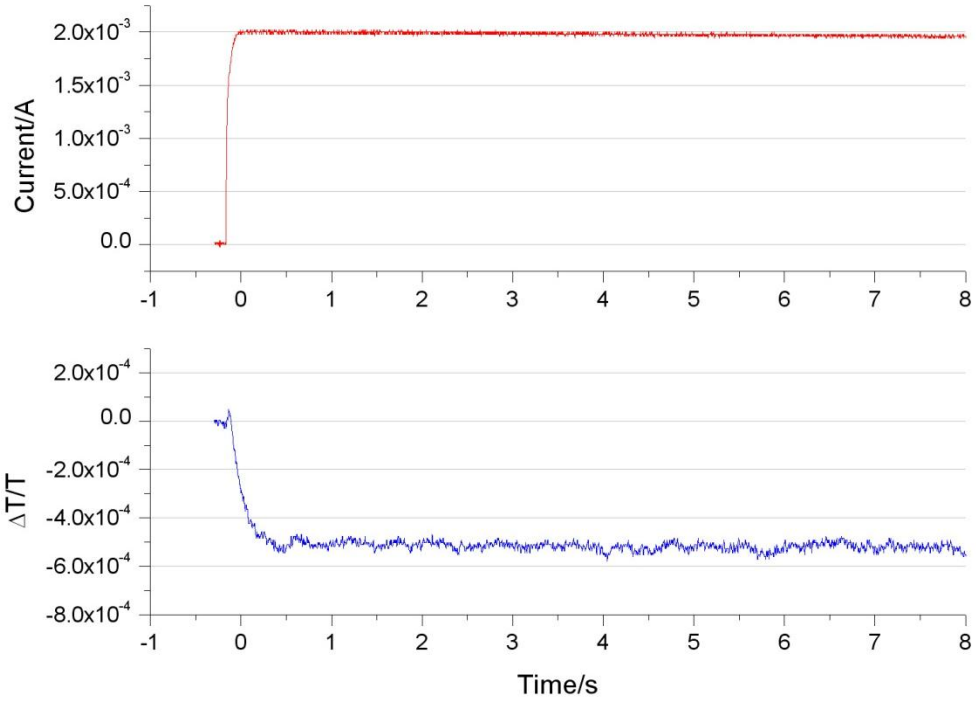

Fig 7.9 Voltage (red) and ΔT/T (blue) transient response of acetonitrile/valeronitrile cell (T183, dyed in 0.3mM Z907, electrolyte contained 0.6M PMII, 0.05M I_2, 0.1M GSCN and 0.5M tBP) under short circuit condition upon green (530nm) light illumination. IR wavelength = 1550 nm. Light on at ~ t = 0.

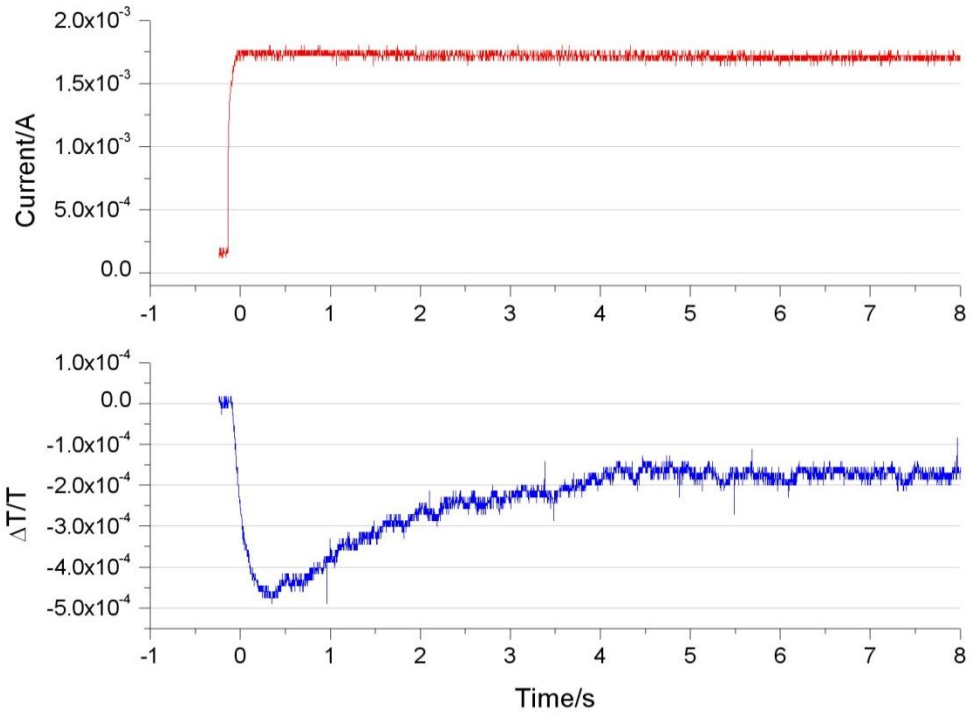

Fig 7.10 Voltage (red) and ΔT/T (blue) transient response of water cell (T201, dyed in 0.3mM Z907, electrolyte contained 2M PMII, 0.05M I_2, 0.1M GSCN, 0.5M tBP and 1% Triton X-100) under short circuit condition upon green (530nm) light illumination. IR wavelength = 1550 nm. Light on at ~ t = 0.

The effect of illumination intensity on this behaviour can be seen in Fig 7.11 and Fig 7.12. In acetonitrile the transmission response has the same square shape at all light intensities and the change in transmission upon illumination increases with intensity. In water, the observed response is similar to that seen in Fig 7.10 at illumination intensities above $8.8x10^{15}s^{-1}$. Below this intensity the initial trough is not seen. This suggests that one of the two parts of the signal does not occur at low light intensity; at lower light intensity nE_F in the film is lower and so it is possible that this component of the signal is affected by the electrochemical potential of electrons in the semiconductor.

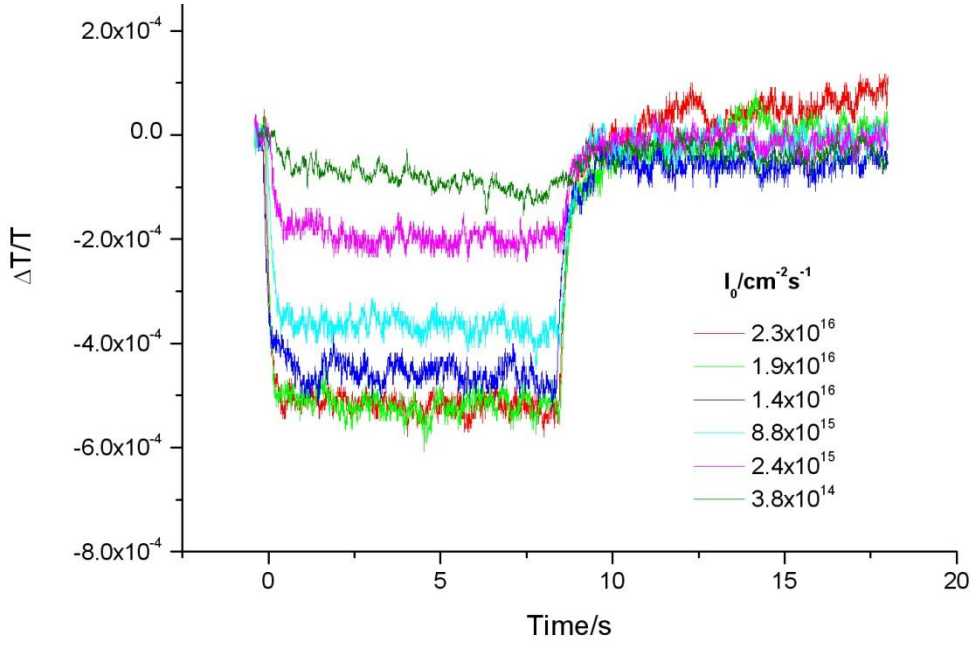

Fig 7.11 ΔT/T values for acetonitrile/valeronitrile cell (T183, dyed in 0.3mM Z907, electrolyte contained 0.6M PMII, 0.05M I_2, 0.1M GSCN and 0.5M tBP) under short circuit conditions at different green (530nm) light intensities. Square wave starting at approximately 0s is for light on. IR wavelength = 1550 nm. Light on at ~ t = 0, light off at ~ t = 8.5 s.

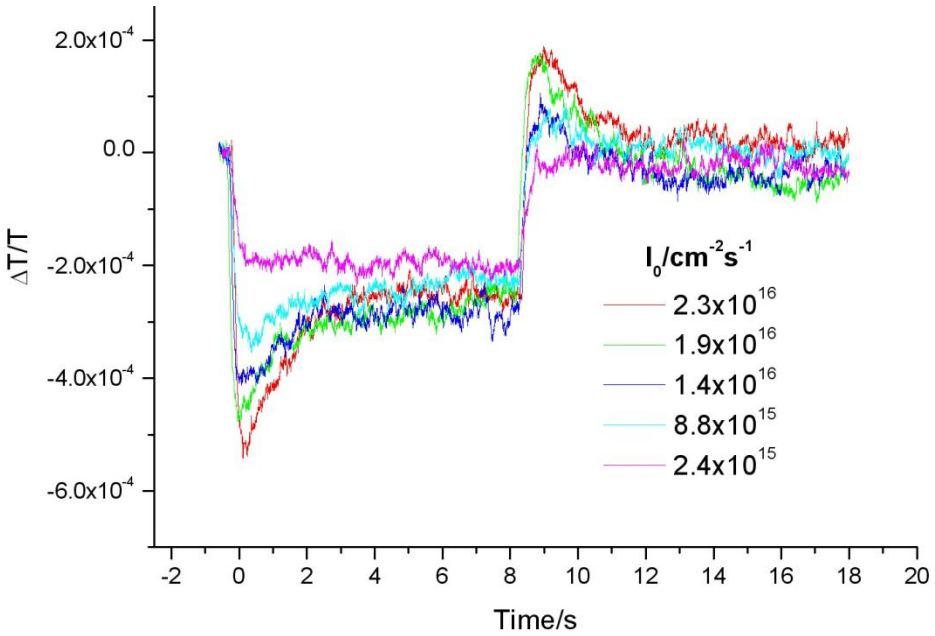

Fig 7.12 ΔT/T values for water cell (T201, dyed in 0.3mM Z907, electrolyte contained 2M PMII, 0.05M I_2, 0.1M GSCN, 0.5M tBP and 1% Triton X-100) under short circuit conditions at different green (530nm) light intensities. Square wave starting at approximately 0s is for light on. IR wavelength = 1550 nm. Light on at ~ t = 0, light off at ~ t = 8.5 s.

7.2.3.3 Water cell IR response model

A model that explains the observed behaviour is introduced below. Firstly, the response of IR light as a function of wavelength is considered to describe what is being measured. Secondly, changes in the cell under different conditions are described along with their affect on the absorption of the wavelengths being measured. Finally, a model that explains the observed behaviour is proposed. A semi-quantitative approach is used to examine the validity of the model.

IR light can be absorbed by a number of different entities depending on its wavelength. Fig 7.13 is a reproduction of the absorption spectrum of dyed TiO_2 on FTO substrate and dyed TiO_2 on quartz substrate as published by Spijker et al[12]. The absorption peak between 600 nm and 900 nm is attributed to absorption by the dye cation and the electrolyte. At wavelengths above about 1300 nm the absorption increases which is attributed to absorption by electrons in FTO, whereas absorption between ~900 nm and ~1300 nm is due to absorption primarily by electrons in TiO_2. In addition, the work by Spijker et al determines the optical cross section of electrons in TiO_2 and in FTO. In TiO_2, $\sigma(950)_{TiO2}$ is ~ $1x10^{-17}cm^2$ and $\sigma(1550)_{TiO2}$ is ~$2.2x10^{-18}$ cm^2 whereas in FTO $\sigma(950)_{FTO}$ is zero and $\sigma(1550)_{FTO}$ is $8.2x10^{-17}$ cm^2. If these values are correct, it is possible they will result in the two different signals required to produce the transient behaviour observed in water at I_{SC}. It is also expected that a different response will be observed at different wavelengths depending on the relative optical cross section of electrons, and this will be considered when describing a model which explains the observed behaviour. On the basis of the optical cross sections of electrons it is anticipated that for measurements made at 1550 nm the signal will be dominated by electrons in FTO unless $nE_{F,FTO}$ does not change, and that measurements made at 950nm will be dominated by electrons in TiO_2.

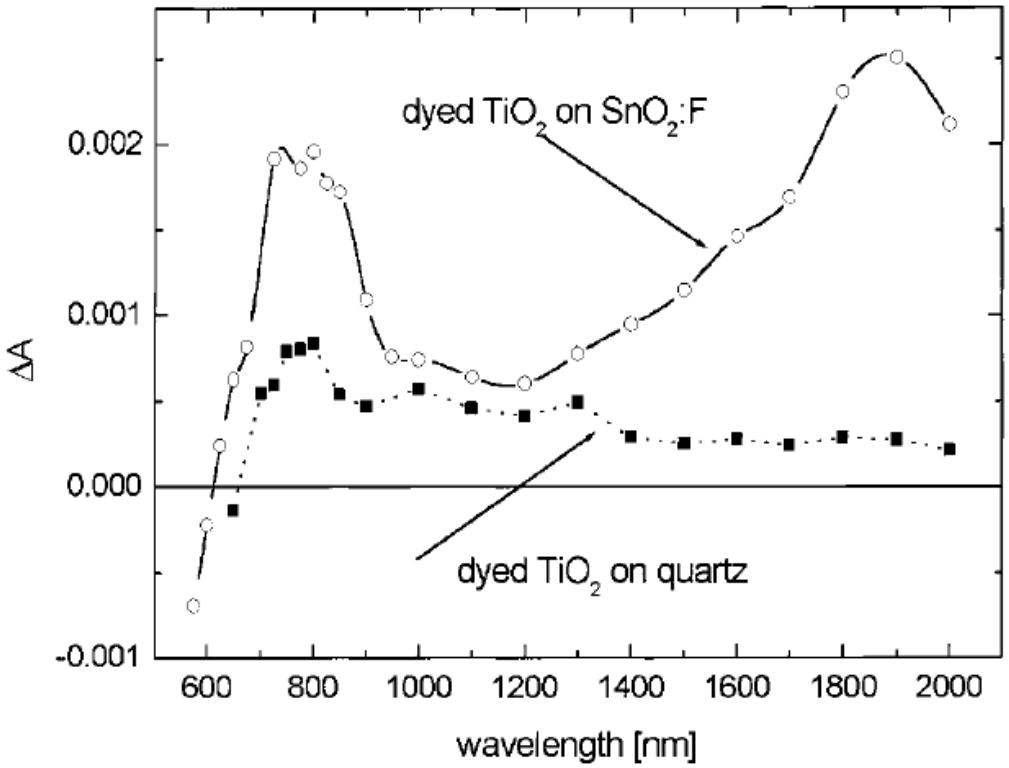

Fig 7.13[12] 'Absorption change of a dye-sensitized nanoporous TiO_2 film (thickness 2.3 μm) on a quartz and SnO_2:F substrate in 10 mM KI/1 mM I_2, upon 532 nm laser flash excitation of a pulsed Nd:YAG laser at a laser power of 100 μJ/cm^2. The presented ΔA is the average absorption change within the first 20 μs after laser flash excitation.'[Quoted from Ref[12]]

The response of electrons in the FTO is considered first of all. FTO has an electron affinity of approximately 0.3eV[13] greater than TiO_2. Upon contact with TiO_2 nanoparticles and the electrolyte in the dark, equilibration of Fermi energies moves the FTO Fermi level to a lower energy and a significant depletion layer is created at the FTO surface[13]. If the Fermi energy is altered as will be the case upon illumination at V_{OC}, the thickness of the depletion layer will change as the degree of band bending changes, which in turn will alter the free electron density. Electrons in the FTO will absorb IR light and change the IR transmittance of the film. Other factors which alter the degree of band bending will also affect the IR signal, for example changes to the position of the CB edge.

Electrons in TiO_2 are now considered. As described in chapter 2, it has been shown that the number of trapped electrons in an illuminated sensitized TiO_2 film are approximately four orders of magnitude higher than the number of free

electrons[14]. This means that a response due to electrons in TiO_2 is dominated by trapped electrons. Assuming that the equilibrium between free and trapped electrons is fast ($\partial n_t/\partial n_c >> 1$) both the number of free and trapped electrons in the film will alter depending on the position of the quasi electron Fermi energy and in the case of Fermi level pinning a change in the CB edge will also alter the number of trapped electrons.

An explanation for the open circuit response is given first. Fig 7.14 & 7.15 show the response of one water cell with an electrolyte pH of 7.45 to blue light illumination under open circuit conditions when measuring with IR light having a wavelength of 950 nm or 1550 nm. The open circuit response is approximately 4 times larger at 1550 nm than at 950 nm. Based on the values of optical cross section, the response due to electrons in FTO is expected to be significantly larger at 1550 nm than at 950 nm, whereas the opposite is true for electrons in the TiO_2. This implies that the V_{OC} response at 1550 nm is dominated by electrons in the FTO, while at 950 nm it is dominated by electrons in TiO_2. Upon illumination at V_{OC}, the Fermi energy in FTO and TiO_2 is increased by a similar amount; in the cell measured here, approximately 0.65 V. This significantly reduces the band bending in FTO resulting in a much smaller depletion layer thickness which increases the number of electrons and subsequently decreases the transmission signal. The number of electrons in TiO_2 also increases as nE_F increases, resulting in a decrease in the transmission signal. The two effects work in the same direction and so long as the optical cross section of electrons in either material is not zero, the total response is the sum of both responses. However slightly different decay behaviour is observed at the two wavelengths when the light is turned off.

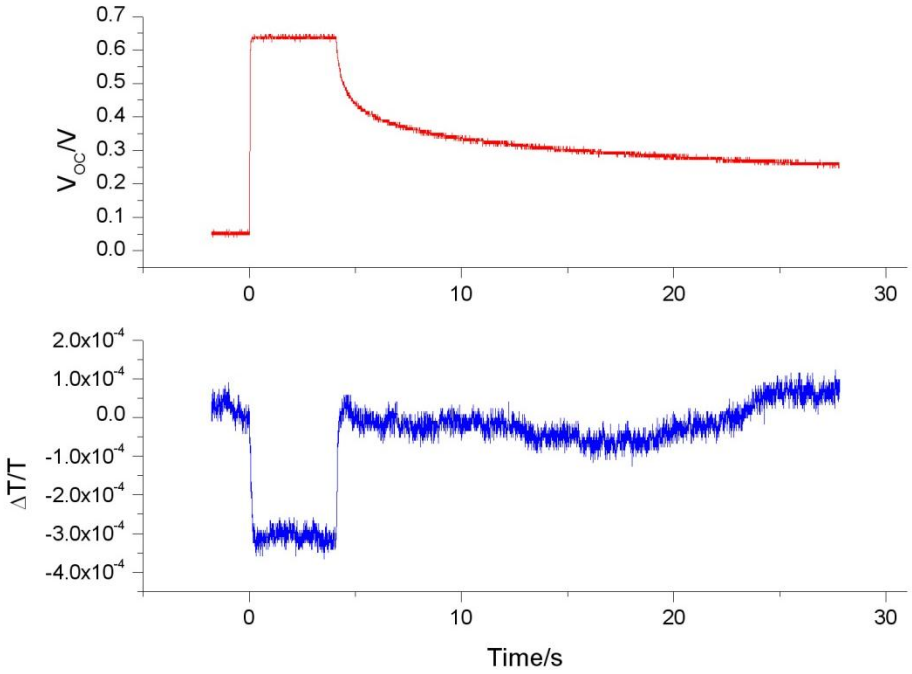

Fig 7.14 Voltage (red) and ΔT/T (blue) transient response of water cell (2M PMII, 0.05M I_2, 0.1M GSCN, 0.5M tBP, 1% Triton X-100) with an electrolyte pH of 7.45. Measured under open circuit condition with blue light (470 nm) illumination pulse with a light intensity of 3.77x10^{15} cm^{-2}s^{-1}. IR wavelength = 950 nm. Light on at t = 0, light off at ~ t = 4 s.

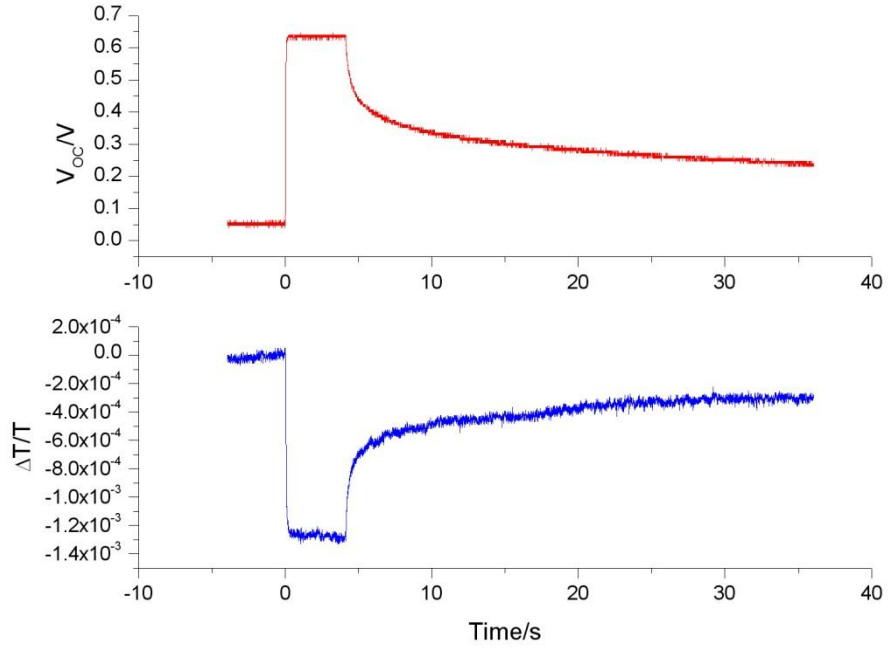

Fig 7.15 Voltage (red) and ΔT/T (blue) transient response of water cell (2M PMII, 0.05M I_2, 0.1M GSCN, 0.5M tBP, 1% Triton X-100) with an electrolyte pH of 7.45. Measured under open circuit condition with blue light (470 nm) illumination pulse with a light intensity of 3.77x10^{15} cm^{-2}s^{-1}. IR wavelength = 1550 nm. Light on at t = 0, light off at ~ t = 4 s.

The more complex short circuit behaviour is now considered. Fig 7.16 & 7.17 show the response of one water cell with an electrolyte pH of 7.45 to blue light (470nm) illumination under short circuit conditions when measuring with IR light having a wavelength of 950 nm or 1550 nm. At both wavelengths there is an initial decrease in transmission followed by a slow increase in transmission until a steady response is reached. Upon illumination, fast electron injection into the semiconductor is expected increasing the electron density in the film and so the initial decrease in transmission is assigned as being due to this. The response of this peak at 950 nm is approximately 1.8 times greater than that at 1550 nm. The electron optical cross-section in TiO_2 is 4.5 times bigger at 950 nm than at 1550 nm. However, in FTO $\sigma(950)_{FTO} << \sigma(1550)_{FTO}$. Therefore if electrons in the FTO were dominating the response, it would be expected that the difference in the transmission signal between the two wavelengths would be much larger. This suggests that electrons in the FTO are not dominating the response and it is possible that the signal observed at both wavelengths is essentially due only to electrons in the TiO_2. This will be the case if the Fermi energy in the FTO is unchanged from its value in the dark, which is possible in the ideal case where there is a negligible iR drop in the FTO electrode, a negligible overpotential at the cathode and no pH changes at the FTO surface when the cell is illuminated. A small iR drop in the FTO is likely as impedance results suggest the series resistance of the cell is approximately 10Ω and the current is less than 0.2mA, so the potential drop will be less than 2mV. Low resistance to charge transfer (R_{CT}) at the counter electrode is shown in Fig 6.5 and according to equation 7.2[15] this means that the exchange current (i_0) is high. This in turn means that the standard rate constant (k_0) for the reaction at the counter electrode is also high[16] therefore only a small overpotential will be required to drive significant currents according to the Butler-Volmer equation (Equation 2.10). Based on the low current produced by the cell, it is possible that the overpotential at the counter electrode will indeed be small; in further discussion it will be assumed that both this and the iR drop in FTO are negligible under short circuit conditions. However, changes in pH are not known and will be considered further.

$$R_{CT} = \frac{RT}{Fi_0} \quad \text{Equation 7.2}$$

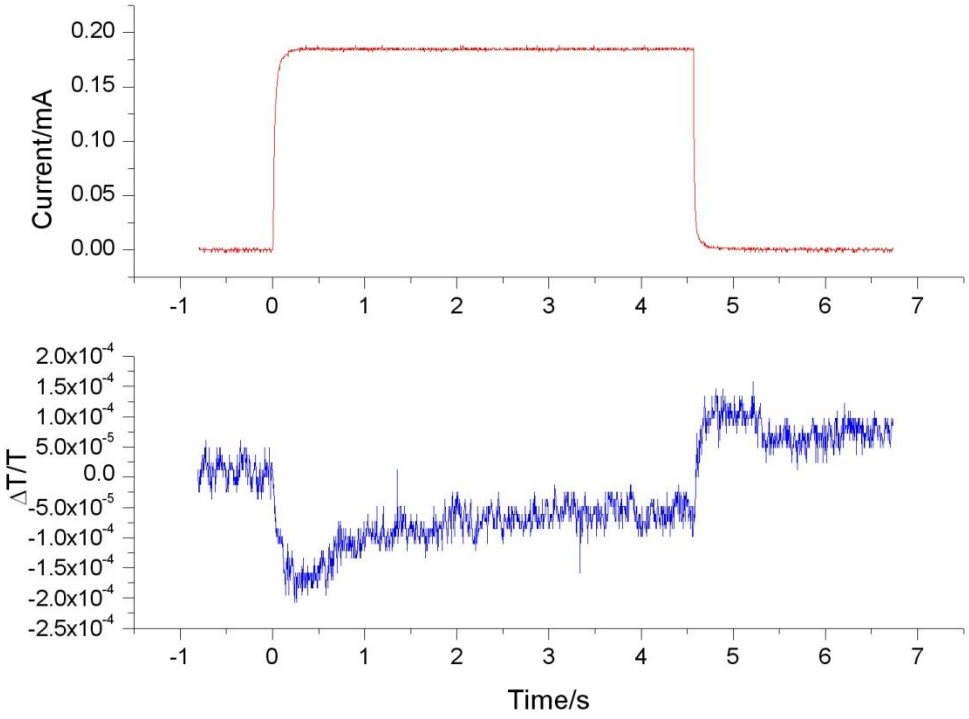

Fig 7.16 Voltage (red) and ΔT/T (blue) transient response of water cell (2M PMII, 0.05M I_2, 0.1M GSCN, 0.5M tBP, 1% Triton X-100) with an electrolyte pH of 7.45. Measured under short circuit condition with blue light (470 nm) illumination pulse with a light intensity of 3.77×10^{15} $cm^{-2}s^{-1}$. IR wavelength = 950 nm. Light on at t = 0, light off at ~ t = 4.5 s.

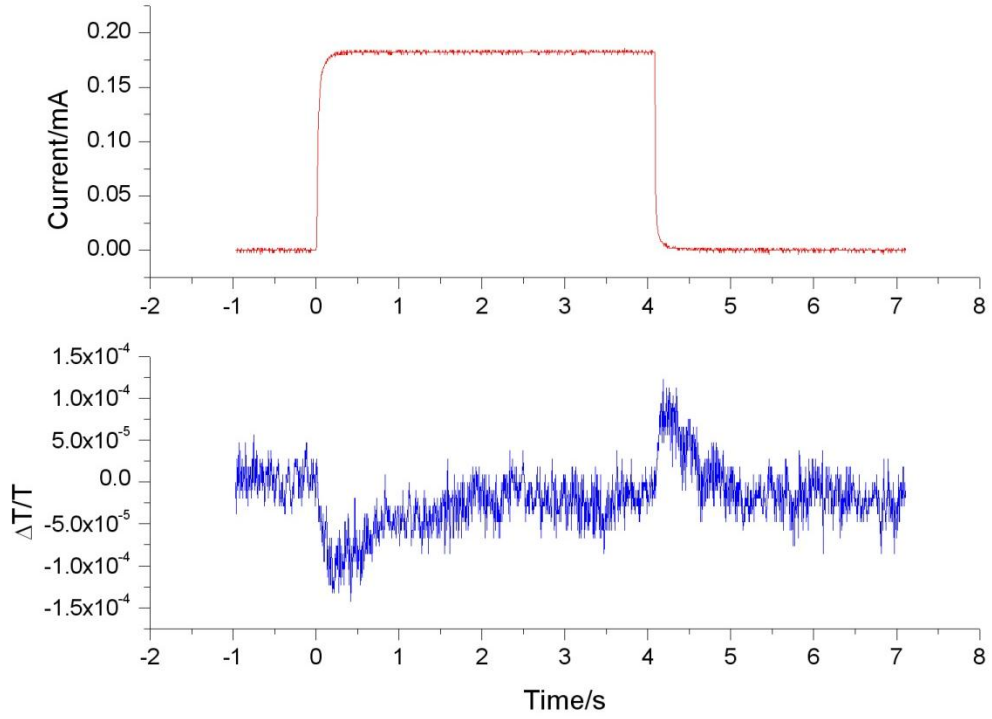

Fig 7.17 Voltage (red) and ΔT/T (blue) transient response of water cell (2M PMII, 0.05M I_2, 0.1M GSCN, 0.5M tBP, 1% Triton X-100) with an electrolyte pH of 7.45. Measured under short circuit condition with blue light (470 nm) illumination pulse with a light intensity of 3.77×10^{15} $cm^{-2}s^{-1}$. IR wavelength = 1550 nm. Light on at t = 0, light off at ~ t = 4 s.

In discussion focussing on Fig 7.7 and 7.8 the possibility of H^+ intercalation was introduced as described in equation 7.1, along with the possibility that this would generate shallow trap states with slow detrapping rates. It was seen from Fig 7.12 that the second part of the response only occurred above a certain light intensity, implying that it was dependant on sufficient driving force. Papers describing the H^+ intercalation show that a small driving force was required for the intercalation reaction. It is therefore likely that the slow increase in transmission following the initial fast decrease observed in water cells is caused either directly or indirectly by this intercalation process. However, the actual nature of the change is harder to determine.

Two possible scenarios are now examined, both of which could explain the slow increase in ΔT/T with time after the initial fast decrease. In the first, the effect of the intercalation process on pH is considered. The intercalation of H^+ into the TiO_2 will result in a decrease in the proton concentration at the surface and the substrate. This will continue until either further intercalation is not possible as no sites for this process are available, or until equilibrium is reached between H^+ intercalation and diffusion to the surface. This process will result in a higher pH at the surface, which as discussed earlier will increase the CB energy and the nE_F. At the FTO substrate, an increase in the CB energy will increase the band bending and the width of the depletion layer, resulting in a decrease in the number of electrons. However, the fact that a very similar signal is observed at both 950 nm and 1550 nm suggests that changes in electron density in FTO are not significantly influencing the signal.

The effect of bulk electrolyte pH on the signal is compared in Fig 7.18 and 7.19. It can be seen that at the higher pH of 7.45, the signal behaviour is as described previously for the water cell. However, at lower pH, the behaviour becomes similar to that of an acetonitrile cell and there is no slow increase in ΔT/T with time. At lower pH, it is expected that there is minimal pH change near the surface as the high bulk H^+ concentration quickly replenishes any H^+ lost through intercalation. This would mean the conduction band position is not greatly altered from its original position by the light pulse. Therefore at low pH, H^+ intercalation does not lead to a slow increase in ΔT/T with time. As discussed above, at higher pH H^+ intercalation could result in a change in the local pH and lead to the

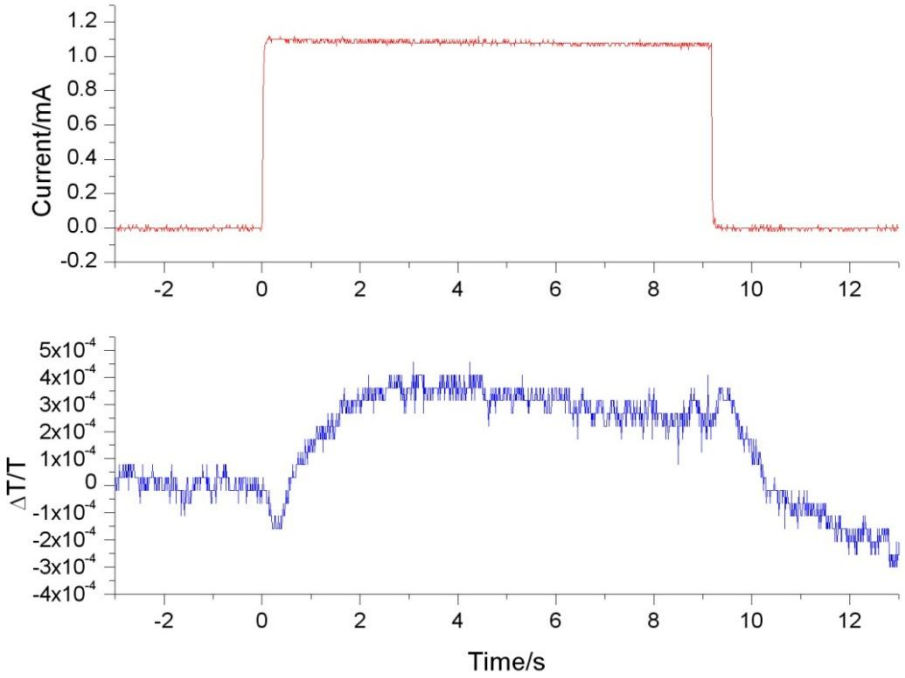

Fig 7.18 Voltage (red) and ΔT/T (blue) transient response of water cell (2M PMII, 0.05M I_2, 0.1M GSCN, 0.5M tBP, 1% Triton X-100) with an electrolyte pH of 7.45. Measured under short circuit condition with green light (530 nm) illumination pulse. IR wavelength = 1550 nm. Light on at t = 0, light off at ~ t = 9 s.

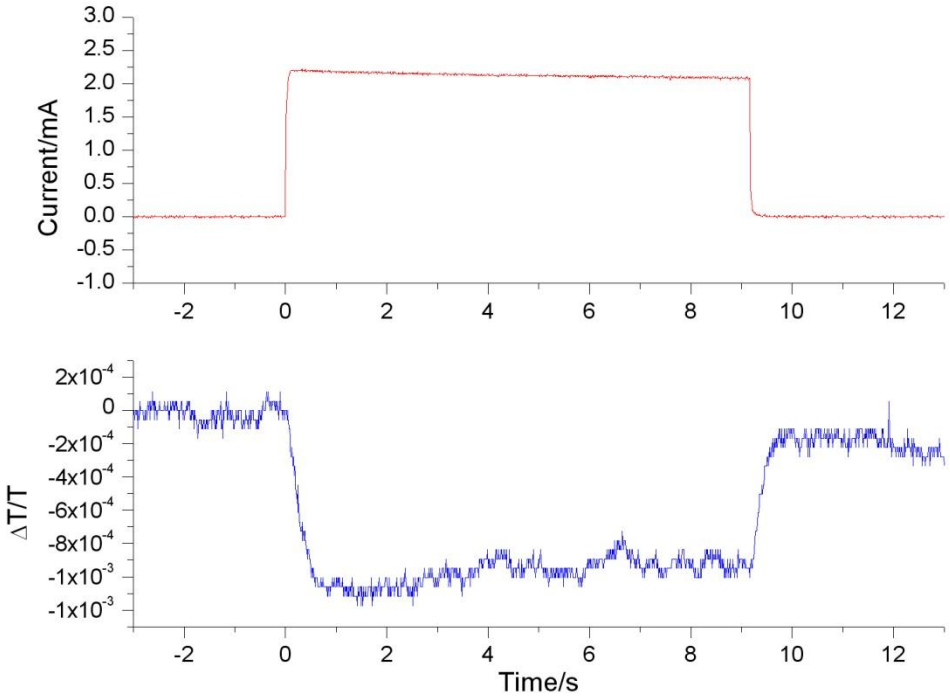

Fig 7.19 Voltage (red) and ΔT/T (blue) transient response of water cell (2M PMII, 0.05M I_2, 0.1M GSCN, 0.5M tBP, 1% Triton X-100, pH adjusted with 1M HCl) with an electrolyte pH of 4.99. Measured under short circuit condition with green light (530 nm) illumination pulse. IR wavelength = 1550 nm. Light on at t = 0, light off at ~ t = 9 s.

differences in the IR transmission observed. This scenario is reasonable if a mechanism by which an increase in the TiO_2 CB position results in a decrease in the number of electrons observed in the TiO_2 can be provided. A possible mechanism could be envisaged as follows. Upon an increase of the conduction band edge, the nE_F will be raised by a similar amount if the number of electrons in the film remains the same. However, such an increase in electrochemical potential will increase the rate of the reaction between electrons in the semiconductor and I_3^- which will result in an increased flow of charge out of the semiconductor, lowering electron density.

A second scenario is as follows. The intercalation of protons results in a change in the film as described in equation 7.1 involving the reduction of Ti^{IV} states to Ti^{III} states. The optical cross sectional values recorded above are based on films measured in acetonitrile (Sigma Aldrich, HPLC grade)[12] with a water content ≤0.01%. It is expected in this case that the intercalation of protons to form the shallow trap state described above will be much less likely, though there may be a low H^+ concentration due to dye adsorption. It is possible that the intercalation of protons may alter the optical cross section for electrons in the TiO_2. At the same time, the change in Ti oxidation states alters the material to a certain extent, which could reduce the availability of other traps. In this scenario, it is envisaged that the increase in the transmission signal after the fast initial decrease is due directly to the intercalation of H^+ and subsequent changes in the optical cross section rendering electrons trapped in this way invisible at the wavelengths used. However the effect of bulk pH is less consistent with this scenario. At low pH it might be expected that intercalation would be faster or similar to the high pH case. However, it is seen that at low pH (Fig 7.19) the effect does not occur.

It is not entirely clear which, if any, of these scenarios are correct. The first appears to fit the data more completely assuming a mechanism is present that allows for a decrease in charge upon an increase in CB energy. However, though a mechanism is presented, it is not certain if it does occur particularly as it is seen earlier in this chapter that the nE_F increases with pH at the same rate as the expected CB increase. Further experimentation is required to fully understand the transient IR response of aqueous DSSCs. For example, the response of the two substrates without TiO_2 or dye may contribute to this. It would also be useful

to obtain data over a wider pH range and at a higher pH resolution. It has been observed however that water does have a particular transient response and this has been shown to be linked to the intercalation of H^+ and dependant on pH. Furthermore, it is likely that this produces shallow trap states which have a low detrapping rate, slowing electron transport for electrons in these traps which is in agreement with work by Halverson et al[1].

7.2.3.4 Continuity equation modelling of trapped electrons under short circuit/open circuit conditions

By modelling the trapped electron density using the continuity equation, it is possible to get more information about what is occurring at the different wavelengths. At 950 nm, the ratio between the open circuit IR response and the initial peak in the short circuit response is 1.7 and at 1550 nm the ratio is 13. Based on the continuity equation it is possible, using typical parameter values, to calculate the expected trapped electron density under these two potential conditions and compare ratios. Trapped electron density (n_t) values were determined using equation 7.3 where ΔE_F is calculated from equation 7.4 and n_c is found from the solution of the continuity equation (equation 2.27). Fig 7.20 shows the calculated ratio between the open circuit and short circuit responses as a function of L_n/d. L_n data is not available for this cell, but a preliminary EIS analysis suggests that L_n/d is less than or equal to one. In this case, the $n_t(OC)/n_t(SC)$ ratio is expected to be 2.5 or less. This fits well with the response at 950 nm, suggesting that this is indeed due primarily to electrons in TiO_2 trap states. However, at 1550 nm, the ratio is significantly higher, which agrees with the interpretation that UV light at this wavelength is mainly absorbed by electrons that are not localized in TiO_2 trapping states.

$$n_t(x) = N_{t,0} \exp\left(\frac{-E_c}{k_B T_c}\right)\left(\left(\exp\left(\frac{\Delta E_F}{k_B T_c}\right)\right)-1\right) \qquad \text{Equation 7.3}$$

$$\Delta E_F = E_C + k_B T \ln\left(\frac{n_c}{N_c}\right) \qquad \text{Equation 7.4}$$

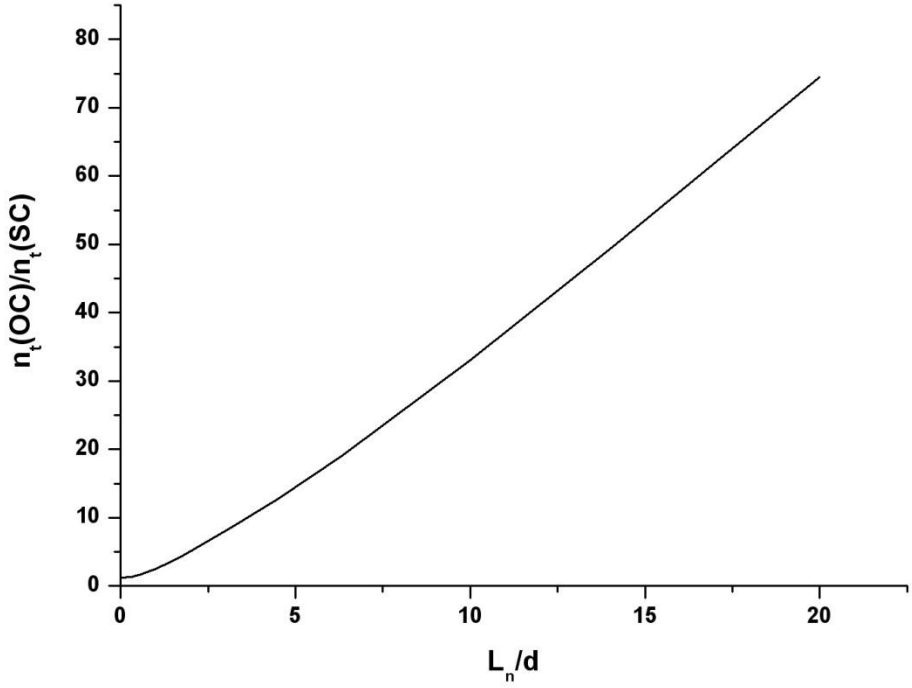

Fig 7.20 Ratio between trapped electron density at open circuit and short circuit conditions vs L_n/d as calculated based on the continuity equation. Based on N_{t0} = 10^{19}, T_c = 500 K (determined from OCVD response of cell used in section 7.2.3.3), $N_C = 10^{21}$, D_0 = 0.4 cm^2s^{-1}, d = 10 μm, $I_0 = 4x10^{15}$, α = 1500 cm^{-1}, k_{ext} = 10^5 cms^{-1}, E_C = 1.

7.3 Conclusions

The pH of the electrolyte has been seen to have several effects on aqueous DSSC performance. Firstly desorption of dye has been seen to occur as the electrolyte is taken to pH values of ten and above and this may begin to occur at lower pH values as well. This has been explained in terms of the effect of pH on surface charge and the dye adsorption/desorption equilibrium. It has also been observed that cell V_{OC} increases with pH whereas J_{SC} decreases though no overall change in efficiency was recorded. This is likely to be due primarily to an increase in the energy of the conduction band with pH. As has been seen in a previous chapter, some unexpected changes in the redox potential were observed which are considered to be due to changes in the liquid junction potential. The effect of tBP was examined and seen to cause changes primarily due to it increasing the cell pH. However, it was also seen that adsorption of the basic form of tBP onto the TiO_2 surface may occur and reduce the total dye coverage under certain conditions. Finally, the transient behaviour of electrons in

the cell was examined under several conditions using infrared illumination. It was seen that the behaviour of aqueous cells was considerably different to acetonitrile cells particularly under short circuit conditions. This was found to be due to proton intercalation into the TiO_2 film, and a model describing the behaviour observed was proposed. It was seen that the response of the film depended on the wavelength of the IR light and that electrons in the TiO_2 and the FTO dominated the response at 950 nm and 1550 nm respectively.

7.4 References

(1) Halverson, A. F.; Zhu, K.; Erslev, P. T.; Kim, J. Y.; Neale, N. R.; Frank, A. J. *Nano Lett* **2012**, *12*, 2112.

(2) Matylitsky, V. V.; Lenz, M. O.; Wachtveitl, J. *J Phys Chem B* **2006**, *110*, 8372.

(3) (a) Enright, B.; Redmond, G.; Fitzmaurice, D. *J Phys Chem-Us* **1994**, *98*, 6195(b) Lyon, L. A.; Hupp, J. T. *J Phys Chem B* **1999**, *103*, 4623.

(4) O'Regan, B.; Li, X. E.; Ghaddar, T. *Energ Environ Sci* **2012**, *5*, 7203.

(5) Lipta\k, B. l. G. *Instrument engineers' handbook*; 4th ed. / Béla G. Lipták, editor-in-chief. ed.; CRC Press: Boca Raton, Fla. ; London, 2003.

(6) (a) Preocanin, T.; Kallay, N. *Croat Chem Acta* **2006**, *79*, 95(b) Parks, G. A. *Chem Rev* **1965**, *65*, 177.

(7) Yu, Z.; Vlachopoulos, N.; Gorlov, M.; Kloo, L. *Dalton T* **2011**, *40*, 10289.

(8) Fernandez-Nieves, A.; Richter, C.; de las Nieves, F. J. *Progress In Colloid and Polymer Science* **1998**, *110*, 21.

(9) Nusbaumer, H.; Moser, J. E.; Zakeeruddin, S. M.; Nazeeruddin, M. K.; Gratzel, M. *J Phys Chem B* **2001**, *105*, 10461.

(10) Boschloo, G.; Haggman, L.; Hagfeldt, A. *J Phys Chem B* **2006**, *110*, 13144.

(11) Sigma-Aldrich, 360457 product specification, www .sigmaaldrich.com/catalog/product/sial/360457?lang=en&region=GB, 08.07.13.

(12) van't Spijker, H.; O'Regan, B.; Goossens, A. *J Phys Chem B* **2001**, *105*, 7220.

(13) Peter, L. M. *Phys Chem Chem Phys* **2007**, *9*, 2630.

(14) Nguyen, T. T. O.; Peter, L. M.; Wang, H. X. *J Phys Chem C* **2009**, *113*, 8532.

(15) Bard, A. J.; Faulkner, L. R. *Electrochemical methods : fundamentals and applications*; 2nd ed. ed.; John Wiley: New York ; Chichester, 2001.

(16) Fisher, A. C. *Electrode dynamics*; Oxford University Press: Oxford, 1996.

Chapter 8: Dye regeneration and mass transport in aqueous dye sensitized solar cells

8.1 Introduction
8.2 Experimental
    8.2.1 SECM
8.3 Results
    8.3.1 Dye regeneration
    8.3.2 Spectroelectrochemistry
    8.3.3 Diffusion in the electrolyte
        8.3.3.1 Potential effect
    8.3.4 Photocurrent limits at high light intensity
    8.3.5 Scanning Electrochemical Microscopy
8.4 Conclusions
8.5 References

8.1 Introduction

Under operating conditions, several electrochemical processes are occurring in the DSSC including the reduction of I_3^- at the counter electrode and the regeneration of oxidised dye molecules by I^-. These processes are affected by parameters such as the reaction rate for the reduction or oxidation and the diffusion constant of I_3^- or I^- through the electrolyte. In changing to water from acetonitrile, these parameters are likely to be affected by, for example, the different viscosity of the two solvents which is expected to result in an altered cell performance. In this chapter, several electrochemical experiments are presented looking particularly at dye regeneration by I^- and the effect of possible diffusion limits in water cells.

It has been observed in previous chapters that the major performance difference between cells made using water and acetonitrile is in the photocurrent. It is seen in this chapter that this is likely to be at least partly due to limits caused by slow I_3^- diffusion in the nanoporous semiconductor. Analysis of cyclic voltammograms shows that while in acetonitrile dye regeneration by LiI is fairly easy to measure in a three electrode cell, in water it is not clearly observed. Some dye regeneration must be occurring to enable a photocurrent, however it is possible that this process is occurring more slowly in water.

8.2 Experimental

Details of the equipment used for experiments shown in this chapter can be found in chapter 3. Electrochemical measurements were performed in a three electrode setup using 5mL of background electrolyte which was either 0.1M tetrabutylammonium hexafluorophosphate (tBAHFP) (Sigma-Aldrich) in acetonitrile (Sigma-Aldrich) or 0.2M KNO_3 (Sigma-Aldrich) in water (Milli-RO, in-house). Small volumes of LiI (Sigma-Aldrich) in the appropriate background electrolyte were added to the cell during experiments. Electrodes used are described in the results section.

8.2.1 SECM

Scanning electrochemical microscopy was carried out using a SEM system (CHI 900b) incorporating an XYZ stage and potentiostat. The Pt ultramicroelectrode (UME) was 10 μm at the tip and its position was controlled by the XYZ stage. The reference electrode was $Ag/AgNO_3$ (10 mM, Sigma-Aldrich) in acetonitrile (Sigma-Aldrich) and when used the counter electrode was Pt wire. Electrochemistry was carried out in 0.1M tetrabutylammonium perchlorate (TBAP) (Sigma-Aldrich) in acetonitrile containing either 1 mM ferrocenemethanol (FcMeOH) (Sigma-Aldrich) or 0.6M LiI (Sigma-Aldrich). The electrochemical cell was made of Teflon and had two parts which could be used to clamp the electrode securely; leaks were prevented by using a rubber O-ring. A hole below the electrode allowed a short light pulse, provided by a white light OLED light source controlled by a sourcemeter (Kiethley, 2440), to be shone onto the electrode. Electrodes were made of single layer TiO_2 dyed in Z907 as described in an earlier section.

8.3 Results

8.3.1 Dye regeneration

One of the key processes that must occur for a DSSC to work effectively is that of dye regeneration by the reduced form of the redox mediator. After electron injection from the excited dye, the dye is left in an oxidised state which must be reduced before further electron injection can occur. If electron transfer into TiO_2 is fast, and it has been shown to be in the order of picoseconds and faster for dyes such as N719 in acetonitrile[1], then dye regeneration can become the limiting factor for electron injection.

Electrochemistry in the form of cyclic voltammetry can be used to determine if dye regeneration is working effectively in a given electrolyte system. By using a three electrode cell with a dyed TiO_2 film, equivalent to a DSSC photoanode, as the working electrode and the relevant redox species in the electrolyte, processes at the photoanode which are similar to those expected in a dye cell can be measured. Cyclic voltammetry (CV) can be used to oxidise and, provided

no desorption or degradation occurs, reduce the dye to its original state on the reverse scan. If a redox species capable of reducing the oxidised dye is present as would be the case in a dye cell, the dye oxidation peak in the cyclic voltammogram (CV) increases because the dye is immediately reduced after oxidation and can be oxidised again. At the same time, the reduction peak is lost as the oxidised dye species has been chemically reduced by the redox species rather than at the electrode surface. This is called an EC' mechanism where C' describes a catalytic process (Equation 8.1). A quantitative study is not made of this data, but it is used qualitatively to judge the efficacy of this process in different electrolyte systems. Measurements have been performed previously by Fattori et al who showed EC' behaviour occurring for N719 in acetonitrile containing LiI[2]. The aim of this experiment was to determine if the regeneration of oxidised dye by I^- could be observed in the manner described above when LiI was added to the system where Z907 was the dye and water was the electrolyte solvent.

$$D \rightleftharpoons D^+ + e^-$$
$$3D^+ + 3I^- \rightarrow 3D + I_3^- \qquad \text{Equation 8.1}$$

At the potentials used in this experiment, TiO_2 is insulating so electron transport requires a different route than the semiconductor conduction band. Fattori et al[2-3] discuss hole transport where holes travel across the film by 'hopping' between adjacent dye molecules and this has several implications which are now considered. In a hole hopping charge transport mechanism, all the charge transferred to the substrate must go through the dye molecules adsorbed onto or very close to the FTO, so these molecules are likely to have a significant influence on the measured signal. If a dye molecule is rendered electrochemically inactive or desorbed from the surface it can no longer carry a signal. If the dye closest to the FTO substrate is degraded the signal will not continue even if the rest of the dye on the TiO_2 is still active.

Fig 8.1 shows the effect of scan rate on the electrochemical response of N719 adsorbed onto a nanoporous TiO_2 film working electrode in acetonitrile. It can be seen that the oxidation peak increases linearly with scan rate as shown in Fig 8.2 which is expected for a species adsorbed directly onto the electrode surface[4], but

that the reduction peak only begins to be seen at scan rates of 1V and above. This is consistent with the results reported by Fattori et al[2] who suggested that the oxidised dye undergoes irreversible chemical change to an electrochemically inactive species. In the faster scans the time that the dye spends in the oxidised state is too short for this to occur allowing the reduction peak to be clearly seen. Interestingly, the change in oxidation peak height with scan rate is still linear at the slower scan rates suggesting that the active dye is still present on the surface after the previous scan. A possible reason for this is that the inactive species produced desorbs from the surface and dye molecules from other parts of the film are able to adsorb in its place. This is most likely if the species inactivated is mostly the layer on or close to the FTO as this is only a small number of molecules relative to the TiO_2 film. In solution it is likely that physisorbed dye molecules are adsorbing and desorbing from the film so there should be free molecules present to replace damaged dye, which would result in a restored signal.

Fig 8.3 shows a CV measured for a TiO_2 film dyed with the Z907 dye and using water as the electrolyte solvent. Between the first and second scan there is a significant drop in the height of the oxidation peak and the reduction peak disappears. When the solution was vigorously degassed the signal recovered somewhat, but the shape of the CV did not return to that seen in the first scan. The reduction peak did not recover and the oxidation peak was broader and less pronounced. This suggests that dye degradation was also occurring here, but could mean that agitation/mixing of the solution aids the replacement of the damaged dye on the FTO surface.

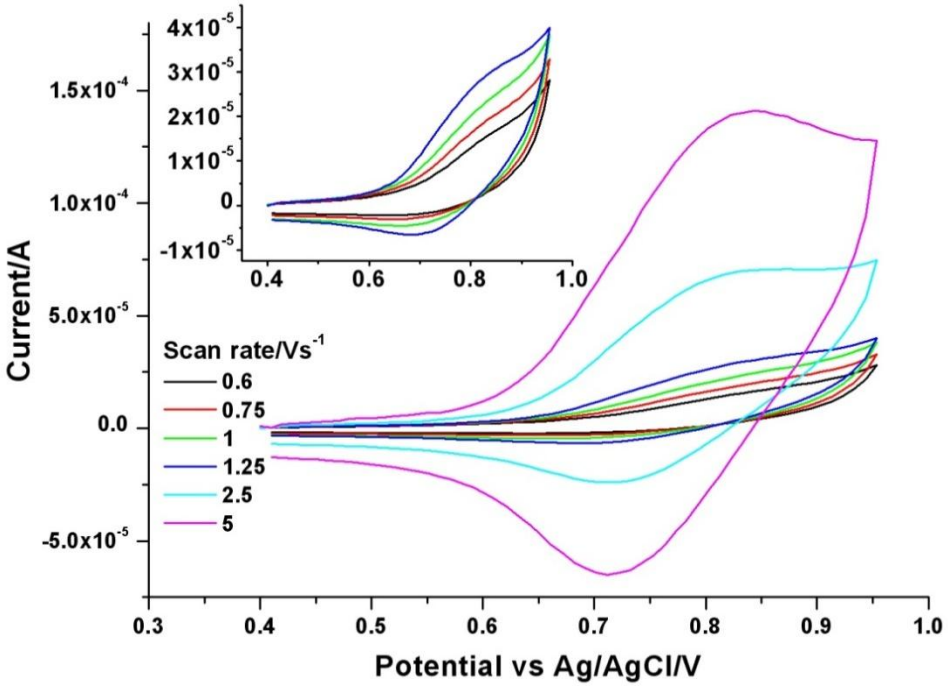

Fig 8.1 Cyclic voltammogram in 0.1M tBAHFP in acetonitrile. Working electrode is dyed (0.3mM N719) TiO_2 on FTO, counter electrode is Pt foil, reference electrode is Ag/AgCl (3M KCl). Showing effect of scan rate on system. Measurements were taken on one film starting at the highest scan rate.

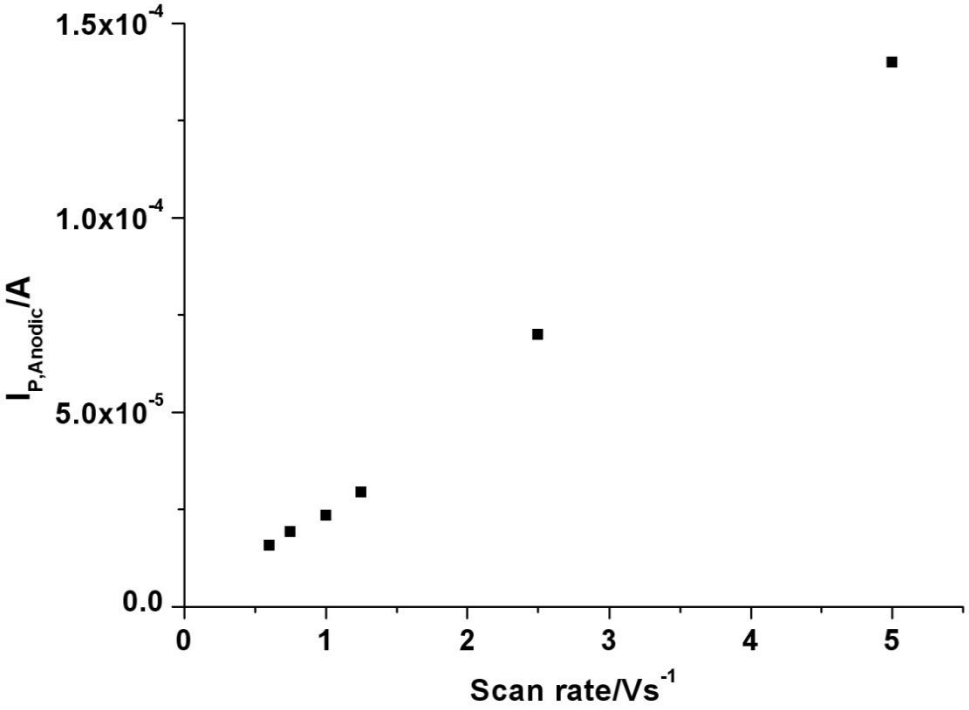

Fig 8.2 Effect of scan rate on oxidative peak current based on Fig 8.1. Linear increase up to ~1.5Vs^{-1} suggests oxidising species is adsorbed to surface. Change in gradient at higher scan rates may be related to behaviour changes seen as increase in reduction peak at higher scan rates as discussed in the text.

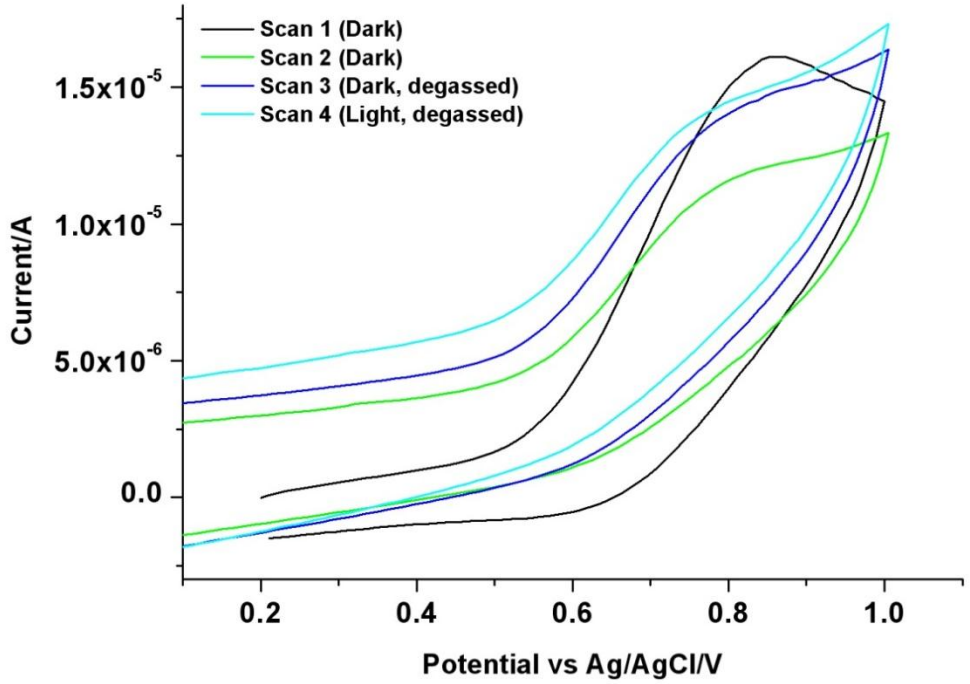

Fig 8.3 Cyclic voltammogram in 0.2M KNO_3 in water. Working electrode is dyed (0.3mM Z907) TiO_2 on FTO, counter electrode is Pt foil, reference electrode is Ag/AgCl (3M KCl). Scan rate is 1 Vs^{-1}. Showing peak variation for successive peaks with several minutes delay between each reading. Electrochemical setup was kept in the dark for scan 1-3 and opened to light before and during scan 4. Solution was degassed vigorously before scan 3 and 4.

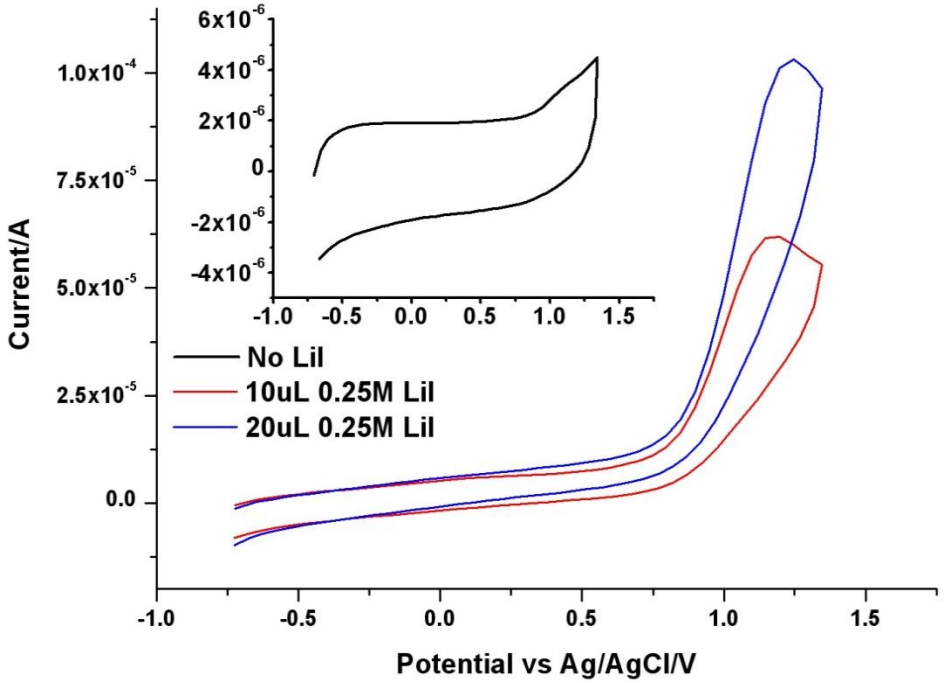

Fig 8.4 Cyclic voltammogram in 0.1M tBAHFP in acetonitrile. Working electrode is FTO glass, counter electrode is Pt foil, pseudo reference electrode is Pt wire later corrected to Ag/AgCl. Inset is control with no LiI present. Scan rate is 16Vs^{-1}. Showing oxidative electrochemistry of LiI in acetonitrile.

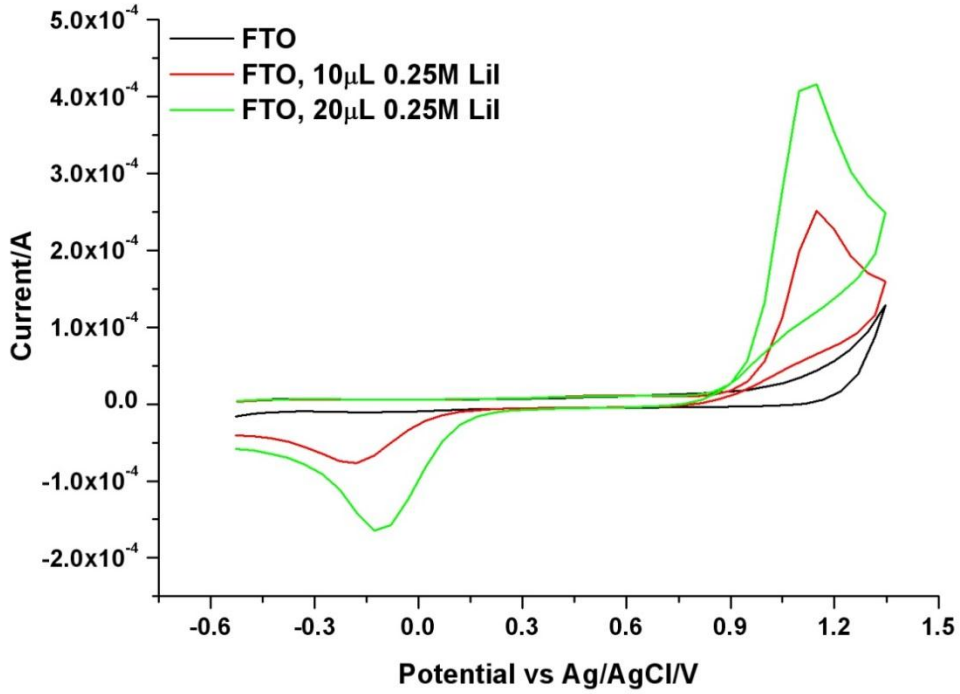

Fig 8.5 Cyclic voltammogram in 0.2M KNO_3 in water. Working electrode is FTO glass, counter electrode is Pt foil, pseudo reference electrode is Pt wire later corrected to Ag/AgCl. Scan rate is $16Vs^{-1}$. Showing electrochemistry of LiI in water.

Fig 8.4 and Fig 8.5 show background CVs measuring the effect of LiI on the FTO glass substrate when dye was not present. In Fig 8.6 which examines a TiO_2 film dyed in N719 in acetonitrile, it can be seen that when LiI is added the expected catalytic increase in the oxidation peak and loss of the reduction peak occurs. This indicates that the I^- is reducing the oxidised dye effectively. It is noted that there is a slight shift in the peak position and this is thought to be due to the effect of LiI on the surface charge of the FTO, which could alter the potential drop across the Helmholtz layer. FTO dyed with N719 also shows an EC' mechanism, although the peaks are shifted slightly to lower potentials.

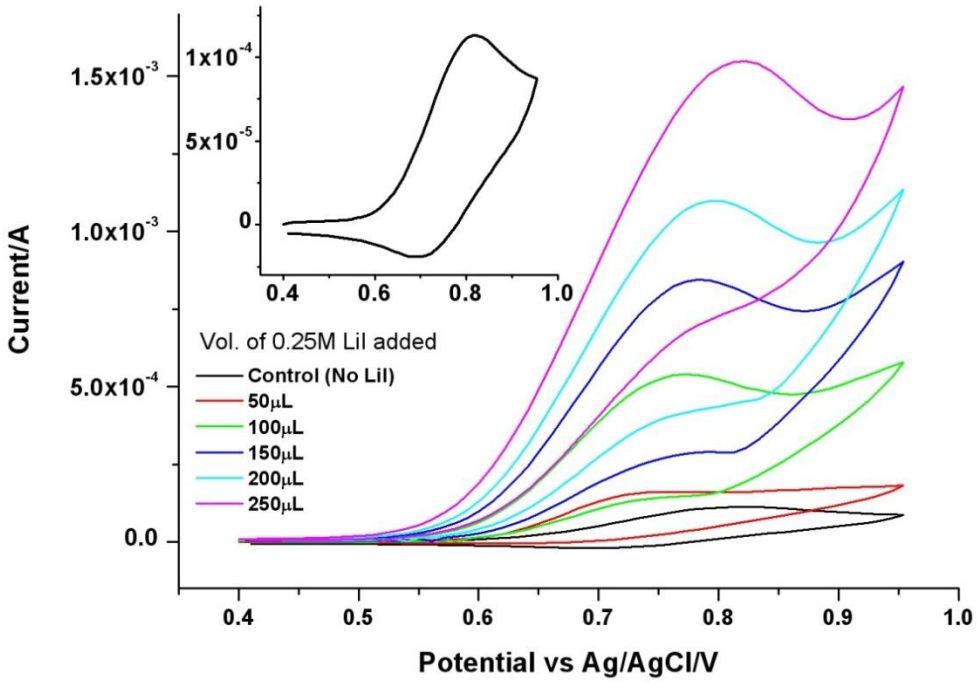

Fig 8.6 Cyclic voltammogram in 0.1M tBAHFP in acetonitrile. Working electrode is dyed (0.3mM N719) TiO_2 on FTO, counter electrode is Pt foil, reference electrode is Ag/AgCl (3M KCl). Scan rate $1.5Vs^{-1}$. Effect of increasing LiI concentration in acetonitrile.

Fig 8.7 shows a CV for an FTO film dyed with Z907 examined in water. In the inset it can be seen that on the first scan when no LiI was present, there is only one distinct reversible peak due to the dye. However, on subsequent scans with increasing LiI concentrations an additional oxidation peak is seen and the shape of the reduction changes, thought the response is the same at all LiI concentrations >0. The second peak is likely to be caused by dye degradation (which is covered in further detail in section 8.3.2) and as the response does not change with LiI concentration there is no evidence here that the EC' mechanism is occurring. Comparison of the main CV with Fig 8.5 shows that the large peak at ~1.0V is due to oxidation of LiI.

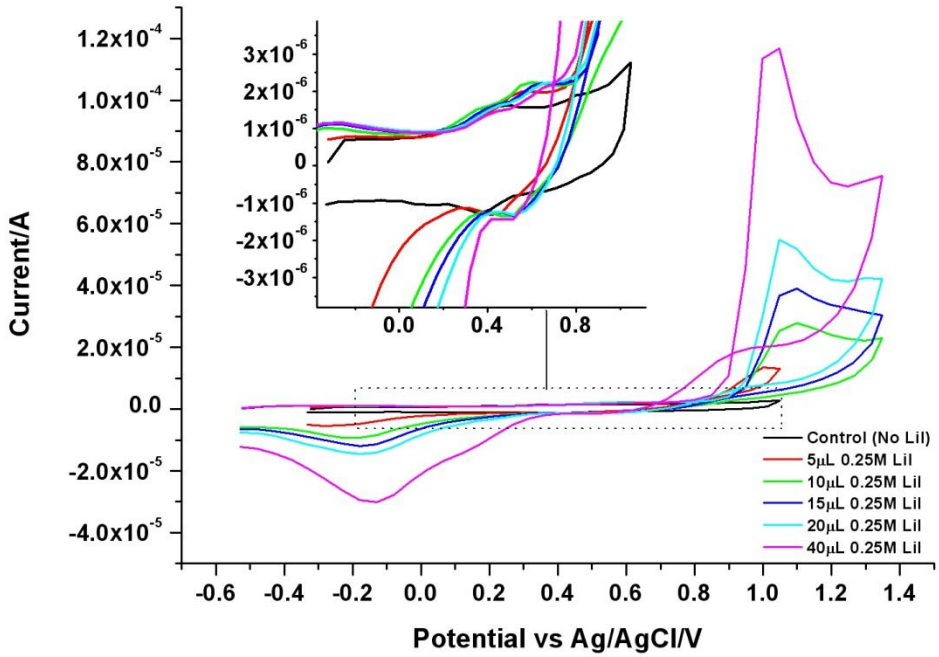

Fig 8.7 Cyclic voltammogram in 0.2M KNO_3 in water. Working electrode is FTO glass dyed with 0.3mM Z907, counter electrode is Pt foil, pseudo reference electrode is Pt wire later corrected to Ag/AgCl. Inset zooms in on reversible (in control) dye peaks. Scan rate is 16Vs^{-1}. Effect of increasing LiI concentration.

In Fig 8.8, the response for a TiO_2 film dyed with Z907 and examined in water is shown. In the background scan the oxidation peak maximum due to dye is at ~0.6V whereas when LiI is added it appears between 0.8 and 0.9V. The peak height increases significantly as LiI is added, however due to the change in position it is difficult to determine if it is due to oxidation of dye or LiI. The peak maximum due to LiI oxidation on FTO has been seen to occur between 1.0 and 1.1V. On dyed FTO (Fig 8.7) there was no evidence of the EC' mechanism occurring for Z907 in water and it seems likely that the situation is the same on TiO_2 as no significant change to the dye is expected on the two different substrates. If this is the case, then the oxidation peak observed in Fig 8.8 is due to LiI oxidation. However, further experimentation could be done to obtain a clearer idea of which species is causing the peak.

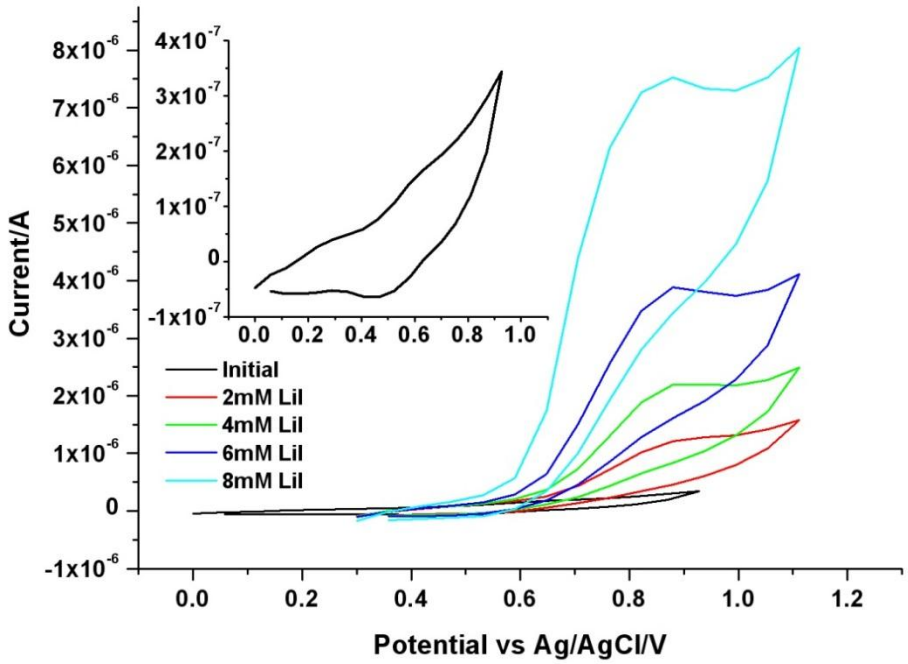

Fig 8.8 Cyclic voltammogram in 0.2M KNO_3 in water. Working electrode is dyed (0.3mM Z907) TiO_2 on FTO, counter electrode is Pt foil, reference electrode is Ag/AgCl (3M KCl). Scan rate $16Vs^{-1}$. Effect of increasing LiI. Data from 2nd of two consecutive scans in each case.

In this section it is seen that in acetonitrile, oxidised N719 is clearly reduced by LiI. However, when measuring CVs for Z907 in water the response is not as clear. On FTO some dye degradation was observed to occur and the oxidised dye did not appear to be reduced by LiI. On TiO_2 an increase in the oxidation peak was observed with increasing LiI, but it was possible that this was due to LiI oxidation at the FTO surface. Because aqueous cells have been shown to function effectively, it is known that dye regeneration must be functioning to some degree. The results measured on FTO in water may indicate that dye regeneration of Z907 is slow in water. If this is the case, it would be expected to limit the photocurrent production at a certain light intensity and this may be an alternative explanation for the limit observed in section 8.3.3 below, though such an interpretation would not be completely consistent with reference [6][6].

8.3.2 Spectroelectrochemistry

The possibility that degradation of the dye may occur when it is held in its oxidised state for a period of time and that this can cause difficulties in electrochemical measurements has been discussed above. A technique that can

be used to get additional information relating to dye degradation is spectroelectrochemistry. Because the dye interacts in a measureable way with both light and current, it is possible to combine measurements from UV/Vis spectroscopy with electrochemistry.

Fig 8.9 shows the initial electrochemical response of a TiO_2 film on FTO substrate dyed with Z907 measured in an aqueous electrolyte. The second scan shows a significant decrease in the oxidative peak, but after leaving for several minutes the signal is largely restored. This is slightly varied from the effect seen in Fig 8.3 above which may suggest that the recovery of the signal is very dependant on the TiO_2 film.

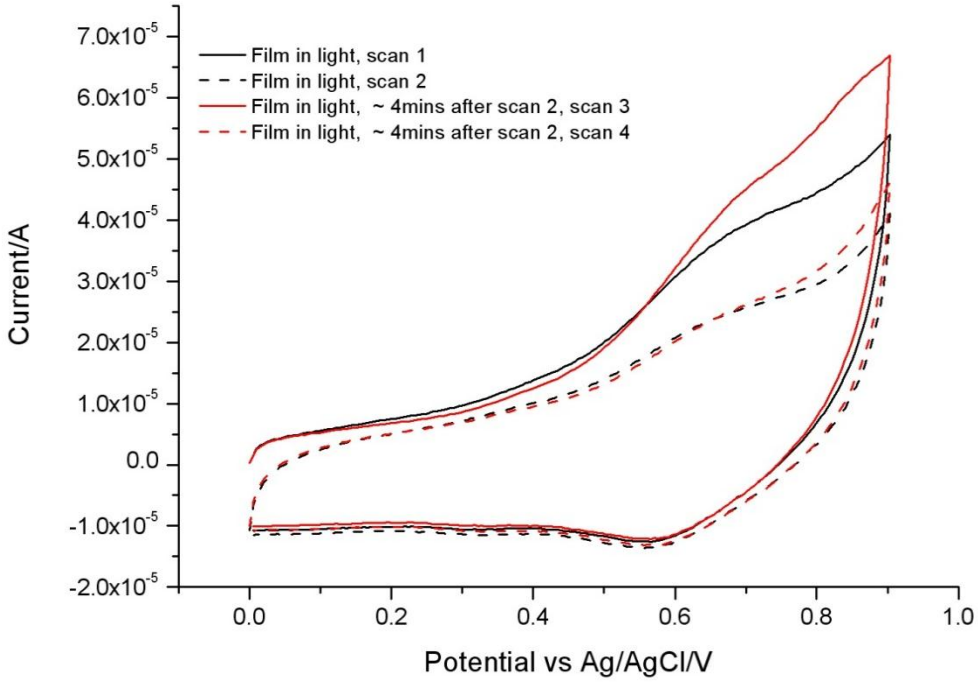

Fig 8.9 Cyclic voltammogram in 0.2M KNO_3 in water. Working electrode is dyed (0.3mM Z907) TiO_2 on FTO, counter electrode is Pt foil, reference electrode is Ag/AgCl (3M KCl). Scan rate $1.5Vs^{-1}$. Showing loss of signal after immediate measurement and subsequent increase in signal with time.

Previous to these CV measurements being taken, a UV/Vis spectrum (M1 in Fig 8.10) of the dyed film was measured. Having measured the CV, chronoamperometric measurements were then taken with simultaneous measurement of the UV/Vis spectrum (Fig 8.10) at several potentials based on the initial CV. Potentials examined were; 0.2V and 0.3V, where the dye is

expected to be fully reduced (M3 and M4); 0.5V, matching the onset of the oxidation peak (M5); 0.7V, the peak of the oxidation signal (M6) and 0.8V, where there is a significant overpotential for oxidation (M7). In the spectral range examined, it can be seen that as soon as a CV was measured for the dyed film there was a drop in the dye absorption maximum (ca. 530nm) and simultaneous increase in absorption around 800nm. A similar behaviour has been noted elsewhere in acetonitrile[3], however in that case the peak change occurred when the potential was at a position where oxidation of the dye took place, but returned to the initial situation on scanning to reducing potentials. In that work, degradation of dye on the FTO surface was considered to be most likely to be affecting the signal. The results shown here suggest that the initial CV damages the dye layer on or near the surface, preventing further changes when the additional measurements are made. Fig 8.11 shows clearly that there has been some chemical change to the dye as a result of the measurements as shown by the additional peak. This could correspond to dye which has degraded while oxidised and so the Ru centre now has a different ligand environment.

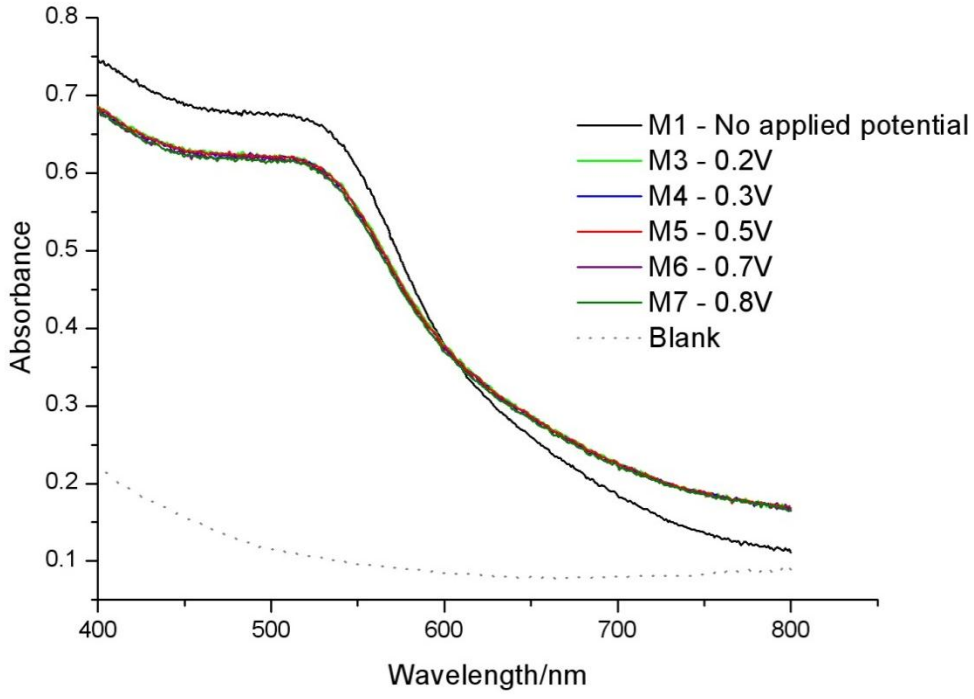

Fig 8.10 UV/Vis measurements of dyed (0.3mM Z907) TiO_2 on FTO substrate measured in aqueous 0.2M KNO_3 solution within quartz cuvette. M1 was taken before any electrochemical measurements performed. Subsequent readings taken during chronoamperometry at several potentials (0.2, 0.5, 0.7 and 0.8V).

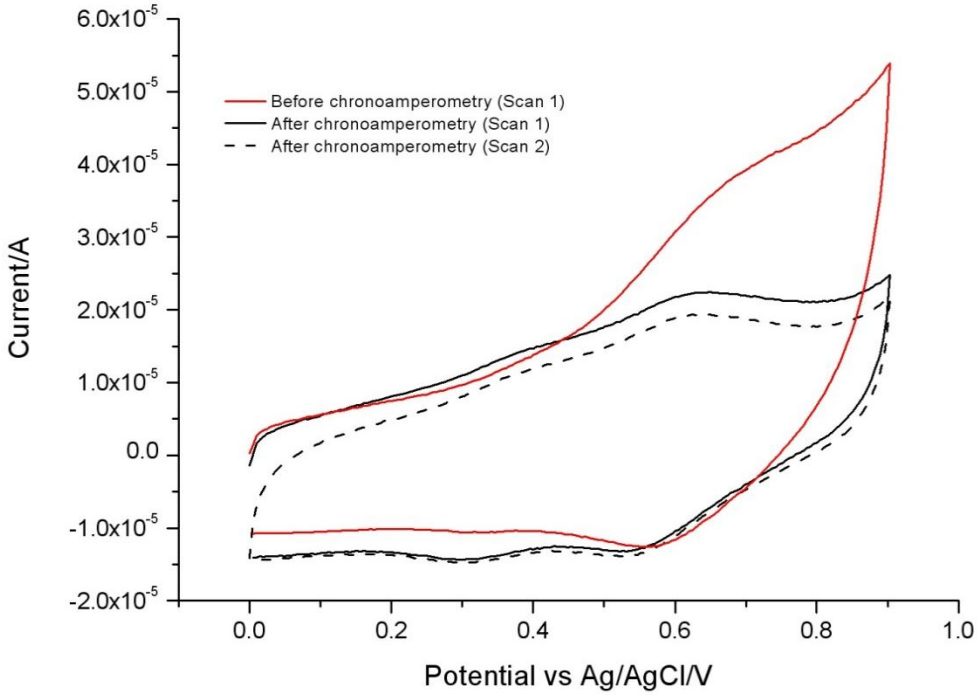

Fig 8.11 Cyclic voltammogram in 0.2M KNO_3 in water. Working electrode is dyed (0.3mM Z907) TiO_2 on FTO, counter electrode is Pt foil, reference electrode is Ag/AgCl (3M). Scan rate 1.5Vs^{-1}. Comparing voltammetric response before and after chronoamperometry and UV/Vis measurements shown in Fig 8.10.

In this section it is seen the there is a change in the spectral response of the dye after performing voltammetry on a dyed film. Applying further bias at increasingly oxidising potentials appears to cause no further change to this response, however a second reversible peak was seen in the CV after these analysis, suggesting that some of the dye has been chemically altered.

8.3.3 Diffusion in the electrolyte

When measuring IV curves for aqueous DSSCs, it has been noted that an initial current peak not seen in acetonitrile cells is often observed when the cell is scanned from 0V to higher voltages (Fig 8.12). The parameter 'short circuit current density' (J_{SC}) used to calculate cell efficiency is the current density measured when the cell potential is zero. As such, the analysis of cells showing this feature is complicated. An easy way to simplify analysis is to measure the cells from a lower initial potential (-0.1V has typically been used) which can be seen to move the current peak away from the measurement point of interest. However, the current peak is of interest in itself as it shows that for a short period

the cell is capable of sustaining higher photocurrent. If the mechanism behind it can be determined, it may enable cells to be developed that can consistently produce this higher current. Electrochemical measurements focussing on this feature were performed to determine the cause of these peaks.

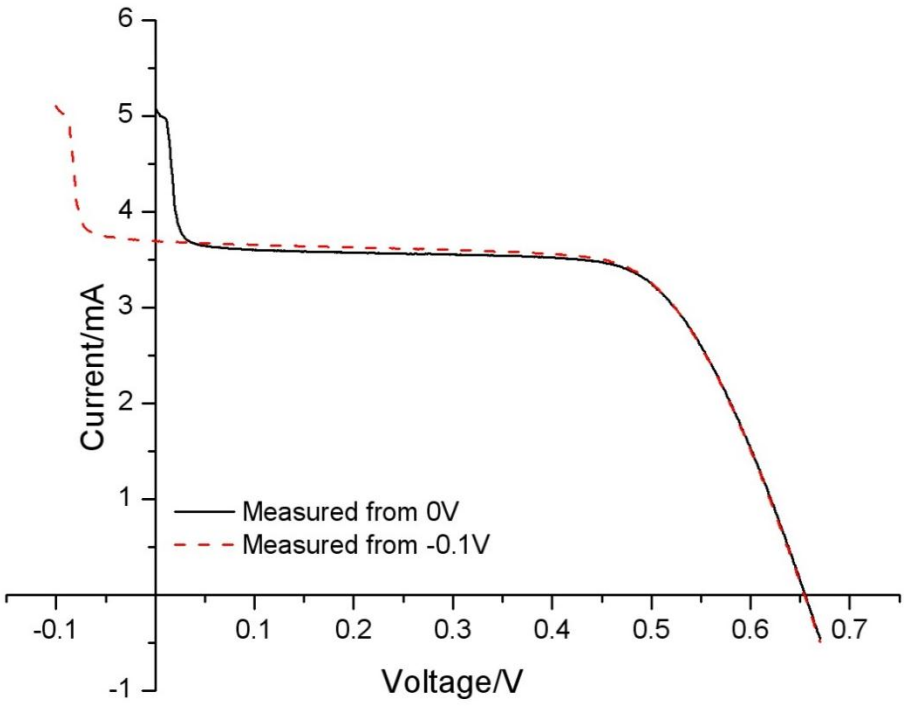

Fig 8.12 IV curves for a water cell (T193, dyed in 0.3mM Z907, electrolyte contained 2M PMII, 0.05M I_2, 0.1M GSCN, 0.5M tBP and 1% Triton X-100) measured under 1 sun AM1.5 illumination. Potential scanned from 0V to higher voltage (black solid line) and from -0.1V to higher voltage (dashed red line).

Cyclic voltammetry was first performed on a dye cell made using the Z907 dye and containing aqueous electrolyte with standard composition (chapter 3). The efficiency of this cell at 1 sun was 1.9%. Firstly, five consecutive scans were made of the cell between zero and 0.15V (fig 8.13). On the first scan a large peak is seen which decays by 0.11V and is not present on the return scan. Further scans do not show this peak, suggesting that it is caused by either a build up in charge or of a species which is then able to react but is not replenished by the conditions set for the measurement. A second measurement set (fig 8.14) taken with a pause of more than ten seconds between each measurement followed by a conditioning step where the cell was held at 0V for one to four seconds shows the peak reappearing on scans other than the initial scan, but the conditioning step causing the peak to decrease to nearly zero after

4s. It is noted that the experimental equipment holds the cell at its open circuit potential (nE_F approximately 0.7V vs redox potential under illumination) in between measurements, and it seems likely this causes the process that 'recharges' the initial peak. The conditioning step at 0V then allows some process to occur (probably linked to the flow of current) that removes the additional charge/species.

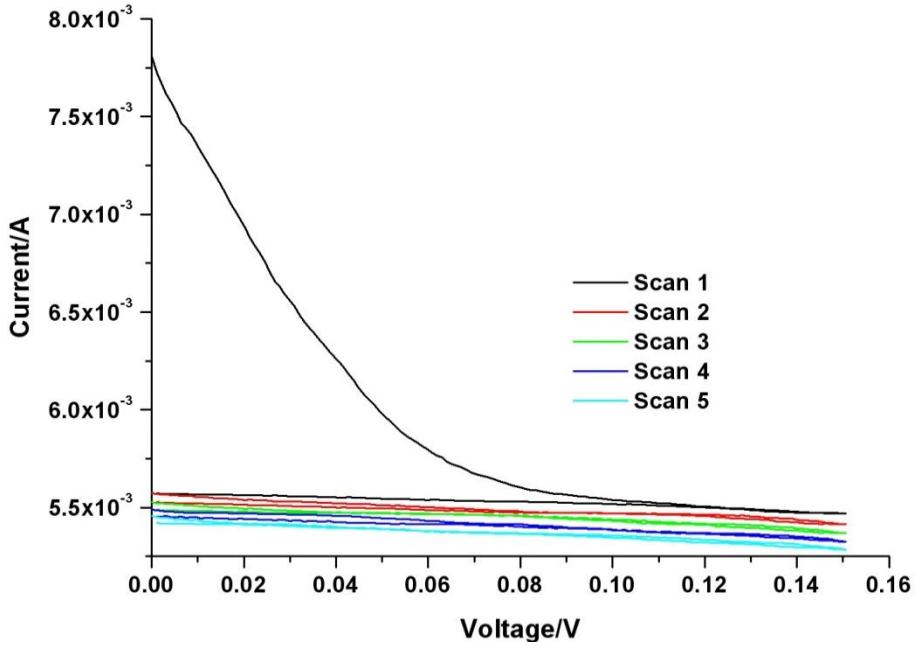

Fig 8.13 Cyclic voltammetry of water dye cell T193 (dyed in 0.3mM Z907, electrolyte contained 2M PMII, 0.05M I_2, 0.1M GSCN, 0.5M tBP and 1% Triton X-100) under 1 sun AM1.5 illumination. Five consecutive scans from 0V to 0.15V to 0V, scan rate 20mVs^{-1}. Showing initial peak disappearing completely on consecutive scans.

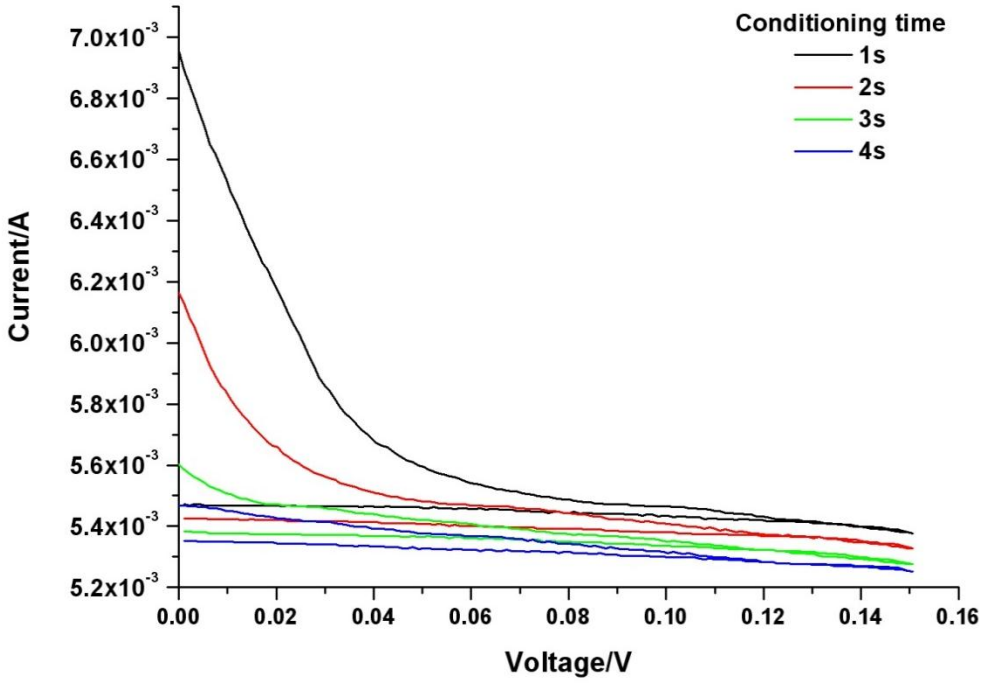

Fig 8.14 Cyclic voltammetry of water dye cell T193 (dyed in 0.3mM Z907, electrolyte contained 2M PMII, 0.05M I_2, 0.1M GSCN, 0.5M tBP and 1% Triton X-100) under 1 sun AM1.5 illumination. Five scans from 0V to 0.15V to 0V. Pause between each measurement, cell then held at 0V for a set condition time, scan rate 20mVs^{-1}.

8.3.3.1 Potential effect

In order to determine more precisely the conditions that generate the charges or species that generate the peak observed, several linear sweep measurement sets were performed involving five consecutive scans ensuring that the potential was only held at the values being measured. In these sets, the voltage range was increased up to values close to that seen in a dye cell under open circuit conditions.

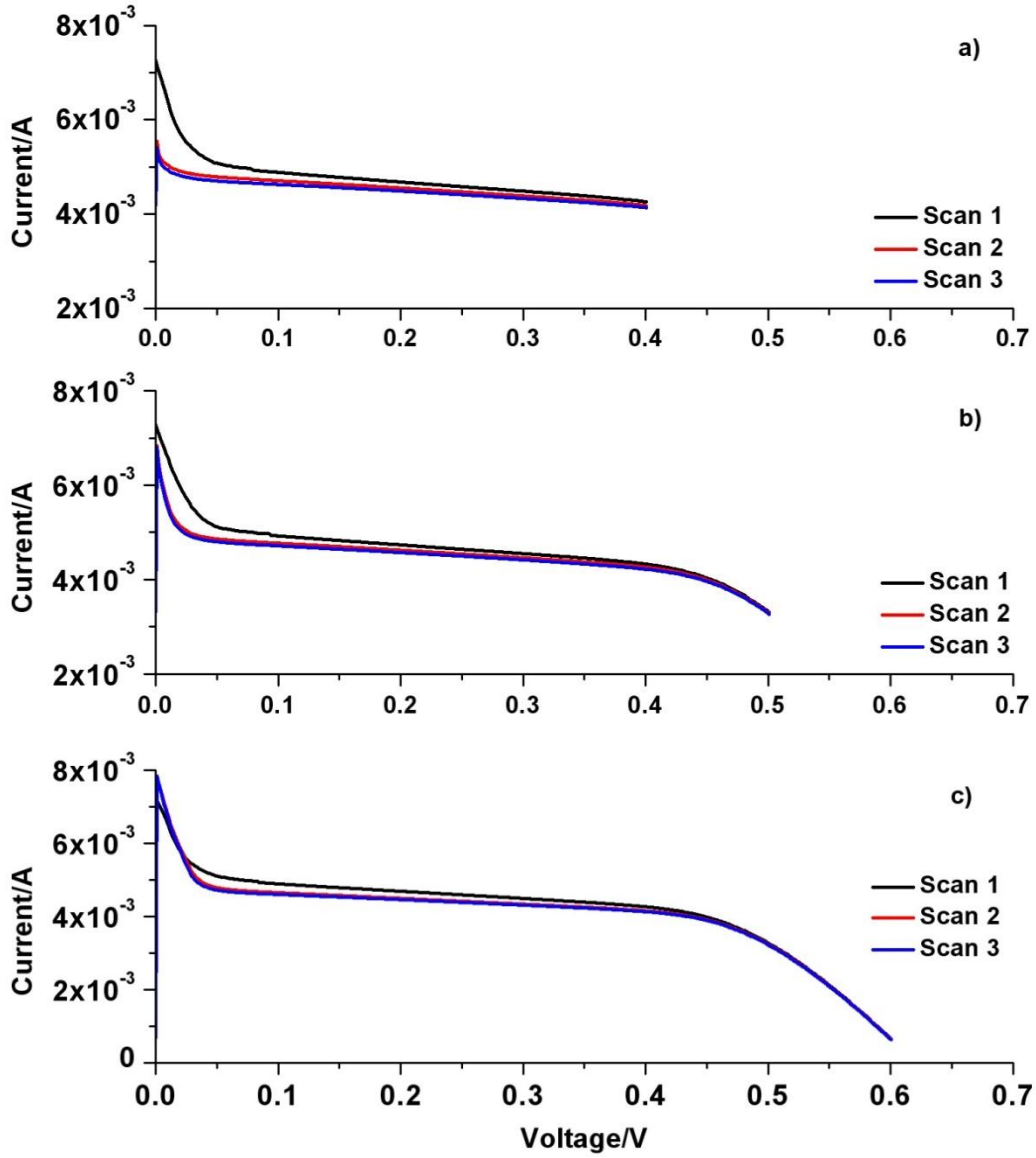

Fig 8.15 Linear sweep voltammetry of water dye cell T193 (dyed in 0.3mM Z907, electrolyte contained 2M PMII, 0.05M I_2, 0.1M GSCN, 0.5M tBP and 1% Triton X-100) under 1 sun AM1.5 illumination. Three consecutive scans from 0V to a) 0.4V, b) 0.5V and c) 0.6V. Scan rate 20mVs^{-1}.

When scanned to low potentials (not shown), there is a large peak in the first scan which is not seen in subsequent scans as in fig 8.13. Very small peaks are seen following an initial drop caused by the cell potential being instantaneously changed by ≥0.1V and these may be due to charging effects. As potentials are scanned to 0.4V (Fig 8.15a), the peak in subsequent scans starts to become larger and this becomes very obvious as the potential is increased further (Fig 8.15b, 8.15c). This indicates that a process that is occurring close to this

potential (~0.4→0.5V) is responsible for producing the charge/species involved in creating the peak seen at the beginning of the scan.

Several scans were measured and are shown in appendix D where the scan rate was altered for scans between 0 and 0.3V. These were calculated to take the same time as the measurements shown in Fig 8.15, and show no significant peak in the 2nd-3rd scans, and no change. This confirms that the effect seen here is caused by potential and not scan time.

There are several differences in the cell caused by an increase in potential. At low cell potentials the electron gradient in the semiconductor near to the FTO substrate is large and there is a high electron flux, limited by the rate of electron injection and the reaction of electrons with I_3^- at the counter electrode. As the cell potential is increased by increasing the external resistance between the electrodes, the electron density in the semiconductor increases. Above potentials at which electrons have a high enough electrochemical potential to allow rapid reaction with I_3^- to occur, the photocurrent starts to decrease rapidly as the cathodic current flow at the semiconductor|electrolyte interface decreases the local electron concentration while the electrochemical potential at the substrate continues to rise, resulting in a lower electron concentration gradient across the semiconductor. At V_{OC}, the gradient is flat and no current flows. However, there are more electrons in the electrode in localised and conduction band states than under short circuit conditions.

In terms of redox species, when the cell is at 0V (I_{SC}), the $[I_3^-]_{TiO2,surface}$ concentration is high compared to at higher potentials (e.g.V_{OC}) as there is less reaction with semiconductor electrons occurring, and $[I^-]_{TiO2,surface}$ concentration is low as this back reaction produces I^-. The $[I_3^-]_{Pt,surface}$ concentration is likely to be low at 0V as the electron flux is limited by the reaction between electrons and I_3^- at this interface and electron injection, whereas $[I^-]_{Pt,surface}$ concentration will be high as it is produced in this reaction. In quickly changing from open circuit potential to 0V, there is suddenly a higher electron concentration than when at open circuit, along with a high $[I_3^-]_{Pt,surface}$ and high $[I^-]_{TiO2,surface}$. There is also a lower $[I_3^-]_{TiO2,surface}$ than usual and lower $[I^-]_{Pt,surface}$. The relative concentrations of

the different redox species under short circuit and open circuit conditions are represented in a simplified diagram in Fig 8.16.

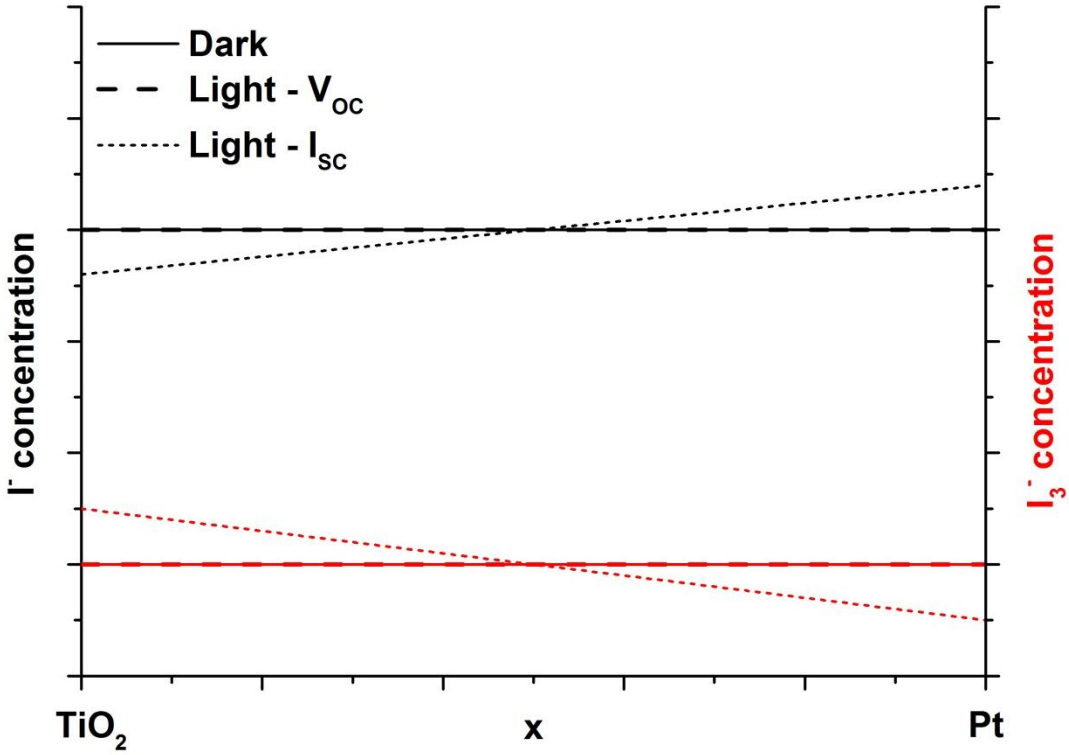

Fig 8.16 Simplified qualitative representation of the concentration of I^- (black) and I_3^- (blue) in the DSSC between the TiO_2 substrate and the Pt. This representation neglects the influence of the nanoporous semiconductor; concentration gradients and absolute values are not to scale.

Several of these fast changes caused by the step change in potential could result in a higher short lived photocurrent than under normal conditions involving scanned potential changes. With the charge now available, the higher $[I_3^-]_{Pt,surface}$ allows for greater electron flux, which will decrease based on the diffusion constant of I_3^- in the bulk and the rate of electron injection. If the injection of electrons is limited by the regeneration of dye, the higher $[I^-]_{TiO2,surface}$ will allow for increased injection flux and decrease based on the I^- diffusion constant in the semiconductor pores. The lower $[I_3^-]_{TiO2,surface}$ is less likely to significantly influence the photocurrent as at 0V the nE_F at the semiconductor surface is lower than at higher potential, so the reaction between electrons in TiO_2 and I_3^- is slower. The low $[I^-]_{Pt,surface}$ is unlikely to have much effect as any anodic current at the Pt is generally small.

[I^-] is at a much higher concentration than [I_3^-] and also has a faster diffusion coefficient. It is also possible that dye regeneration is fairly slow in water anyway as suggested above and by Boschloo et al[7], making it unlikely that the concentration of I^- near to the semiconductor will change in a fashion that significantly alters dye regeneration here. In order to explain this peak fully it must also be considered that it is not typically observed in acetonitrile cells. Electron transport rates are likely to be comparable between the cells - there are essentially no transport resistance variations based on EIS measurements between cell types (see Fig 6.3). This leaves the diffusion of species in the electrolyte. Based on the relative concentration of the species and their relative size and respective diffusion constants, it is most likely that [I_3^-] is the limiting species. However, if the limit is based on the bulk diffusion rate we would expect all water DSSCs to show a current peak limit at similar photocurrents. This is not seen and the limit (based on the appearance of the current peak) does not always occur. Therefore it is suggested that the limit is due to the slow diffusion of I_3^- though the semiconductor pores. A calculation based on the diffusion constant for I_3^- (1.1×10^{-9} $m^2 s^{-1}$. A precise value could not be found for this system. An approximate value was calculated as shown in equation 8.2 from literature values for the diffusion of I^-, Br_3^- and Br^- [8]) and equation 8.3 allows an approximate diffusion layer thickness to be calculated as a function of time (figure 8.17). Considering that the current peak typically took 5s or less to decay, this corresponds to a calculated diffusion layer of between 100 and 150 μm. This clearly shows that on the time scales of interest the diffusion layer would be influenced by diffusion of I_3^- through the semiconductor pores based on a cell thickness of 25 μm and semiconductor thickness of 10 μm.

$$D_{I_3^-} \approx D_{I^-}(D_{Br_3^-} / D_{Br-}) \qquad \text{Equation 8.2}$$

$$L_D = \sqrt{\pi D t} \qquad \text{Equation 8.3}$$

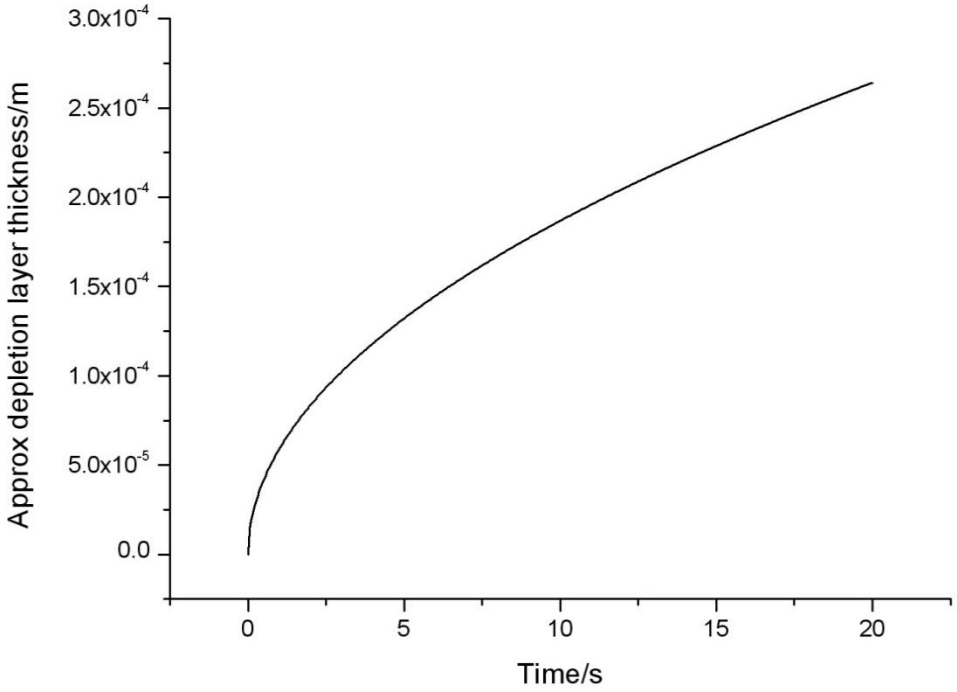

Fig 8.17 Calculated approximate depletion layer thickness for I_3^- in water based on a diffusion constant of 1.1×10^{-9} $m^2 s^{-1}$ (A precise value could not be found for this system. Value used calculated from equation 8.2[8]) and equation 8.3.

The implication is that either through selection of a redox mediator with a higher diffusion coefficient, or through engineering of the semiconductor to generate larger pores, the photocurrent limit in water cells could be increased resulting in higher cell efficiencies.

This section shows that initial current peaks observed in water cells are likely to be caused by the slow diffusion of I_3^- through the semiconductor pores. To measure CV plots that show I_{SC} values which correspond to the real limited current, measurements are started at -0.1V rather than 0V. It is suggested that engineering of the porous structure of the semiconductor could result in improved photocurrents.

8.3.4 Photocurrent limits at high light intensity

Another method that has been used to examine the effect of diffusion limitation on dye cells involves recording the cell photocurrent as a function of light intensity. As light intensity is increased the electron injection flux increases and under short circuit conditions this should directly lead to an increase in

photocurrent. This will continue until a limit is reached caused by either kinetic or mass transport limits which will show as a plateau region in the plot. Possible kinetic limits include the rate of electron injection, the rate of dye regeneration or the rate of the reaction at the counter electrode. Mass transport limits include the transport of I^- to the oxidised dye or the transport of I_3^- to the counter electrode. Law et al[6] show that in water cells there is an excess of charge built up in the TiO_2 at higher light intensities, implying that injection processes are occurring faster than the reduction of I_3^- at the counter electrode. Based on other measurements they also saw evidence of diffusion limitation and proposed that the diffusion of I_3^- through the nanoporous TiO_2 was the ultimate cause of such a limitation. The analysis performed above also shows that slow diffusion of I_3^- results in current limitations.

Fig 8.18 shows a direct comparison of J_{SC} vs I_0 plots between acetonitrile and water cells based on several cell repeats; no photocurrent limit is observed up to 6.5mAcm^{-2}. Similar plots are examined for cells made with several variations and the cell T323 is included in most graphs to enable simple comparison; T323 is an acetonitrile cell that has 3M PMII in the electrolyte and is dyed with Z907. Fig 8.19 shows the effect of using a thinner film. If two films are identical apart from the TiO_2 thickness, it is expected that the thinner film would produce a lower photocurrent due to the reduction in adsorbed dye because of the lower surface area. However, it should also show a higher photocurrent limit because the porous film, which is suggested to cause the diffusion limitation, is thinner. In the case of these cells it can be seen that there is a photocurrent limit at around 1.5mAcm^{-2}. It is interesting to compare these with cells made with double layer films which show no photocurrent limit up to 6.5mAcm^{-2}. These cells were made in different batches and it appears that the diffusion coefficient is very sensitive to the cell fabrication – this is consistent with a limit caused by the porous structure which is likely to vary a little between different fabrications.

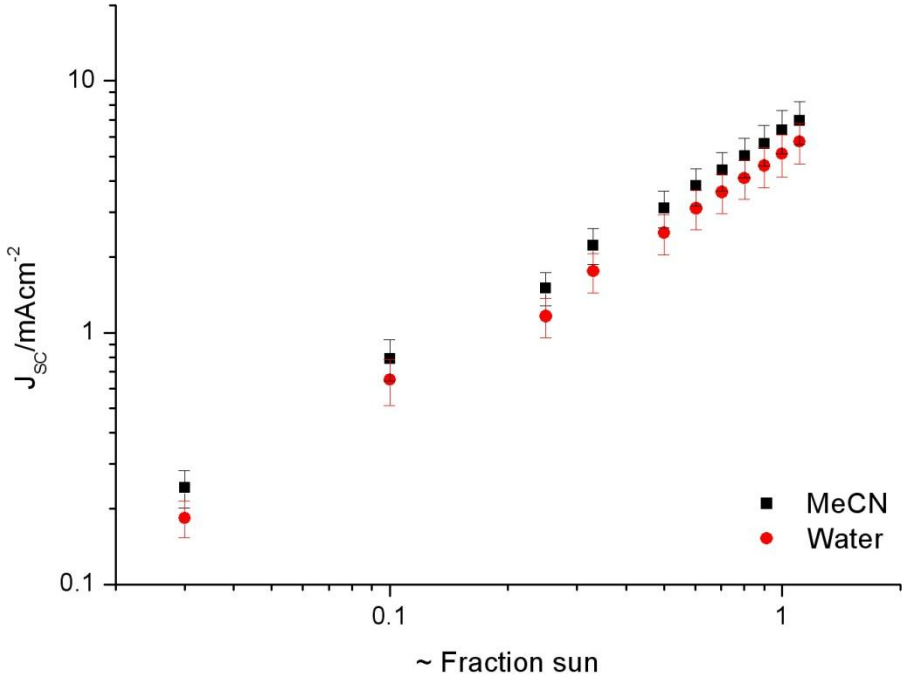

Fig 8.18 Current density as a function of light intensity (recorded as a fraction of AM1.5 1 sun illumination) for cells made using acetonitrile/valeronitrile and water based electrolytes (2M PMII, 0.05M I_2, 0.1M GSCN and 0.5M tBP. Water electrolytes also contain 1% Triton X-100) dyed with 0.3mM Z907. Error bars based on n=4 repeats.

Fig 8.20 shows cells made using additional treatments – a post annealing $TiCl_4$ treatment and a scattering layer deposited on the normal double layer TiO_2 film. These cells produce a higher photocurrent which is not limited up to 10mAcm^{-2}, comparable with the best literature values reported to date[9]. This shows that improvements to water cells are still possible and that water cells need not be limited by this problem. By careful optimization of the pore structure it should be possible to improve the photocurrent limit when it is next reached through other cell optimization methods.

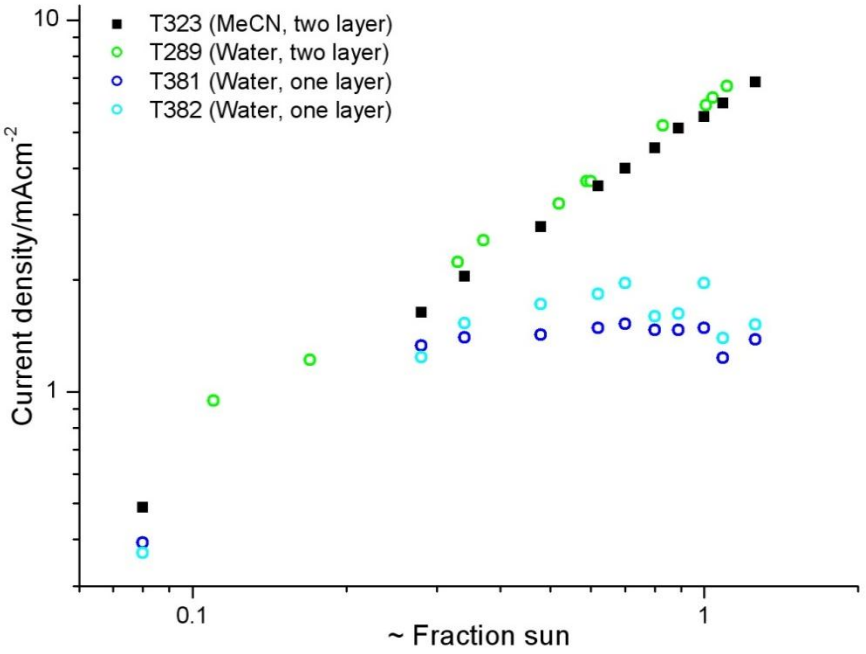

Fig 8.19 Current density as a function of light intensity (recorded as a fraction of AM1.5 1 sun illumination) for cells made using acetonitrile/valeronitrile and water based electrolytes (2M PMII, 0.05M I_2, 0.1M GSCN and 0.5M tBP. Water electrolytes also contain 1% Triton X-100), films dyed in 0.3mM Z907. T381 and T382 were made using only a single layer film, T323 with a double layer film. T323 is used as a comparison between different graphs.

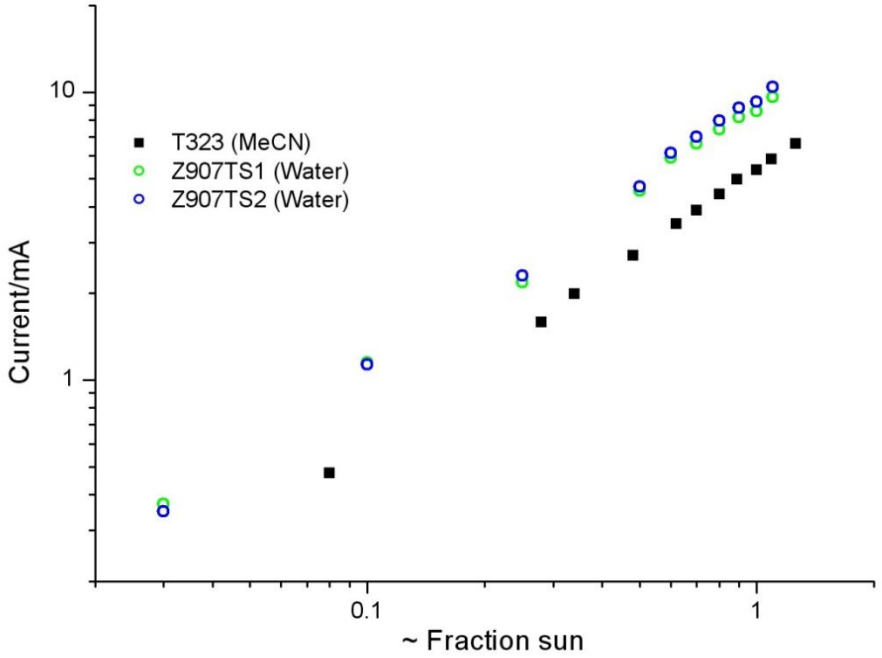

Fig 8.20 Current as a function of light intensity (recorded as a fraction of AM1.5 1 sun illumination) for cells made using acetonitrile/valeronitrile and water based electrolytes (2M PMII, 0.05M I_2, 0.1M GSCN and 0.5M tBP. Water electrolytes also contain 1% Triton X-100) dyed with 0.3mM Z907. TiO_2 films used to make Z907TS1 and Z907TS2 were post treated with $TiCl_4$ before dyeing and utilised a scattering layer. T323 is used as a comparison between different graphs.

Fig 8.21 shows the effect of changing the PMII concentration. It appears that at high PMII concentration there is a photocurrent limit whereas at lower PMII concentrations, the current limit increases to the point that it does not appear on the graph. This suggests that PMII is detrimental for the diffusion of I_3^- through the porous structure. Cells shown earlier e.g. Fig 8.20 used 2M PMII and this appears to be the best concentration for good cell performance, however it may be better to move away from using PMII and other high viscosity ionic liquids in the future.

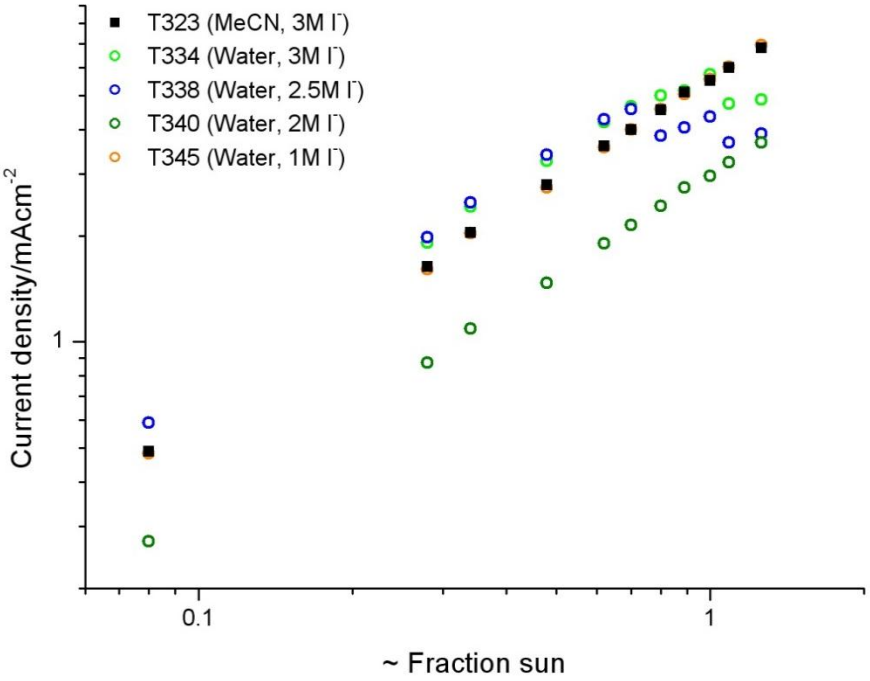

Fig 8.21 Current density as a function of light intensity (recorded as a fraction of AM1.5 1 sun illumination) for cells made using acetonitrile/valeronitrile and water based electrolytes (0.05M I_2, 0.1M GSCN and 0.5M tBP. Water electrolytes also contain 1% Triton X-100) containing different concentrations of PMII. Cells dyed in 0.3mM Z907. T338 and T351 were made from different batches of TiO_2 films. T323 is used as a comparison between different graphs.

8.3.5 Scanning Electrochemical Microscopy

Scanning Electrochemical Microscopy (SECM) can be used to perform a number of experiments not practical in standard electrochemistry. Because of the small size of electrodes used it is possible to take measurements very close to a substrate and to spatially examine a material electrochemically at high resolution. Here, this ability to accurately closely approach a material is used to examine the diffusion of species through a nanoporous TiO_2 film. In previous work[10] it has been observed that by holding an ultramicroelectrode (UME) at a certain distance from a dyed film in a solution containing a suitable redox mediator in its reduced form, it is possible to detect the presence of the oxidised form of that mediator produced by the regeneration of oxidised dye molecules when the dyed film is illuminated. Several studies have taken this further by using the time-of-flight for this oxidised species to determine diffusion constants[10-11]. Bozic et al have used this technique to obtain a diffusion constant for Fc^+ through a nanoporous film[10]. The aim of this work is to obtain diffusion constant values for the I_3^- species in bulk solution and through nanoporous TiO_2 in acetonitrile and water.

To perform this experiment, an SECM cell was set up as outlined in the experimental section above. To position the UME tip approach curves were measured in FcMeOH (Fig 8.23). Under the approach curve measurement conditions the surface was insulating and the tip was positioned at a point where the current was 75% of the initial current (in bulk solution). Based on equation 8.4, which is a numerical solution for the expected tip current response (i_T) as a function of the separation (d) from an insulating surface[12] ($I_{tip} = i_T/i_{T,\infty}$ where $i_{T,\infty}$ is tip response in bulk solution, L = d/a where a is tip diameter), the equivalent d/a value when I_{TIP} = 0.75 (Fig 8.22) shows that the initial distance between the tip and the TiO_2 surface should be 8.65 μm based on a 10 μm tip radius.

$$I_{Tip}(L) = (0.292 + \frac{1.5151}{L} + 0.6553\exp\left(\frac{-2.4035}{L}\right))^{-1} \qquad \text{Equation 8.4}$$

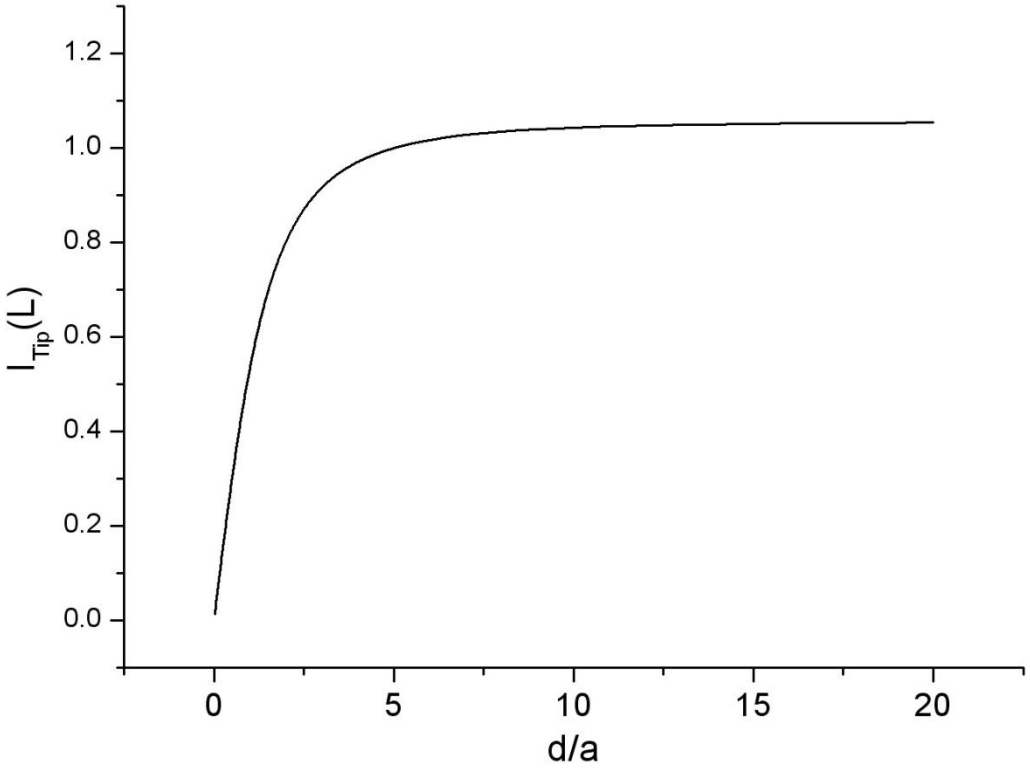

Fig 8.22 Graphical analysis of equation 8.4 showing expected change in tip current with respect to position from an insulating surface when taking into account tip current in bulk solution and electrode size.

Having replaced the solution with 0.6M LiI, chronoamperometric measurements were performed with the UME held at -0.2V relative to the $Ag/AgNO_3$ reference electrode (collection mode) (Fig 8.24 and 8.25). Current was measured before and after a short light pulse was applied to the dyed film (visible as a spike before the cathodic current peak in Fig 8.24 and 8.25). The UME was then retracted by several microns and the measurement repeated; this was done several times. The light pulse leads to the absorption of photons and excitation of electrons in the dye. These are injected into the TiO_2 and the oxidised dye is then regenerated by I^- in the electrolyte. The resulting species generated by this process (I_3^-) then diffuses away and is reduced at the UME resulting in a cathodic current.

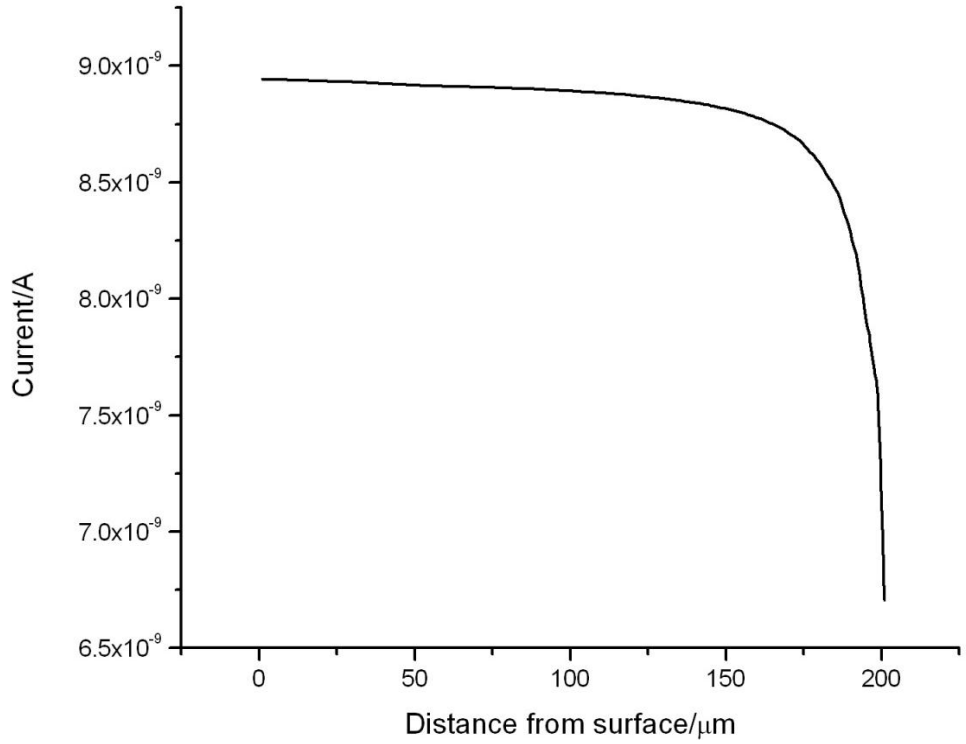

Fig 8.23 SECM approach curve for 10μm Pt UME to dyed (0.3mM Z907) TiO_2 film on FTO substrate in 1mM FcMeOH in 0.1M $tBAHFP_{(MeCN)}$. Reference electrode was 10mM $Ag/AgNO_{3(MeCN)}$.

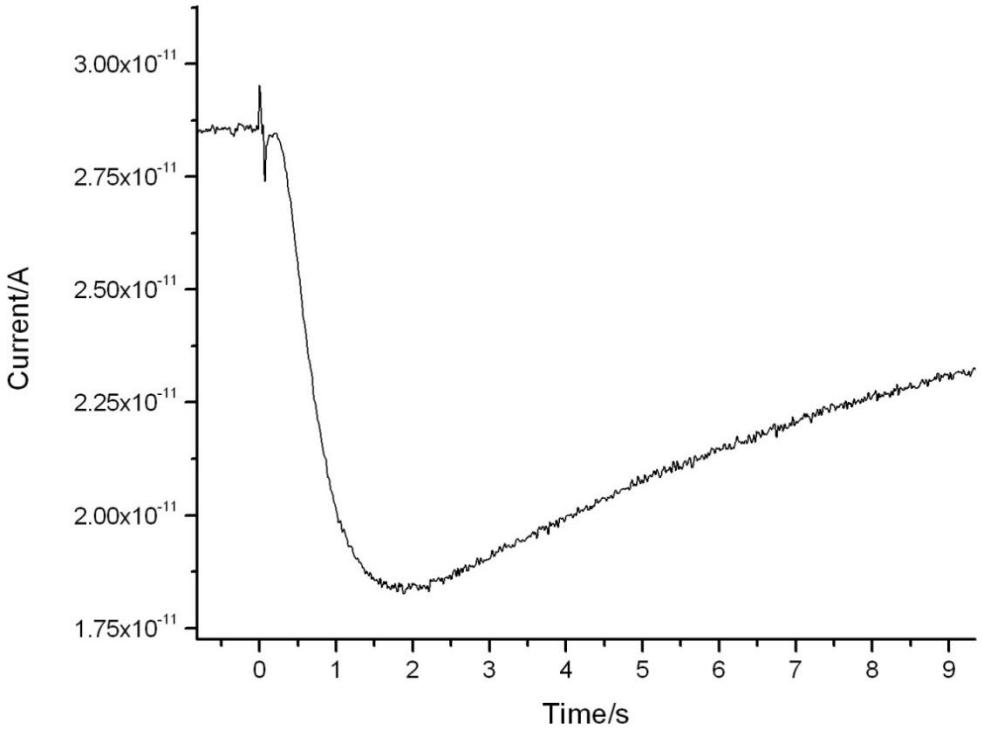

Fig 8.24 Transient current response for Pt UME held 28.65 μm above a dyed TiO_2 surface. Film is dyed (Z907) TiO_2 on FTO substrate. Electrolyte was 0.6M LiI in 0.1M $tBAHFP_{(MeCN)}$. Reference electrode was 10 mM $Ag/AgNO_{3(MeCN)}$. Spike at ~0s was taken as t_0.

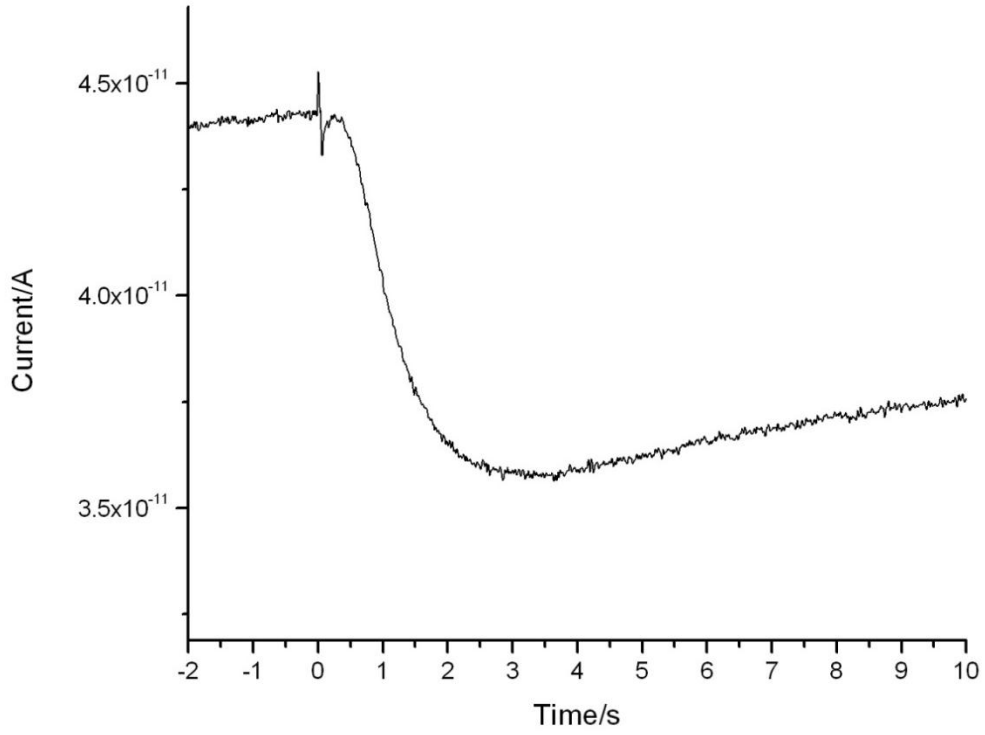

Fig 8.25 Transient current response at Pt UME held at 58.65 μm from dyed TiO_2 surface. Film was dyed (0.3mM Z907) TiO_2 on FTO substrate. Electrolyte was 0.6M LiI in 0.1M $tBAHFP_{(MeCN)}$. Reference electrode was 10mM $Ag/AgNO_{3(MeCN)}$. Spike at ~0s was taken as t_0.

To determine the diffusion coefficient (D), the following equation (equation 8.5)[10] is used which is linked to a random walk model of diffusion[12].

$$t_{\min} = \frac{\theta d^2}{D} \qquad \text{Equation 8.5}$$

In this equation t_{min} corresponds to the time at the point of minimum current after the light pulse and θ is a constant linked to the ratio of d and the UME radius[10] – in calculations this will be set as 0.11 based on other work using similar UME tips[10-11]. In this system, the species under examination diffuses through both bulk solution and the nanoporous film and so equation 8.5 can be written as

$$t_{\min} = t_{film} + \frac{\theta d_{sol}^2}{D_{sol}} \qquad \text{Equation 8.6}^{10}$$

where t_{film} is the time taken for species to diffuse through the film. As species will be generated across the whole film, this is an approximation and means that results give only an estimate for D_{film}. By plotting t_{min} as a function of d_{sol}^2 it is possible to determine D_{sol} (Diffusion constant in solution) and t_{film} (time taken for diffusion of species through the film) based on equation 8.6. Values of t_{film} and d_{film} (film thickness) can then be used to determine a diffusion constant for I_3^- through the film based on equation 8.5. The results of this measurement in acetonitrile are shown in Fig 8.26. A diffusion constant in solution is obtained as $1.67 \times 10^{-10}\ m^2 s^{-1}$, which is lower than literature values (e.g. $1.24 \times 10^{-9}\ m^2 s^{-1}$, Kron et al[13]) by around an order of magnitude. For diffusion in the film, a value of $9.5 \times 10^{-12}\ m^2 s^{-1}$ was obtained. This is similar to the value obtained for Fc^+ in the work by Bozic[10] ($2.6 \times 10^{-12}\ m^2 s^{-1}$) but is lower than values obtained through other techniques (e.g. $4.4 \times 10^{-10}\ m^2 s^{-1}$, Kron et al[13]). However, it is clear that I_3^- diffusion is indeed a lot slower through the nanoporous TiO_2. Unfortunately, experiments in water were not successful as it was not possible to get a clear current peak after the light pulse. It is expected that a similar trend i.e. slower diffusion in the pores, would also be seen in water.

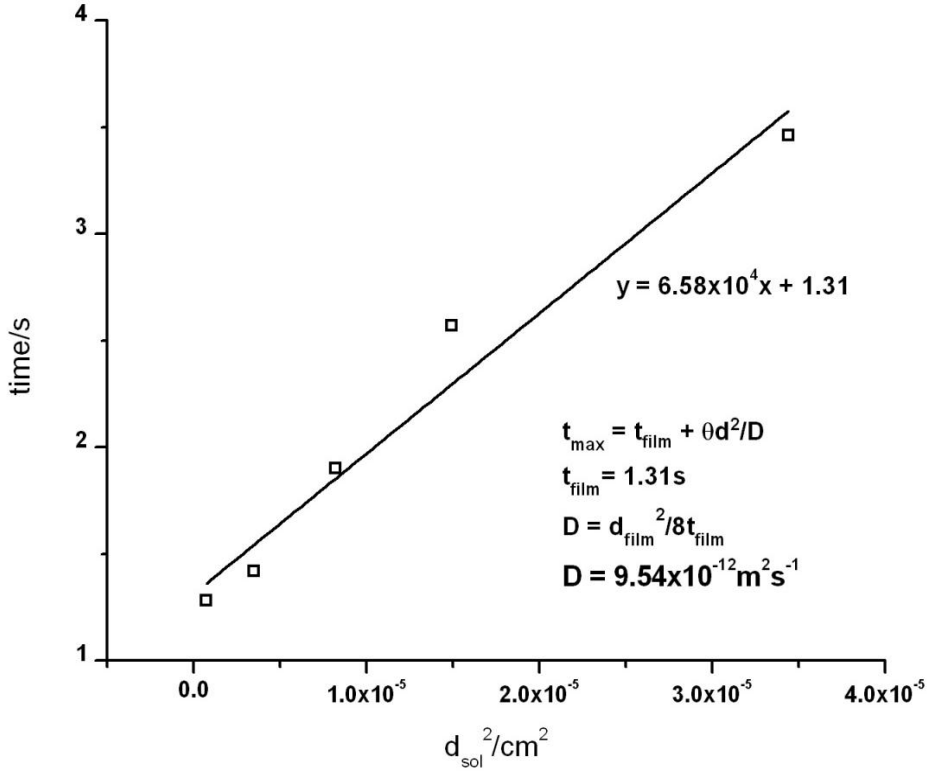

Fig 8.26 Straight line fitting for $t(I_{min})$ vs d_{sol}^2 determined by transient current response and SECM measurements. Showing calculations for I_3^- diffusion constant in nanoporous TiO_2 film based on equation 8.6.

Papageorgiou et al[14] have proposed a model (equation 8.7) which allows the limiting current based on the diffusion of I_3^- to the counter electrode to be determined for a particular system.

$$J_{\lim} = \frac{6PFD_{I_3^-}[I_3^-]}{d} \qquad \text{Equation 8.7}$$

P is porosity, F is the Faraday constant and d is the thickness of the film. Assuming a porosity of 50%, a film thickness of 10 μm, an I_3^- concentration of 0.001M (see appendix B) and the D_{film} determined in the experiment above, a current limit of 0.27 mA is obtained. This increases to 12.7 mA when using the literature value from Kron et al[13]. This suggests that the values obtained in this experiment were unrealistically low. The values obtained by Bozic et al were similarly low compared to other literature values which may mean that this experimental technique is invalid, though a reason for this is unknown.

8.4 Conclusions

It has been seen in this chapter that while efficient regeneration of the dye Z907 appears to occur in acetonitrile, it is unclear if this is the case in water. By comparing data for this experiment measured on both dyed FTO and dyed TiO_2 it is seen that this is not due to problems caused by degradation of the dye layer on FTO and its influence on the hole hopping electron transport mechanism. On the basis that aqueous cells produce a photocurrent it is known that dye regeneration must be working to some extent, however results from this chapter may mean that it is slower than in acetonitrile which could decrease the cell photocurrent. Changes to the UV/Vis response were seen after voltammetry was performed on a dye film and the CV response of the dye was seen to change after several chronoamperometry experiments were measured. This may be due to some dye degradation.

Analysis of initial peaks observed when measuring IV curves for water cells suggests that these are caused by slow I_3^- diffusion through the semiconductor pores. Further measurements show that non-limited photocurrents up to $10mAcm^{-2}$ could be produced and it is thought that changes to the pore structure

of the semiconductor might improve this limit further. Analysis of diffusion coefficients using SECM time of flight measurements showed that I_3^- diffusion is slower in the TiO_2 film than the bulk solution, though there is some doubt as to the validity of this experimental technique.

8.5 References

(1) Pijpers, J. J. H.; Ulbricht, R.; Derossi, S.; Reek, J. N. H.; Bonn, M. *J Phys Chem C* **2011**, *115*, 2578.

(2) Fattori, A.; Peter, L. M.; Belding, S. R.; Compton, R. G.; Marken, F. *J Electroanal Chem* **2010**, *640*, 61.

(3) Fattori, A.; Peter, L. M.; McCall, K. L.; Robertson, N.; Marken, F. *J Solid State Electr* **2010**, *14*, 1929.

(4) Compton, R. G.; Banks, C. E. *Understanding voltammetry*; 2nd ed. ed.; Imperial College Press: Singapore ; London, 2011.

(5) Fisher, A. C. *Electrode dynamics*; Oxford University Press: Oxford, 1996.

(6) Law, C. H.; Pathirana, S. C.; Li, X. O.; Anderson, A. Y.; Barnes, P. R. F.; Listorti, A.; Ghaddar, T. H.; O'Regan, B. C. *Adv Mater* **2010**, *22*, 4505.

(7) Boschloo, G.; Gibson, E. A.; Hagfeldt, A. *J Phys Chem Lett* **2011**, *2*, 3016.

(8) Haynes, W. M.; Bruno, T. J.; Lide, D. R. *CRC handbook of chemistry and physics*; 94th ed., 2013-2014 / editor-in-chief, W.M. Haynes ; associate editor, Thomas J. Bruno ed.; CRC: Boca Raton, Fla. ; London, 2013.

(9) Law, C.; Moudam, O.; Villarroya-Lidon, S.; O'Regan, B. *Journal of Materials Chemistry* **2012**, *22*, 23387.

(10) Bozic, B.; Figgemeier, E. *Chem Commun* **2006**, 2268.

(11) Mirkin, M. V.; Arca, M.; Bard, A. J. *J Phys Chem-Us* **1993**, *97*, 10790.

(12) Bard, A. J.; Faulkner, L. R. *Electrochemical methods : fundamentals and applications*; 2nd ed. ed.; John Wiley: New York ; Chichester, 2001.

(13) Kron, G.; Rau, U.; Durr, M.; Miteva, T.; Nelles, G.; Yasuda, A.; Werner, J. H. *Electrochem Solid St* **2003**, *6*, E11.

(14) Papageorgiou, N.; Gratzel, M.; Infelta, P. P. *Sol Energ Mat Sol C* **1996**, *44*, 405.

Chapter 9: Conclusions

In this work a large number of DSSCs have been fabricated. Generally these have differed only in the composition of the electrolyte and in particular the electrolyte solvent. The aim of this thesis was to examine the effect of using an aqueous electrolyte on cell performance and to determine what changes such an electrolyte causes in the cell compared to the more standard electrolyte solvent, acetonitrile.

It was generally seen that aqueous DSSCs produced a lower short circuit current than those made with acetonitrile and several reasons for this were examined. Practically, it was more difficult to fill cells with the aqueous electrolyte than the acetonitrile electrolyte. If the cell is not completely filled then the current produced will be lower as some of the dye is not being regenerated after electron injection. The contact angle of water on dyed TiO_2 is larger than that for acetonitrile due to weaker surface/solvent interactions with water which means that surface wetting does not occur so readily. To try and counter this problem three approaches were taken. The first involved changing the properties of the electrolyte using surfactants. Using increasing concentrations of Triton X-100 was found to improve cell filling, however this did not coincide with increased performance, and it is possible that the surfactant may have been adsorbed onto the counter electrode and reduced the charge transfer rate constant. 1vol% Triton X-100 was found to lead to the best cell performance and gave slightly improved cell filling compared to the case with no surfactant. The second approach involved altering the surface of the dyed TiO_2 to make it more hydrophilic. Using UV light was not found to be effective as the dye dominated the hydrophilicity, however certain coadsorbates were found to reduce the contact angle and so improve wetting. This was partly caused by the replacement of some dye molecules by coadsorbate molecules and so this approach did not ultimately improve cell performance although some changes to the open circuit voltage were seen. Finally, the physical method of filling cells was altered and it was found that when the cell was heated to 80°C under vacuum followed by increasing the pressure to introduce electrolyte into the cell, the cell performance and cell filling were both improved. However, incomplete

wetting of the pores in the nanoporous TiO_2 structure is still likely to be one reason for a lower photocurrent in aqueous cells.

In many cases, a limit in the photocurrent was observed for aqueous cells at a certain light intensity, and this is another possible reason for why the photocurrent was lower. This was generally attributed to slow I_3^- diffusion in aqueous solution particularly through the nanoporous TiO_2 structure where it is expected to be lower than in the bulk. If there is incomplete wetting this is likely to exacerbate this problem. It is also likely that part of the reason for slow diffusion was the use of ionic liquids in the electrolytes. It was seen that it is possible to produce cells that show no limit up to the maximum light intensity used with a photocurrent of 10 $mAcm^{-2}$ at this maximum. It is also suggested that this limit is very sensitive to the pore structure and fabrication method of the film. A second possible reason for the photocurrent limit observed in many cases is if the regeneration of oxidised dye after electron injection is slow in water. Analysis using cyclic voltammetry showed that the regeneration by I^- occurred in acetonitrile, however this was not clearly the case in water. Though it must be occurring to a certain degree in water to generate any current, it is possible that if it is occurring slowly then the photocurrent will be reduced. In particular it is likely that this would lead to a photocurrent limit at a certain light intensity.

Finally, it was seen that dye is more likely to be desorbed from the TiO_2 surface in water than in acetonitrile. For this reason the hydrophobic dye Z907 was used in preference to N719 and found to have better surface attachment stability. It was shown that dye desorption increased at high pH and it was observed on a number of occasions that dye desorbed from the surface of TiO_2 near to the electrolyte filling hole upon electrolyte addition. This was shown in particular using photocurrent and transmission mapping techniques where the dye coverage was determined before and after making the cell. Dye was thought to be desorbed from the surface via an OH^- catalysed ester hydrolysis mechanism and this was believed to be followed by strong binding of 4-tert-butylpyridine to the surface, gradually depleting the surface coverage of dye. If there is less dye on the surface it will result in a decreased photocurrent.

In contrast to the difference in photocurrent between the two types of cells, it was shown that the photovoltage did not markedly differ with solvent. Measurement of the redox potential of I_3^-/I$^-$ initially suggested a difference of ~100mV for this couple in the two different solvents. However, calculations suggested that effectively no change should be expected and several results suggested that the position of the redox potential was the same in both solvents. Assuming this to be the case, it was seen that the position of the conduction band did not significantly change between the two types of cells. The voltage dependence of the effective electron lifetime was also very similar, suggesting that the reaction of electrons in the TiO_2 with I_3^- had a similar rate constant in the two cell types. It was also found that the distribution of electron traps was similar regardless of the solvent used. Interestingly it was also shown that the gradient of the illumination dependence of the photovoltage was identical between the two types of cells, meaning that the non-ideality factor was the same. As it is expected that the change in solvent will cause some change in the surface environment of the semiconductor, this suggests that the reason often put forward for non-ideal behaviour (reaction between electrons in the TiO_2 and I_3^- via surface states) is incorrect. Instead, it is suggested that the origin of non-ideality is linked to a fundamental property of the TiO_2. For example, it may be due to the reaction between electrons in the TiO_2 and I_3^- via bulk trap states. Though the open circuit voltage did not alter with solvent, it was seen to alter as a function of I$^-$ concentration. As this increased, the open circuit voltage decreased and this was seen to be mainly due to the negative change in the Nernst potential of I_3^-/I$^-$.

The effect of electrolyte pH was examined in the aqueous cell and it was seen that the open circuit potential increased with pH whereas the short circuit current decreased. This was interpreted as due to a change in the conduction band position, particularly as the open circuit voltage change was 57mV/pH unit. Transient measurements of electrons using infrared light showed markedly different behaviour in the two different solvents examined. In particular the response of aqueous cells under short circuit conditions was different to that of acetonitrile cells. It was seen that electrons in different parts of the cell (the substrate or the TiO_2 film) dominated the signal response at different infrared wavelengths. Results were consistent with the intercalation of H^+ into TiO_2 upon

illumination and two possible interpretations were put forward to describe the signal response.

Overall, changes in the water cell seem to be largely due to problems with the permeation of electrolyte into the cell and through the nanoporous semiconductor. The electronic properties of the semiconductor did not appear to change significantly when altering the solvent system (though pH did have some effect on these) and redox energy levels were also shown to probably be unchanged. In addition, the influence of the aqueous electrolyte on the dye binding is also thought to have a slightly negative effect on the cell performance. The fact that there are no obvious significant fundamental changes to the workings of the cell that stop it from working with an aqueous electrolyte suggests that future studies in this area would be worthwhile and this is considered in more detail in chapter 10.

Over the course of this work, aqueous cell efficiency was improved by several different methods. The highest efficiency achieved was 3.5% and there are several known optimization techniques yet to be attempted which would be expected to improve this further. Although this is relatively low compared to state of the art DSSCs, when compared to the equivalent best cells made using an acetonitrile electrolyte in our lab with an efficiency of ~5%, there is a much smaller difference. As mentioned, some cells were made with no photocurrent limit up to the highest light intensity available in our lab. If the cause of a photocurrent limit is the main limiting factor for cell performance, then this result suggests that if aqueous cells were produced using state of the art fabrication techniques, it should be possible to obtain higher cell performance.

Chapter 10: Future work

10.1 Outlook

10.2 Future experimental work

10.3 References

10.1 Outlook

In chapter 9 it was concluded that the problem of poor permeation of the aqueous electrolyte into the cell and the nanoporous TiO_2 was a significant cause for the lower cell performance seen when using water as a solvent, but that there are many aspects of the cell that are largely unchanged including the electronic properties of the semiconductor. It has also been seen in this work that it is possible to produce aqueous DSSCs which have reasonable efficiencies. This has some similarities with the situation when solid hole conductors are used. When using solid hole conductors it is often found that pore filling is difficult, limiting the performance of the cell. Several methods have been employed to address this; one of these is to use only thin layers of nanoporous semiconductor and a high molar extinction coefficient dye[1]. In other areas, large redox mediators with small diffusion coefficients have been used and seen similar problems[2]; one method of getting round this has been to optimize the pore structure of the semiconductor to hinder the diffusion of species as little as possible[2-3]. Both of these approaches could be taken in order to further improve the performance of aqueous DSSCs. Furthermore, most of the materials used in this work were designed in the context of a field dominated by DSSC electrolytes incorporating organic liquid solvents. Though cell optimization was done in this work using these materials, it is likely that cell performance could be further improved by choosing or designing materials specifically for the aqueous system; for example by finding dyes which have improved surface binding characteristics in water. In summary, there is potential for further performance improvements to be made with aqueous DSSC's. Whether such improvements can be sufficient to compete with devices using more standard electrolytes in terms of performance and stability is currently unknown. At present, devices which use conventional electrolyte solvents have much better performance and the possible benefits of using aqueous electrolytes as discussed in chapter 1 are not currently significant or unique enough to justify investing large amounts into research in this area. If the suggestions discussed above were found to be particularly successful however, this assessment would need to be revised.

10.2 Future experimental work

Several experiments which relate to work already done as part of this thesis that could be continued if time or equipment/materials allowed are briefly discussed below.

In terms of cell performance, it would be informative to improve the 'baseline' performance, that is, the performance of standard cells made using the acetonitrile electrolyte and N719 dye. If this could be done, for example by increasing the quality of the TiO_2 films produced then it would be possible to see if aqueous cells could also be improved or whether for example the photocurrent limit often observed did become a major problem. It is hoped that such an improvement would also increase the L_n/d value. In addition, it would be interesting to determine the effect of a number of different dyes. In particular, the dye D35 was seen to show equivalent performance to Z907 in low efficiency cells and it would be interesting to see its performance in improved cells. The dye Z955 is an analogue of Z907 that has phosphonic acid binding groups instead of carboxylic acid groups. These are expected to bind more strongly to TiO_2 and it would be interesting to determine if this produced a higher photocurrent in aqueous cells than Z907 and if it allowed electrolytes with a higher pH to be used. Finally, it is likely that cells that did not use PMII would have faster diffusion of species in solution. Though it was seen that using LiI and I_2 did not lead to high cell performance, the effect of additives on such a system was not examined and so studying cells made with aqueous electrolytes that used LiI instead of PMII along with other additives would be informative.

Regarding the mapping technique, it should be possible to develop this further. In particular if problems of light stability can be overcome, it should be possible to use the transmission technique to obtain quantitative information. If the film thickness over the entire film was known, it should be possible to obtain dye coverage maps using the molar absorption coefficient of the dye on TiO_2. Alternatively, if it is assumed that dye coverage is uniform across the film, these techniques could be used to determine film thickness. Dye coverage could then be linked closely to photocurrent.

Extending analysis of the cell non-ideality factor to cells made with electrolytes containing other solvents would help to confirm whether or not this is linked to the reaction of electrons in the TiO_2 with I_3^- via surface states. Analysis of this as a function of pH may also yield information on this process. It would also be useful to better understand the relationship between the measured and actual values of E(I_3^-/I^-) in the two different solvents examined in this work.

Additional experiments could be done in order to fully understand the aqueous cell infrared response under short circuit conditions. Additional background measurements including the response of the substrate and the response of the platinised counter electrode would be helpful. Quantifying the effect of the electrolyte pH on the response of both the FTO and TiO_2 separately would also be useful, as well as any pH effect on the absorption of the electrolyte itself.

10.3 References

(1) Moon, S.-J. PhD, École Polytechnique Fédérale De Lausanne, 2011.

(2) Tsao, H. N.; Comte, P.; Yi, C. Y.; Gratzel, M. *Chemphyschem* **2012**, *13*, 2976.

(3) Yang, G. J.; Li, C. J.; Fan, S. Q.; Gao, J. C. *Surf Coat Tech* **2011**, *205*, 3205.

Appendices

Appendix A: Dye adsorption/desorption

In order to determine surface concentration, the molar absorption coefficient of N719 in 0.1M $KOH_{(aq)}$ was first measured by UV/Vis spectroscopy at 632.8nm using concentration curves fitted to the Beer-Lambert law (Fig A1). Several TiO_2 films of known area and thickness were dyed overnight in $3x10^{-4}$M N719 in 1:1 acetonitrile (MeCN):t-butanol solution, then rinsed with the same solvent and dried. Each slide was then placed in a known volume of 0.1M $KOH_{(aq)}$ solution for 5 minutes, after which the absorbance of the solution was measured at 632.8 nm. This value was used to calculate the concentration of dye in the film. Measurements were taken for two films, giving an average of $1.22x10^{-4}\pm1.18x10^{-5}$ molcm^{-3} where the volume corresponds to film volume. From this data it is possible to estimate how many dye molecules there are per TiO_2 particle (Table A1) – the average value is 628 which is in good correlation with literature values[1].

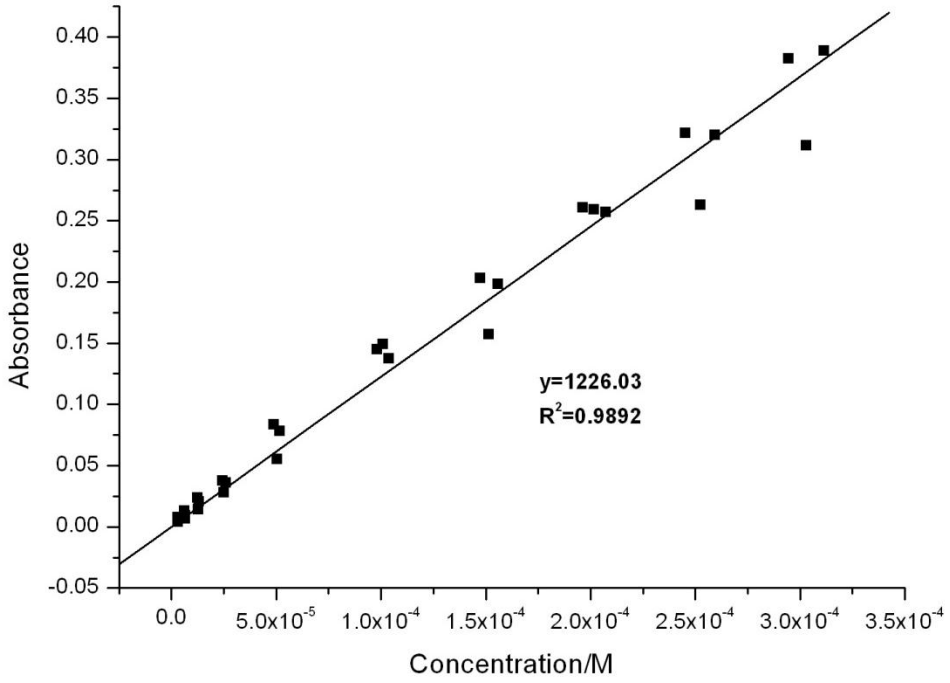

Fig A1 UV/Vis Calibration curve for N719 in 0.1M $KOH_{(aq)}$ measured at 632.8nm.

It is also possible to determine dye coverage values θ according to equation A1 based on the molecular footprint (a_{DF}) for Z907 of 2nm^2 as determined by Fattori et al[2].

$$\theta = \frac{A_D}{A_{Surf}} \qquad \text{Equation A1}$$

where A_D is the surface area covered with dye and A_{Surf} is the total surface area. The surface area covered with dye is calculated according to

$$A_D = a_{DF} n_D \qquad \text{Equation A2}$$

where n_D is the number of dye molecules according to

$$n_D = n_{D,mol} N_A \qquad \text{Equation A3}$$

where $n_{D,mol}$ is the number of mols of dye desorbed in the measurement summarised in Table A1 and N_A is the Avogadro number. A_{surf} is calculated according to

$$A_{surf} = 4\pi r^2 n_{TiO_2} f \qquad \text{Equation A4}$$

where r is the radius of the nanoparticles, n_{TiO2} is the number of TiO_2 particles and f is a factor determining the fraction of surface area available for dye adsorption. This factor is difficult to determine and so an alternative calculation of A_{surf} is

$$A_{surf} = A_{SS} \rho_{TiO_2} V_{film} p \qquad \text{Equation A5}$$

where A_{SS} is the specific surface area for a particular nanoparticle size, ρ_{TiO2} is the density of anatase, V_{film} is the total film volume and p is the porosity. Values calculated in table A1 show that the average surface coverage is 0.96, which suggests that a monolayer is formed.

Table A1: Variables and calculated values used in determining approximate value for number of dye molecules per TiO_2 particle. [a]Based on average A_{SS} value for particle sizes 23nm and 17nm from reference [3].

Parameter	**Slide 1**	**Slide 2**
TiO_2 area/cm^2	0.852	0.848
TiO_2 average thickness/nm	10569	10558
Approximate porosity (%)[4]	50	50
Average particle size (diameter)/nm[5]	20	20
Dye quantity/mol	$1.21x10^{-7}$	$1.02x10^{-7}$
Dye concentration/$molcm^{-3}$	$1.3x10^{-4}$	$1.133x10^{-4}$
No of TiO_2 nanoparticles	$1.07x10^{14}$	$1.069x10^{14}$
Dye molecules/particle	681	575
Z907 molecular footprint/nm_2	2	2
Specific surface area of 20nm[a] TiO_2 nanoparticles[3]/m^2g^{-1}	80	80
TiO_2 (anatase) density[6]/gcm^{-3}	3.9	3.9
Area covered by dye/m^2	0.146	0.123
Surface area/m^2	0.140	0.140
Surface coverage	**1.04**	**0.88**

Another UV/Vis technique was developed to determine film concentration without desorbing the dye i.e. a non-destructive technique. This involved measuring the UV/Vis absorption of a dyed film in air. In order to obtain a result using this method several measurements are required: a background absorption measurement of the undyed film, the film thickness, the dyed film absorption and a molar absorption coefficient for the dye adsorbed onto a film. This was obtained by first preparing a number of TiO_2 films of known area, thickness and absorption at 530 nm. These were then dyed for different lengths of time in order to give different total concentrations. UV/Vis was measured for each film, then the dye quantity was measured as above using $KOH_{(aq)}$ desorption. Again using the Beer-Lambert law this data was used to calculate a molar absorption

coefficient where the film thickness was considered to be the path length. The calibration curves at obtained at 530nm are shown in fig A2. Table A2 summarises the molar absorption coefficients obtained from calibration curves for a number of different systems.

Table A2: Showing molar absorption coefficient values measured at 530nm for N719 and Z907 in two different solvents.

	Molar absorption coefficient/$M^{-1}cm^{-1}$	
	Acetonitrile:t-butanol	**0.1M $KOH_{(aq)}$**
N719	13212	9268
Z907	-	6827

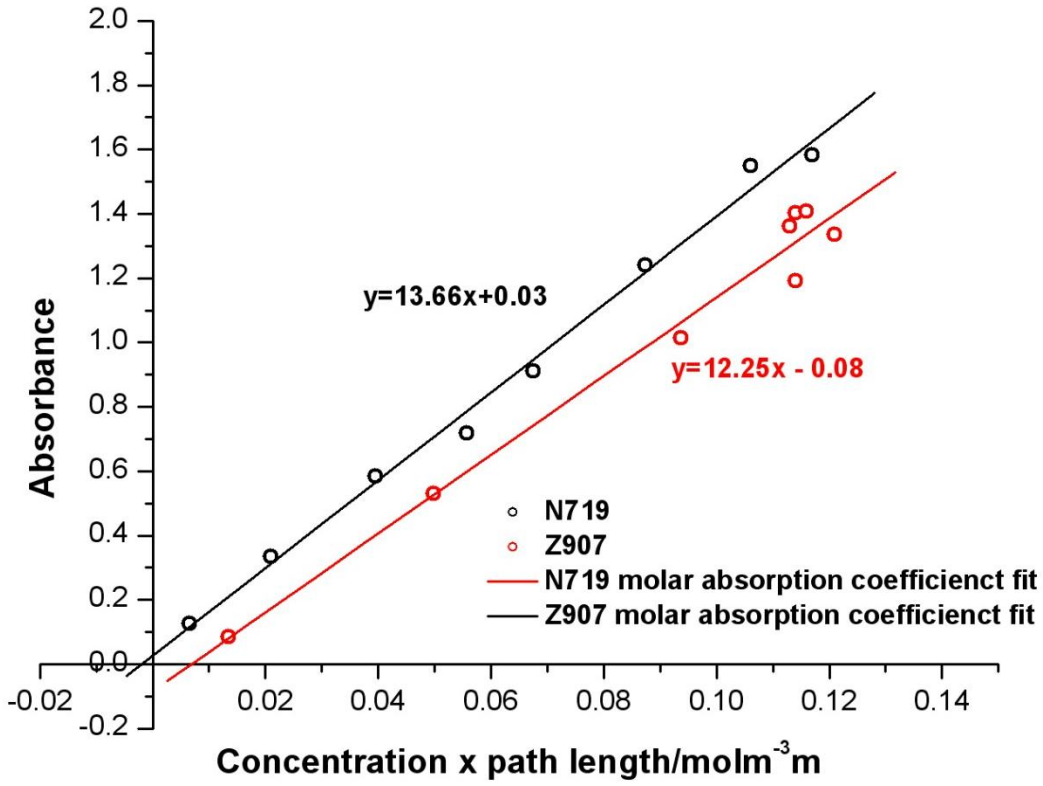

Fig A2 UV/Vis calibration curves for dyed nanoporous TiO_2 films in air measured at 530nm.

Appendix B: Redox species equilibrium concentrations

Calculations were performed to determine the equilibrium concentration of redox species in acetonitrile and water. Equilibrium constants were from the literature. For acetonitrile[7], the value used was $5.7 \times 10^{6} M^{-1}$ and was based on a system initially containing 0.5M LiI and 0.05M I_2. For water[8], the value was $826 M^{-1}$ and was based on a system initially consisting of 0.015M KI and 1.12×10^{-3}M I_2. The systems are not precisely the same, but are able to give an indication of approximate expected equilibrium values. Values are based on the following equilibrium:

$$I_2 + I^- \rightleftharpoons I_3^- \qquad \text{Equation B1}$$

The equilibrium constant for this equation is

$$K = \frac{[I_3^-]}{[I_2][I^-]} \qquad \text{Equation B2}$$

At equilibrium, concentration values will be

$$\begin{aligned} [I_3^-]_{eq} &= \alpha \\ [I_2]_{eq} &= [I_2]_0 - \alpha \\ [I^-]_{eq} &= [I^-]_0 - \alpha \end{aligned} \qquad \text{Scheme B1}$$

where the first term is the initial concentration and α is the concentration of I_3^- at equilibrium. Substituting these values into the equilibrium constant equation gives

$$K = \frac{\alpha}{([I_2]_0 - \alpha)([I^-]_0 - \alpha)} \qquad \text{Equation B3}$$

When simplified, the quadratic equation can then be used to determine α.

$$x = \frac{-b \pm \sqrt{b^2 - 4ac}}{2a} \qquad \text{Equation B4}$$

Equilibrium concentrations determined via this method are shown in table B1.

Table B1: Example of calculated equilibrium concentrations for two different electrolyte solvents.

	Acetonitrile		**Water**	
	Initial conc/M	**Equilibrium conc/M**	**Initial conc/M**	**Equilibrium conc/M**
I_3^-	0	0.05	0	0.001
I^-	0.5	0.45	0.081	0.080
I_2	0.05	2×10^{-8}	1.13×10^{-3}	1.63×10^{-5}

Appendix C: Calculated Nernst potentials based on equilibrium concentration of redox species

Calculations determining the expected Nernst potential of the redox couple for several I^-/I_3^- ratios were carried out. Calculations are based on equilibrium constants and systems and used the same values as in Appendix B. Calculations assumed Nernstian behaviour according to the Nernst equation

$$E = E^{\ominus} - \frac{RT}{nF}\ln\left(\frac{[red]}{[ox]}\right) \quad \text{Equation C1}$$

where E is the potential, $E^{\ominus}$ is the standard redox potential for the system in question, R is the gas constant, T the absolute temperature, n the number of electrons transferred in the reaction and [red] and [ox] the concentration of the reduced and oxidised species at equilibrium. Calculations were made assuming that the activity of the species was constant across the concentration range of interest so that the above use of concentration in place of activity was valid. However, it is possible that this was no longer the case, particularly at higher concentrations. In order to measure $E^{\ominus}$ for the system in different solvents, initial I_2 and LiI concentrations which led to an equilibrium where $[I^-] = [I_3^-]$ were calculated. As described in scheme B1, equilibrium concentrations will be

$$[I_3^-]_{eq} = \alpha$$
$$[I_2]_{eq} = [I_2]_0 - \alpha \qquad \text{Scheme C1}$$
$$[I^-]_{eq} = [I^-]_0 - \alpha$$

where the first term is the initial concentration and α is the concentration of I_3^- at equilibrium. In order to meet the above requirement, the equilibrium situation must be found where

$$[I^-]_0 - \alpha = \alpha \qquad \text{Scheme C2}$$
$$[I^-]_0 = 2\alpha$$

Including the values in the equilibrium constant equations results in

$$K = \frac{\alpha}{([I_2]_0 - \alpha)([I^-]_0 - \alpha)} \qquad \text{Equation C2}$$
$$\alpha = K([I_2]_0[I^-]_0 - ([I^-]_0 + [I_2]_0)\alpha + \alpha^2)$$

and substituting $[I^-]_0 = 2\alpha$ leads to

$$[I^-]_0 = 2\left([I_2]_0 - \frac{1}{K}\right) \quad \text{Equation C3}$$

Based on this, electrolytes made up in acetonitrile with 0.05M I_2 and 0.1 M LiI and in water with 0.05M I_2 and 0.09758M LiI should have equal concentrations of I^- and I_3^- at equilibrium which should result in $E^{\ominus}$ being measureable. Values of E determined using two electrodes and a digital voltmeter are shown below in table C1. Small errors in calculations resulted in concentration errors of 4% in the water case.

Table C1: Measured standard potential values for systems containing equal concentrations of oxidised and reduced redox species.

Solvent	**E vs SCE/V**
Acetonitrile/valeronitrile	0.312
Water (+1% Triton X-100)	0.087

Using the initial concentration values that were present in the different electrolytes made, equilibrium concentrations were calculated using the methods described in Appendix B. These were then put into the Nernst equation along with the standard potentials measured above, and the expected Nernst potentials determined.

Appendix D: Linear sweep measurement of aqueous water cell, scan rate/time dependence.

Linear sweep voltammetry measurements are shown for the aqueous DSSC T193. These were swept from 0 → 0.3V at different scan rates. Scan rates were calculated such that the scan time took as long as the scans shown in Fig 8.15 where scans were performed from 0→0.4V, 0→0.5V and 0→0.6V. It can be seen that there are no changes between the plots shown here, eliminating the possibility that the effect seen in the results in Chapter 8 was time related.

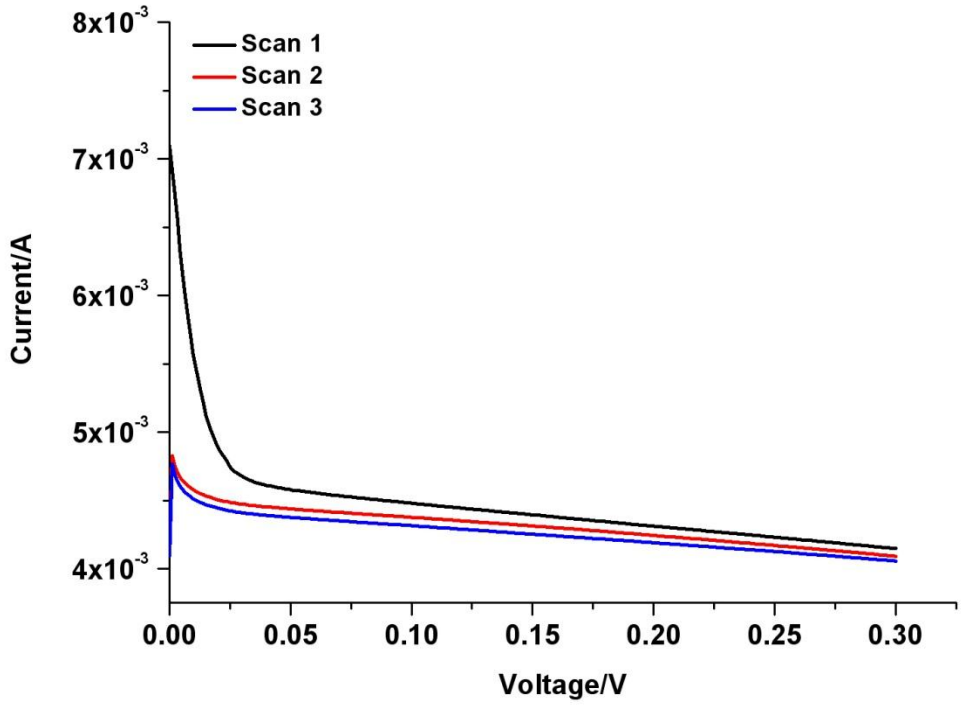

Fig D1 Linear sweep voltammetry of water dye cell T193 (dyed in 0.3mM Z907, electrolyte contained 2M PMII, 0.05M I_2, 0.1M GSCN, 0.5M tBP and 1% Triton X-100) under 1 sun AM1.5 illumination. Five consecutive scans from 0V to 0.3V, scan rate 15mVs^{-1}.

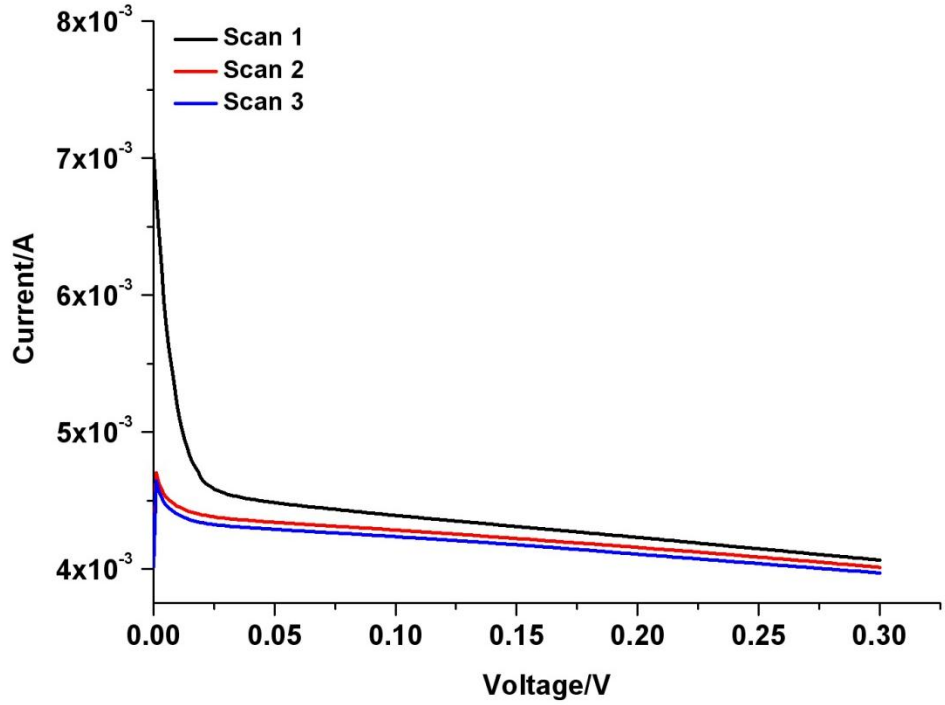

Fig D2 Linear sweep voltammetry of water dye cell T193 (dyed in 0.3mM Z907, electrolyte contained 2M PMII, 0.05M I_2, 0.1M GSCN, 0.5M tBP and 1% Triton X-100) under 1 sun AM1.5 illumination. Five consecutive scans from 0V to 0.3V, scan rate 12mVs^{-1}.

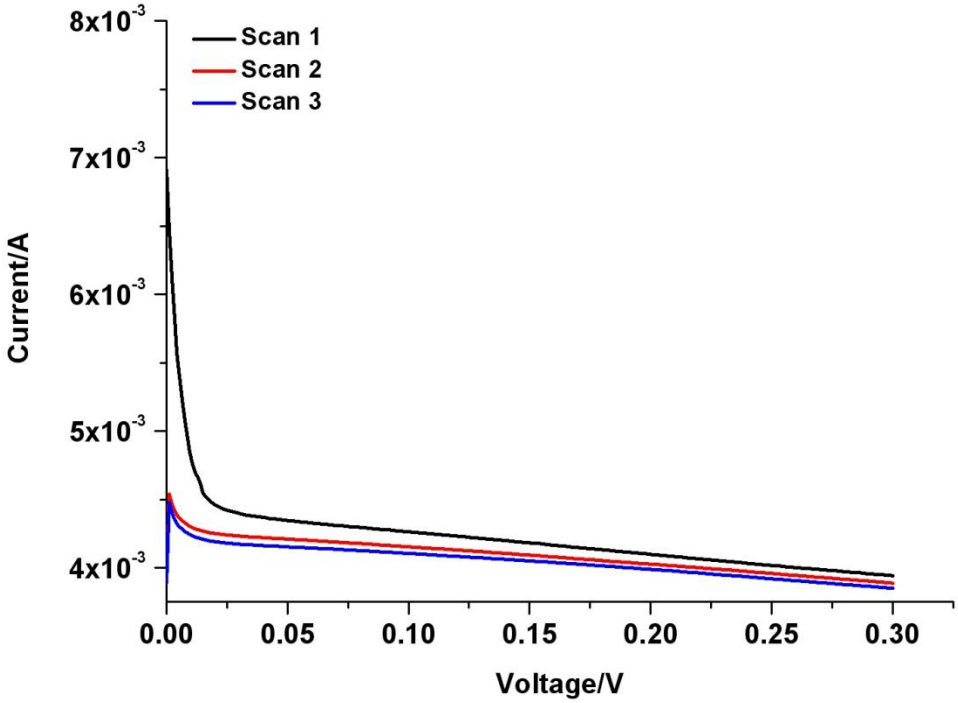

Fig D3 Linear sweep voltammetry of water dye cell T193(dyed in 0.3mM Z907, electrolyte contained 2M PMII, 0.05M I_2, 0.1M GSCN, 0.5M tBP and 1% Triton X-100) under 1 sun AM1.5 illumination. Five consecutive scans from 0V to 0.3V, scan rate 10mVs^{-1}.

Appendix E: Examples of EIS data for DSSCs

Two examples of raw EIS data are shown here plotted on Nyquist plots. In the case of water an additional semicircle can be observed at low frequencies corresponding to the slow diffusion of species in the electrolyte.

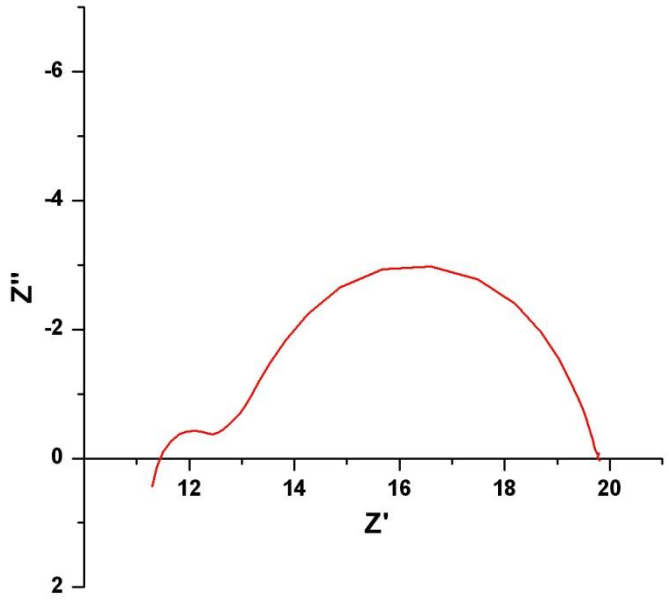

Fig E1 EIS response of acetonitrile/valeronitrile cell containing 0.6M PMII, 0.05M I_2, 0.1M GSCN and 0.5M tBP, dyed in 0.3mM N719.

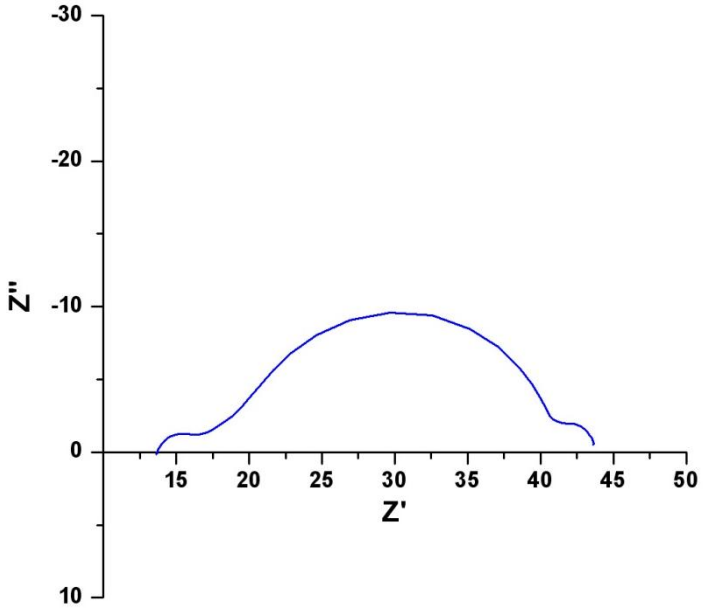

Fig E2 EIS response of aqueous cell containing 2.5M PMII, 0.05M I_2, 0.1M GSCN, 0.5M tBP and 1% Triton X-100 dyed in 0.3mM Z907.

References

(1) O'Regan, B. C.; Durrant, J. R. *Accounts Chem Res* 2009, *42*, 1799.

(2) Fattori, A.; Peter, L. M.; Belding, S. R.; Compton, R. G.; Marken, F. *J Electroanal Chem* 2010, *640*, 61.

(3) Li, W.; Ni, C.; Lin, H.; Huang, C. P.; Shah, S. I. *J Appl Phys* 2004, *96*, 6663.

(4) Grätzel, M. *J. PhotoCh. PhotoBio. C* 2003, *4*, 145.

(5) http://www.dyesol.com/products/dsc-materials/pastes/18nrt-transparent-titania-paste.html, Accessed 04.06.13.

(6) Haynes, W. M.; Bruno, T. J.; Lide, D. R. *CRC handbook of chemistry and physics*; 94th ed., 2013-2014 / editor-in-chief, W.M. Haynes ; associate editor, Thomas J. Bruno ed.; CRC: Boca Raton, Fla. ; London, 2013.

(7) Datta, J.; Bhattacharya, A.; Kundu, K. K. *B Chem Soc Jpn* 1988, *61*, 1735.

(8) Katzin, L. I.; Gebert, E. *J Am Chem Soc* 1955, *77*, 5814.